

Photon Based Electron Beam Analysis at ELSA Utilizing Synchrotron Radiation and Compton Scattering

Dissertation
zur
Erlangung des Doktorgrades (Dr. rer. nat.)
der
Mathematisch-Naturwissenschaftlichen Fakultät
der
Rheinischen Friedrich-Wilhelms-Universität Bonn

von
Michael T. Switka
aus
Mannheim

Bonn, September 2019

Dieser Forschungsbericht wurde als Dissertation von der Mathematisch-Naturwissenschaftlichen Fakultät der Universität Bonn angenommen und ist auf dem Publikationsserver der Universität Bonn unter <https://nbn-resolving.org/urn:nbn:de:hbz:5-60334> elektronisch publiziert.

1. Gutachter: Prof. Dr. Wolfgang Hillert

2. Gutachter: Prof. Dr. Klaus Desch

Tag der Promotion: 13. Dezember 2019

Erscheinungsjahr: 2020

*A glance at light reveals so many of nature's secrets
And there is much yet to be seen
To my daughter Johanna*

Summary

The beam diagnostic capabilities of the ELSA storage ring have been extended by a synchrotron radiation beamline with a fast optical recorder for three-dimensional photometry of the electron beam and by a laser Compton backscattering polarimeter for monitoring the polarization degree of the stored electrons. The hardware performance of both beamlines allows extensive analysis procedures and parameter monitoring for the improvement of the accelerator's operation.

The M7 photon beamline utilizes visible synchrotron radiation and enables the visualization of the electron beam with up to single bunch resolution. It allows simultaneous monitoring of the horizontal, vertical and longitudinal electron beam profile at multiple observation field spans from 3.1 to 28 mm within time frames of 74 ps to 100 ms. The visualization and measurement quality of important accelerator parameters – such as beam size, tune, damping times, bunch length and filling pattern – are demonstrated. It is observed that the numerical image analysis shows limits of validity in some cases, concerning measurements of the transverse beam size and bunch length. Dynamic beam behavior is, however, well observable and quantifiable. Beam properties such as the storage ring tune and the filling pattern homogeneity can be accurately determined through transverse and longitudinal images of the electron beam.

At the Compton polarimeter beamline circularly left and right polarized photons from a continuous wave laser source scatter off the stored electrons. The vertical profiles of the backscattered γ -photons are digitized by an in-house developed silicon microstrip detector and the electron beam polarization is determined through the shift in the means of profiles obtained from left and right circularly polarized photons. For profile quality enhancement a Pearson type VII peak function fit has shown to increase the measurement accuracy significantly. The polarimeter's analyzing power was obtained through the observation of the Sokolov-Ternov self-polarization effect and was determined to amount $(61.2 \pm 8.9) \mu\text{m}/100\%$ at 2.73 GeV beam energy. A statistical measurement accuracy of 2 % could be obtained within 5 minutes of measurement time and 1.4 % within 15 minutes. Compton polarimeter measurements of source-polarized electrons were able to resolve known spin dynamical effects occurring in the ELSA storage ring such as crossings of integer resonances and spin rotation through the application of solenoid magnetic fields. The polarimeter data was acquired within a limited testing period between October 2016 and January 2017.

Contents

1	Development and Research at the ELSA Facility	1
1.1	The Electron Accelerator and Recent Upgrades	1
1.2	Particle Physics Experiments at ELSA	4
1.2.1	The CBELSA/TAPS Experiment	4
1.2.2	The BGO-OD Experiment	6
1.2.3	The Detector Test Area	7
1.3	ELSA Compared to Other Photoproduction Facilities	8
2	Electron Spin Dynamics and the Emission of Synchrotron Radiation	9
2.1	The Electron in the Magnetic Field	9
2.1.1	Intrinsic Spin and Polarization	9
2.1.2	Spin Precession	10
2.1.3	Depolarizing Impact of Horizontal Magnetic Fields	12
2.2	Synchrotron Radiation	13
2.2.1	Total Radiation Power	13
2.2.2	Spectral, Spatial and Polarization Properties	14
2.3	Quantum Mechanical Effects	18
2.3.1	Influence of the Particle Spin on Synchrotron Radiation	18
2.3.2	Influence of Synchrotron Radiation on Beam Polarization	19
2.3.3	Stochastic Character of Synchrotron Radiation	21
3	The Optical Diagnostic Beamline M7	23
3.1	Photon Beamline	23
3.1.1	Vacuum System	23
3.1.2	Optical Setup	24
3.2	Streak Camera	31
3.2.1	Electron Beam Imaging in Focus Mode	33
3.2.2	Slow Sweep Operation Mode	34
3.2.3	Synchroscan Operation Mode	38
3.2.4	Streak Image Analysis Software	42
3.2.5	Timing and Controls	42
3.3	Radiation Levels and Equipment Protection	44
3.3.1	Radiation Damage on Electronic Equipment	44
3.3.2	Situation at the Experimental Area	45
4	Observation of Particle Dynamics via Synchrotron Radiation	49
4.1	Particle Motion	49
4.1.1	Transverse Equation of Motion	50

4.1.2	Betatron Tune	52
4.1.3	Longitudinal Equation of Motion	52
4.1.4	Synchrotron Tune	55
4.1.5	Optical Resonances	56
4.1.6	Radiation Damping	57
4.2	Energy Spread and Bunch Length	58
4.3	Beam Emittance and Transverse Size	61
4.4	Filling Pattern	63
5	Compton Backscattering and Polarimetry	67
5.1	Compton Scattering	67
5.1.1	Scattering on Relativistic Electrons	68
5.1.2	Backscattered Photons in the Laboratory Frame	69
5.1.3	The Compton Cross Section	69
5.2	Polarization Measurement Technique	72
5.2.1	Count Rate Asymmetry Method	72
5.2.2	Shift in the Means Method	73
5.3	Photon Rates	74
5.3.1	Photon Backscattering Rate	74
5.3.2	Radiation Background	75
5.4	Detection of Backscattered Photons	77
5.4.1	Photon to Charge Conversion	77
5.4.2	Silicon Microstrip Detector	80
5.5	Numerical Simulation of Scattering on a Realistic Electron Beam	81
6	The ELSA Compton Polarimeter	85
6.1	Historical Overview of Compton Polarimetry at ELSA	86
6.1.1	Ar ⁺ Laser Polarimeter	86
6.1.2	DPSS Laser Polarimeter	87
6.1.3	OPSL Polarimeter	88
6.2	The Compton Polarimeter Beamline	89
6.2.1	Electron Beam Size at the Photon Interaction Point	91
6.2.2	The Photon Beam	92
6.3	The Silicon Microstrip Detector	100
6.3.1	Measurement Procedure	101
6.3.2	Beam Profiles	101
6.4	Shift in the Means Analysis	103
6.4.1	Determining the Profile's Center of Gravity	104
6.4.2	Exemplary Measurements with Source-Polarized Electrons	107
6.4.3	Analyzing Power and Detector Calibration Through Self-Polarization	109
6.4.4	Photon Scattering Rates	112
6.4.5	Polarization Measurement Accuracy	112
7	Observation of Spin Dynamics via Compton Scattering	115
7.1	Effects due to Larmor Precession	115
7.2	Depolarizing Resonances	115
7.2.1	Depolarization in the Booster Synchrotron	117

7.2.2	Depolarization in the ELSA Storage Ring	117
7.2.3	Resonance Strength and Spin Flip	119
7.2.4	Equilibrium of Depolarization and Self-Polarization	121
8	Conclusion and Outlook	123
8.1	Synchrotron Radiation Diagnostic Beamline	123
8.2	Compton Polarimeter	124
A	Quantum Mechanical Description of Synchrotron Radiation	127
A.1	Total Emission Power	127
A.2	Photon Polarization	128
B	Exemplary Analysis of Streak Camera Photon Profiles	129
C	Relativistic Kinematics	133
C.1	Kinematic Parameters	133
C.2	Lorentz Transformation and Compton Scattering	134
D	Stokes Parameters and Photon Polarization	135
E	Gaussian Beam Propagation Theory	137
F	Silicon Microstrip Detector Channel Correction	139
	List of Figures	151
	List of Tables	155
	Acronyms	157
	Acknowledgements	161

Development and Research at the ELSA Facility

1.1 The Electron Accelerator and Recent Upgrades

The Physics Institute of Bonn University operates the [Elektronen Stretcher Anlage \(ELSA\)](#) accelerator facility. It accelerates spin-polarized or unpolarized electrons up to 3.5 GeV beam energy¹ utilizing a storage ring based design, capable of quasi-continuous electron beam extraction to three experimental stations.

The injector system consists of a 50 kV source for polarized or thermionic electrons from which a [linear accelerator \(linac\)](#) increases the particles' energy to 26 MeV. A 1.6 GeV combined-function synchrotron [[Alt+68](#)] accelerates the electrons to a typical storage ring injection energy of 1.2 GeV. [Linac](#) and booster synchrotron supply a charge of up to 2 nC at a rate of 50 Hz and fill the storage ring to 50 mA in typically less than 600 ms. With fast ramping magnetic fields and the corresponding [radio frequency \(RF\)](#) infrastructure the beam energy is increased with up to 7 GeV/s, allowing [ELSA](#) to be used as a cyclic spilling machine with high [duty cycle](#).

Extraction takes place via excitation of a third-integer betatron resonance. Rates for stabilized continuous beam extraction range from 100 Hz (attoamperes) to more than 1 GHz (several nanoamperes). A spill cycle – including injection, energy increase and extraction phase – is illustrated in [Fig. 1.1](#). At two experimental stations the extracted beam is used for photoproduction experiments where the electrons are converted into photons via bremsstrahlung. The third extraction beamline is designed for electron extraction onto a detector test irradiation area.

Due to the periodicity of the circular accelerator [lattice](#), beam instability mechanisms and depolarizing resonances may occur and destructively affect the beam or its polarization. Therefore, stable machine operation requires the implementation of adequate countermeasures, particularly during the acceleration phase. To improve the accelerator's performance the machine underwent several infrastructural upgrades within the [collaborative research center \(CRC\) TRR 16²](#) funding period until mid 2016 [[Tho](#)]. Two particular projects within this funding program were the installation of an optical diagnostic beamline utilizing [synchrotron radiation \(SR\)](#) – which is emitted from the circulating electrons – and the development, implementation and commissioning of a polarimeter based on Compton scattering. Both projects are described within the scope of this work. An illustration of the [ELSA](#) facility with highlighted locations of the [SR](#) diagnostic beamline and the Compton polarimeter is shown in [Fig. 1.2](#). A brief motivation for the realization of those projects is given below.

¹Maximum beam energy for standard operation is 3.2 GeV.

²Trans-regional collaboration with the universities of Bochum and Gießen, Germany.

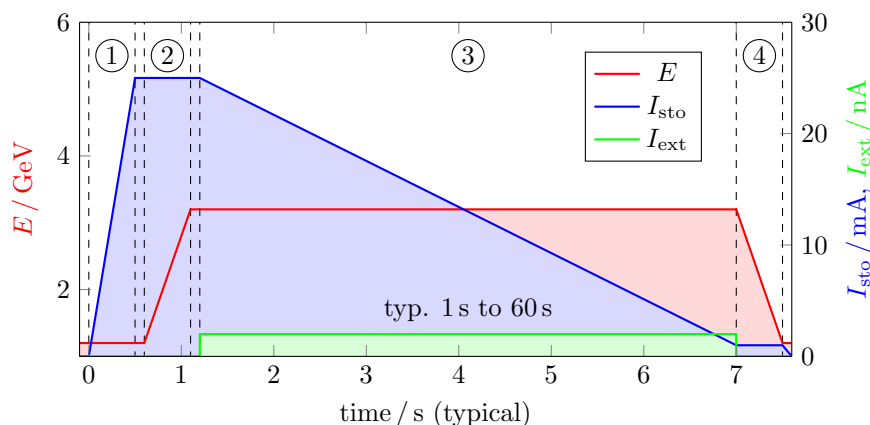


Figure 1.1: Storage ring cycle: The beam injection phase (1) is followed by a short damping period before the beam energy E is increased (2). After a brief preparation phase the stored beam current I_{sto} decreases linearly during extraction (3), providing a constant extraction current I_{ext} . After the spill the energy is decreased (4) before a new injection is prepared.

Optical Diagnostics for Beam Instability and Temporal Precision Measurements

Several devices for the diagnosis and correction of beam instabilities in the storage ring were implemented over the past few years, eventually providing improved beam stability and allowing an increase of the stored beam current towards 200 mA^3 . A crucial component of this upgrade is the [bunch-by-bunch feedback system \(BBB\)](#) [Rot12; Sch15], which is based on [capacitive beam position monitors \(BPMs\)](#). It measures the beam centroid position of each particle ensemble circulating in the storage ring and applies fast corrections through transverse and longitudinal beam kicker devices.

In addition, a diagnostic photon beamline was implemented allowing the observation of the electron beam by detection of [visible photon radiation \(VIS\)](#), which is part of the bending magnet [SR](#) emission spectrum. The optical recorder is a streak camera which has transverse and longitudinal electron beam imaging capability with picosecond time response. In contrast to the [BBB](#), the optical apparatus detects the size (width, height and length) of the circulating particle ensembles. It is therefore used for precise measurements of the electron bunch length or the storage ring's filling pattern and offers a temporal view on beam dynamics and potential beam instabilities.

Acceleration of Polarized Electrons and Polarimetry

In contrast to the acceleration of electrons with no distinct spin orientation, the generation of spin-polarized electrons and the successful spin transfer to the experimental stations is dissimilarly more elaborate. To obtain longitudinally polarized electrons at the [ELSA](#) facility, a GaAs/GaAsP-type strained superlattice crystal is illuminated within [ultra high vacuum \(UHV\)](#) conditions by a circularly polarized, pulsed [infrared \(IR\)](#) photon beam emitted from a Ti:Sa laser. The photoinjector supplies a microseconds long electron beam pulse of 120 mA intensity with a longitudinal polarization degree of 86% [Hei14, Section 1.1]. Before injection into the [linac](#), the longitudinal polarization is transformed into the vertical plane by an electrostatic deflector. The degree of polarization is then measurable by a polarimeter setup based on [Mott scattering](#) [Hil00, Section 4.4.3]. After passing the electrostatic deflector the particle spin

³Sufficient [RF](#) power for this amount of stored current is currently available up to 2.6 GeV beam energy [Sch15, Section 13.1].

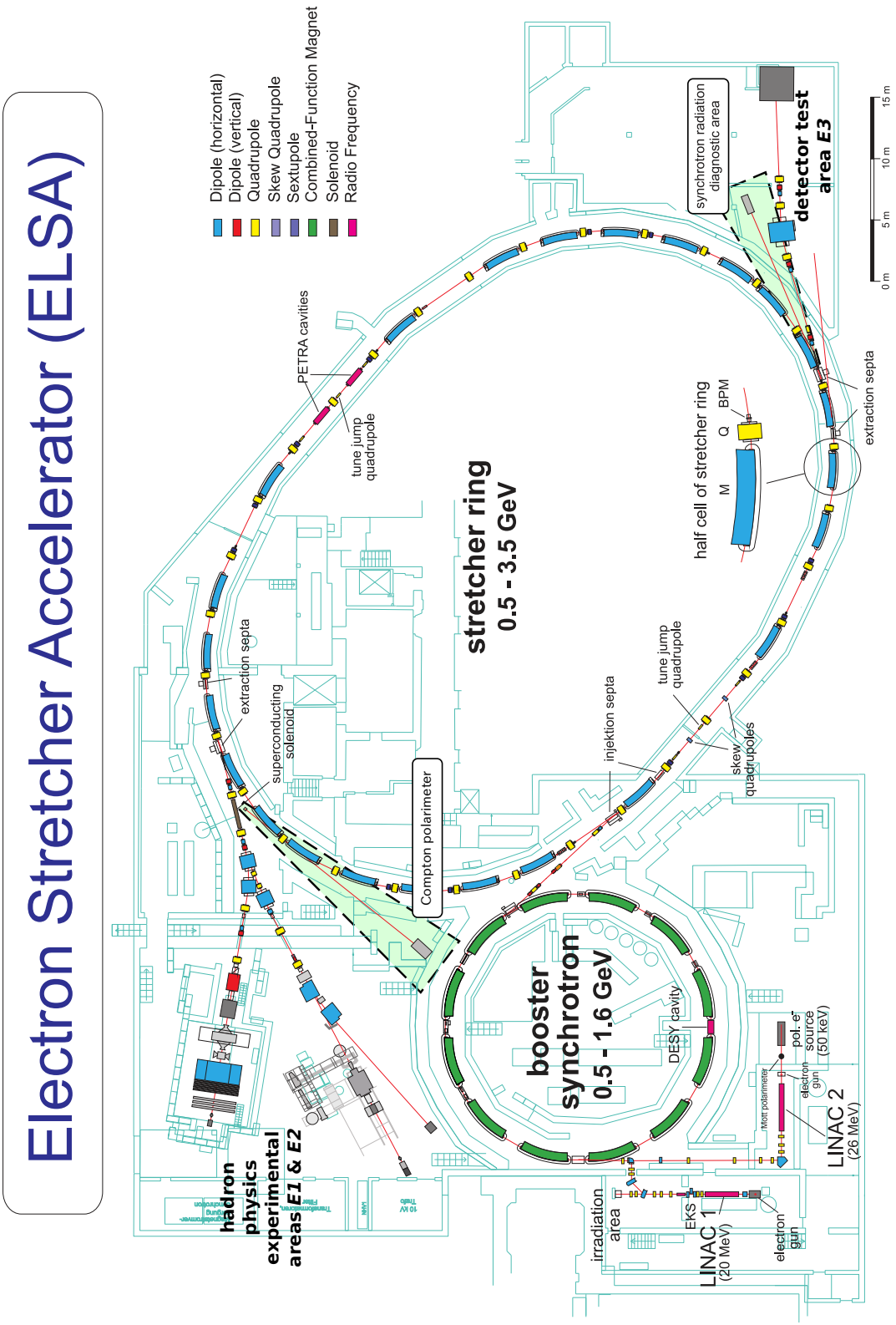


Figure 1.2: Facility drawing of the [ELSA](#) accelerator laboratory with marked locations of the Compton polarimeter and the M7 synchrotron radiation diagnostic beamline (both green).

axis is aligned with the subsequent bending fields of the synchrotron accelerators, which is necessary for a successful polarization transfer to the experimental stations. In contrast to acceleration by the [linac](#), the periodic circulation within the booster synchrotron and the storage ring causes loss of polarization, as several depolarizing resonances are crossed during the energy increase. The polarization degree of the delivered electrons is measurable by [Møller scattering](#) polarimeters, which are installed at each hadron physics experimental station. In practice, however, the Møller measurement procedure is tedious when it comes to the effective implementation of countermeasures for compensating the effect of depolarizing resonances within the storage ring. As certain experimental measurement modes prohibit the use of Møller polarimetry a polarimeter based on [Compton backward scattering \(CBS\)](#) (Compton polarimeter) is required at [ELSA](#), of which multiple versions were implemented over the past 20 years. However, due to spatial and technological restrictions the data quality remained poor until the advent of stable and compact high-power laser sources and a reliable γ -ray detector module. The development of a silicon microstrip detector for the analysis of the backscattered γ -rays was recently completed and first qualitative Compton polarimeter data could be obtained by mid 2016.

1.2 Particle Physics Experiments at ELSA

The three electron extraction beamlines at [ELSA](#) are currently operated for

- the [crystal barrel experiment at ELSA with TAPS photon spectrometer \(CBELSA/TAPS\)](#),
- the [BGO crystal calorimeter and open dipole spectrometer experiment \(BGO-OD\)](#) and
- the [high energy particle physics \(HEP\)](#) detector testing community.

Polarized photons are of importance for the hadron physics photoproduction experiments [CBELSA/TAPS](#) and [BGO-OD](#), where the high energy electrons are used to produce a γ -ray probe beam via bremsstrahlung. Linear photon polarization can be generated by coherent bremsstrahlung of unpolarized electrons from crystalline materials. Circular photon polarization, however, requires the interaction of longitudinally polarized electrons. To obtain the latter, the vertically oriented electron polarization within the storage ring is rotated into the horizontal plane through a superconducting solenoid magnet in the extraction beamline (compare with e.g. [[Kam10](#), Section 3.4]). The subsequent beamline's bending magnets rotate the spin vector eventually towards the longitudinal plane. The bremsstrahlung process of longitudinally polarized electrons produces the desired circularly polarized γ -photons. A sufficient photon polarization is essential for the conduction double-polarization measurements at the [CBELSA/TAPS](#) experiment, which uses a spin-polarized hadronic target. The experimental programs are briefly described below.

1.2.1 The CBELSA/TAPS Experiment

The [CBELSA/TAPS](#) experiment uses a CsI(Tl) calorimeter (*crystal barrel*) and the miniTAPS⁴ photon spectrometer to investigate $\vec{\gamma}\vec{p} \rightarrow X$ reactions. In analogy to atomic spectroscopy, the excitation of target particles provides information about the inner hadron structure. Since hadron constituents interact through the strong nuclear force, lifetimes of excited particle states are short and lie in the order of 10^{-23} s. Consequently, the energy width of the excited states lies in the order of several megaelectronvolts (MeVs). In addition, multiple reaction channels usually overlap in the energy spectrum, which impedes proper identification of individual reaction channels. [Figure 1.3](#) shows the contribution of different reactions to the total photoproduction cross section. Especially at higher energies, identification of the individual

⁴The BaF₂ detector originates from the former Two/three Arm Photon Spectrometer experiment in Darmstadt/Mainz, Germany.

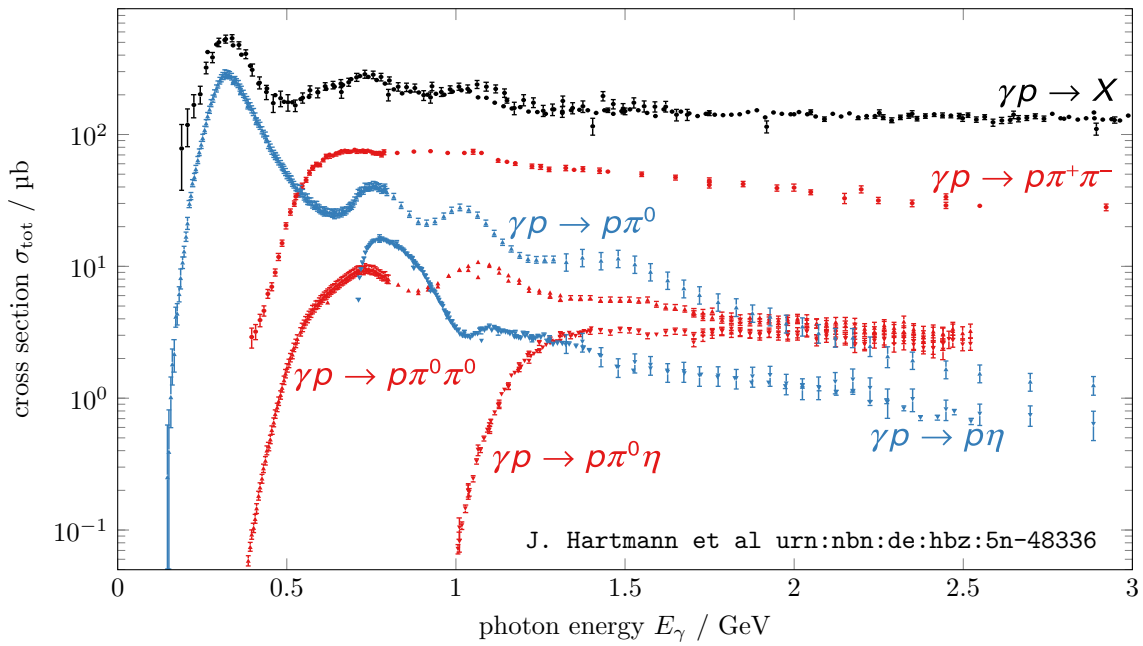


Figure 1.3: Total photoabsorption cross section of $\vec{\gamma}\vec{p} \rightarrow X$ compared to meson photoproduction cross sections of prominent contributing decay channels [Har17, Fig. 2.1].

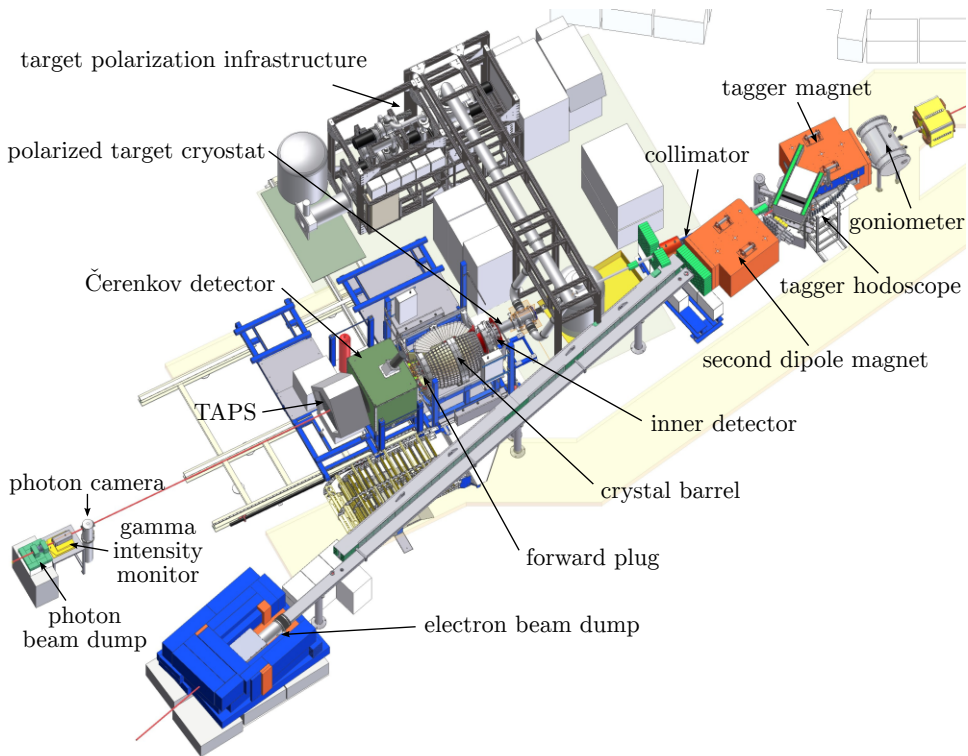


Figure 1.4: Overview of the experimental beamline of the CBELSA/TAPS experiment [Har17, Fig. 3.2].

resonance contributions is only possible via [partial wave analysis \(PWA\)](#) of experimental observables. This technique is utilizable in the mid-energy regime of a few GeVs excitation energy, where the *strong coupling constant* approaches $a_s \rightarrow 1$. For a given linear or circular γ -ray polarization $\mathcal{P}_{\gamma,\text{lin}}$ and $\mathcal{P}_{\gamma,\text{circ}}$, and target polarization degree $\vec{\mathcal{P}} = (p_x, p_y, p_z)$, the observables Σ, H, F, P, T, G and E contribute to the reaction cross section [BDS75]:

$$\begin{aligned} \frac{d\sigma}{d\Omega}(\theta, \phi) = & \left(\frac{d\sigma}{d\Omega}(E_\gamma, \theta) \right)_{\text{unpol}} \{ 1 - P_{\gamma,\text{lin}} \Sigma(E_\gamma, \theta) \cos 2\phi \\ & + p_x \cdot (- P_{\gamma,\text{lin}} H(E_\gamma, \theta) \sin 2\phi + P_{\gamma,\text{circ}} F(E_\gamma, \theta)) \\ & + p_y \cdot (+ P_{\gamma,\text{lin}} P(E_\gamma, \theta) \cos 2\phi - T(E_\gamma, \theta)) \\ & - p_z \cdot (- P_{\gamma,\text{lin}} G(E_\gamma, \theta) \sin 2\phi + P_{\gamma,\text{circ}} E(E_\gamma, \theta)) \} . \end{aligned}$$

Here, θ is the scattering angle and ϕ the angle between the scattering plane and the reaction plane. With the current experimental setup⁵ the observables $\left(\frac{d\sigma}{d\Omega}(E_\gamma, \theta) \right)_{\text{unpol}}$ and $\Sigma(E_\gamma, \theta)$ are obtainable with unpolarized and linearly polarized photon beams, respectively. The observables $G(E_\gamma, \theta)$ and $E(E_\gamma, \theta)$ are obtainable with a linearly and circularly polarized photon beam and a longitudinally polarized target.

Experimental Infrastructure

The extracted electron beam interacts with an exchangeable thin target (e.g. 12 to 300 μm copper foil) on a goniometer mount within the radiator tank, is then deflected by a magnetic dipole field and eventually dumped aside the experimental site (Fig. 1.4). Those electrons, which created a photon by bremsstrahlung off the radiator target, proceed with decreased energy and travel on dispersive trajectories within the downstream dipole magnet. They induce a signal on a scintillator array (tagging hodoscope) behind the magnet yoke which measures the energy distribution of the electrons, and consequently that of the photons. If a magnetized amorphous foil is used in the radiator tank, [Møller scattering](#) electrons can be detected by lead glass scintillators behind the tagger magnet. This Møller polarimeter measures the delivered degree of longitudinal electron polarization.

The bremsstrahlung γ -photons hit a *frozen spin* butanol target in the center of the crystal barrel detector. It covers a solid angle of close to 4π and contains a cylindrical scintillating fiber detector for charged particle detection. Since the particle rate in forward direction is largest, a forward CsI detector with higher resolution and the miniTAPS detector complement the barrel. A Čerenkov gas detector identifies charged particles created from Compton scattering or pair production. To sort out these electromagnetic traces from hadronic events, the inner fiber detector and the Čerenkov detector provide veto signals for the data readout. A photon camera and a gamma intensity monitor (GIM) in front of the photon beam dump measure the beam position, size and intensity.

1.2.2 The BGO-OD Experiment

The [BGO-OD](#) experiment has akin research obligations as [CBELSA/TAPS](#), but focuses on strangeness photoproduction analysis through its forward momentum resolution capability. It uses a [BGO](#) calorimeter combined with a mass spectrometer to investigate meson photoproduction reactions, where neutral and charged reaction channels are of interest. As charged mesons decay due to the weak nuclear force, their lifetimes can be in the order of 10^{-8} s and particle traces may reach lengths of a few meters. The electron

⁵The target polarization is longitudinal (p_z) or unpolarized.

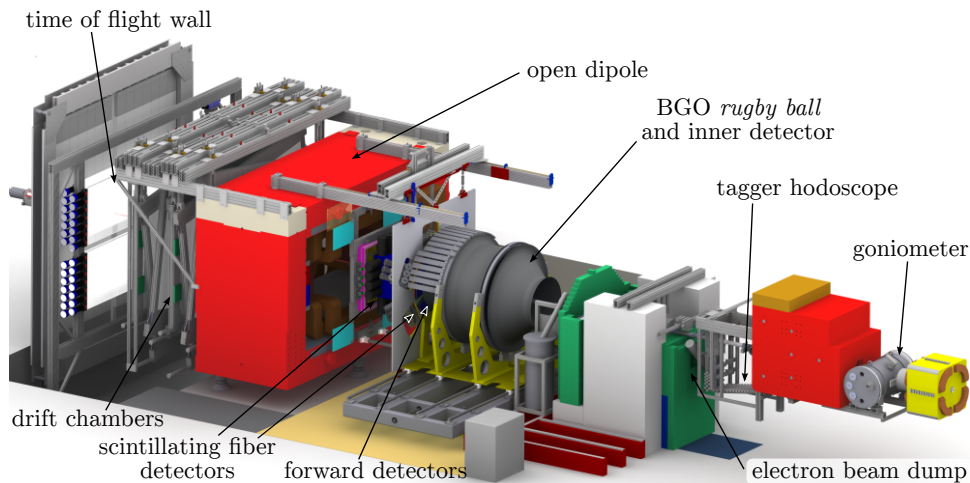


Figure 1.5: Overview of the experimental beamline of the BGO-OD experiment at ELSA [Fre17, Fig. 2.1].

extraction beamline is similar to that of CBELSA/TAPS and shares the same features regarding tagging and polarimetry (Fig. 1.5). The unpolarized target within the BGO calorimeter consists of liquefied hydrogen or deuterium. The calorimeter is equipped with an inner cylindrical detector and a multi-wire proportional chamber (MWPC) for trace reconstruction within the BGO ball. A silicon-strip detector and a multi-gap resistive plate chamber (MRPC) covers trace reconstruction and calorimetry in the forward direction. Before the particles enter the spectrometer magnet, their initial position is measured by two scintillating fiber detectors. As kaons and pions show similar trace and detection characteristics in the subsequent time of flight measurements, the installation of an aerogel Čerenkov detector is planned, which distinguishes between these particle types. The dipole magnet then separates particles with different mass and charge ratios. To reconstruct the individual curved traces within the magnetic field, eight drift chambers with two layers each are installed behind the magnet. Time of flight (TOF) walls made of scintillator beams allow to measure the particles' velocities, from which their momenta and energies can be reconstructed.

1.2.3 The Detector Test Area

The recently commissioned detector test beamline [Heu17] offers an irradiation area for HEP detector development. The magnet optics of the extraction beamline allow for beam size and divergence manipulation before the electrons leave the vacuum system through a Kapton foil window towards a testing target. Beam sizes available at the test site range from $\sigma_{x,z} = 1$ to 10 mm. Controlled extraction rates of down to 100 Hz are possible, featuring a spill of single, consecutive electrons for well-defined detector test conditions. To protect sensitive equipment from machine failure modes, where large amounts of stored electrons ($E_{\text{tot}} \approx 50$ J) are potentially extracted at once, ELSA can be operated in a *low current mode*. Therein, a low rate extraction is ensured through a controlled low-current injection into the ELSA storage ring, where approximately 100 nA can be stored ($E_{\text{tot}} \approx 100$ μ J) and slowly extracted. Beam intensity monitoring is performed through a photomultiplier setup which measures the low amount of SR emitted from the storage ring. The primary electron beam offers testing opportunities for the development of novel semiconductor detector types. Research involves the improvement of detection capabilities of ionizing particles and the investigation of reliability and radiation hardness of detector module prototypes. For example, the new generation of pixel detectors required for the high luminosity upgrade of the LHC

and the ATLAS⁶ detector are collaboratively developed, constructed and tested at Bonn University.

1.3 ELSA Compared to Other Photoproduction Facilities

There are currently four facilities worldwide providing medium-energetic (GeV) circularly polarized photons for nuclear research with comparable beam specifications (see Table 1.1). Recent advances in superconductor and laser technology allowed the realization of machine-specific upgrade programs at some facilities, whose operation modes require less correction mechanisms regarding the delivery of electrons or photons with high polarization degrees, as compared to the ELSA design. Recirculating accelerators such as MAMI⁷ in Mainz, Germany, or CEBAF⁸ in Newport News, VA, USA, are not affected by depolarizing resonances due to lattice periodicity. Their electron beam is guided on separate energy-specific trajectories to an acceleration cavity array and circulates a low number of times through the lattice. This approach provides high and stable beam currents at negligible polarization loss, but requires strong acceleration fields and therefore large building grounds, superconducting technology, or both. For this reason normal conducting MAMI is limited to beam energies of 1.6 GeV. CEBAF, however, has recently upgraded its recirculated superconducting linacs and raised its beam energy from 6 to 12 GeV. Its high current capability allows it to serve multiple experimental stations simultaneously. The CLAS⁹ [Com+17] experiment has similar research objectives as the hadron physics experimental programs in Bonn and data is collaboratively used to improve PWA methods and results. Another storage ring based approach for the production of γ -rays utilizes CBS. At the SPring-8¹⁰ synchrotron radiation facility in Hyogo prefecture, Japan, a polarized laser beam scatters off the 8 GeV stored electron beam. The backscattered γ -photons carry the initial photon polarization and reach energies of up to 2.4 GeV using green laser light, or 2.9 GeV when using an ultraviolet radiation (UV) laser to generate the photon probe beam. At ELSA, the CBS approach for photoproduction is unfeasible due to the limited electron energy and particle density in the storage ring. However, as mentioned above, the CBS effect is utilized for polarimetry purposes at ELSA.

facility	type	photon conversion	$E_{\gamma,\max}$	\dot{N}_{γ}	$I_{e^-,\text{typ}}$	$\mathcal{P}_{\gamma,\max}$
ELSA	synchrotron	bremsstrahlung	3.5 GeV	6 MHz	25 mA \rightarrow 1 nA (extr.)	86 %
MAMI	microtron	bremsstrahlung	1.6 GeV	50 MHz	20 μ A or 100 nA (pol.)	85 %
CEBAF	recirculating linac	bremsstrahlung	12 GeV	> 50 MHz	100 μ A	89 %
SPring-8	synchrotron	CBS	2.9 GeV	2 MHz	100 mA	100 %

Table 1.1: Currently operating mid-energy accelerator facilities providing polarized γ -photon beams for nuclear photoproduction experiments. Comparison of maximum achievable photon energy $E_{\gamma,\max}$, typical photon rate \dot{N}_{γ} , electron current $I_{e^-,\text{typ}}$ provided for the photoproduction beamlines and achievable photon polarization degree $\mathcal{P}_{\gamma,\max}$.

⁶A Toroidal LHC ApparatuS

⁷Mainzer Mikrotron

⁸Continuous Electron Beam Accelerator Facility

⁹CEBAF Large Acceptance Spectrometer

¹⁰Super Photon Ring - 8 GeV

Electron Spin Dynamics and the Emission of Synchrotron Radiation

In circular accelerators a magnetic structure guides particles of charge q repetitively to an electromagnetic cavity, where the particles gain energy. The predominant acting force is the Lorentz force

$$\vec{F}_L = q(\vec{E} + \vec{v} \times \vec{B}) , \quad (2.1)$$

where \vec{E} and \vec{B} are the electric and magnetic fields acting upon the particles with velocity \vec{v} . The scalar product in $\oint \vec{F}_L \cdot d\vec{s} = \Delta E$ allows an energy gain over a distance \vec{s} by applying an electric fields parallel to the velocity. Applying perpendicular electric or magnetic fields results in transverse particle deflection. In turn, this deflection is a source of electromagnetic radiation, which has a major influence on the beam dynamics of relativistic particles. In synchrotron-type accelerators the emission process of the **SR** determines electron beam properties such as size, equilibrium polarization and dynamic behavior. The following chapter specifies the properties of the electron, **SR** and its influence on the electron spin.

2.1 The Electron in the Magnetic Field

The electron is an elementary particle of mass $m = 511 \text{ keV}/c^2$ and hence comparably *light* in relation to e.g. the proton ($m_p = 938 \text{ MeV}/c^2$) or other leptons, such as the muon ($m_\mu = 106 \text{ MeV}/c^2$). Its charge is $q = -e$ and it is a spin-half particle, being categorized as Fermion. The electron spin, its properties and dynamics in the magnetic field are described below.

2.1.1 Intrinsic Spin and Polarization

The idea of an electron intrinsic spin was published by Uhlenbeck and Goudsmit in 1925 [UG25] to explain observed spectroscopy phenomena which were inconsistent with previous theories. Experimental proof of a spin effect was demonstrated by the Stern-Gerlach experiment [GS22], where silver atoms could be separated due to the intrinsic spin of the predominant valence electron. This spin is described quantum mechanically by the spin operator $\vec{S} = (S_x, S_y, S_z)$, whose eigenvalues amount $\pm\hbar/2$:

$$S_z \begin{pmatrix} |\uparrow\rangle \\ |\downarrow\rangle \end{pmatrix} = \frac{\hbar}{2} \begin{pmatrix} +|\uparrow\rangle \\ -|\downarrow\rangle \end{pmatrix} , \quad (2.2)$$

where $|\uparrow\rangle$ and $|\downarrow\rangle$ denote the quantized polarization states as projection of the spin vector $\vec{S} = (S_x, S_y, S_z)$ onto a coordinate axis [Sch95, Ch. 9.1]. For a particle ensemble within a magnetic field, the degree of polarization is given by

$$\mathcal{P} = \frac{N_\uparrow - N_\downarrow}{N_\uparrow + N_\downarrow}, \quad (2.3)$$

where N_\uparrow and N_\downarrow is the number of particles of the corresponding spin state. The mean spin direction is obtained by summation over all individual spin vectors

$$\vec{\mathcal{P}} = \frac{1}{N} \sum_i^N \vec{S}_i. \quad (2.4)$$

In a semi-classical picture, a spin vector \vec{S} precesses about an external magnetic field \vec{B} .

2.1.2 Spin Precession

Equation (2.1) describes the particle deflection and hence, the trajectory of an electron within a magnetic field \vec{B} . When a charged particle orbits with angular momentum \vec{L} within \vec{B} , a torque \vec{M} is exerted due to the particle's magnetic moment $\vec{\mu}_L$:

$$\vec{M} = \vec{\mu}_L \times \vec{B}, \quad \text{with} \quad \vec{\mu}_L = \frac{e}{2m} \vec{L} \quad \text{and} \quad \vec{L} = \vec{r} \times \vec{p}. \quad (2.5)$$

In analogy to this spin-orbit interaction, the intrinsic spin of the particle causes an additional magnetic moment

$$\vec{\mu}_S = g_e \frac{e}{2m} \vec{S}, \quad (2.6)$$

where the g-factor of the electron $g_e = -2.002319304361(82)$ is one of the most precisely measured values in physics [MNT14]. Its deviation from two is called the anomalous magnetic dipole moment

$$a = \frac{|g| - 2}{2}, \quad (2.7)$$

which amounts $a_e = 1.159652193(10) \times 10^{-3}$ for electrons. In analogy to the torque \vec{M} in Eq. (2.5), a time variation of the spin axis occurs according to

$$\frac{d\vec{S}}{dt} = \vec{\mu}_S \times \vec{B} \quad (2.8)$$

$$= -g_e \frac{e}{2m} \vec{B} \times \vec{S} = \vec{\Omega}_L \times \vec{S}. \quad (2.9)$$

If $\vec{\mu}_S$ is not aligned with \vec{B} , Larmor-precession of the spin vector \vec{S} around the magnetic field vector occurs with an angular frequency

$$\omega_L = g_e \frac{e}{2m} B. \quad (2.10)$$

When the electron moves at velocities close to the speed of light, a relativistic kinematic effect occurs in addition due to the rotation of the electron's rest frame within the Lorentz-boosted transverse electromagnetic fields. The angular frequency of the so called Thomas precession amounts [Jac67,

Section 11.5]

$$\omega_{\text{Th}} = \frac{1}{c^2} \frac{\gamma^2}{\gamma + 1} (\vec{a} \times \vec{v}), \quad \text{with} \quad \gamma = (1 - (v/c)^2)^{-1/2} \gg 1, \quad (2.11)$$

and contributes when the acceleration \vec{a} is perpendicular to the relativistic velocity \vec{v} , as is the case for bending magnet deflection in synchrotrons. Using the anomalous magnetic dipole moment a , Bargman, Michel and Telegdi stated a complete description of the spin motion within a homogeneous electromagnetic field [Tho27; BMT59]:

$$\frac{d\vec{S}(t)}{dt} = \vec{\Omega}_{\text{BMT}} \times \vec{S}, \quad (2.12)$$

where the precession axis is described by the explicit term

$$\vec{\Omega}_{\text{BMT}} := -\frac{e}{\gamma m} \left(\underbrace{(1 + \gamma a)\vec{B}_{\perp}}_{\text{Thomas prec.}} + \underbrace{(1 + a)\vec{B}_{\parallel}}_{\text{Larmor prec.}} + \left(\gamma a + \frac{\gamma}{\gamma + 1} \right) \frac{[\vec{E} \times \vec{v}]}{c^2} \right). \quad (2.13)$$

In the case of the ELSA storage ring, no transverse electric fields \vec{E} , nor parallel magnetic fields \vec{B}_{\parallel} in respect to the particle movement are of significance, hence Eq. (2.13) simplifies to

$$\vec{\Omega}_{\text{BMT}} \approx -\frac{e}{\gamma m} (1 + \gamma a) \vec{B}_{\perp}. \quad (2.14)$$

When the spin frequency is transformed into a coordinate system which moves along the particle's orbit, one obtains

$$\vec{\Omega}'_{\text{BMT}} = \vec{\Omega}_{\text{BMT}} - \vec{\Omega}_{\text{c}} = \gamma a \vec{\Omega}_{\text{c}}, \quad (2.15)$$

where $\vec{\Omega}_{\text{c}} = -e/(\gamma m)\vec{B}_{\perp}$ is the relativistic cyclotron frequency. From it, the number of spin revolutions per *lattice* revolution follows as

$$Q_{\text{sp}} := \frac{|\vec{\Omega}'_{\text{BMT}}|}{|\vec{\Omega}_{\text{c}}|} = \gamma a, \quad (2.16)$$

where Q_{sp} is called the *spin tune*. An illustration of the revolving spin vector is shown in Fig. 2.1.

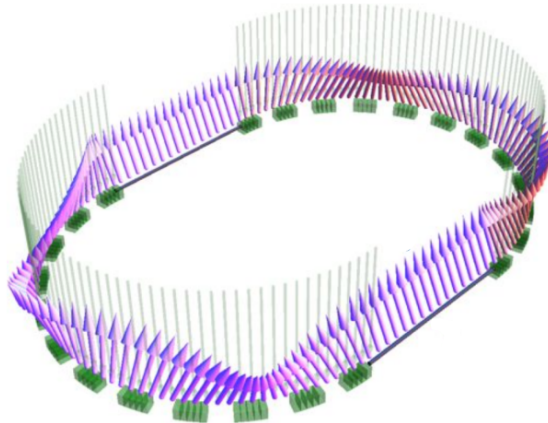


Figure 2.1: Exemplary calculation of an electron spin vector \vec{S} (purple) rotating in the bending field \vec{B} (green) of a circular accelerator *lattice* at $\gamma a = 2.97$ [Bol14, Fig. 3.3(a)].

2.1.3 Depolarizing Impact of Horizontal Magnetic Fields

The particle spin precesses around the synchrotron's vertical bending fields, as described by Eq. (2.14). In a particle ensemble, the individual spin vectors usually rotate without phase correlation (*incoherent*). Hence, the polarization degree of a particle ensemble in a horizontally orientated synchrotron is proportional to the projection of the summed spin vector of Eq. (2.4) to the vertical spin axis within a vertically oriented magnetic field:

$$|\vec{\mathcal{P}}| \propto |S_z^{\vec{}}|. \quad (2.17)$$

While the particles propagate along the lattice, stray magnetic fields may disturb the spin rotation around the predominant vertical spin axis by introducing an additional (e.g. horizontal) rotation axis. Such a disturbing field bends the polarization vector from the vertical plane towards the horizontal plane and the spin vector then proceeds its rotation with reduced $|S_z^{\vec{}}|$, as illustrated in Fig. 2.2. Extensive studies of spin dynamics and particle polarization simulations for the ELSA storage ring lattice have been performed by J. Schmidt [Sch17] and O. Boldt [Bol14]. Their results support the spin dynamics measurements and assumptions made in Section 7.2.

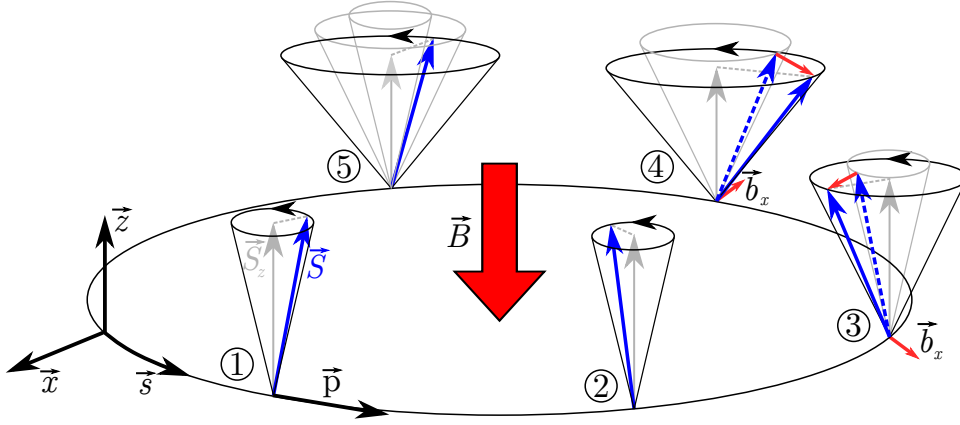


Figure 2.2: The particle spin vector \vec{S} precesses around the vertical spin axis $S_z^{\vec{}}$ which is aligned to the magnetic bending field \vec{B} (① & ②). Horizontal magnetic field disturbances \vec{b} tilt the spin rotation vector towards the horizontal (③ & ④), reducing the length of the vertical polarization vector projection $|S_z^{\vec{}}|$ and hence the polarization degree of the incoherently spinning particle ensemble (⑤).

2.2 Synchrotron Radiation

The properties of [SR](#), such as power, emission spectrum and angular flux distribution, are explained in the following sections. The role of quantum effects in the [SR](#) emission process is explicated as it influences two important properties of an accelerated beam: the size and the intrinsic polarization.

2.2.1 Total Radiation Power

When accelerated, charged particles emit radiation. The total emission power P_γ of accelerated electrons with momentum \vec{p} was first described by Larmor [[Lar97](#)]:

$$P_\gamma = \frac{e^2}{6\pi\epsilon_0 m^2 c^3} \left(\frac{d\vec{p}}{dt} \right)^2, \quad (2.18)$$

where ϵ_0 is the permittivity of free space and m is the electron mass. Liénard extended [Eq. \(2.18\)](#) for relativistic particle velocities, which describes the radiation power obtained from particle accelerators:

$$P_\gamma = \frac{2}{3} \frac{e^2}{4\pi\epsilon_0 c} \gamma^6 \left[\dot{\vec{\beta}}^2 - \left(\vec{\beta} \times \dot{\vec{\beta}} \right)^2 \right], \quad (2.19)$$

with the velocity $\vec{\beta} = \vec{v}/c$ and the relativistic Lorentz factor γ . Here, the summand $\dot{\vec{\beta}}^2$ describes the emission from acceleration parallel to the velocity, as is the case in [linacs](#). However, its contribution is negligible even for state-of-the-art acceleration field gradients of $dE/dx \approx 40 \text{ MeV/m}$. On the contrary, for circular motion the summand $|\vec{\beta} \times \dot{\vec{\beta}}| = \beta \dot{\beta}$ leads to a significantly higher contribution [[Jac67](#), Section 14.2]:

$$P_\gamma = \frac{2}{3} \frac{e^2 c}{4\pi\epsilon_0 \beta^4} \frac{\gamma^4}{R^2}, \quad (2.20)$$

where R is the bending radius of the particle orbit. Note that the power loss increases with the fourth power of the particle's energy $E = \gamma mc^2$. The energy loss per particle and revolution is

$$\Delta E_{\text{SR}} = \int_0^{t_b} P_\gamma \cdot dt, \quad (2.21)$$

where the time of flight within the bending magnets t_b is related to the particle revolution period t_{rev} in a circular [lattice](#) of length L as in

$$t_b = \frac{2\pi R}{\beta c} = \frac{2\pi R}{L} \cdot t_{\text{rev}}. \quad (2.22)$$

The accelerating cavities of an accelerator restore the loss due to [SR](#) emission by adding the [circumference voltage](#) (per revolution):

$$\Delta E_{\text{SR}}/\text{eV} = \frac{e\beta^3}{3\epsilon_0 (mc^2)^4} \frac{E^4}{R} \approx 88.5 \times 10^3 \frac{(E/\text{GeV})^4}{R/\text{m}}, \quad (2.23)$$

where the approximation holds for ultra-relativistic particles ($\beta \rightarrow 1$). The net synchrotron radiation power loss of a circulating beam of current I_{beam} consisting of N electrons is

$$P_{\text{SR}} = \Delta E_{\text{SR}} N / t_{\text{rev}} = \Delta E_{\text{SR}} / \text{eV} \cdot I_{\text{beam}} . \quad (2.24)$$

Figure 2.3 shows the relation $P_{\text{SR}}(E)$ for ELSA ($R = 10.88$ m) at several stored beam currents.

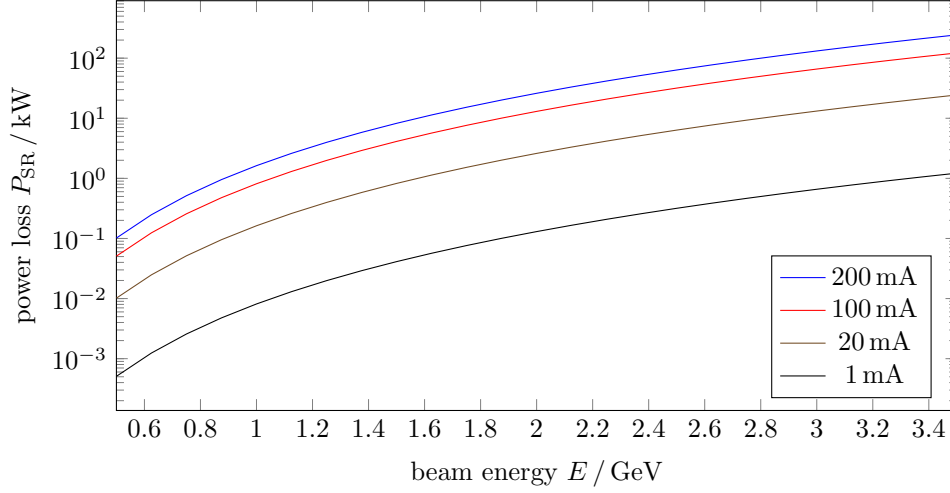


Figure 2.3: Power loss due to the emission of synchrotron radiation at ELSA for several stored beam currents.

2.2.2 Spectral, Spatial and Polarization Properties

In the rest frame of the electron the angular power distribution follows the typical form of a Hertz dipole:

$$\frac{dP_\gamma}{d\Omega} = \frac{e^2}{16\pi^2 \epsilon_0 m^2 c^3} \left(\frac{d\vec{p}}{dt} \right)^2 \sin^2 \Psi , \quad (2.25)$$

where Ψ is the angle between direction of observation and acceleration. In the laboratory frame the $\sin^2 \Psi$ toroidal form of Eq. (2.25) in the rest frame is transformed to a sharply forward-peaked lobe. For a horizontally accelerated electron the spatial distribution per solid angle $d\Omega = \sin \vartheta d\vartheta d\varphi$ with polar angle ϑ and azimuth φ becomes [Jac67, Section 14.3]:

$$\frac{dP_\gamma}{d\Omega} \simeq \frac{e^2 \dot{v}^2}{2\pi^2 \epsilon_0 c^3} \gamma^6 \frac{1}{(1 + \gamma^2 \vartheta^2)^3} \left[1 - \frac{4\gamma^2 \vartheta^2 \cos^2 \varphi}{(1 + \gamma^2 \vartheta^2)^2} \right] . \quad (2.26)$$

However, the **root mean square (RMS)** of the total power distribution $P_\gamma(\vartheta)$ is approximately inverse to the Lorentz γ :

$$\vartheta_{\text{rms}} = \langle \vartheta^2 \rangle^{1/2} \approx 1/\gamma . \quad (2.27)$$

For example the narrow cone of emission at ELSA ranges from 1.02 to 0.26 mrad for energies of 0.5 to 3.2 GeV. The RMS is dominated by the high-energy photons of the broad emission spectrum and visible parts of SR have broader emission angles, as shown below.

Synchrotron Radiation Spectrum

In comparison to the non-relativistic, monochrome Hertz-dipole emission, the **SR** emitted from ultra-relativistic electrons within bending magnets has a broad spectral range. Utilizable intensities often span from THz to hard X-rays, and thus **SR** has become an important tool for spectroscopy applications. The reason for the broad spectrum lies in the uncertainty principle of wave mechanics:

$$\Delta\omega \Delta t \geq 2\pi, \quad (2.28)$$

where $\Delta\omega$ is the span of angular frequencies contained in a wave packet of duration Δt . For bending magnet radiation, this pulse length corresponds to the signal of a light cone sweeping across an observer O , while the source electron travels on a curved trajectory, as depicted in Fig. 2.4. Since the photons

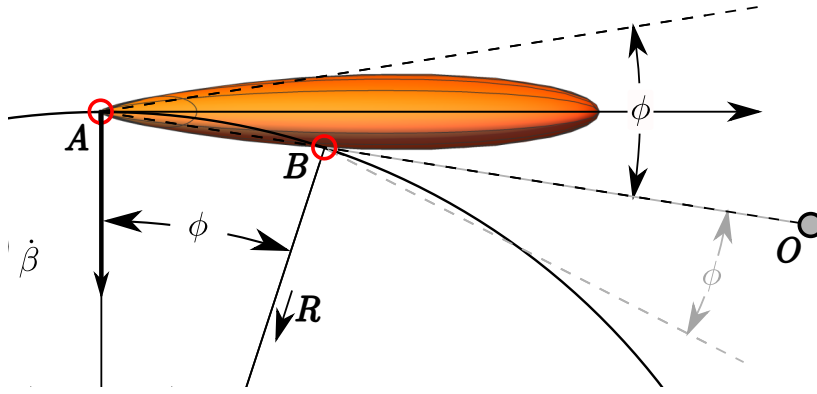


Figure 2.4: Synchrotron radiation cone of width $\phi = 1/\gamma$ sweeping across an observation point O while the photon source is moving from points A to B on the circular trajectory.

travel with finite velocity c , the pulse duration Δt originates from the difference of the photon's and electron's time of flight from point A to B [Wil00, Section 2.3]:

$$\Delta t = t_e - t_\gamma = \frac{2R\phi}{\beta c} - \frac{2R \sin \phi}{c} \stackrel{v \rightarrow c}{\approx} \frac{R}{\gamma^3 c}. \quad (2.29)$$

For example, one obtains a pulse duration of $\Delta t \approx 10^{-19}$ s for $E = 3.2$ GeV electrons under a sweeping angle of $\phi = 2\vartheta_{\text{rms}}$. The corresponding frequency bandwidth is $\Delta\omega \sim 10^{19}$ Hz ($\Delta E_\gamma \sim 40$ keV). This continuous spectrum expands up to a *critical* photon energy [Lee04, Section 4.1.3]

$$E_c = \hbar\omega_c = \hbar \frac{3 c \gamma^3}{2 R} \quad (2.30)$$

after which the intensity decreases significantly. Figure 2.5 shows the **SR** spectrum for different electron beam energies at ELSA as calculated by the X-ray toolkit XOP [RD04]. The photon flux

$$F = \frac{\text{photons}}{\text{s} \cdot 0.1 \% \text{ bw} \cdot \text{A}} \quad (2.31)$$

gives the number of photons emitted per second, finite spectral bandwidth and electron beam current. For visible photons the flux is sufficiently constant for all beam energies and the intensity is directly proportional to the stored electron current.

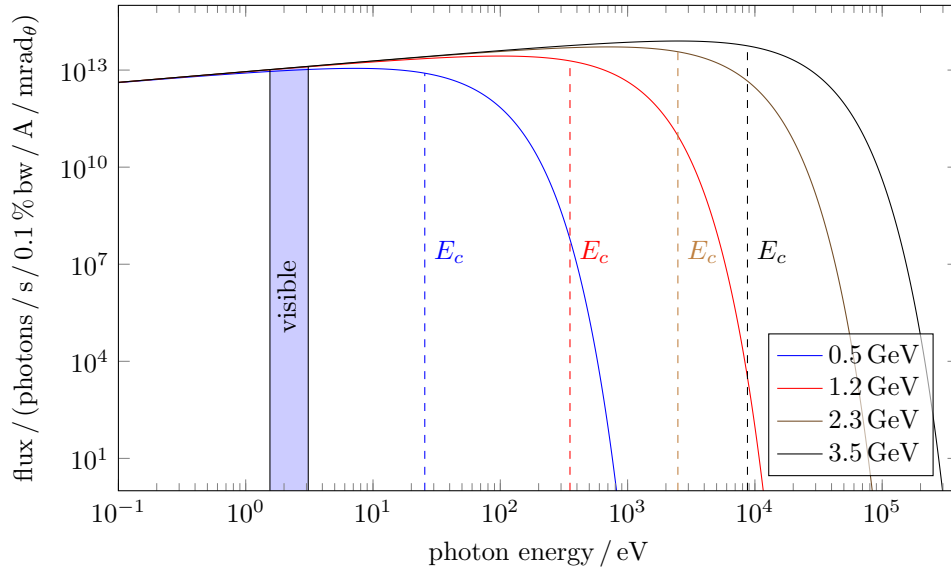


Figure 2.5: Calculated frequency spectrum of the bending magnet radiation power for a horizontal opening angle $\phi = 1$ mrad, a hypothetical beam current $I_{\text{beam}} = 1$ A and different electron beam energies at ELSA.

Spatial Distribution and Photon Polarization

The photon flux distribution is dependent on the photon's energy and given in [Lee04, Section 4.1.3.A]:

$$\frac{d^2 P_\gamma}{d\Omega d\omega} = \frac{3e^2}{16\pi^3 \epsilon_0 c} \gamma^2 \left(\frac{\omega}{\omega_c} \right)^2 (1 + \gamma^2 \vartheta^2)^2 \left[K_{2/3}^2(\zeta) + \frac{\gamma^2 \vartheta^2}{1 + \gamma^2 \vartheta^2} K_{1/3}^2(\zeta) \right] \quad \text{with} \quad \zeta = \frac{\omega}{2\omega_c} \frac{(1 + \gamma^2 \vartheta^2)^{3/2}}{2}, \quad (2.32)$$

where $K_{2/3}$ and $K_{1/3}$ denote the modified Bessel functions. Figure 2.6 visualizes this relation. The divergence of VIS photons lies in the vicinity of 2 mrad, whereas higher energetic photons are emitted under a much smaller angle of order 0.1 mrad. Furthermore, $K_{2/3}$ describes the contribution of photons polarized in the orbital plane (σ -polarized), whereas $K_{1/3}$ describes photons perpendicularly polarized to the plane (π -polarized). Hence, SR is linearly polarized parallel to the orbit plane at $\vartheta = 0$ and increasingly elliptically polarized with increasing ϑ . The spatial contribution of both polarization terms is compared in Fig. 2.7. The total power is composed of [BS82]

$$P_\gamma = P_\sigma + P_\pi \quad \text{with} \quad P_\sigma = \frac{7}{8} P_\gamma \quad \text{and} \quad P_\pi = \frac{1}{8} P_\gamma. \quad (2.33)$$

The respective RMS opening angles for visible radiation are calculated by [Hof98, Section 3.5]:

$$\vartheta_{\text{rms}} = 0.4488 \left(\frac{\lambda}{R} \right)^{1/3} \quad \vartheta_{\sigma\text{-rms}} = 0.4097 \left(\frac{\lambda}{R} \right)^{1/3} \quad \vartheta_{\pi\text{-rms}} = 0.5497 \left(\frac{\lambda}{R} \right)^{1/3}. \quad (2.34)$$

In some applications, such as beam cross section measurements, it may be useful to filter out one of the two polarization components. However, this comes at the expense of beam intensity.

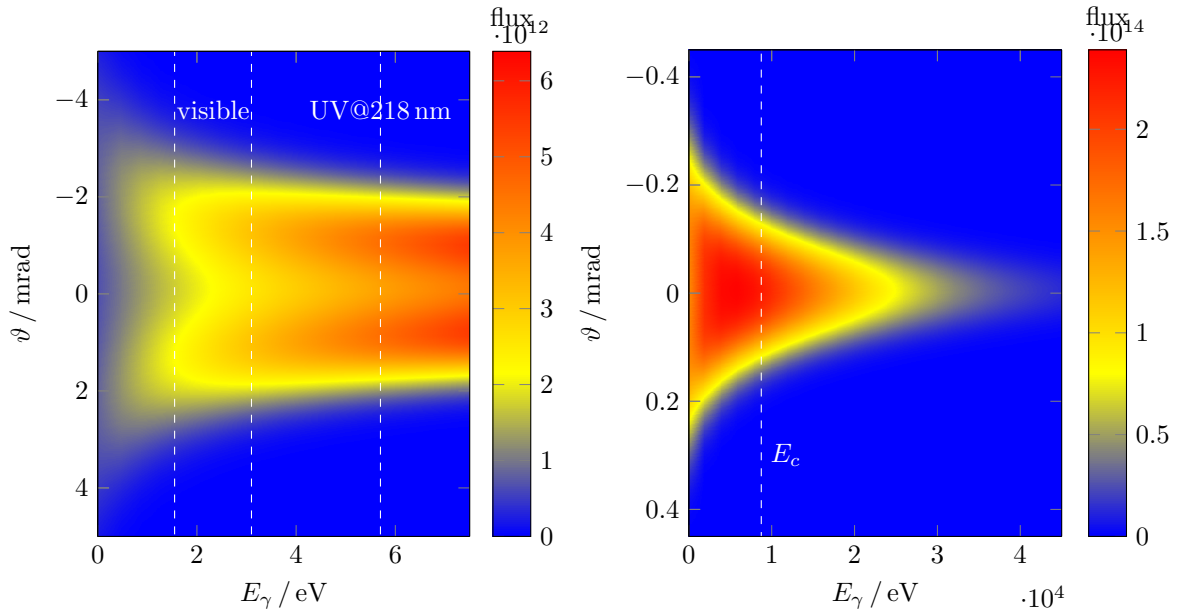


Figure 2.6: Flux dependence on vertical emission angle of **SR** as function photon energy E_γ in the visible range and over the broad spectrum for 3.5 GeV beam energy. Calculated with XOP [RD04].

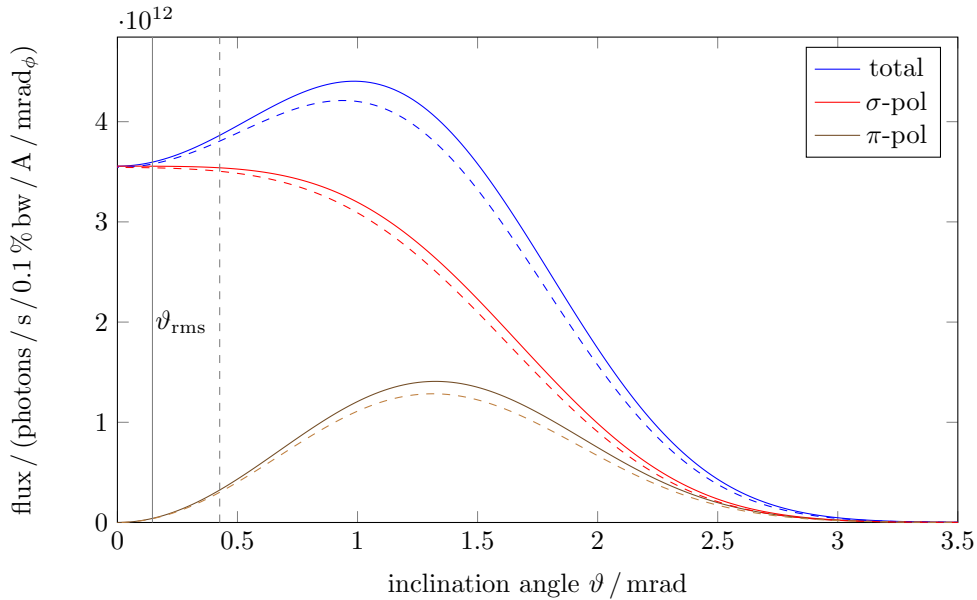


Figure 2.7: Angular flux distribution for **VIS** at $\lambda = 530$ nm from a 1.2 GeV (dashed) and 3.5 GeV (solid) electron beam at **ELSA**. The σ polarized component overpowers the π component, which is nonzero away from the orbit plane. The majority of power (X-ray regime) is found within the narrow angle of ϑ_{rms} .

2.3 Quantum Mechanical Effects

Sokolov & Ternov developed a comprehensive theory describing synchrotron radiation [ST86] including quantum effects. In comparison to the relations above, quantum effects significantly dominate the SR emission power at very strong magnetic fields, e.g. at the order of 10^9 T. Corresponding electron energies are $E \approx 10^{19}$ eV and therefore far out of reach for modern accelerators. However, measurable effects already manifest themselves at much lower energies of order $E \approx 500$ MeV, such as the self-polarization effect of a stored electron beam. The degree of electron polarization is in principle measurable through the observation of high-energetic SR. The feasibility of this approach at ELSA is discussed in the following.

2.3.1 Influence of the Particle Spin on Synchrotron Radiation

Bordovitsyn [BT08] characterizes SR as composition of multiple emission processes contributing to the total observable radiation power

$$P_{\text{SR}}^{\text{tot}} = P_{\text{SR}} \left(f_e + f_r + f_{e\mu} + f_{\mu}^{\text{L}} + f_{\mu}^{\text{Th}} + f_{\mu}^{\text{L-Th}} + f_{\mu}^{\text{a}} \right), \quad (2.35)$$

where P_{SR} is the radiation power obtained from Eq. (2.24), and the summands describe the impact of

- charge radiation f_e , being the dominating effect at contemporary accelerator beam energies,
 - recoil effects of radiation f_r ,
 - interference of charge and intrinsic magnetic moment $f_{e\mu}$,
 - magnetic moment radiation due to Larmor precession f_{μ}^{L} ,
 - magnetic moment radiation due to Thomas precession f_{μ}^{Th} ,
 - interference of Larmor and Thomas radiation $f_{\mu}^{\text{L-Th}}$, and
 - radiation due to the anomalous magnetic moment of the electron f_{μ}^{a} .
- $\left. \vphantom{\begin{matrix} \bullet \\ \bullet \\ \bullet \\ \bullet \\ \bullet \\ \bullet \\ \bullet \end{matrix}} \right\} \text{spin light}$

The radiation contributions induced by the electron's intrinsic spin are referred to as *spin light*. The corresponding formulae of the summands in Eq. (2.35) are listed in Appendix A. The spin light effects are proportional to the ratio of critical energy ϵ_c and particle energy E :

$$\xi := \frac{\epsilon_c}{E} = \frac{3 \hbar \gamma^2}{2 mcR}. \quad (2.36)$$

For example, at the highest ELSA energy of 3.5 GeV one obtains $\xi = 1.6 \times 10^{-5}$, which contributes to σ - and π -polarized light according to [MSY05]

$$P_{\sigma}^{\uparrow\uparrow} = P_{\text{SR}} \left\{ \frac{7}{8} - \xi \left(\frac{25\sqrt{3}}{12} - \zeta \right) + \xi^2 \left(\frac{335}{18} + \frac{245\sqrt{3}}{48} \zeta \right) + \dots \right\}, \quad (2.37)$$

$$P_{\sigma}^{\uparrow\downarrow} = P_{\text{SR}} \frac{\xi^2}{18}, \quad (2.38)$$

$$P_{\pi}^{\uparrow\uparrow} = P_{\text{SR}} \left\{ \frac{1}{8} - \xi \frac{5\sqrt{3}}{24} + \xi^2 \frac{25}{18} + \dots \right\}, \quad (2.39)$$

$$P_{\pi}^{\uparrow\downarrow} = P_{\text{SR}} \xi^2 \frac{23}{18} \left\{ 1 + \zeta \frac{105\sqrt{3}}{184} \right\}. \quad (2.40)$$

Therein, ζ represents the polarization state of a single particle (± 1), or the polarization degree of a particle ensemble. The arrows indicate if a spin flip ($\uparrow\downarrow$) or no spin flip ($\uparrow\uparrow$) occurred during the emission process. The total emitted power to first order of ξ is

$$P_{\xi} = P_{\text{SR}}^{\text{tot}} \left[1 - \xi \left(\frac{55\sqrt{3}}{24} - \zeta \right) + \dots \right]. \quad (2.41)$$

As the **SR** contribution due to quantum effects scales with ξ , one can generalize that spin light appears as weak reduction of radiation intensity in contemporary synchrotron accelerators.

Measurement of Electron Polarization via Emission of Synchrotron Radiation

Despite of a generally low spin light contribution to the total emission power, polarization measurements via **SR** observation were successfully demonstrated by Belomestnykh [Bel+84] at the 5 GeV VEPP-4 storage ring in Novosibirsk. Bondar et al. [BS82] state that at large frequencies $y = \omega/\omega_c \gg 1$ the difference of spin light and ordinary **SR** is given by

$$\delta = \pm \zeta \xi y. \quad (2.42)$$

The sign of ζ marks the intensity difference for antiparallel (+) or parallel spin orientation (-). Equation (2.42) indicates that a polarization measurement is best performed at the high energetic end of the **SR** spectrum. Therefore, a three-pole wiggler magnet (2.1 T) was used to generate photons in the **hard X-ray** regime, which were detected by a Čerenkov counter through X-ray conversion to Compton scattered electrons. The contribution of lower energetic photons was cut off by lead shielding and hence, the detector was only sensitive for photons above 328 keV. The corresponding δ was estimated to be 10^{-3} to 10^{-4} with a photon rate of 10^{10} to 10^{11} Hz [BS82]. The brightness of two circulating electron bunches was compared in the experiment, while one bunch was continuously depolarized by **RF** fields and functioned as intensity reference. The quality of this count-rate asymmetry measurement suggests that the condition described above marks a lower limit of measurement feasibility.

Feasibility of Polarimetry via Synchrotron Radiation Analysis at ELSA

At highest energies of **ELSA**, ξ lies in the order of 10^{-5} . According to Fig. 2.5, 10^{10} photons are obtainable at $y = 1$ for a beam energy of 3.5 GeV and 10 mA of beam current. To obtain the necessary count rate, measurements at $y \approx 1$ were required, as the number of emitted photons drops by several orders of magnitude for $y > 1$. This circumstance sets $\delta \approx \xi \zeta$. As the magnitude of ξ cannot be significantly raised at **ELSA** (compare with Eq. (2.36)), measurements utilizing the dependence of polarization and **SR** intensity is not considered feasible. Therefore another analysis technique based on **CBS** is used to measure the polarization degree of stored electrons (see Chapter 5). The contribution of spin light is, however, essential to the operation of the Compton polarimeter: its calibration is based on the *self-polarization effect*, which is caused by the emission of spin light.

2.3.2 Influence of Synchrotron Radiation on Beam Polarization

The radiation power of spin light is dependent on the particle polarization ζ (compare with Eq. (2.41)) as well as the initial and final spin state of the emission process ($\uparrow\uparrow$, $\uparrow\downarrow$, etc. as in Eqs. (2.37) to (2.40)). The

fraction of radiation power with occurring and non-occurring spin-flip is [Jac76]

$$\frac{P_{\text{spin-flip}}}{P_{\text{non-flip}}} = \frac{4}{3} \xi^2 \left(1 \pm \frac{35 \sqrt{3}}{64} \right). \quad (2.43)$$

As the ratio scales with ξ^2 , it is evident that a spin-flip due to radiation emission occurs with extraordinary low probability, as calculated by Sokolov & Ternov [ST86]:

$$w(\zeta) = \frac{1}{2\tau_{\text{ST}}} \left(1 + \frac{\zeta^8}{5 \sqrt{3}} \right), \quad (2.44)$$

with a time constant τ_{ST} typically lying in the order of minutes and hours at temporary synchrotrons. Due to the factor ζ , the polarization-dependent emission probability is asymmetric, which leads to an intrinsic self-polarization. By integrating over the transport equations describing the evolution of polarization in a storage ring

$$\frac{dN_{\downarrow}}{dt} = N_{\uparrow} w_{\uparrow\downarrow} - N_{\downarrow} w_{\downarrow\uparrow} \quad \text{and} \quad \frac{dN_{\uparrow}}{dt} = N_{\downarrow} w_{\downarrow\uparrow} - N_{\uparrow} w_{\uparrow\downarrow}, \quad (2.45)$$

where $w_{\zeta\zeta'}$ denotes the probability for the corresponding spin transition, the number of electrons N populating the polarization states is obtained:

$$\begin{pmatrix} N_{\downarrow} \\ N_{\uparrow} \end{pmatrix} = \frac{15 \pm 8 \sqrt{3} (1 - e^{-t/\tau_{\text{ST}}})}{30} \cdot N. \quad (2.46)$$

For $t \rightarrow \infty$ the asymptotic polarization degree then computes to

$$\mathcal{P}_{\text{ST}} = \frac{N_{\downarrow\infty} - N_{\uparrow\infty}}{N_{\downarrow\infty} + N_{\uparrow\infty}} = \frac{8}{5 \sqrt{3}} \approx 92.38 \%, \quad (2.47)$$

where the polarization build-up follows the exponential relation

$$\mathcal{P}(t) = \mathcal{P}_{\text{ST}} (1 - e^{-t/\tau_{\text{ST}}}). \quad (2.48)$$

For a storage ring of circumference C with bending radius R , the time constant can be obtained via [Bar+93]

$$\tau_{\text{ST}} = \frac{8}{5 \sqrt{3}} \frac{c \lambda_C r_0}{2\pi C} \oint \frac{ds}{|R|^3}, \quad (2.49)$$

where $\lambda_C = \frac{h}{mc}$ is the Compton wavelength of the electron and r_0 is the classical electron radius. In the case of ELSA only positive and uniform bending radii R are present, simplifying the above integral factor:

$$\frac{1}{C} \oint \frac{ds}{|R|^3} = \frac{1}{\bar{R} R^2}, \quad (2.50)$$

with $\bar{R} = C/2\pi \approx 26.17$ m. A numerical approximation of Eq. (2.49) is

$$\tau_{\text{ST}} \approx \frac{3.06 \times 10^5 \text{ s}}{(E/\text{GeV})^5}. \quad (2.51)$$

For example, at 1.2 GeV and 3.2 GeV beam energy τ_{ST} amounts 34.1 h and 15.2 min, respectively. The effective build-up time constant τ , however, results from an interplay between the above described

polarizing effects and potentially occurring depolarizing effects (see Sections 2.1.3 and 7.2.4 for details) [Bar+93]:

$$\tau = \tau_{\text{ST}} \frac{\tau_{\text{d}}}{\tau_{\text{ST}} + \tau_{\text{d}}}, \quad (2.52)$$

where τ_{ST} and τ_{d} represent the magnitude of polarization and depolarization, respectively. The asymptotic polarization degree of Eq. (2.47) is then reduced accordingly:

$$\mathcal{P}_{\infty} = \mathcal{P}_{\text{ST}} \frac{\tau_{\text{d}}}{\tau_{\text{ST}} + \tau_{\text{d}}}. \quad (2.53)$$

If no depolarizing effects were present, 92.38 % of the particle spins will be orientated anti-parallel to the bending field after a time $t \gg \tau$, independent of the amount of initial polarization [ST86, Section 21.3].

2.3.3 Stochastic Character of Synchrotron Radiation

The emission of SR from a single electron is not continuous but underlies a stochastic distribution of emitted light quanta $E_{\gamma} = \hbar\omega$. The emission rate per electron computes to [Lee04, Section 4.1.4]

$$\mathcal{N}_{\gamma} = \int_0^{\infty} n_{\gamma}(E_{\gamma}) dE_{\gamma} = \frac{15\sqrt{3}}{8} \frac{P_{\gamma}}{\hbar\omega_c} = \frac{5\alpha c}{2\sqrt{3}} \frac{\gamma}{R}, \quad (2.54)$$

where α is the fine structure constant and $n_{\gamma}(E_{\gamma})$ is the number of emitted photons per unit time within a frequency bandwidth dE_{γ} , as shown in Fig. 2.5. The number of photons emitted per turn is then

$$N_T = \mathcal{N}_{\gamma} \frac{2\pi R}{c} = \frac{5\pi}{\sqrt{3}} \alpha \gamma. \quad (2.55)$$

At ELSA this corresponds to 65 to 450 photons emitted per revolution and electron in the energy range 0.5 to 3.5 GeV. These quantum fluctuations cause a finite energy spread of the revolving electrons due to the recoil from emission. In a synchrotron, this effect eventually determines the bunch length and transverse beam size (see Chapter 4), which is observable through photometry of the emitted SR.

The Optical Diagnostic Beamline M7

The **SR** emitted from an electron bunch provides information about its spacial and temporal structure. The broad spectrum of **SR** allows the usage of diagnostic devices operating between the terahertz and the **X-ray** frequency regime, but a practical spectral range is **VIS**, for which sophisticated camera systems exist on the commercial market. The electron beam size in the **ELSA** storage ring lies in the order of millimeters and is well measurable in contrast to electron beams with smaller cross-sections, whose images suffer from broadening due to diffraction. For this diagnostic beamline a streak camera functions as fast optical recorder with picosecond time response, allowing to resolve longitudinal beam structures such as single revolving bunches. With two parallel optical light branches the beamline provides three-dimensional information of the stored electron beam by providing *top* and *side-view* simultaneously. An overview of the optical system is given in this chapter.

3.1 Photon Beamline

To obtain an image of the radiating electron beam, the emitted **VIS** has to be transferred from the evacuated beam pipe to an opto-electronic device, such as a **charge-coupled device (CCD)** camera, **position sensitive detector (PSD)** or photomultiplier tube. To prevent damage to the electronics by elevated radiation levels from ionizing **SR** and stray radiation from the circulating electron beam, the diagnostic equipment of the M7¹ beamline is placed outside of the accelerator's shielding tunnel. The beam pipe expands tangentially from the source point through the heavy concrete shielding into an external laboratory (see Fig. 1.2). The **VIS** is separated from the ionizing radiation by optical mirrors, of which the primary mirror is located within the accelerator's vacuum system. The vacuum system of the photon beamline was commissioned in 2013 and first electron beam images could be obtained by [Zan13], where a detailed description of the beamline's vacuum-related hardware can be found. The following section briefly describes the vacuum system and explicates the optics of the photon beamline.

3.1.1 Vacuum System

The beamline's front-end consists of a 12 m long evacuated pipe, whose vacuum pressure is reduced towards its back-end by multiple **ion getter pumps (IGPs)**. A pressure difference of two orders of magnitude between the storage ring's vacuum² ($\sim 5 \times 10^{-8}$ mbar) and the mirror sector ($\sim 5 \times 10^{-10}$ mbar) is

¹The photon source point lies within bending magnet M7.

²pressure with stored electron beam

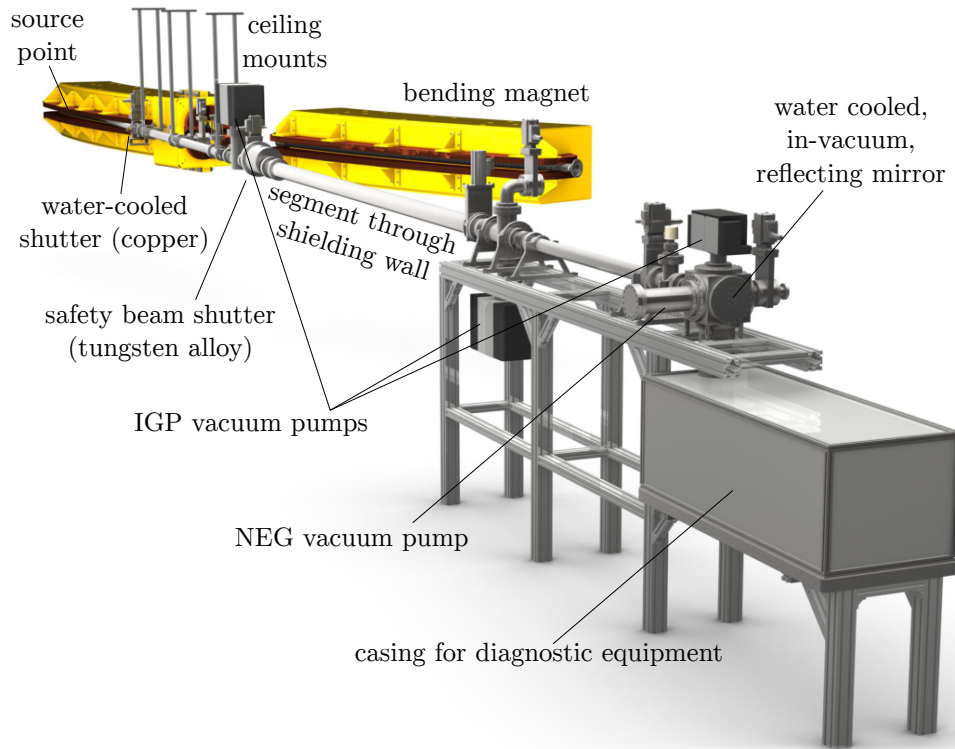


Figure 3.1: Technical drawing of the M7 SR diagnostic beamline. The 12 m long vacuum pipe is pumped differentially to create a mirror protection vacuum at the beamline back-end. The in-vacuum aluminum mirror deflects VIS and UV radiation downwards into a container, which houses the diagnostic equipment.

achieved. The primary deflecting mirror is fully exposed to the energetic X-ray beam, but surface deteriorating processes are minimized as the number of chemically reacting stray molecules is significantly reduced due to the low vacuum pressure [Zan+12]. The aluminum³ primary reflecting mirror is mounted in-vacuum and its rear surface is water cooled to minimize material elongation and deformation through heating [Zan13]. VIS and UV are deflected downwards out of the vacuum sector through a fused-silica window onto an encased optical table. The X-ray radiation is partially absorbed by and transmitted through the primary mirror and the downstream flange at the vacuum pipe's end. The optical equipment and electronic devices are placed below the accelerator plane. A technical visualization of the beamline is shown in Fig. 3.1.

3.1.2 Optical Setup

The VIS beamline optics form a modified Keplerian telescope which provides the required image properties for the diagnostic devices, such as size, orientation and intensity. Its layout is adjusted to the given space and conditions in the laboratory. For example, the evacuated beam pipe is multiple times longer than the beamline on the optical table with its limited mounting space. This imposes that the image distance b to the imaging lens is much shorter than the distance from lens to source point $g = (13.48 \pm 0.05)$ m, which represents the tangential intersection of the optical path with the electron

³The reflecting surface is made of aluminum alloy AW3003.

beam's design orbit. The uncertainty

$$\Delta g \equiv \Delta s = \left(\frac{\Delta a}{2L_{\text{BL}}} + \varphi_{\text{rms}} \right) R = 0.05 \text{ m} . \quad (3.1)$$

results from considerations of a variable longitudinal path length Δs with curvature R at which the SR with finite emission angle $\varphi_{\text{rms}} = 1.84$ mrad for VIS (compare with Eq. (2.34)) reaches the mirror of horizontal size $\Delta a = 50$ mm at distance $L_{\text{BL}} = 12.81$ m. On the basis of geometric optics, the condition $b \ll g$ yields an initial image magnification

$$M_{\text{init}} = \frac{B}{G} = \frac{b}{g} \ll 1 , \quad (3.2)$$

where B and G are image and object sizes, respectively. At the M7 beamline, the condition $M \ll 1$ is favored for the operation of the streak camera, as the available VIS intensity⁴ is to be maximized at the camera's photocathode. It is later shown in Section 4.3 that the desired object field of the electron beam and its vicinity spans across

$$G = 3.1 \text{ to } 28 \text{ mm} . \quad (3.3)$$

For the streak camera, a beam image of size B has to be projected onto the input optics which contain a $0.15 \text{ mm} \times 4.41 \text{ mm}$ large photocathode [Ham16]. It represents the smallest field stop aperture in the beamline and therefore determines the allowable range for B . Hence, a total magnification factor of

$$M_{\text{tot}} = 48 \times 10^{-3} \text{ to } 5.4 \times 10^{-3} \quad (3.4)$$

is required to fit the 0.15 mm aperture. Due to the narrow input slit and the streak camera's principle of functionality, it visualizes a given input signal in one transverse and the longitudinal plane. As simultaneous observation of both transverse and the longitudinal plane is desired in some cases, the photon beamline is required to provide both: a horizontally and a vertically orientated electron beam image. In addition, it must be ensured by beam or aperture positioning, that observation of both or only one transverse image is selectable during beamline operation. Furthermore, the beamline is installed in a radiation protection area and is not accessible when the beamline or a neighboring experimental area is operating. Therefore, remote control (RC) capability for crucial components is essential. To meet these requirements, the photon beamline provides RC options for

- adjustable image magnification to account for varying electron beam sizes and observation fields,
- variable photon beam attenuation for intensity adjustment,
- beam positioning capabilities for two separated photon beams, and
- selection of the transverse beam orientation by aperture positioning.

An overview of the corresponding optics layout is shown in Fig. 3.2 and is explained below.

⁴Photon power per unit area: $I_{\text{ph}} = P_{\text{ph}}/A$.

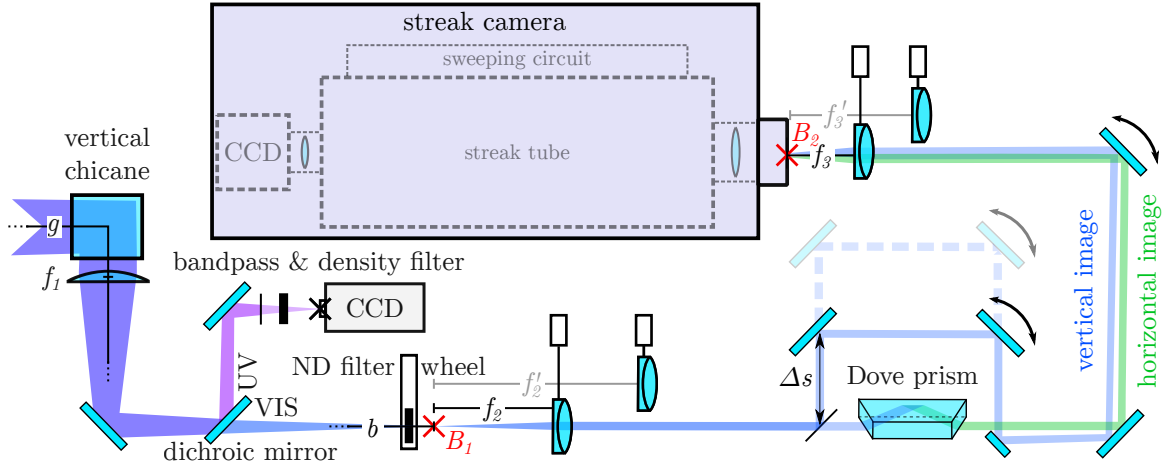


Figure 3.2: Close-to-scale layout of the M7 diagnostic beamline optics. The **UV** component of **SR** is monitored by a CCD camera while the **VIS** part is collimated for further (de)magnification. It is partially rotated transversely by a **Dove prism**, while the original image bypasses it with variable time delay through the additional path length $2\Delta s$. Both beams are refocused onto the streak camera input optics, providing a horizontal and vertical image of the electron beam.

Image Magnification

The primary plano-convex 3" imaging lens has a focal length of $f_1 = (501.8 \pm 10.1) \text{ mm}$ ⁵. Using the thin lens equation

$$\frac{1}{f_1} = \frac{1}{b} + \frac{1}{g}, \quad (3.5)$$

the primary lens creates an image at distance $b = (521 \pm 11) \text{ mm}$ behind its position (see Fig. 3.2). Due to the mirror's tilt within the previous vertical chicane, the initially horizontally orientated image⁶ is rotated transversely by 90° and exits the chicane upright. Equation (3.5) provides the magnification of the initial image B_1 at image distance b :

$$M_{\text{init}} = \frac{B_1}{G} = \frac{b}{g} = \frac{f_1}{g - f_1} = (38.7 \pm 0.9) \times 10^{-3}. \quad (3.6)$$

Before the first image B_1 is obtained, a thin dichroic mirror separates the **VIS** component from the **UV** and reflects the latter sideways. A bandpass filter narrows the **UV** wavelength to $\lambda = (218 \pm 6) \text{ nm}$ and a **CCD** camera digitizes the transverse beam profile.

In the **VIS** branch behind the transmissive dichroic mirror interchangeable object lenses with focal lengths $f_2 = 65 \text{ mm}$ or 200 mm are placed in the respective distances f_2 behind the initial image B_1 . Each forms a parallel light bundle and hence, creates an optical relay line whose length towards another refocusing lens is arbitrary. Interchangeable imaging lenses with focal lengths $f_3 = 100 \text{ mm}$ and 50 mm are placed at the respective distances f_3 in front of the camera's input optics. The additional magnification factor of the relay line $M_{\text{relay}} = f_3/f_2$ is determined by the fraction of the utilized lens pair's focal lengths.

⁵An error of 2% is assumed, comprehending manufacturing tolerance (1%) and estimated effects due to the broad-band **VIS** application.

⁶The transverse beam cross section corresponds to a flat ellipse.

setting	M_{init}	f_2	f_3	M_{bl}
①	$(38.7 \pm 0.9) \times 10^{-3}$	200	50	$(9.7 \pm 0.5) \times 10^{-3}$
②	"	200	100	$(19.3 \pm 0.7) \times 10^{-3}$
③	"	65	50	$(29.7 \pm 1.1) \times 10^{-3}$
④	"	65	100	$(59.5 \pm 2.1) \times 10^{-3}$

Table 3.1: Magnification factors M_{bl} available for streak camera operation at the M7 diagnostic beamline, assuming 2% error on the focal distances f_i .

The total obtainable beamline magnification is

$$M_{\text{bl}} = \prod_i M_i, \quad \text{and explicitly} \quad (3.7)$$

$$M_{\text{bl}} = M_{\text{init}} \cdot M_{\text{relay}} = \frac{f_1}{g - f_1} \cdot \frac{f_3}{f_2}. \quad (3.8)$$

Table 3.1 lists the available image magnification factors M_{bl} for the corresponding photon beamline magnification settings ①–④. These meet the specifications of Eq. (3.4) sufficiently close, compromising commercial lens availability, mounting space, and the allowable margin of the desired object field size.

Dual Transverse Imaging

To provide two separate images for the streak camera, a 50% beam-splitter divides the parallel light bundle at the beginning of the optical relay line. One bundle bypasses the Dove prism, whereas the second bundle is transversely rotated by it, providing a horizontally orientated image⁷. The bypassed bundle is deflected close to the original beam path by a rectangular mirror (compare with Fig. 3.2). The bypass length is adjustable, as two bypass mirrors are mounted on a common linear stage. This allows to match or to delay the photon propagation time between the vertical and horizontal branch. The time delay Δt_{ph} corresponds to

$$\Delta t_{\text{ph}} = \frac{1}{c} (2\Delta s - d_{\text{Dove}} \cdot (n - 1)), \quad (3.9)$$

where c is the vacuum speed of light, $5 \text{ cm} < \Delta s < 10 \text{ cm}$ is the variable path based on the travel distance of the motorized linear stage, $d_{\text{Dove}} \approx 8.6 \text{ cm}$ the optical path length within the Dove prism and $n \approx 1.52$ its refractive index at 587 nm (N-BK7 glass). The corresponding delay adjustment range is approximately $200 \text{ ps} < \Delta t_{\text{ph}} < 500 \text{ ps}$, which is required to prevent signal overlap during single bunch measurements when the streak camera is operated in synchroscan mode (see Section 3.2.3).

A photograph of the diagnostic beamline is shown in Fig. 3.3.

Estimated Measurement Errors of the Optical System

An accurate image of an arbitrary luminous object requires error-free point-to-point mapping from the source topology into image space. As this ideal transformation is never met in reality, common optical errors and corresponding image enlargement effects are discussed in the following. While the M7 beamline was originally optimized to provide transverse beam images in the UV frequency range ([Zan13, ch. 8.2]), operation experience with the streak camera has shown that a maximum achievable

⁷The Dove prism is tilted by 45° and therefore rotates an image transversely by 90° .

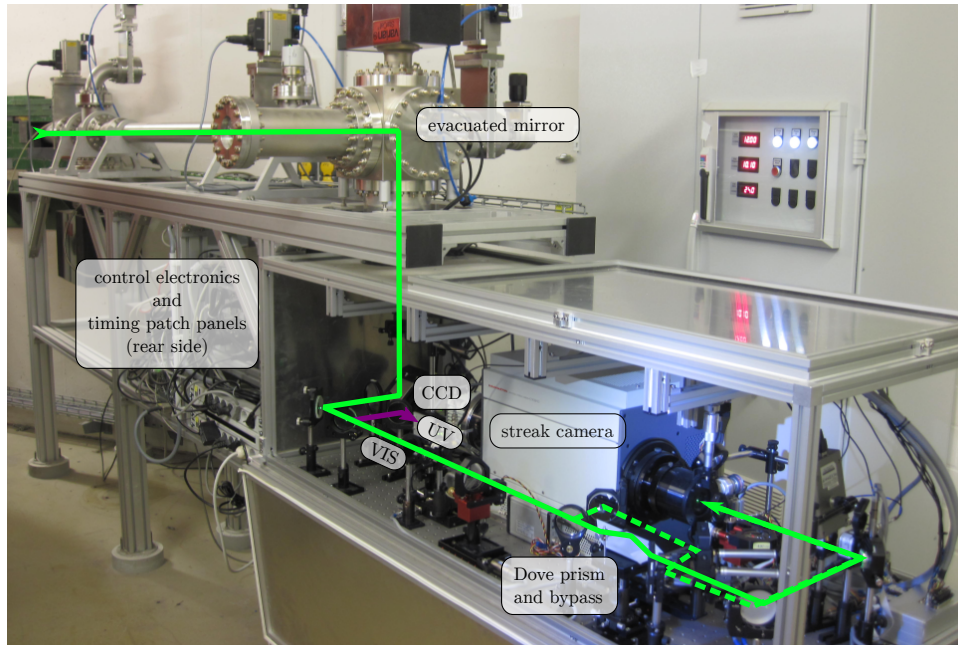


Figure 3.3: Photograph of the M7 diagnostic beamline's back-end behind the accelerator shielding wall. The optical box encases the photon beam manipulation section and the streak camera, which receives a horizontal and vertical electron beam image.

intensity transfer to the optical device is favorable. Compromising photon intensity and image quality, the beamline apertures for the current setup were chosen sufficiently large and are effectively given by the cross-section of the reflecting mirrors in the vertical chicane. Those yield the angular acceptance for the horizontal and vertical half SR cone opening angles:

$$\theta_H = 2.0 \text{ mrad} \quad \theta_V = 2.2 \text{ mrad} , \quad (3.10)$$

where both transverse acceptances are marginally larger than the natural emission angle ϑ_{rms} of the utilized SR spectrum (see Figs. 2.6 and 2.7 and Eq. (2.34)). The following optical error estimation assumes the above acceptance angles θ_H and θ_V .

Curvature of the electron beam trajectory: When the luminous object of width x_0 follows a curved trajectory and its par-axial rays sweep across an aperture of width a (compare with Fig. 2.6), a defines the angular acceptance θ_H . In case of a tangentially emitting, point-like source, the arching trajectory causes a horizontal enlargement of the beam image at a given screen [Sab73]:

$$\sigma_{\text{curv}} = \frac{1}{2} R \theta_H^2 \approx 22 \mu\text{m} . \quad (3.11)$$

The magnitude of enlargement due to curvature affects only the horizontal plane.

Depth of field: An optical system with finite depth of field (DOF) resolution projects multiple transverse images from different longitudinal positions onto an observation screen, causing image enlargement due to the contribution of various circles of confusion. The DOF range d_{DOF} due to the first

imaging lens of the M7 beamline is dependent on its [hyperfocal distance](#) [Der06, ch. 6]:

$$d_h \approx \frac{fD}{Z}, \quad (3.12)$$

where D is the aperture size and Z the maximum resolvable [circle of confusion](#). For the 3" lens ($D = 76.2$ mm) and an exemplary case of $Z = 6 \mu\text{m}$ ⁸ one obtains $d_h = 6.37 \times 10^3$ m. As $g \ll d_h$, the approximate [DOF](#) range thus becomes [Haf81, ch. 6.4.3]

$$d_{\text{DOF}} = d_f - d_n \quad \text{with} \quad d_f \approx \frac{1}{\frac{1}{g} - \frac{1}{d_h}} \quad \text{and} \quad d_n \approx \frac{1}{\frac{1}{g} + \frac{1}{d_h}}. \quad (3.13)$$

Here, d_n and d_f are the *near* and *far* points⁹, respectively. For the given setup, one obtains $d_{\text{DOF}} = 57$ mm, which corresponds to the result of [Eq. \(3.1\)](#). Hence, the luminous electron beam contributes to an image only from within this short longitudinal range.

The [DOF](#) enlargement error on a screen for a uniform, disk-like source is estimated to be [BV06]

$$\sigma_{\text{DOF}} = \frac{R}{\sqrt{6}} \frac{b}{2g} \vartheta_{\text{rms}} (\theta_{\text{H}} + \vartheta_{\text{rms}}) \approx 0.7 \mu\text{m}. \quad (3.14)$$

As the source intensity distribution is Gaussian and not uniform, this error is considered to be an overestimation.

Diffraction: Apertures truncating the photon beam will cause diffraction, and hence create diffraction patterns. The enlargement due to Fraunhofer diffraction of a point-like source amounts [AC90]

$$\sigma_{\text{diff}} = 0.18 \frac{\lambda}{\theta_{\text{H,V}}}. \quad (3.15)$$

For a central wavelength $\lambda_c = 600$ nm one therefore obtains

$$\sigma_{\text{diff,H}} = 54 \mu\text{m} \quad \text{and} \quad \sigma_{\text{diff,V}} = 49 \mu\text{m} \quad (3.16)$$

for the given setup. The vertical diffraction is only contributing if the beam is truncated by an actual aperture, which is avoided in the contemporary setup. Comparing with the above enlargement errors, diffraction has the largest effect on the beam image size. For electron beams of micrometer size, diffraction causes significant difficulties for beam size measurements utilizing [VIS](#). However, at [ELSA](#) the beam size is sufficiently large (compare with [Section 4.3](#)) and the enlargement effect is insignificant.

Total enlargement of the transverse images: The above imaging errors correspond to the total beam enlargement according to

$$\epsilon_x = \sqrt{\sigma_{\text{curv}}^2 + \sigma_{\text{DOF}}^2 + \sigma_{\text{diff}}^2} \approx 58 \mu\text{m} \quad (3.17)$$

$$\epsilon_z = \sqrt{\sigma_{\text{DOF}}^2 + \sigma_{\text{diff}}^2} \approx 49 \mu\text{m} \quad (3.18)$$

⁸ $Z = 6 \mu\text{m}$ represents a typical pixel size of contemporary CCD cameras.

⁹Near and far points correspond to the limit distances at which a [circle of confusion](#) is yet resolvable by the optical system.

and contribute to the measured beam sizes as in

$$\sigma_{\text{meas},i} = \sqrt{\sigma_{\text{beam},i}^2 + \epsilon_i^2}, \quad i \in \{x, z\}. \quad (3.19)$$

The above quantification of imaging errors amount for $< 5\%$ of the minimum expected beam size G of Eq. (3.3) and represent an overestimation. In addition, common imaging errors through imperfect optical components such as chromatic and spherical aberration, astigmatism, etc. influence the measurable image size additionally. The exact impact, however, is unknown, as various potential error sources are added by the multitude of optical components in the optical relay line, the streak camera's optics and the streak tube's ion-optical properties (compare with Section 3.2), where space-charge effects and electrical field-inhomogeneities within the streak-tube may lead to additional imaging errors. Overall, the multitude of error sources impedes a quantifiable error estimate for measurements of the absolute transverse electron beam size with the streak camera, as later demonstrated in Section 3.2.1. It is therefore predominantly used for qualitative or relative transverse size and position measurements with emphasis on visualization of beam dynamics.

Dispersion and longitudinal elongation of the signal: To utilize the maximum available intensity of the VIS spectral range, broad-band optical components are used for the photon beamline. This includes achromatic lenses with non-negligible thickness, which correct for chromatic aberration and improve the ability to focus the beam. The chromaticity of the optical components, however, influences the photon propagation time and introduces a wavelength-dependent dispersive delay $\Delta t_{\text{disp}}(\lambda)$ within an optical glass bulk of thickness d and refractive index $n(\lambda)$:

$$\Delta t_{\text{disp}}(\lambda) = \frac{d}{c} (n(\lambda) - 1). \quad (3.20)$$

To estimate the beamline's effect on bunch length measurements, the propagation through a $d_v = 4$ cm long glass bulk of NBK-7 glass is assumed to represent the overall thickness of the optical components in the vertical image branch. For the horizontal image branch, the overall glass thickness is estimated to amount $d_h = 10.5$ cm, including the Dove prism. Figure 3.4 shows the refractive index $n(\lambda)$ and the corresponding time delay $\Delta t_{\text{disp}}(\lambda)$ relative to the delay at the central wavelength $\lambda_c = 600$ nm. While the signal dispersion spans over 7.6 ps between 400 to 750 nm, the standard deviation from the central wavelength amounts 2.1 ps. The streak camera's photocathode sensitivity $I_0(\lambda)$ varies with wavelength as shown in Fig. 3.5. Therefore, wavelength-dependent spectral transmission coefficients have to be taken into account to estimate the overall signal elongation due to dispersion. The remaining beamline components have sufficiently constant spectral properties over the considered range. The total signal elongation $\Delta\sigma$ manifests itself as difference between the original signal duration σ_0 and the summed up signal duration of all delayed spectral contributions σ_Σ :

$$\Delta\sigma = \sigma_\Sigma - \sigma_0. \quad (3.21)$$

The difference $\Delta\sigma$ can be simulated through numeric integration by comparing multiple input signals of equal duration σ_0 with their specific chromatic delays $\Delta t_{\text{disp}}(\lambda)$

$$S(t) = \int_{\lambda_1}^{\lambda_2} I_0(\lambda) \cdot \exp\left\{-\frac{(t - \Delta t_{\text{disp}}(\lambda))^2}{2\sigma_0^2}\right\} d\lambda. \quad (3.22)$$

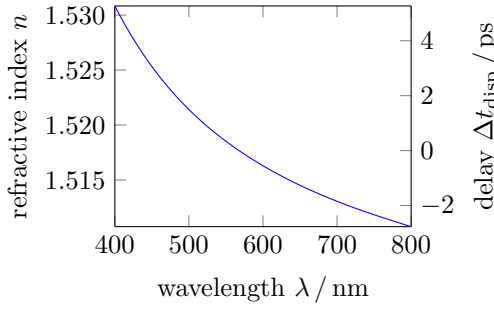


Figure 3.4: Refractive index of NBK-7 glass [Pol] and signal delay relative to $\lambda_c = 600$ nm, according to Eq. (3.20) for $d_h = 10.5$ mm.

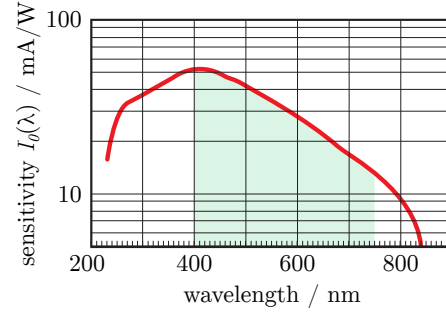
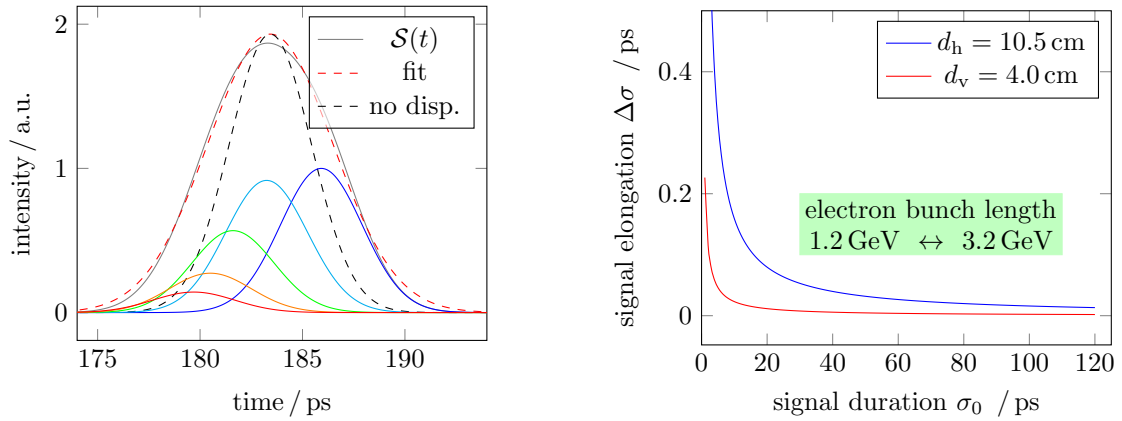


Figure 3.5: The streak camera's photocathode sensitivity $I_0(\lambda)$ [Ham16] is decreasing exponentially for longer wavelengths.

A fit of $\mathcal{S}(t)$ to a Gaussian function estimates the measurable σ_Σ , as visualized in Fig. 3.6(a). Figure 3.6(b) shows the signal elongation for varying σ_0 at both transverse image branches. The signal elongation $\Delta\sigma$ does not exceed 0.1 ps for $\sigma_0 > 20$ ps. Therefore, the elongation effect due to dispersion is below 1% and insignificant for electron bunch length measurements at ELSA (see Section 4.1.3).



(a) Effective signal width $\mathcal{S}(t)$ and fit for $\sigma_0 = 2$ ps as sum of chromatic contributions compared to a signal without dispersive influence.

(b) Simulation of signal elongation $\Delta\sigma$ as function of initial signal duration σ_0 due to dispersion. The effect is insignificant for $\sigma_0 > 20$ ps.

Figure 3.6: Signal elongation due to dispersive light propagation in NBK-7 glass.

3.2 Streak Camera

The streak camera displays the temporal structure of photon signals with picosecond time response. It operates similar to an electron tube oscilloscope: a photocathode converts the incident photons into photo-electrons, which are longitudinally accelerated and propagate through an evacuated tube. Lateral capacitor plates deflect the electrons vertically or horizontally, depending on the time-varying voltage provided by their respective sweeping circuits. Thus, the tube electrons are streaked across a luminous phosphorous screen, which is monitored by a CCD camera. The obtained digital image is a projection of the temporal (longitudinal) photon intensity distribution onto the screen, where signal amplification

type	device number	sweep direction	min.	max.
slow sweep	M10913-11	vertical	1.3 ns	1.02 ms
synchroscan	M10911-01	vertical	74 ps	1.4 ns
dual time base	M10916-01	horizontal	60 ns	100 ms

Table 3.2: Available streak camera deflection units and corresponding time ranges.

is achieved by a [micro-channel plate \(MCP\)](#) within the streak tube. It intensifies the streaked electron beam and enables single photon detection for low-intensity applications. An illustration of the streaking process is shown in [Fig. 3.7](#). The commercially available streak camera model C10910 by Hamamatsu [[Ham16](#)] is used at the M7 diagnostic beamline.

Interchangeable sweeping circuits (sweeping units) with selectable repetition rates and sweeping speeds allow measurements within various time spans along the vertical or horizontal image axis. The respective time ranges for the available sweeping units are listed in [Table 3.2](#). The available operation modes and performable electron beam measurements are listed in the following.

Focus Mode The sweeping circuits are switched off, used for beamline adjustment and transverse beam monitoring.

Slow Sweep Mode Vertical down-streaks and blanked up-streaks, used for monitoring of the circulating electron beam (bunch train) and measurement of its intensity distribution.

Synchroscan Mode Sinusoidal vertical up- and down-streaks, used for bunch length measurements and monitoring of longitudinal beam dynamics.

Dual Time Base Extension Mode Horizontal side-streaks and blanked back-streaks in combination with each of the above modes, used for measurements of multiple beam structures aside.

Exemplary measurements and operation details for each mode are described below.

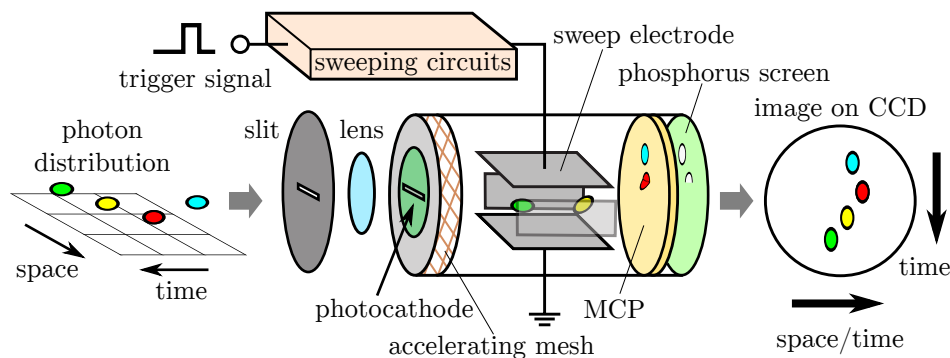


Figure 3.7: Working principle of a streak camera: photo-electrons are deflected transversely and illuminate a phosphorous screen, where the intensity can be adjusted by the [MCP](#) gain voltage. The image contains information about the longitudinal photon distribution and is digitized by a [CCD](#) camera. In addition to spacial information, the horizontal axis may contain temporal information when a corresponding sweeping circuit is operated.

3.2.1 Electron Beam Imaging in Focus Mode

To achieve an optimum light intensity transfer to the streak camera input optics, the camera is preferably operated in focus mode with turned off sweeping circuits. The camera then displays the transverse, elliptical shape of the electron beam. The built-in CCD camera¹⁰ has a resolution of 1344×1024 pixels of $6.45 \mu\text{m} \times 6.45 \mu\text{m}$ size. However, the MCP limits the resolution to 672×512 pixels and hence, the CCD is operated in a 2×2 binning mode in which it achieves repetition rates up to 28.4 Hz. The image of the streak tube's phosphorous screen is projected by output optics with magnification $M_{\text{tube}} = 1.43$. Table 3.3 lists the available final image magnifications $M_{\text{streak}} = M_{\text{bl}} \cdot M_{\text{tube}}$ (compare with Eq. (3.8)) and the respective pixel scaling factor for each beamline setting ① – ④. Exemplary images with corresponding beam size measurements are shown in Table 3.4. Therein, the measured size of a 2.9 GeV electron beam spans from 4.25 ± 0.30 to 5.26 ± 0.34 mm horizontally and 1.23 ± 0.09 to 2.76 ± 0.21 mm vertically for varying optical settings. The corresponding mean values are $\bar{\sigma}_h = (4.8 \pm 0.8)$ mm and $\bar{\sigma}_v = (1.5 \pm 0.5)$ mm. It is apparent that systematic errors dominate the measurement, which likely originate from imperfect positioning of e.g. the focusing optical components. As the presented settings were sufficient for the observation of beam dynamics, further-fine tuning of the magnification optics was foregone due to time-consuming adjustments with the RC opto-mechanics in the non-accessible experimental area during beamline operation.

BL setting	f_3/f_2	M_{streak}	scale/mm/px
①	200/50	$(13.8 \pm 1.0) \times 10^{-3}$	0.467 ± 0.033
②	200/100	$(27.6 \pm 1.7) \times 10^{-3}$	0.233 ± 0.015
③	65/50	$(42.5 \pm 2.6) \times 10^{-3}$	0.152 ± 0.010
④	65/100	$(85.0 \pm 5.2) \times 10^{-3}$	0.076 ± 0.005

Table 3.3: Beamline image magnifications M_{streak} at the streak camera CCD and corresponding pixel-to-beamsize conversion factors.

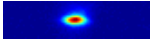
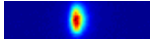
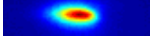
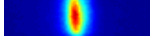
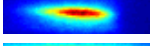
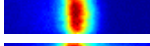
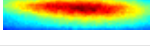
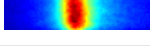
BL setting	hor. image	σ_x/px	σ_x/mm	ver. image	σ_z/px	σ_z/mm
①		8.62 ± 0.11	4.02 ± 0.29		4.49 ± 0.19	2.10 ± 0.18
②		18.23 ± 0.71	4.25 ± 0.31		6.00 ± 0.11	1.40 ± 0.09
③		35.22 ± 0.70	5.34 ± 0.35		9.41 ± 0.28	1.43 ± 0.11
④		72.81 ± 0.75	5.52 ± 0.35		12.46 ± 0.23	0.94 ± 0.06

Table 3.4: Exemplary horizontal and vertical images and corresponding measured sizes of a stored 2.9 GeV electron beam. The errors correspond to the quality of a Gaussian fit and the optical error estimated by Eq. (3.19).

The horizontal and vertical projections of the stored electron beam are usually recorded aside in a single image, as exemplarily shown in Fig. 3.8. The measured intensity distributions of the beam cross-sections are obtained from the pixel brightness within a **line of interest (LOI)**¹¹ (dashed) or **area of interest (AOI)**¹² (solid), where intensities of the horizontal and vertical images are best comparable through LOI

¹⁰Hamamatsu ORCA-R2

¹¹The LOI represents the CCD values of a single pixel row or column, e.g. through the maximum of the distribution.

¹²Pixel values of rows and columns are summed in AOIs.

projections (see profile comparison in Fig. 3.8). Streaking images will, however, represent an intensity distribution similar to AOIs, because the multitude of transverse images sum up as overlap from different longitudinal positions. Hence, two identical initial beam intensities may result in unsimilar streak trace intensities. In addition, non-optimal photon beam steering through the RC mirrors may result in intensity loss when an aperture partially blocks the light bundle.

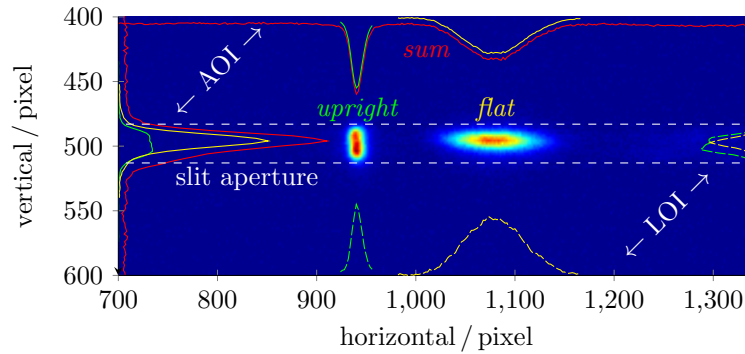


Figure 3.8: Streak camera operating in focus mode: Two perpendicular projections of the stored 3.2 GeV electron beam are obtained simultaneously in one image. The slit aperture limits both images vertically and likely truncates the vertical (*upright*) image. The respective beam profiles are shown at the image border: the profiles at the top and left (solid) are generated from an AOI, at the bottom and right (dashed) from an LOI which crosses the respective profile maximum.

Apertures and Aperture Implications

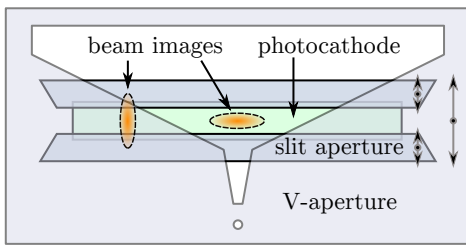
As visible in Fig. 3.8, the vertical image is likely to be truncated by the streak camera's slit aperture or the narrow photocathode. For image enhancement during streaking mode operation, the streak camera is equipped with two vertically moving aperture types (Fig. 3.9(a)):

1. The slit aperture consists of two parallel horizontal blades, which reduce the vertical photon acceptance in front of the 150 μm high photocathode. The aperture height is continuously adjustable, but resolveable increments are approximately 5 μm .
2. The so-called V-aperture reduces the horizontal photon acceptance. It is used to select the horizontal or vertical image by blocking the other, if the beam of interest is centered. In addition, it may truncate the beam transversely, if only longitudinal information is desired.

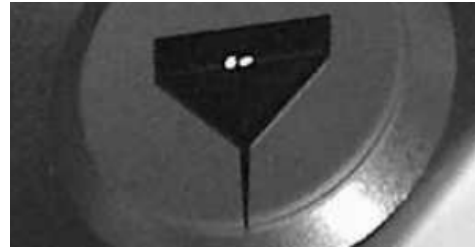
An illustration of both slit types and a photograph of the streak camera aperture setup is given in Fig. 3.9. Aside from enhancing the quality of the streak tube's optical properties, the narrow vertical aperture has implications on the visualization of transverse dynamics: vertical beam movement is truncated at a given point, resulting in position-dependent intensity reduction. This measurement artifact may be confused with factual intensity fluctuations from the real photon signal (compare e.g. with Fig. 3.11 in the following section).

3.2.2 Slow Sweep Operation Mode

In slow sweep operation mode, the streak tube's vertically deflecting electric field is changed linearly with time. After a trigger pulse is received, a vertical down-sweep occurs at which the vertical image information is lost in favor for visualization of the temporal (longitudinal) dimension. As two perpendicular



(a) Schematic drawing of slit and V-apertures in front of the input optics. The beams can be blocked from the photocathode by movable apertures.

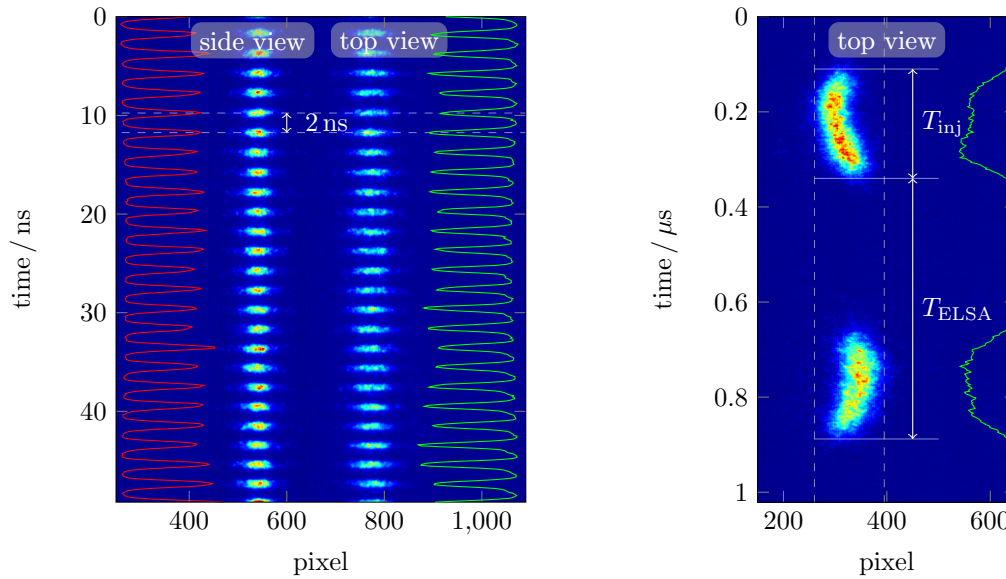


(b) Front view of the slit system. The image is taken by a network camera, which gives visual feedback for beamline adjustment using the motorized mirrors.

Figure 3.9: RC slit and V-aperture of the streak camera input optics. By positioning the beam images accordingly, the aperture may be used for blocking one of the two beam images. The reduced aperture enhances time-resolved measurements, but limits the available intensity.

transverse images may be displayed simultaneously (see Fig. 3.8), the horizontal temporal information is preserved in the streaked *flat* image of the beam ellipse (*top view*), and the vertical temporal information is preserved in the streaked *upright* image of the beam ellipse (*side view*). The camera unit is blanked during the voltage returning up-sweep.

Examples of prominent resolvable light signal structures at ELSA are single bunches ($\sigma_s \approx 0.1$ ns) and the filling pattern of the 548 ns long bunch train¹³, as exemplarily shown in Fig. 3.10.

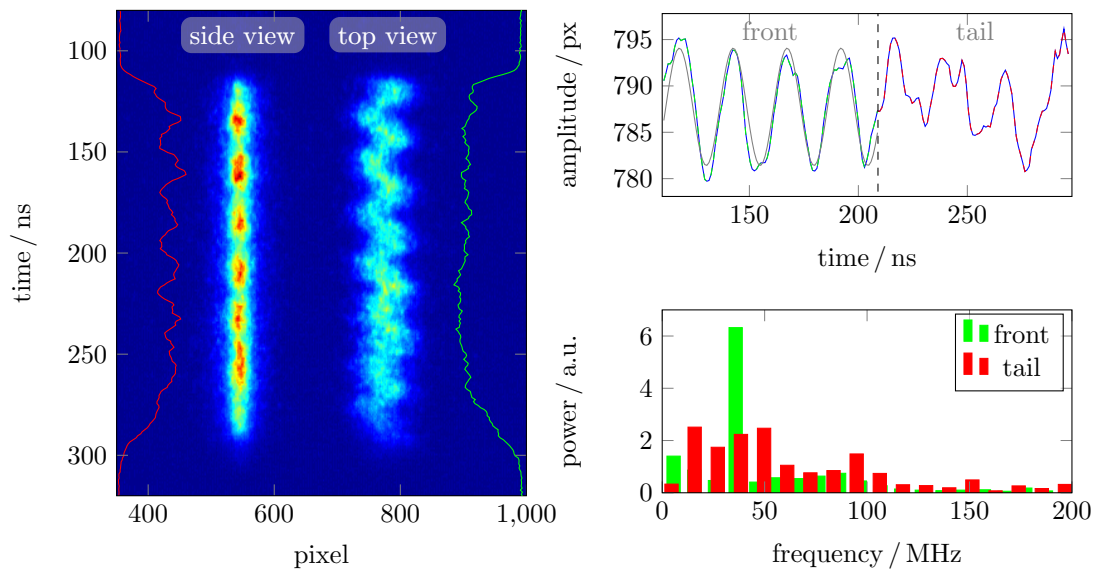


(a) Slow sweep measurement with single bunch resolution. The AOI sum profile of the side view is shown left (red), of the top view on the right (green).

(b) Horizontal image (top view) of the first two revolutions of the injected bunch train in ELSA.

Figure 3.10: Exemplary streak camera measurements in slow sweep operation.

¹³Intensity of the consecutive 274 electron bunches circulating in the storage ring.



(a) Side and top-view of the injected beam. Horizontal oscillations of a homogeneous filling pattern (green) induce intensity fluctuation artifacts on the vertical image (red).

(b) Horizontal beam oscillation, sinusoidal fit (gray) and the corresponding fast Fourier transform (FFT) power spectra of the oscillation at the bunch train's front and tail.

Figure 3.11: Measurement of an injected bunch train shortly before total beam loss, demonstrating intensity fluctuation artifacts and spectral analysis capabilities on transverse beam dynamics.

Imaging of Single Electron Bunches

Single electron bunches are resolved in Fig. 3.10(a), where peak-to-peak measurements yield a mean bunch distance of $T_{RF} = (1.98 \pm 0.02)$ ns, corresponding to an acceleration frequency of $f_{RF} = (505 \pm 6)$ MHz. The set accelerating RF of 499.67 MHz is covered by the measurement error margin, which is mostly determined by the image granularity. More precise longitudinal measurements are obtainable in synchroscan operation mode (see Section 3.2.3). Slow sweep measurements are preferably used to monitor the filling pattern, or to visualize transverse beam dynamics.

Imaging of Transverse Dynamics

Figure 3.10(b) shows the horizontally oscillating bunch train injected into the storage ring: The signal duration $T_{inj} = 232$ ns corresponds to the revolution period in the injector synchrotron with circumference $L_{boost} = 69.6$ m. The oscillating bunch train reappears after $T_{ELSA} = L_{ELSA}/(\beta c) = 548$ ns. In this case a detectable, but uncritical amount of electrons was seemingly lost at the bunch train's tail during the first revolution.

Another measurement of the injected bunch train with *top-* and *side-view* is shown in Fig. 3.11(a). Here, the beam image reveals partial instability: A horizontal, sinusoidal oscillation at $f_h = (40 \pm 1)$ MHz is visible at the bunch train's front section, which becomes increasingly chaotic towards the tail. The movement of the beam's center of gravity is displayed in Fig. 3.11(b). The FFT verifies the broadening of the oscillation spectrum and demonstrates the temporal analysis capabilities of the obtained streak camera image.

The image analysis software used to obtain the numerical values of the streak images is described in Section 3.2.4.

Artifacts Due to the Limiting Vertical Aperture

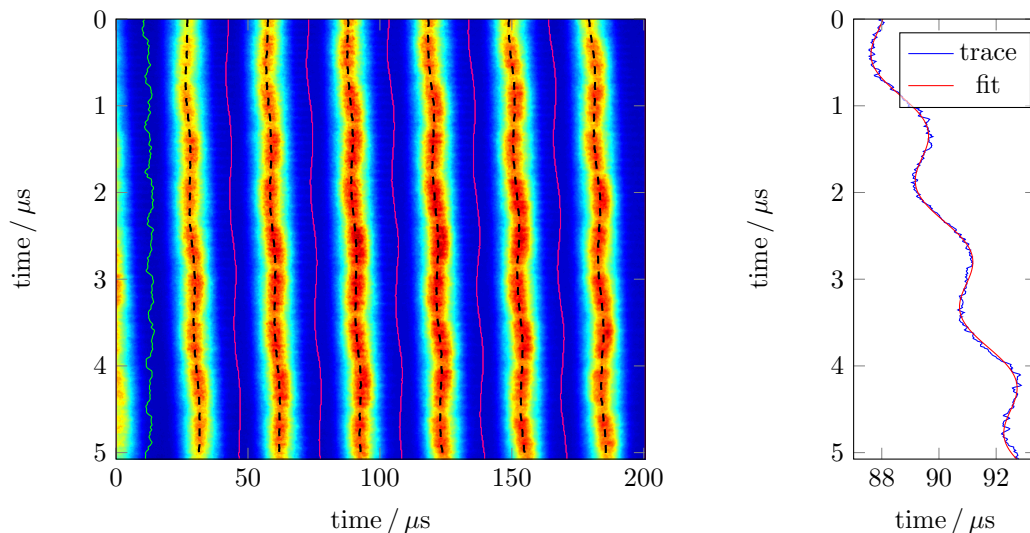
The traces of the streak image in Fig. 3.11(a) originate from the same photon signal, but differ in intensity. The periodic modulation of the vertical trace (red) correlates to the sinusoidal horizontal movement, which, on the contrary, shows a homogeneous intensity distribution (green). This represents an artifact due to movement within the narrow photocathode of the streak camera's input optics (compare with Fig. 3.9(a)). A horizontal displacement of the *flat* image is translated to a vertical displacement of the *upright* image. The intensity is reduced when one of the images exceeds the aperture. In some cases, monitoring both transverse images simultaneously may therefore be required to distinguish between signal properties and imaging artifacts.

Dual Time Base Extension

The dual time base extension unit is used in slow sweep mode to display multiple down-streaks aside, as individual vertical streaks may only obtain a small horizontal proportion of the available screen space. For example, Fig. 3.12(a) shows a *top view* measurement observing a horizontal beam instability over a time span of 200 μs . The vertical streaks show horizontal oscillations of the beam, which is exemplarily parameterized in Fig. 3.12(b). The numerical image analysis (see Section 3.2.4) indicates an oscillation frequency of (687 ± 2) kHz. The vertical tilt of the streak traces results from the superposition of both transverse deflecting electric streaking fields.

Limits of Resolution

The faster the streak velocity, the lesser of the available photon signal power is distributed along a unit area. Hence, the *signal-to-noise ratio* (SNR) decreases with increasing sweeping velocity (compare with granularity of Fig. 3.10(a)). Low intensity measurements may therefore require integration of multiple



(a) Multiple streaks with indication of the signal centroid (black), intensity distribution (green) and dynamic area of interest (magenta) for the Gaussian fits over the horizontal cross-sections.

(b) Oscillating centroid position and fit function of third streak in Fig. 3.12(a).

Figure 3.12: Slow sweep image with dual time base extension. The repetitive pattern displays multiple turns of the bunch train with observable horizontal beam oscillations at (687 ± 2) kHz.

images, which is possible if the signal is of repetitive nature. This, in turn, requires fast and precise trigger signals and synchronization capabilities. As jitter¹⁴ phenomena raise technical limits to the repeatability of **transistor-transistor logic (TTL)** trigger signals at the precision level of a few picoseconds, the *synchroscan* operation mode with phase-lock capability is preferably used for precise longitudinal measurements.

3.2.3 Synchroscan Operation Mode

In synchroscan operation the linear ramp of the slow sweep unit's electric field is replaced by a sinusoid whose operating frequency f_{scan} is a sub-harmonic of the accelerator's master RF f_{RF} ¹⁵. The present setup operates at $f_{\text{scan}} = f_{\text{RF}}/4 = 125 \text{ MHz}$. This signal is phase-locked to f_{RF} and therefore well synchronized to the electron bunch spacing period $T_{\text{RF}} = 2 \text{ ns}$, enabling precise measurements of the repetitive longitudinal bunch structure. Sufficient linearity of the sinusoidal sweeping voltage is given around its zero-crossing (screen area). Naturally, a down-streak and an up-streak image are placed onto the same horizontal screen position. A marginal delay between $f_{\text{RF}}/4$ and f_{scan} is used to separate the signals vertically, as shown in Figs. 3.13 and 3.14(a). The schematic drawing in Fig. 3.13 illustrates the observed signal arrangement on the screen, when the horizontal linear deflection of the dual time base extension unit with sweeping time t_h is superimposed on the vertical sinusoid with sweeping time t_v . Since the fourth sub-harmonic of f_{RF} is used, two out of four bunches are detected simultaneously. The subsequent missing pairs can be observed when f_{scan} is further delayed. Therefore, a synchrotron measurement at **ELSA** shows either *evenly* or *oddly* numbered electron bunches at a time.

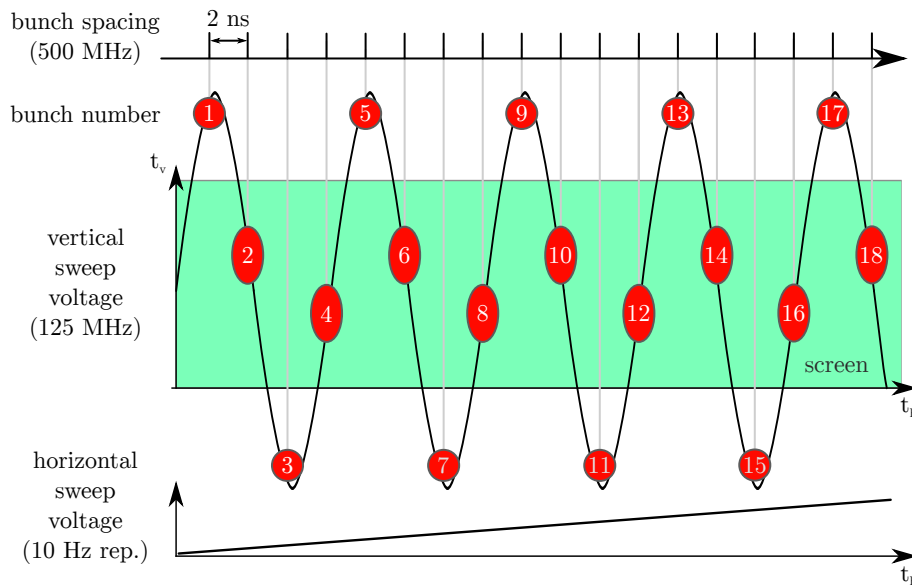


Figure 3.13: Schematic drawing of the synchroscan measurement principle with dual time base extension. The red dots mark the electron streaks on the phosphorous screen obtained from a light signal with 500 MHz repetition rate, representing the electron bunches within the **ELSA** storage ring. At the 4th sub-harmonic of f_{RF} , only odd or even bunches can be displayed on-screen. A linear horizontal electric field separates the temporal signals horizontally.

¹⁴Jitter as deviation from true periodicity of e.g. a clock signal due to noise on a finitely fast rising signal pulse.

¹⁵A master RF generator provides the reference signal for all accelerator's time-critical components.

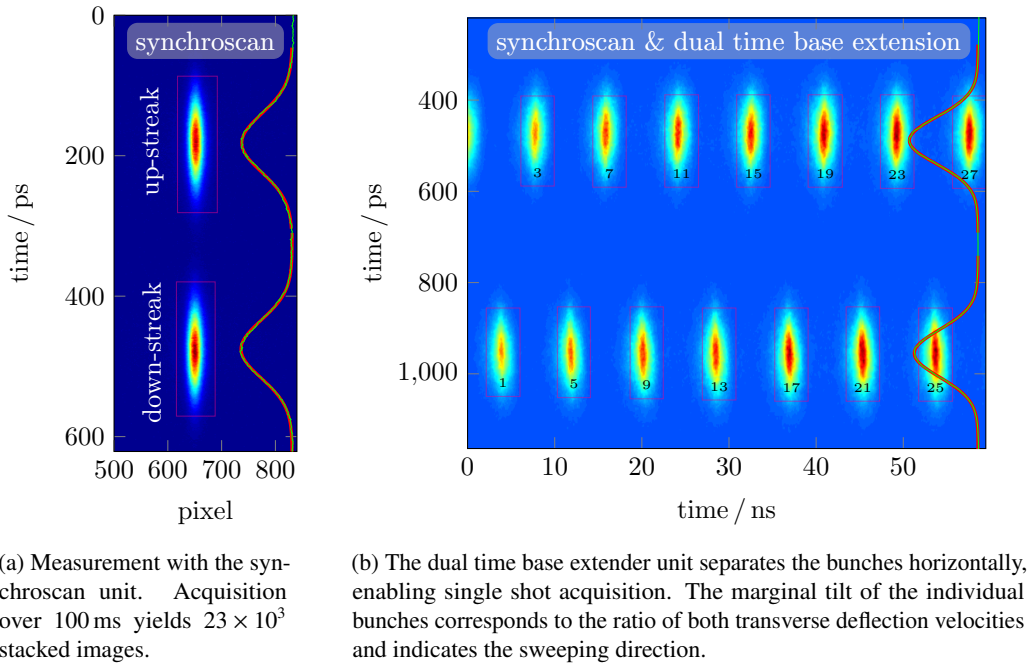


Figure 3.14: Bunch length measurements in one transverse dimension. The fit to a Gaussian function (red) is applied to the profile of the horizontally summed profiles (green).

Single Bunch Resolution

Figure 3.14(a) shows a synchroscan measurement without dual time base extension. As every fourth bunch signal is accumulated on the same spot, the SNR is high and no granularity is observable, providing a small error for the obtained bunch length: $\sigma_s = (40.6 \pm 0.4)$ ps at 1.2 GeV beam energy. However, an accumulated bunch length measurement requires precise phase stability of the signal, as a dynamic signal smears out the true bunch structure. In cases where longitudinal stability cannot be guaranteed – or to allow the observation of a single, non-overlapping bunch signal – the dual time base extension unit is used to separate the signals. In the case of the measurement shown in Fig. 3.14(b), the individual signal widths yield a bunch length of (51.1 ± 2.6) ps for a 1.73 GeV electron beam. The increase of the error is due to the increased image granularity and consequent lower SNR. In analogy to the dual time base extension in slow sweep mode, the superposition of both transverse deflection velocities adds a marginal tilt onto the signal images (compare with Fig. 3.12). For fast horizontal streaks (e.g. 60 ns) this allows to identify up- (\nearrow) and down-streak (\searrow) signals, as noticeable in Fig. 3.14(b).

Synchroscan at Long Time Spans in Dual Time Base Mode

When the horizontal sweeping time t_h is increased, the individual spatial extent of the consecutive light signals overlap, forming a horizontally joint trace. Longitudinal particle motion is visible through vertical deviations of the trace centroid. Figure 3.15 shows an exemplary image of the upper half of a synchroscan measurement with dual time base extension. Image analysis shows that the electron bunches oscillate at a longitudinal frequency of $f_s = (88.85 \pm 0.11)$ kHz. A simultaneous measurement of f_s with the BBB yields (87.8 ± 0.8) kHz, suggesting that a systematic error of at least 0.2 kHz (0.2 %) should be assumed when obtaining the oscillation frequency from a streak image. A description of longitudinal particle beam dynamics in synchrotrons is given in Section 4.1.3.

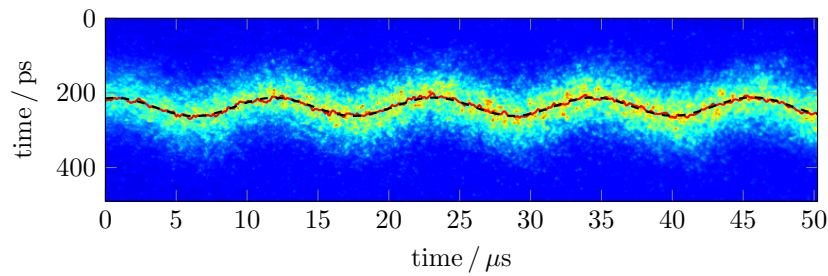


Figure 3.15: Longitudinal beam oscillations at (88.85 ± 0.11) kHz observed with the streak camera's synchroscan and dual time base extension unit. The image shows the upper half of a synchroscan measurement and a sinusoidal fit (black, dashed) to the trace centroid (red).

The vertical width of the horizontally joint synchroscan trace represents the bunch length. With the given amount of 672 horizontal pixels per upper and lower trace a total of 1344 (vertical) Gaussian fit functions can be obtained per image for refining the precision of bunch length measurements. This way a meaningful statistical error may be deduced from a single image. For example, the rather granular and dynamic measurement in Fig. 3.15 yields a bunch length of $\sigma_s = (47.4 \pm 6.3)$ ps with a precision of 13.3 %, while Fig. 3.16 shows a longer exposure time and yields a bunch length of $\sigma_s = (46.2 \pm 0.5)$ ps with a precision of 1.1 %. For the latter, the first 672 column measurements are compared to bunch length mean and standard deviation in the bottom of Fig. 3.16. One notices that the image shows an intensity variation with a maximum in the center despite of a constant irradiation intensity. The variation is assumed to be an intrinsic property of the streak tube which shows, however, no clear influence on the bunch length measurement. The obtained standard deviation is in accordance with the specified resolution of < 1 ps. Further synchroscan operation related bunch length measurements are presented in Section 4.2 and Appendix B.

Three-dimensional Synchroscan Operation

Side- and *top views* of the individual bunches can be displayed in synchroscan mode when both transverse images are coupled onto the photocathode (compare with Fig. 3.8). A corresponding synchroscan image

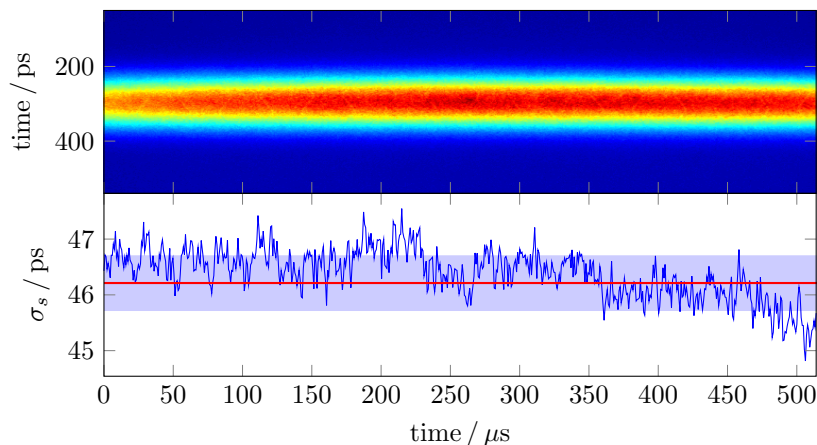
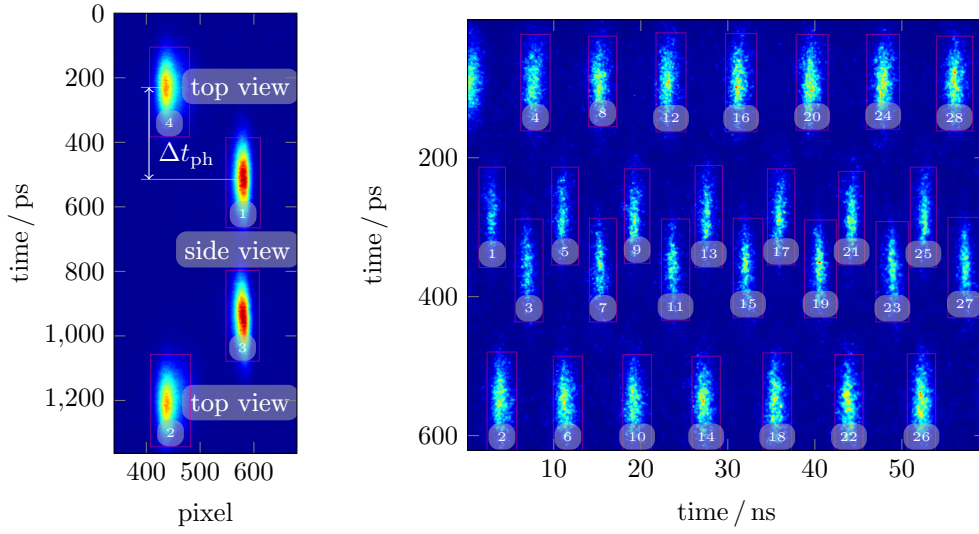


Figure 3.16: Dual time base synchroscan measurement showing upper joint horizontal trace (top) for precision bunch length measurement (bottom). The mean (red) and the standard deviation is shown (blue, background).



(a) Synchroscan image with *top-* and *side view* signals separated by $\Delta t_{\text{ph}} \approx 285$ ps for up- and down-sweep.

(b) Single shot of a three dimensional synchroscan image with comparable configuration as in Fig. 3.17(a) regarding *top-* and *side views*. The bunches and corresponding AOIs are tagged for image analysis.

Figure 3.17: Synchroscan measurement including both transverse images. The vertical signal distance is adjustable through the TOF manipulation Δs of the Dove prism bypass in the optical beamline (compare with Eq. (3.9)).

is given in Fig. 3.17(a), while Fig. 3.17(b) shows the result with dual time base extension. To prevent signal overlap, the signal's on-screen positions are arrangeable:

- Vertically, by manipulating the delay between $f_{\text{RF}}/4$ and f_{scan} , which separates up-streak from down-streak signals. To separate the *top-* and *side view* images, the optical path length in the beamline's bypass can be altered (see Eq. (3.9)).
- Horizontally, by re-positioning the beam images on the photocathode with the RC mirrors of the photon beamline (Fig. 3.2).

The dual transverse imaging capability allows three-dimensional, single-bunch monitoring. This, in turn, allows investigations of potential machine instability modes, whose characteristics are expressed through head-tail oscillations of individual electron bunches.

Effect of Optical Dispersion The effect of signal lengthening due to optical dispersion described in Section 3.1.2 can be investigated with three-dimensional measurements. Figure 3.17(a) shows longer bunches (beam energy of 2.5 GeV) than Fig. 3.17(b) (1.2 GeV), allowing a comparison to the span of the simulation results in Fig. 3.6(b). Tables 3.5(a) and 3.5(b) show the corresponding results of the obtained bunch lengths, where the even numbers represent *top view* measurements and the odd numbers *side view* measurements. Each group is expected to be identical in length (allowing the signal dispersion to set a difference between the groups), yet a difference of up to approximately 2 ps is evident within the *top view* measurement in Table 3.5(a) (bunches #2 and #4) and in the *side view* measurement (bunches #1 and #3). One may conclude that the systematic error due to the image quality and analysis technique is the dominating error compared to fit errors and statistical errors in Table 3.5. Affirming the results of Fig. 3.6, the effect of bunch lengthening due to dispersion is negligible for measurements at the M7 beamline.

bunch #	σ_s / ps	$\Delta\sigma_{s,\text{fit}}$ / ps	bunch #	$\overline{\sigma}_s$ / ps	$\Delta\sigma_{s,\text{stat}}$ / ps	$\overline{\Delta\sigma_{s,\text{fit}}}$ / ps
1	73.51	0.22	1, 5,...	37.79	0.60	1.57
2	73.94	0.18	2, 6,...	36.90	0.42	1.18
3	73.33	0.23	3, 7,...	39.30	0.65	1.65
4	71.80	0.20	4, 8,...	36.52	0.45	1.13

(a) Data of the 2.5 GeV electron beam shown in Fig. 3.17(a) with corresponding error from fit.

(b) Data of 549 sequence images of the 1.2 GeV electron beam shown in Fig. 3.17(b) with mean bunchlength $\overline{\sigma}_s$, its standard deviation $\Delta\sigma_{s,\text{stat}}$ and mean fit error $\overline{\Delta\sigma_{s,\text{fit}}}$ shown for each row.

Table 3.5: Comparison of bunch length measurements with *top*- and *side view*.

3.2.4 Streak Image Analysis Software

The image analysis tools used in Chapters 3 and 4 were written within the scope of this work in the *high-level interactive language for numerical computations* GNU OCTAVE¹⁶ [Eat+17]. It can be used for top-level control of the streak camera as well as the numerical analysis of images or sequences of images, where the parameterization is based on fitting Gaussian functions to the intensity profiles via nonlinear regression using the Levenberg–Marquardt algorithm¹⁷ (see e.g. [DS81]). The software identifies intensity maxima within the pixel matrix and provides height, position and width parameters with corresponding errors through the computed covariance matrix of the fit algorithm. Using the streak camera manufacturer’s time calibration data, the location of photon spots and traces is transformed from pixel to temporal values.

3.2.5 Timing and Controls

The trigger signals provided for each streak camera operation mode are generated by a variety of signal generators, each adjustable through the manufacturer’s control software (HPD-TA [Ham16]) on the streak camera’s control computer – or through the ELSA control system (ELSA CS) via transmission control protocol (TCP)¹⁸. Figure 3.18 gives an overview of the controls and timing utilities required to operate the streak camera. The accelerator’s time-critical subsystems are synchronized to the RF master generator, typically through TTL pulses generated by count-down units (e.g. the accelerator’s 1.82 MHz orbit clock¹⁹). The fourth subharmonic of f_{RF} is generated by the C10658-02²⁰ countdown and delay unit, which provides the phase-locked reference voltage signal f_{scan} for the synchroscan unit M10911-01²⁰. The slow sweep unit M10913-01²⁰ and dual time base extension unit M10916-011²⁰ receive TTL type trigger signals generated by two DG645²¹ delay generators. The trigger distribution to and from the delay generators is adjustable, as the specific measurement modes require different trigger arrangements. Measurements may be synchronized to the half orbit clock or to a customized trigger signal provided by the ELSA timing system. A patch panel mounted close to the optical setup (compare with Fig. 3.3) allows the user to re-arrange the trigger cables. Figure 3.19 gives a schematic overview of the trigger distribution for the respective operation modes.

¹⁶A free and open source scientific programming language similar to MATLAB.

¹⁷Implemented through GNU OCTAVE’s `optim` package.

¹⁸TCP commands are transferred through a remote client of HPD-TA.

¹⁹The orbit clock signal indicates one full revolution of a particle in the storage ring.

²⁰Product of Hamamatsu Photonics Deutschland GmbH.

²¹Product of Stanford Research Systems, Inc.

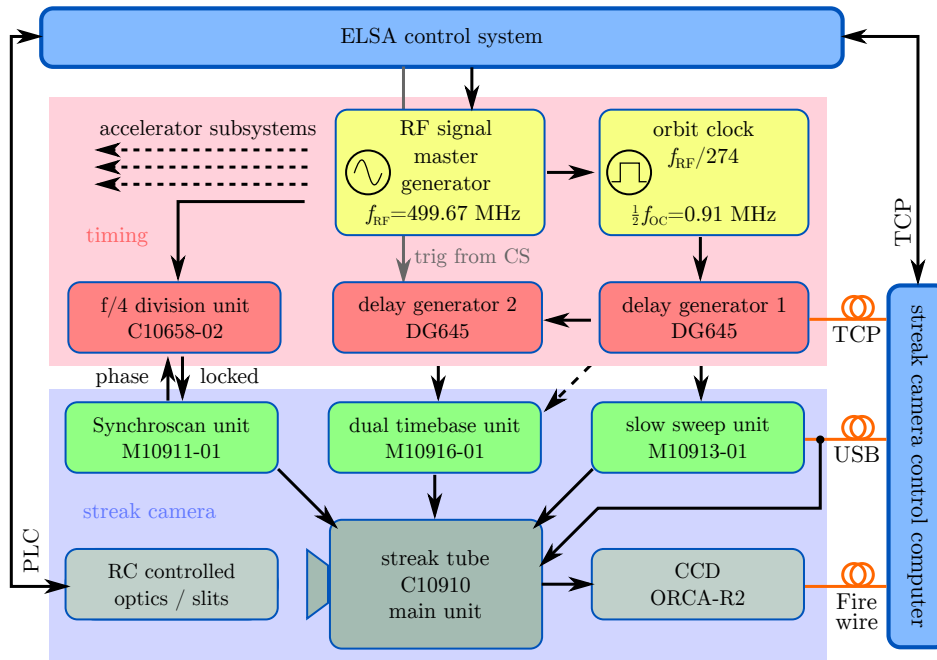


Figure 3.18: Simplified flow diagram of the streak camera's subsystems, its control and timing units.

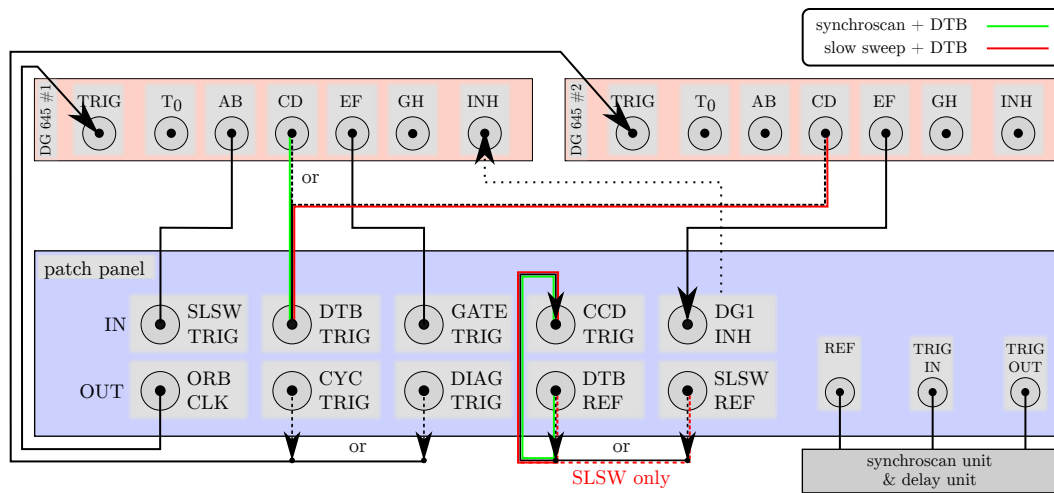


Figure 3.19: Wiring at the patch panel for the streak camera's trigger (TRIG) distribution. Synchronscan operation (green) and slow sweep mode (red) require different settings for synchronization. The channel names (AB, etc.) refer to the generic DG645 notation; the key for the remaining notation is SLSW: slow sweep, DTB: dual time base, GATE: gate for streak tube, CCD: gate for CCD, DG1 INH: inhibiting gate for delay generator #1, ORB CLK: orbit clock, CYC: ELSA cycle, DIAG: ELSA diagnosis trigger, DTB REF: timing reference from DTB, SLSW REF: timing reference from SLSW.

3.3 Radiation Levels and Equipment Protection

The SR diagnostic beamline and its electronic equipment is located in the experimental area *E3* for detector tests (see Fig. 3.20). The neighboring electron extraction beamline and the ionizing SR are potential radiation hazards for personnel and electronic equipment. As area access is restricted during beamline operation, concerns remain for sensitive electronic equipment such as the streak camera electronics, including its high-end CCD camera. Radiation damage to electronic equipment such as cameras are a common phenomenon at accelerator facilities, where devices are operated close to areas with elevated radiation levels. Attention is drawn here to determine how harmful the radiation may be to the electro-optical equipment of the M7 photon beamline.

3.3.1 Radiation Damage on Electronic Equipment

Ionizing radiation may disrupt electric potentials or displace atoms in microelectronic circuitry, leading to destruction of sensitive electric infrastructure. In case of CCD chips, high levels of radiation affect the dark current, threshold voltage, charge transfer efficiency and linearity, eventually resulting in *hot pixels*²² and increased noise [MB06; Bas02]. This, on the other hand, may result in measurement inaccuracy, permanent damage or complete destruction of an electronic device. Two types of damage to silicon structures are predominant [Abe+01, ch. 8.1.3]:

- *surface damage*, creating trapped charges in the transistor's intrinsic Si-SiO₂ interfaces from nonreversible electron-hole pair generation through ionization, and
- *bulk damage* through elastic scattering, where individual Si-atoms (point-defect) or clusters of atoms (cluster damage) are displaced from their atomic lattice positions.

While surface damage may be well correctable through pixel operating voltage adjustments or annealing, bulk damage has a more destructive and nonreversible impact. Neutrons with kinetic energies > 190 eV or electrons > 260 keV suffice to create point-defects, whereas cluster damage with impact of up to tens of nanometers is caused by ~ 15 keV neutrons or ~ 5 MeV electrons [Wun97]. Photons do not provide the required recoil momentum for causing *bulk damage*, but are a cause of *surface damage*.

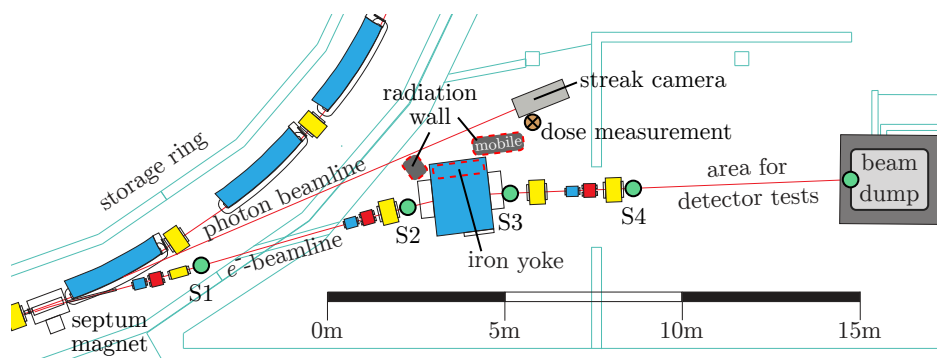


Figure 3.20: Experimental area *E3* with electron and photon beamline. Potential e^- -beam interaction with insertable fluorescence screens (S1 to S4) or the designated beam dump is indicated by green dots. Shielding walls are indicated. The wall between iron yoke and streak camera is mobile.

²²Defect pixels, whose charge transmission is disturbed, usually resulting in significantly higher pixel values.

3.3.2 Situation at the Experimental Area

The electronic and opto-electronic equipment is placed below the accelerator's plane, preventing direct interaction with stray electrons from the accelerator. However, GeV electrons colliding with the vacuum chamber produce a continuous bremsstrahlung photon spectrum. Those γ -photons may additionally generate neutron radiation due to photoneutron production. The cross section of the latter process becomes significant for 10 to 20 MeV photons interacting with atomic nuclei [Kri07, ch. 4.5]. Predominant interacting materials in the *E3* area are the vacuum chamber of the e^- -beamline, inserted fluorescence screens for e^- -beam position diagnostics, or the designated beam dump (see Fig. 3.20).

To estimate the magnitude of exposure to radiation of the opto-electronic equipment, radiation dose measurements close to the streak camera were conducted²³. The measurements were performed as test scenario with beam energy of 3.2 GeV, 25 mA of initially stored, and 500 pA²⁴ of extracted electron current. The results for various scenarios are shown in Fig. 3.21. When the beam is placed at the designated beam dump (on target), a low radiation background of photons and neutrons is observable (20 to 40 $\mu\text{Sv h}^{-1}$). The neutron and photon equivalent dose is, however, significantly increased ($\approx \times 20$), when the e^- -beam interacts with the insertable diagnostic fluorescence screens S1 & S2 in the electron beamline (compare with Fig. 3.20). Electron scattering on subsequent screens (S3 & S4) or electron loss in the storage ring (trip) do not significantly contribute to the neutron equivalent dose at the measurement location. The photon contribution is also significantly increasing in a storage ring failure²⁵ scenario and

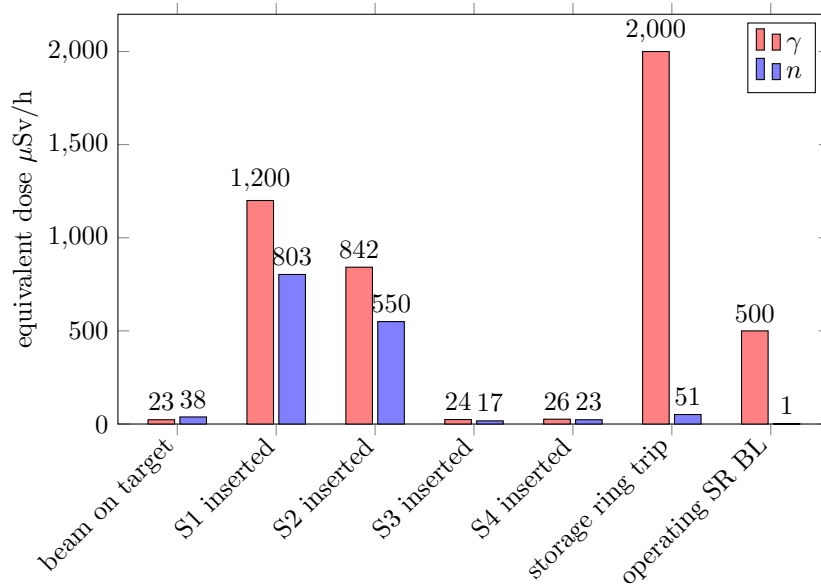


Figure 3.21: Equivalent dose of photons (γ) and neutrons (n) measured at the streak camera for operation scenarios at 25 mA stored 3.2 GeV beam and an extraction current of 500 pA. The background radiation with beam on target increases significantly when diagnostic screens are inserted into the e^- -beamline. Electron loss in the storage ring or the operation of the photon beamline raise the levels of γ -radiation.

²³Radiation dose measurements conducted with proportional counter LB 1236-H10 (γ) and neutron probe LB 6411 by Berthold Technologies GmbH & Co. KG. and corresponding UMo LB 123 readout electronics.

²⁴Regular operation allows extraction currents of up to 100 pA.

²⁵The dose amount is dependent on the electron loss rate and failure severeness and should be considered an indicator for the approximate order of magnitude. A sufficient error estimation requires more precise radiation surveys, which would exceed the scope of this work.

during regular SR beamline (BL) operation.

Rausch et al. [Rau99] report that the maximum total radiation dose for a CCD test device amounted 30 Gy before malfunctioning was registered. In that study, the radiation included γ -photons and neutrons, where the neutron flux was in the order of $10^6 \text{ cm}^{-2} \text{ s}^{-1}$. Simulations with the Monte Carlo code FLUKA [Fer+05] show for regular electron extraction into the E3 area [Heu17, ch. 6.5.4,] that the neutron flux at 3.5 GeV and 1 nA extraction current amounts approximately $10^2 \text{ cm}^{-2} \text{ s}^{-1}$ at the electro-optical equipment's location, causing a total neutron radiation equivalent dose of $25 \mu\text{Sv h}^{-1}$. In comparison, the extrapolated measurement value for 1 nA extraction current in Fig. 3.21 amounts $76 \mu\text{Sv h}^{-1}$, which sufficiently matches the simulation results with simplified geometry.

Despite the low background radiation level, progressive damage was observed as sudden appearance of approximately 280 hot pixels²⁶ (0.8 %) on the streak camera CCD after the E3 beamline commissioning period. For investigating the cause and to prevent further damage, the scenarios with elevated radiation dose due to inserted fluorescence screens were closer investigated with FLUKA simulations²⁷. Figure 3.22 compares the results for the 3.2 GeV electron beam extracted with 1 nA. With screen S1 inserted (Fig. 3.22(a)), elevated radiation levels are localized within and after the beamline's dispersive bending magnet: Ionizing radiation is produced by off-momentum electrons colliding with the vacuum aperture due to their deviating beam energy from previous collisions with the screen material. A total equivalent dose of approximately 5 mSv h^{-1} is estimated for the measurement location, being in good proximity with the measurement in Fig. 3.21. However, Fig. 3.22(b) shows that the simulated neutron contribution is with $50 \mu\text{Sv h}^{-1}$ too low to confirm the measurement. The simulation result deviates by more than a factor of 30 from the extrapolated measurement ($1.6 \text{ mSv h}^{-1} \text{ nA}^{-1}$) and appears to systematically underestimate the radiation dose contribution of neutrons.

Assuming that a realistic neutron dose rate may be higher by a factor of 30, the impact of ionizing photons remains the dominating effect. Therefore, the observed CCD pixel damage can be identified as *surface damage*. With the screen S1 insertion scenario, the above mentioned destructive dose of 30 Gy would be reached after approximately $6 \times 10^4 \text{ h}$ (seven years of continuous screen monitoring at 100 pA beam current). As this time span estimates the dose for complete device destruction, it may be a valid assumption that the accumulation of more than 10 % of the destructive dose is to be avoided. Under this assumption, the maximum tolerance of beam monitoring with screen S1 should not exceed 6 000 h.

To further reduce the neutron dose, a mobile shielding wall was installed between the electrical equipment and the radiation hot spot behind the bending magnet (compare with Fig. 3.20). It consists of a water tank barrier of 50 cm thickness, placed on top of two heavy concrete blocks on a movable platform, which can be removed for maintenance purposes. Simulations show that this barrier suppresses the neutron dose by a factor of approximately 20. This was tested by measurements with and without the water barrier, as shown in Table 3.6. In both critical screen insertion cases the water shielding reduces the measured dose by a factor of five, being in close proximity to the simulation result (factor of 20). The impact of the mobile protection barrier is significant and its usage is recommended.

²⁶Pixel with intensity value significantly deviating from the neighboring values.

²⁷Calculations conducted with friendly support of Dr. N. Heurich, ELSA.

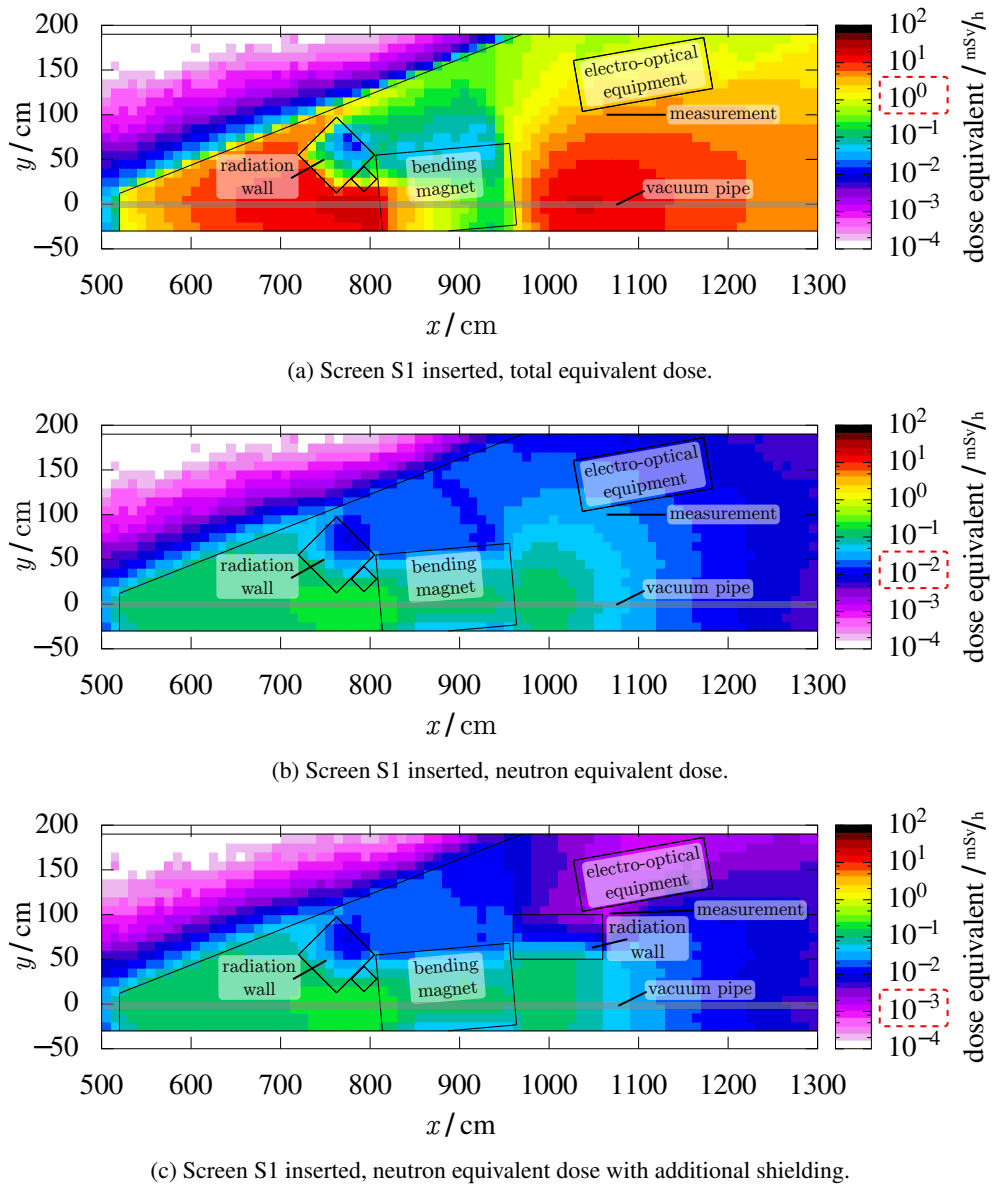


Figure 3.22: Simulated radiation dose in the *E3* area for screen S1 insertion. Subfigure (a) shows the total equivalent dose, subfigure (b) the equivalent dose of neutrons only and (c) the effect of the mobile shielding wall. The boxed values represent the order of ionizing radiation at streak camera level (approximately 1 m above ground).

shielding	screen insertion		
	S1	S2	S3
no shielding	160 $\mu\text{Sv/h}$	66 $\mu\text{Sv/h}$	3.7 $\mu\text{Sv/h}$
water shielding	34 $\mu\text{Sv/h}$	14 $\mu\text{Sv/h}$	3 $\mu\text{Sv/h}$

Table 3.6: Neutron equivalent dose measurements for 100 pA extraction current at streak camera level with and without a water barrier for neutron moderation in front of the electro-optical equipment.

Observation of Particle Dynamics via Synchrotron Radiation

The theoretical concept of particle dynamics in circular accelerators is introduced in this chapter and important figures are compared to the results of photometry measurements performed with the SR diagnostic beamline M7 (see [Chapter 3](#)). The observation performance is demonstrated by measurements of the electron beam's dynamic behavior, its bunch length, damping times and the filling pattern.

4.1 Particle Motion

The entirety of single particle dynamics form the shape and determine the properties of the observable macroscopic electron beam. In circular accelerators, the ion-optical [lattice](#) guides particles repeatedly to one or multiple accelerating cavities. A hypothetical design particle defines a reference orbit, from which all realistic particles generally deviate with individual displacements in all three spatial dimensions. The deviations are commonly described in a six-dimensional, right-handed, curvilinear coordinate system, including displacements and corresponding angular deviations ([Fig. 4.1](#)):

$$\vec{X} = (x, x', z, z', s, \delta)^T, \quad (4.1)$$

where x and z refer to radial and axial displacements from the orbit plane, x' and z' to the corresponding angular deviations, s to the longitudinal displacement and

$$\delta = \frac{\Delta p}{p} = \frac{1}{\beta^2} \frac{\Delta E}{E} \quad (4.2)$$

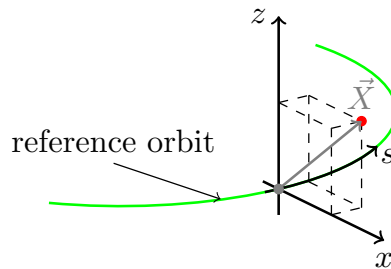


Figure 4.1: Orientation of the moving, curvilinear coordinate system for electrons at [ELSA](#).

refers to the momentum deviation and hence, an energy deviation. At the [ELSA](#) storage ring, electrons propagate counterclockwise and due to the negative electron charge the coordinate system is effectively left-handed.

4.1.1 Transverse Equation of Motion

Magnetic Fields and Transverse Focusing

The magnetic configuration determines the ion-optical properties of the [lattice](#). The acting magnetic guiding-, focusing- and correction fields can be expanded as multipole series at an arbitrary longitudinal position s , as exemplarily shown for the vertical magnetic field strength B_z of upright magnets along the horizontal:

$$B_z(x)|_{x=0} = B_0 + \frac{\partial B_z}{\partial x} x + \frac{1}{2} \frac{\partial^2 B_z}{\partial x^2} x^2 + \dots \quad (4.3)$$

Multiplying [Eq. \(4.3\)](#) by e/p introduces the magnetic *strength* for each multipole type:

$$\frac{e}{p} B_z(x)|_{x=0} = \frac{1}{R} + k \cdot x + m \cdot x^2 + \dots, \quad (4.4)$$

where $1/R$, k and m correspond to dipole- quadrupole- and sextupole strength, respectively. Higher order magnetic fields are always present in a lattice, but usually manifest themselves as field errors, whose effect may be partially compensated through additionally installed higher order magnets.

In the case of the [ELSA](#) storage ring, all magnet types are installed separately (compare with [Fig. 1.2](#)): The main lattice consists of 24 dipole magnets, which bend the beam to a radius of $R = 10.88$ m. The beam is focused by 32 quadrupole magnets (two families), operating at $k \approx 0.5 \text{ m}^{-2}$. The lattice configuration is referred to as *FODO* (compare e.g. [[Wil00](#), Section 3.13.3]). The 12 installed sextupole magnets (three families) correct for *chromaticity* (see e.g. [[Wi100](#), Section 3.16]) and are used for introducing a non-linear magnetic response, utilized for the electron extraction process (see e.g. [[Zan13](#), Chapter 5]). Additionally, 30 dipole corrector magnets are installed for vertical orbit correction (additional coil windings on the bending magnets allow for horizontal correction), four air quadrupoles influence the synchrotron's [betatron tune](#) (see [Section 4.1.2](#) and [Eq. \(4.12\)](#)) during the extraction process, and two tune-jump quadrupoles [[Ste99](#), Chapter 5] allow for a rapid change of the [betatron tune](#) for the preservation of electron polarization by fast resonance crossing (see [Section 7.2.3](#)).

Equation of Motion

If up to first order magnetic fields are present¹, the ion-optics are linear and single particle trajectories are described by *Hill's* differential equations [[Wil00](#), Section 3.2]

$$x''(s) + \left(\frac{1}{R^2(s)} - k(s) \right) \cdot x(s) = \frac{1}{R(s)} \frac{\Delta p}{p}, \quad (4.5)$$

$$z''(s) + k(s) \cdot z(s) = 0, \quad (4.6)$$

where bending takes place solely in the horizontal plane and no coupling between the planes is assumed. The solution of [Eq. \(4.5\)](#) yields an oscillatory single particle trajectory around the reference orbit.

¹This is approximately the case in storage mode, where no beam extraction occurs.

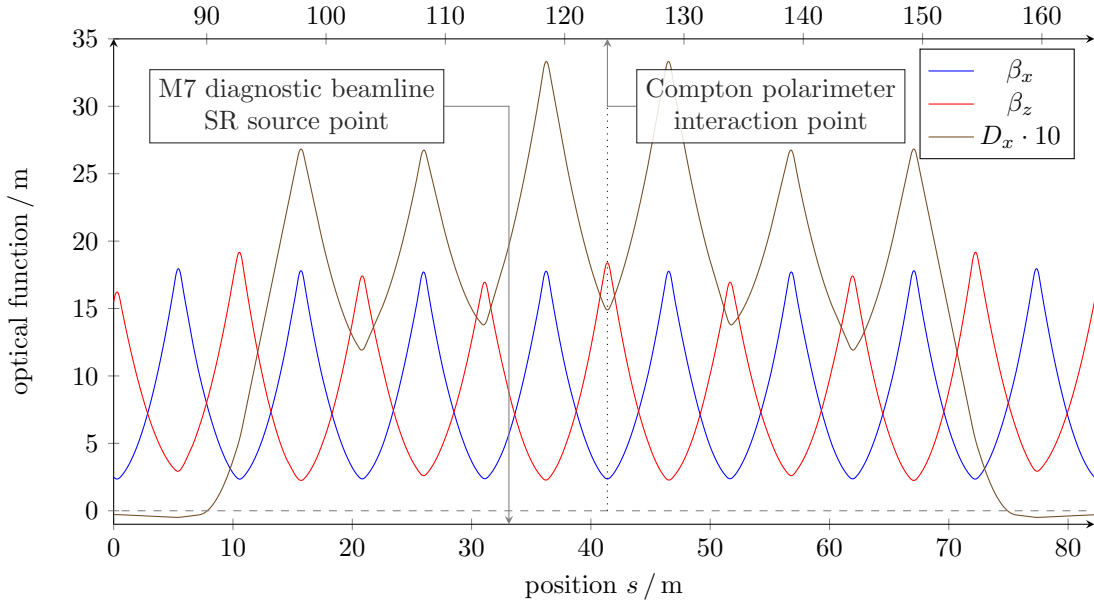


Figure 4.2: Exemplary optical functions $\beta_x(s)$, $\beta_z(s)$ and $D_x(s)$ of the *FODO* type ELSA lattice (calculated with ELEGANT [Bor01] for a tune of $Q_{x,z} = (4.612, 4.431)$, see Section 4.1.2). The lattice pattern repeats itself at 82.2 m, as indicated by the top axis (superperiodicity $P = 2$, compare with Section 7.2). Since no vertical bending takes place, $D_z(s)$ has no contribution. The locations of the M7 diagnostic beamline source point and the Compton polarimeter laser interaction point are indicated.

Exemplarily for the horizontal case, a trajectory solution has the form

$$x(s) = \underbrace{\sqrt{\tilde{\epsilon}_x \beta_x(s)} \cos(\psi_x(s) + \phi_x)}_{\text{betatron oscillations}} + \underbrace{D(s) \frac{\Delta p}{p}}_{\text{dispersion}}, \quad (4.7)$$

where $\tilde{\epsilon}_x$ is the *Courant-Snyder invariant* [CS58, Eq. (3.22)], $\beta_x(s)$ the lattice-specific amplitude function, ϕ_x an arbitrary start parameter of the particle's *betatron oscillation* phase

$$\psi_x(s) = \int_0^s \frac{ds'}{\beta_x(s')}, \quad (4.8)$$

and $D(s)$ is the dispersion function, which describes the displaced trajectory $x_D(s)$ of a particle with momentum deviation $\Delta p/p = 1$. The $\beta_{x,z}(s)$ and $D_{x,z}(s)$ functions are lattice- and ion-optic specific, and exemplarily shown in Fig. 4.2 for a typical ELSA storage ring setting. The amplitude function $\beta(s)$ determines the two parameters

$$\alpha(s) \equiv -\frac{\beta'(s)}{2} \quad \text{and} \quad \gamma(s) \equiv \frac{1 + \alpha^2(s)}{\beta(s)}, \quad (4.9)$$

which express the *Courant Snyder invariant*, exemplarily for the horizontal plane:

$$\tilde{\epsilon}_x = \gamma(s) x^2(s) + 2\alpha(s) x(s) x'(s) + \beta(s) x'^2(s). \quad (4.10)$$

Therefore, a particle with displacement x and divergence x' follows an elliptical trajectory in phase space (x, x') while propagating through the **lattice**. Applied to a particle ensemble, the *Courant Snyder invariant* yields the beam emittance (see [Section 4.3](#)), which determines the transverse beam size (see [Section 4.3](#)) in combination with the optical functions.

4.1.2 Betatron Tune

The **betatron oscillation** of [Eq. \(4.7\)](#) is pseudo-harmonic, because the oscillation frequency is a function of the longitudinal position s . The oscillation is described through the phase advance per revolution

$$\Delta\psi_x = \psi_x(s + L) - \psi_x(s) \quad (4.11)$$

in the **lattice** of length L and the number of transverse oscillations per revolution is called the **betatron tune**

$$Q_{x,z} = \frac{\Delta\psi_{x,z}}{2\pi} = \frac{1}{2\pi} \oint \frac{ds'}{\beta_{x,z}(s')} . \quad (4.12)$$

The centroid of a particle ensemble may represent the trajectory of a single particle when the ensemble performs **coherent** oscillations. An example of a transverse, **coherent** oscillation is shown in [Fig. 3.12](#), where the beam performs horizontal oscillations with a spatial frequency of $f_{\text{spat}} = (687 \pm 2)$ kHz. The **betatron tune** can be determined by measuring the amplitude and phase of a repetitively revolving part of the bunch train, as shown in [Fig. 4.3](#). Therein, a sinusoidal function² is fit to the revolution-repetitive, but arbitrary reference point (e.g. marking the head of the bunch train). The matching oscillation frequency f_x gives the **betatron tune**

$$Q_x = \frac{f_x}{f_0} , \quad (4.13)$$

where $f_0 = 1.82$ MHz is the particle revolution frequency within the **ELSA** storage ring. For the streak trace shown in [Fig. 4.3](#) and by assuming a tune $4 < Q_x < 5$ one obtains $f_x = (8.44 \pm 0.01)$ MHz and consequently $Q_x = 4.624 \pm 0.002$, which corresponds to a typical storage ring setting of close to $Q_x = 4.6$ and $Q_z = 4.4$.

In analogy to the transverse tunes, a longitudinal tune is introduced in [Section 4.1.5](#). Typically, longitudinal oscillations occur at larger time scales ($Q_s \ll Q_{x,z}$). Hence, **coherent** longitudinal oscillations, which may in principal distort the trace visible in [Fig. 4.3](#), have no significant impact in this measurement method.

The tune measurement capability of the streak camera supplements the dedicated **betatron tune** measurement systems installed in the **ELSA** storage ring (see e.g. [[Ebe10](#); [Rot12](#); [Sch15](#)]).

4.1.3 Longitudinal Equation of Motion

Accelerating Fields and Longitudinal Focusing

The circulating particles within the storage ring repeatedly gain energy (see [Eq. \(2.1\)](#)) by a harmonically oscillating, longitudinal electric field within the accelerating cavities. The accelerating field is induced by the cavity voltage

$$U(t) = U_0 \sin(\omega_{\text{RF}}t + \phi) , \quad (4.14)$$

²The pseudo-harmonic **betatron oscillation** may be transformed into a revolution-periodic, harmonic oscillation through the Floquet transformation [[Wi100](#), Section 3.14.2] to obtain a well-defined oscillation frequency.

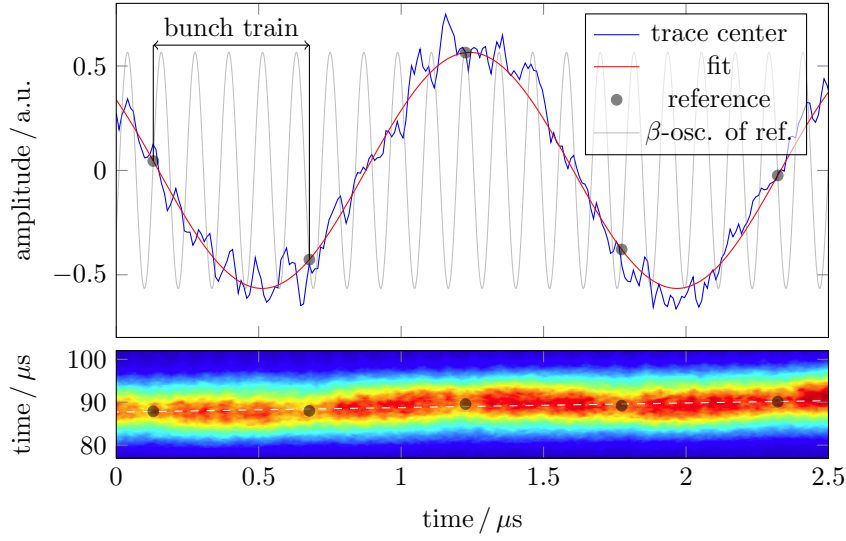


Figure 4.3: Determining the horizontal betatron tune Q_x through a streak image. The observable trace (blue, third trace in Fig. 3.12(a)) shows a spatial modulation with $f_{\text{spat}} = (687 \pm 2)$ kHz (red). The tune is measurable by matching a sinusoidal function (gray) to a reference point within the repeating 548 ns long bunch train (black dots). The resulting frequency $f_x = (8.44 \pm 0.01)$ MHz yields $Q_x = 4.624 \pm 0.002$. Note that the harmonic form is only valid for the location of the reference point, but is nevertheless shown for lucidity.

where $\omega_{\text{RF}} = 2\pi f_{\text{RF}}$ is the cavity's angular resonance frequency and ϕ is an arbitrary initial phase. Due to the sinusoidal form and the consequent periodic change of field direction, the particles circulate in separated bunches, where the number of buckets is called the harmonic number h . It is given by the fraction of electron path L and RF wavelength $\lambda_{\text{RF}} = c/f_{\text{RF}}$:

$$h = \frac{L}{\lambda_{\text{RF}}} = \frac{\omega_{\text{RF}}}{\omega_0}, \quad (4.15)$$

where ω_0 is the angular revolution frequency. The circumference of the ELSA storage ring $L = 164.4$ m yields $h = 274$ buckets with $\lambda_{\text{RF}} = 0.6$ m ($f_{\text{RF}} = 500$ MHz or 2 ns) spacing. The spacing is well observable by streak camera images, as shown in Fig. 3.10(a).

When a synchrotron is operated in storage mode³, the affecting acceleration voltage U_a is determined by the circumference voltage ΔE_{SR} (compare with Eq. (2.23)), as the accelerating cavity compensates the losses from SR emission:

$$U_a = \Delta E_{\text{SR}}/e \stackrel{!}{=} U_0 \sin \varphi_s, \quad (4.16)$$

where φ_s is called the synchronous phase. As shown below, the slope $U_0 \cos \varphi_s$ at $U(\varphi_s)$ determines the magnitude of restoring moments for longitudinal oscillations and is calculated from Eq. (4.16):

$$U_0 \cos \varphi_s = \pm \sqrt{U_0^2 - U_a^2}. \quad (4.17)$$

The negative signum holds for 2π multiples of $\pi/2 < \varphi_s < 3\pi/2$, and is positive otherwise.

The dispersive character of bending magnets (compare with Section 4.1.1) implies that revolving relativistic particles ($\beta \rightarrow 1$, $\gamma \gg 1$) with momentum deviation $\delta > 0$ cover an additional path $L + \Delta L$ after one lattice revolution. The momentum compaction factor α_c describes the fraction of relative path

³The magnetic guiding field and hence, the set particle energy remains constant.

elongation to relative momentum deviation [Wil00, Section 3.6]:

$$\alpha_c = \frac{\Delta L/L}{\Delta p/p} = \frac{1}{L} \oint \frac{D(s)}{R(s)} ds . \quad (4.18)$$

Its precise value is depending on the dispersion function $D(s)$ which may alter with the ion-optical setting. For particles with $\delta \neq 0$ momentum compaction effectuates longitudinal particle movement: The circumference deviation ΔL alters the revolution period $\Delta T = \Delta L/(\beta c)$ and causes a phase variation $\Delta\varphi = \omega_{RF}\Delta T$ upon re-arrival at the cavity. When the **synchronous phase** $\varphi_s(\Delta T = 0)$ is

$$\frac{\pi}{2} < \varphi_s < \pi , \quad (4.19)$$

relativistic particles with $\delta > 0$ experience a phase lag $\Delta\varphi$ at re-arrival at the cavity and gain less energy on the consecutive revolution, and vice versa. This way, acceleration and phase focusing are both achieved and particles with $\delta \neq 0$ perform longitudinal **synchrotron oscillations** around φ_s , as illustrated in Fig. 4.4.

Equation of Motion

Energy oscillations with small amplitudes⁴ are described by the differential equation

$$\Delta\ddot{E} + 2\alpha_s\Delta\dot{E} + \omega_s^2\Delta E = 0 , \quad (4.20)$$

where $\Delta E = E - E_0$ denotes the particle's deviation from the design energy E_0 and α_s is a damping constant, which is determined by the amount of beam excitation (e.g. through emission of **SR**) and the counteracting restoration of only longitudinal energy in the accelerating cavities. For $\alpha_s < \omega_s$ a damped, harmonic energy oscillation follows:

$$\Delta E(t) = \Delta E_0 e^{-\alpha_s t} e^{i\omega_s t} . \quad (4.21)$$

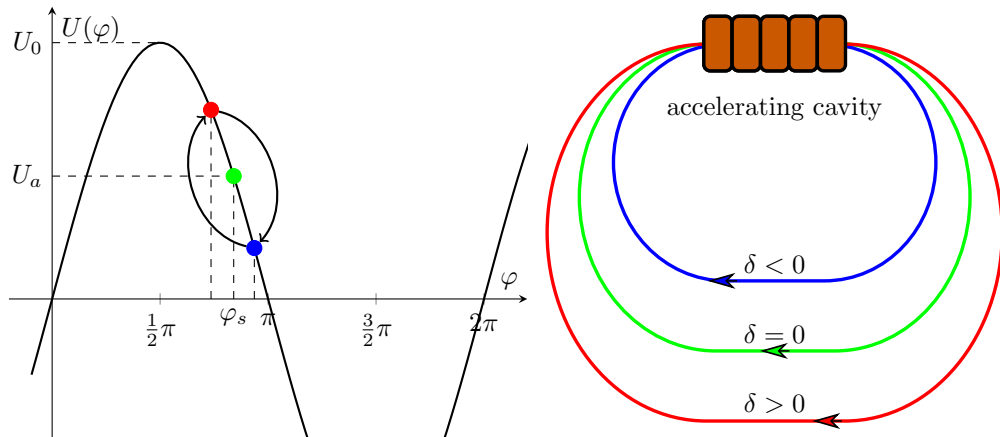


Figure 4.4: Longitudinal phase focusing of relativistic particles in synchrotrons. Particles with $\delta \neq 0$ travel on dispersive orbits and experience a phase-lag and hence a voltage variation upon re-arrival at the accelerating cavity. Particles with $\delta > 0$ (red) re-arrive after φ_s and gain less energy for the next turn. Hence, δ is temporarily reduced. The opposite occurs for $\delta < 0$ (blue). The particles perform longitudinal oscillations around φ_s .

⁴Amplitudes in which the potential is sufficiently linear.

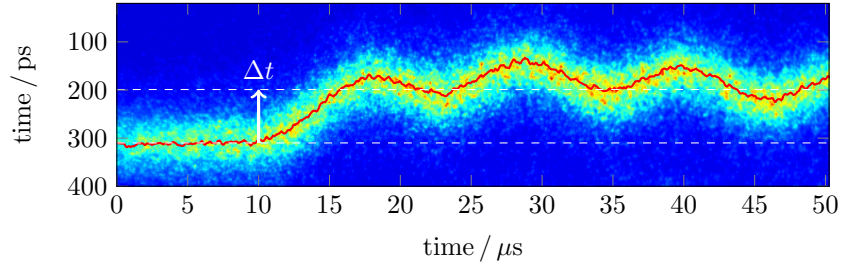


Figure 4.5: Longitudinal beam oscillations of a 2 GeV beam observed with the streak camera’s synchroscan and dual time base extension units. The phase jump and the subsequent oscillation is caused by an induced RF phase change $\Delta\varphi$ of the accelerating cavities at approximately 10 μs . The oscillatory behavior at a later time observed in Fig. 3.15 is caused by this phase jump.

Equation (4.21) is visualized on the streak camera synchroscan images in Figs. 3.15 and 4.5. The oscillation therein was induced by an abrupt phase jump of the accelerating cavities’ electric field, where the RF phase was set to $\varphi_s \rightarrow \varphi_s + \Delta\varphi$ with $\Delta\varphi = 20^\circ$ ($\Delta t = 111$ ps). The initial beam response to the phase shift is shown in Fig. 4.5. The particle bunches move towards the renewed synchronous phase and begin to oscillate around it. The oscillation centroid is overshoot within a time window of approximately 30 μs due to the finite cavity’s voltage response (compare with [Sch15, Section 12.5.2, Fig. 12.11]). Thereafter, the oscillation centroid coincides with the set Δt . The phase shift resulting from an energy deviation ΔE is [Wil00, Eq. (5.76)]

$$\Delta\varphi = \frac{2\pi h}{\beta^2} \left(\alpha_c - \frac{1}{\gamma^2} \right) \frac{\Delta E}{E} \stackrel{\beta \rightarrow 1}{=} 2\pi h \alpha_c \frac{\Delta E}{E}. \quad (4.22)$$

In the above example the oscillation span amounts $\Delta\varphi_{\min}^{\max} = 9.0^\circ$ (50.2 ps). Solving Eq. (4.22) for ΔE , one observes an energy oscillation with an amplitude of $\Delta E_0 = 1.47$ MeV. Since $\alpha_s < \omega_s$ (compare with Sections 4.1.4 and 4.1.6), the impact of oscillation damping is not visible within the displayed time interval (see Section 4.1.6 for damping measurements).

4.1.4 Synchrotron Tune

For harmonic synchrotron oscillations⁵, the angular synchrotron frequency ω_s can be calculated using Eqs. (4.18), (4.20) and (4.22) (compare with e.g. [Wil00, Section 5.6]):

$$\omega_s = \omega_0 \sqrt{-\frac{heU_0 \cos \varphi_s}{2\pi\beta^2 E} \left(\alpha_c - \frac{1}{\gamma^2} \right)} \stackrel{\beta \rightarrow 1}{=} \omega_0 \sqrt{-\frac{heU_0 \cos \varphi_s \alpha_c}{2\pi E}}, \quad (4.23)$$

where the approximation holds for relativistic particles. The radicand is positive for a negative signum in Eq. (4.17), if the synchronous phase φ_s obeys Eq. (4.19). In analogy to the betatron tune in Section 4.1.2, the fraction of synchrotron and revolution frequency is called the synchrotron tune

$$Q_s = \frac{\omega_s}{\omega_0}, \quad (4.24)$$

⁵Oscillations at small amplitudes are approximately harmonic.

stating the number of **synchrotron oscillations** per revolution. Figures 3.15 and 4.5 show **coherent synchrotron oscillations** at $f_s = (88.85 \pm 0.11)$ kHz, representing a typical **synchrotron tune** for the ELSA storage ring: $Q_s = 0.049 \pm 0.001$.

When Q_s and U_0 are measured, the momentum compaction factor (Eq. (4.18)) can be determined via Eqs. (4.17), (4.23) and (4.24):

$$\alpha_c = \frac{2\pi E Q_s^2}{h e \sqrt{U_0^2 - U_a^2}}. \quad (4.25)$$

4.1.5 Optical Resonances

In reference to Section 4.1.2, the tune triplet (Q_x, Q_z, Q_s) is referred to as the *working point* of an accelerator. In general it has to be carefully chosen to avoid the excitation of beam destructive resonances which occur for tunes $Q_{x,z,s}$ set to integer, half-integer, third-integer, etc. (for details see e.g. [Wie93, Section 7.4]). Stability is granted if the tunes are non-rational numbers, so that particles do not occupy previous regions in phase space (compare with Eq. (4.10)) when repeatedly arriving at the same location of the accelerator.

As coupling between the planes is always present (compare e.g. with Section 4.3), the condition

$$m_x Q_x + m_z Q_z + m_s Q_s = p \quad m_i \in \mathbb{N} \quad (4.26)$$

defines *stop bands*, where $\mathcal{O} = |m| + |n| + |q|$ is the order of an ion-optical resonance. As the driving force of these resonances are electromagnetic field errors – which are generally unknown – the affecting severity and width of the individual stop bands differ. An extensive analysis and characterization of the relevant stop bands close to the typical ELSA *working point* can be found in [Pro18, Chapter 8]. In general, the resonance strength decreases strongly with order. Resonances beyond 4th order have usually negligible effect. A tune diagram with typical ELSA storage ring *working point* (4.62, 4.44, 0.05) is shown in Fig. 4.6.

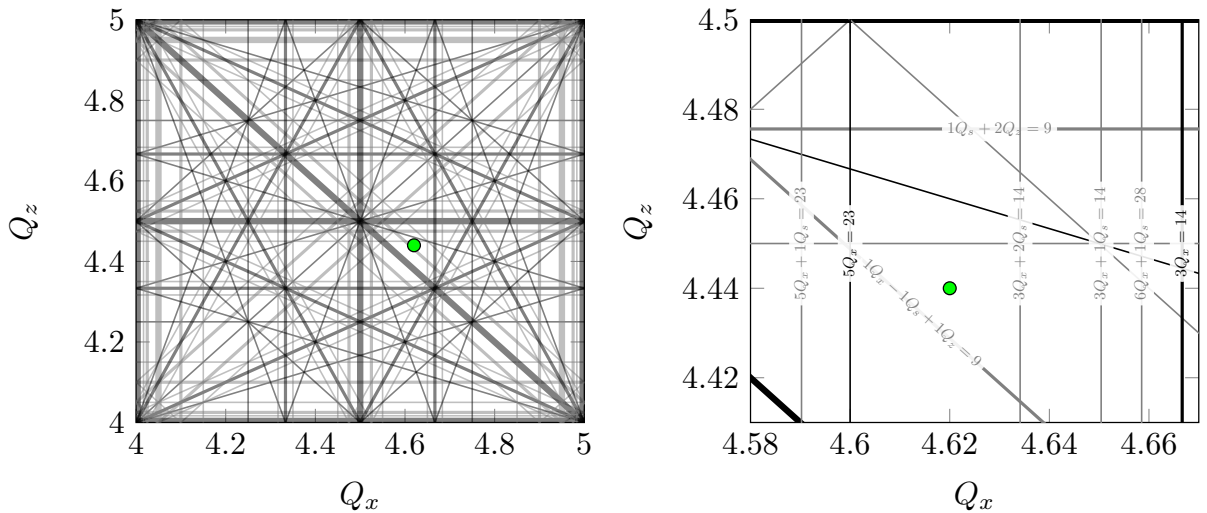


Figure 4.6: Tune diagram with resonance stop bands up to 4th order (a) and close-up to the vicinity of a typical ELSA storage ring working point (green) up to 7th order (b) at a **synchrotron tune** $Q_s = 0.05$. For beam extraction the working point is intendedly moved towards the third order resonance $3Q_x = 14$ to create a controlled horizontal beam instability.

4.1.6 Radiation Damping

The signum of the damping constant α_s in Eq. (4.21) – and in analogy α_x and α_z for the transverse planes – determines if the oscillation is damped or excited. Damping is granted for $\alpha_i > 0$, $i \in \{x, z, s\}$, where the signum generally depends on the lattice configuration (compare e.g. with [Wil00, Section 5.6]). The damping constant computes to [Wil00, Section 6.3]

$$\alpha_i = \frac{1}{\tau_i} = \frac{\Delta E_{\text{SR}}}{2T_0 E} \cdot J_i \quad \text{with } i = \{x, z, s\}, \quad (4.27)$$

where T_0 is the revolution period and J_i a plane-specific factor:

$$J_s = 2 + \mathcal{D}, \quad (4.28)$$

$$J_x = 1 - \mathcal{D}, \quad (4.29)$$

$$J_z = 1. \quad (4.30)$$

Here, the *magnetic structure parameter* \mathcal{D} describes the effect of magnetic dispersion in a lattice [Wil00, Eq. (6.20)]:

$$\mathcal{D} = \frac{\oint \left[\frac{D_x}{R} \left(2k + \frac{1}{R^2} \right) \right] \cdot ds}{\oint \frac{ds}{R^2}} \approx \frac{\oint \frac{D_x(s)}{R(s)} \cdot ds}{2\pi R} = \frac{\alpha_c L}{2\pi R}, \quad (4.31)$$

where R is the bending radius and k the quadrupole strength (compare with Eq. (4.4)). The approximation holds for isomagnetic⁶, *separated-function* synchrotrons⁷ and is valid for the ELSA storage ring. As α_c is of order 10^{-2} , $\mathcal{D} \approx 0$ follows and hence, damping takes place simultaneously in all planes of a storage ring due to $\alpha_i > 0$.

The longitudinal damping process can be visualized in a dual time base synchroscan measurement, as exemplarily shown in Fig. 4.7. Therein, the electron beam (at 1.5 GeV) is initially stabilized by the BBB, which is switched off at 5 μs . The beam is then longitudinally excited by higher order modes (HOMs) of the acceleration field (see details about HOMs in e.g. [Sch15, Chapter 8]). The BBB is switched on around 10 μs and re-stabilizes the beam centroids. However, particles performing incoherent synchrotron oscillations cannot be corrected and remain visible as damped longitudinal beam envelope, as described

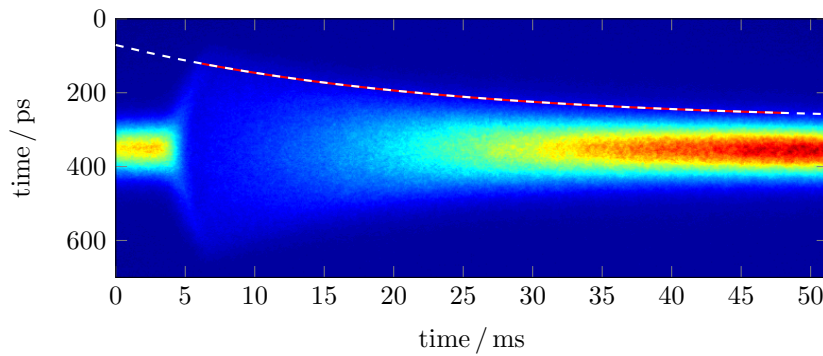


Figure 4.7: Synchroscan measurement of an excited and damped longitudinal oscillation of a 1.5 GeV beam. The marked beam envelope follows an exponential decay according to Eq. (4.21) and amounts $\tau_s = 22.3$ ms.

⁶The bending radius is equal in all bending magnets.

⁷In *separated-function* synchrotrons beam focusing occurs outside of bending magnets, hence $\int \frac{k(s)}{R(s)} \cdot ds = 0$.

by Eq. (4.21). The envelope is obtained from the streak image by choosing an intensity threshold value, whose temporal (vertical) position is determined for every image column. An exponential fit to its temporal development yields the damping constant α_s . Measurements and expected values of $\tau_s(E)$ in dependence of beam energy are shown in Fig. 4.8.

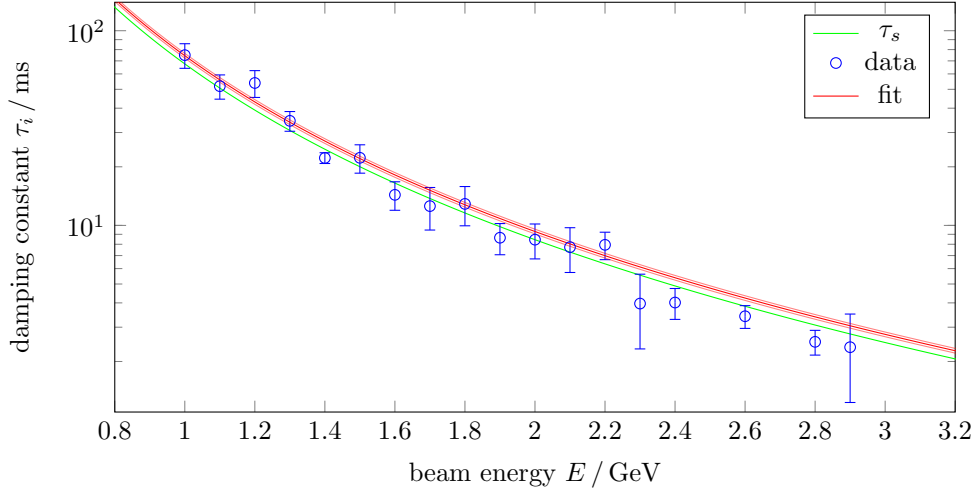


Figure 4.8: Streak camera measurements of the longitudinal damping time at different beam energies E in comparison to the calculated τ_s with $J_s = 1.998$ (Elegant [Bor01] storage ring model calculation). The error represents the standard deviation of multiple measurements for a specific beam energy.

4.2 Energy Spread and Bunch Length

The radiation damping process described above is counteracted by the particle's stochastic energy loss due to the quantum-character of SR emission (compare with Section 2.3.3). The equilibrium of damping and excitation eventually results in a Gaussian distributed energy spread σ_E/E , which computes to [Lee04, Section 4.II.4.B]

$$\frac{\sigma_E}{E} = \gamma \sqrt{\frac{C_q}{J_s R}}, \quad \text{with} \quad C_q = \frac{55}{32 \sqrt{3}} \frac{\hbar c}{E_{0,e}} \approx 3.83 \cdot 10^{-13} \text{ m} \quad (4.32)$$

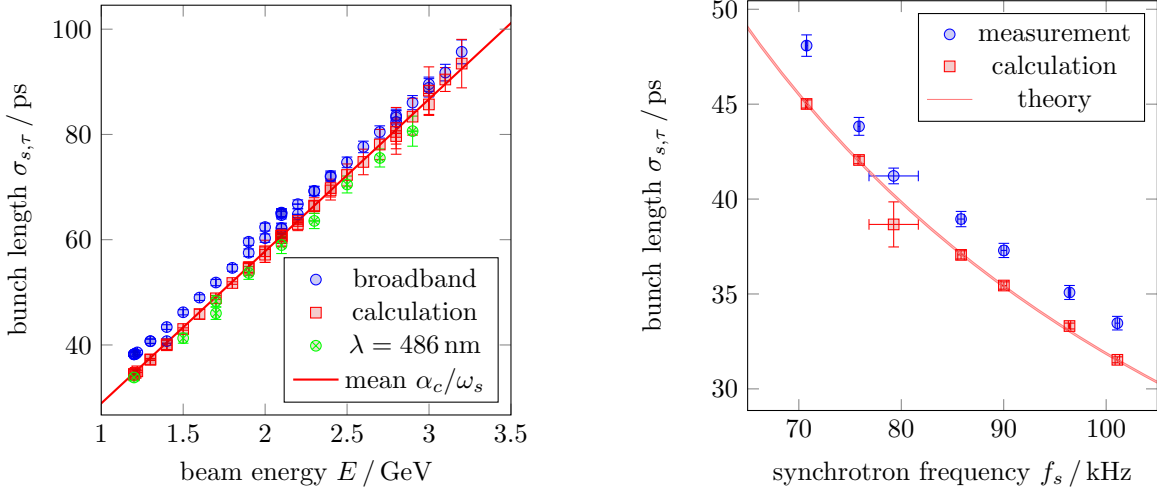
in the case of relativistic particles orbiting in an isomagnetic lattice. For the ELSA storage ring energies of 1.2 to 3.2 GeV one obtains $\sigma_E/E = 3.1 \times 10^{-4}$ to 8.3×10^{-4} .

The temporal electron bunch length $\sigma_{s,\tau}$ is given by the RMS phase distribution $\Delta\varphi_{\text{rms}}$ (compare with Eq. (4.22)) of particles in a bunch ensemble. Its dependence on the energy spread is derived e.g. in [Wie93, Section 8.1.2] and computes to [Wie93, Eq. (8.70)]:

$$\sigma_{s,\tau} \stackrel{\beta \rightarrow 1}{=} \frac{\alpha_c}{\omega_s} \left(\frac{\sigma_E}{E} \right). \quad (4.33)$$

At the ELSA storage ring the calculated bunch length $\sigma_{s,\tau}$ varies from 34.7 to 92.4 ps between beam energies of 1.2 to 3.2 GeV at a typical synchrotron frequency of $f_s = \omega_s/(2\pi) = 88.85$ kHz and momentum compaction $\alpha_c = 0.062$.

Streak camera measurements demonstrating Eq. (4.33) in the ELSA storage ring are shown in Fig. 4.9.



(a) Bunch length dependency on beam energy E with broadband VIS and monochromatic light measurements at $\lambda = 486$ nm compared to calculations.

(b) Bunch length and varying synchrotron frequency f_s at 1.2 GeV beam energy. An offset of approximately 2.5 ps is observable.

Figure 4.9: Bunch length measurements at ELSA with varying beam energy E and synchrotron frequency f_s . The measurement was conducted in storage mode, where the remaining parameters in Eq. (4.33) were approximately constant. Bunch length measurement data is compared to ELSA CS parameter based calculations.

In Fig. 4.9(a) the beam energy was increased in storage mode, while the remaining parameters were held approximately constant⁸. The bunch length measurements were performed with broadband VIS and monochromatic light at $\lambda = 486$ nm to test the effect of dispersive signal broadening (compare with Section 3.1.2). The bunch length for varying ω_s at fixed beam energy $E = 1.2$ GeV is shown in Fig. 4.9(b). In both figures the bunch length was additionally calculated via Eq. (4.33) using the measurement values E , U_0 and f_s obtained from the ELSA CS data base.

The majority of the presented data shows deviations from the calculated values above the specified resolution limit of the device (< 1 ps). The following types of deviations are noticeable:

1. bunch length independent positive or negative offsets ranging from -1.7 to 2.4 ps (data set average), and
2. discontinuities in the linear succession of the data sets in the order of 2 ps.

To eliminate the influence of machine parameter variations (ω_s varied by approximately 5% in Fig. 4.9(a)), Fig. 4.10 shows Eq. (4.33) with the data sets of Figs. 4.9(a) and 4.9(b) as normalized linear relation with proportionality constant ς consisting of natural constants only. The independent variable \mathcal{E} includes the measured ELSA CS machine parameters and machine constants of Eqs. (4.25) and (4.32):

$$\sigma_{s,\tau} = \varsigma \mathcal{E}, \quad \text{with} \quad \varsigma = \frac{\sqrt{C_q}}{E_{0,e}} \quad \text{and} \quad \mathcal{E} = \frac{1}{f_0^2 h \sqrt{J_s R}} \frac{f_s E^2}{\sqrt{U_0^2 - U_a^2}}. \quad (4.34)$$

Figure 4.10 confirms the observation of Fig. 4.9(a): The monochromatic data set underestimates the bunch length, whereas the broadband VIS data set is generally overestimating it by a similar amount of

⁸Minor variations of ω_s and α_c may result from imperfect RF voltage calibration and energy-dependent choice of the transverse tunes $Q_{x,z}$.

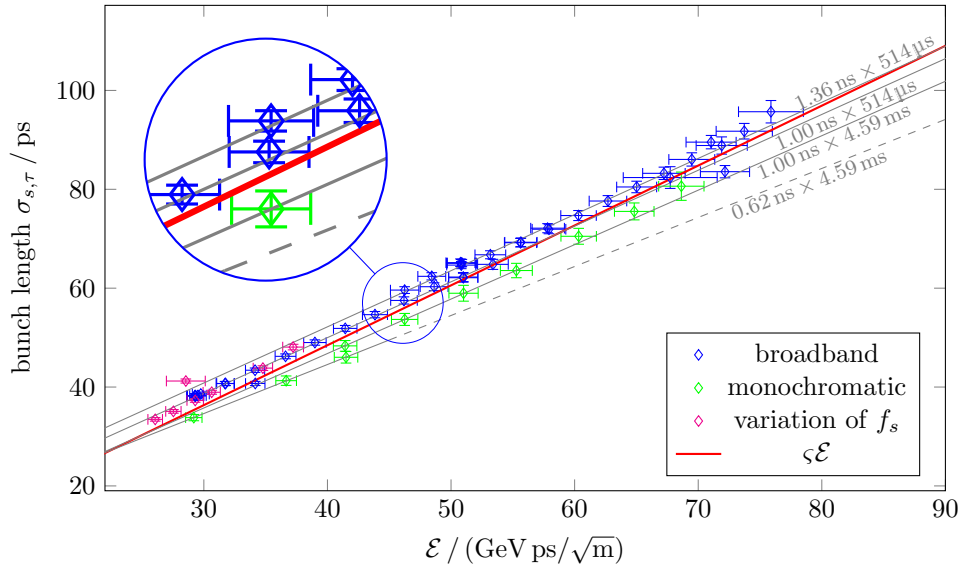


Figure 4.10: Bunch length in dependence of normalized beam energy \mathcal{E} . The proportionality constant ζ is based on nature constants (compare with Eq. (4.34)). The linear fits for the four groups of data (gray) indicate the chosen time windows of the streak tube. Their mismatch indicates an imperfect calibration.

approximately 2 ps. As visible in Eq. (4.34), it is evident that the result is dependent on the beamline and streak camera settings.

Data Quality and Error Sources

The cause for the above mentioned data discrepancies may be associated with systematic measurement errors from the streak camera device, the photon profile analysis method, and the accelerator parameter measurement systems:

The streak camera sweep range variation is the main cause of the inconsistent data observed in Fig. 4.10. The cause may be an imperfect pixel-to-time calibration of the specific sweep settings, a non-linear intensity response, an influence of the image granularity, a non-linear response of the photon profile's position on the CCD matrix, or a combination of the above. The highlighted example in Fig. 4.10 shows a data inconsistency of 10.3 % for comparable accelerator settings, but different streak camera and beamline settings. The data processing of these data points is exemplarily shown in more detail in Appendix B. The effect of the CCD position-dependent variation (non-linear position response) is shown in Figs. 3.16 and B.1 to B.3. The manufacturer reports non-linearities of below 1.3 % [Ham13], but this effect may be amplified by stray magnetic and electric fields at the present streak camera location. It is, however, of minor influence compared to the effect due to variation of sweeping ranges. Therefore, the imperfect calibration of the device is considered to have the largest contribution to the systematic error of the bunch length measurement. A re-calibration based on gauge photon signals (SR or short-pulsed laser radiation) were not performed within the scope of this work. This would, however, significantly increase the measurement precision.

The profile analysis method may influence the photon profile analysis result e.g. through variation of the size of an AOI, when the data set deviates from a true Gaussian profile. The effect of a varying AOI is compared in Fig. B.5 in Appendix B for the exemplary measurement of the broadband and monochromatic data examples given in Figs. B.2 and B.3. The measurement error is 5 % at an AOI width⁹ of $> 1.5 \sigma$ (1 % at $> 2.4 \sigma$) for Fig. B.2 and 5 % at $> 2.1 \sigma$ (1 % at $> 3.3 \sigma$) for the more granular image of Fig. B.3. As the profile analysis AOI usually spans across $> 3.5 \sigma$, the effect is considered to be generally $< 1 \%$.

The accelerator parameter measurement may be corrupted by false values recorded in the data history or by systematic errors introduced by imperfect calibration of the individual measurement devices or systems. Whereas false values among logically correct data pairs were filtered out in the image analysis by identifying statistical fluctuations in a measurement series, the impact of systematic errors can only be estimated. These would result in a horizontal displacement of the linear relations in Fig. 4.10. However, due to the vertical data spread (positive and negative), this error contribution cannot be determined in this measurement.

4.3 Beam Emittance and Transverse Size

In analogy to the consideration of energy spread and bunch length in Section 4.2, the transverse beam size is formed by a multitude of individual particles which perform *incoherent betatron oscillations*. In comparison to the single particle trajectory of Eq. (4.7), the figure for the macroscopic beam size results from a statistical description of the particle entirety (e.g. the number of electrons in a circulating bunch), where the beam emittance is given exemplarily for the horizontal plane as

$$\epsilon_x = \sqrt{\langle x^2 \rangle \langle x'^2 \rangle - \langle xx' \rangle^2}, \quad (4.35)$$

based on the squared mean of displacements x , angular deviations x' and the correlation xx' of the particle population in phase space (x, x') (compare with [Lee04, Section 2.II.5.A] and Eq. (4.10)). The horizontal and vertical emittances $\epsilon_{x,z}$ as well as the optical functions (see Section 4.1.1) determine the corresponding transverse beam sizes according to

$$\sigma_{x,z} = \sqrt{\epsilon_{x,z} \beta_{x,z}(s) + \left(\frac{\Delta p}{p} D_{x,z}(s) \right)^2}. \quad (4.36)$$

For ideal planar synchrotrons the emittance of the vertical plane ϵ_z and the dispersion function $D_z(s)$ are effectively zero. In practice, however, the beam deflection is not entirely planar and when observed, the electron beam shows a significant vertical size (compare with Table 3.4). The cause of it lies in the imperfection of magnetic fields and the corresponding presence of skewed quadrupole, and other higher order fields, which cause plane coupling¹⁰. The emittance coupling factor is

$$\kappa = \frac{\epsilon_z}{\epsilon_x} \quad (4.37)$$

⁹The width of σ corresponds to an effective fit span of 2σ .

¹⁰Vertical beam motion becomes dependent on horizontal motion, and vice versa.

and typically has a value between 1 to 10 % in contemporary synchrotrons. The sum of the transverse beam emittances is preserved and form the *natural emittance* of a [lattice](#):

$$\epsilon_0 = \epsilon_x + \epsilon_z, \quad (4.38)$$

With [Eqs. \(4.37\)](#) and [\(4.38\)](#) one obtains for the transverse emittances

$$\epsilon_x = \frac{\epsilon_0}{1 + \kappa} \quad \text{and} \quad \epsilon_z = \frac{\kappa \epsilon_0}{1 + \kappa}. \quad (4.39)$$

The *natural emittance* ϵ_0 can be obtained in analogy to the energy spread σ_E/E (compare with [Eq. \(4.32\)](#)): The damping and quantum excitation through [SR](#) emission in storage rings (compare with [Sections 2.3.3, 4.1.6](#) and [4.2](#)) results in a horizontal beam excitation equilibrium state, which allows to calculate ϵ_0 for electron beams [[Wil00](#), Eq. (6.48)]

$$\epsilon_0 = \frac{55}{32} \frac{\hbar c}{\sqrt{3} E_0} \gamma^2 \frac{\langle 1/R^3 \cdot \mathcal{H}(s) \rangle}{J_x \langle 1/R^2 \rangle}, \quad (4.40)$$

with the *Lorentz* factor γ , the horizontal damping constant J_x (see [Eq. \(4.29\)](#)) and the *Courant Snyder invariant* of [Eq. \(4.10\)](#) for a dispersive particle in phase space (x, x') at $\Delta p/p = 1$:

$$\mathcal{H}(s) = \gamma(s) D^2(s) + 2\alpha(s) D(s) D'(s) + \beta(s) D'^2(s). \quad (4.41)$$

For isomagnetic [lattices](#), [Eq. \(4.40\)](#) simplifies to [[Wil00](#), Eq. (6.49)]

$$\epsilon_0 = 1.47 \times 10^{-6} \frac{E^2}{R \cdot L} \int_0^L \mathcal{H}(s) \cdot ds, \quad (4.42)$$

where E is the beam energy in GeV, R the bending radius and L the length of the [lattice](#). For the [ELSA](#) storage ring one obtains $\epsilon_0 \approx 120$ to 900 mm mrad¹¹ between 1.2 to 3.2 GeV for a tune of $Q = (4.64, 4.43)$.

Beam Size

The optical functions around the source point of the M7 beamline are shown in [Figs. 4.2](#) and [4.11](#) and their values are listed in [Table 4.1](#). The expected beam sizes for the [ELSA](#) storage ring energies from 1.2 to 3.2 GeV are illustrated in [Fig. 4.12](#) for an assumed emittance coupling factor of $\kappa = 10$ %. The uncertainty of the source point's position is indicated. It introduces an error of the $\beta(s)$ -function's value of approximately 2 %. [Table 4.2](#) shows examples for beam size calculations with emittance coupling of 1 % and 10 %. Compared to the results of the measurements in [Table 3.4](#), which span from $\sigma_h = 4.0$ to 5.5 mm

s / m	$\beta_x(s) / \text{m}$	$\beta_z(s) / \text{m}$	$D_x(s) / \text{m}$
33.13 ± 0.05	5.69 ± 0.09	8.78 ± 0.11	1.97 ± 0.01

Table 4.1: Optical functions at the M7 beamline source point. The error marks the deviation for a longitudinal source point uncertainty of $\Delta g = \pm 0.05$ m (compare with [Section 3.1.2](#)).

¹¹Values calculated by the in-house developed [ELSA](#) simulation software SIMLIB [[Wen94](#)].

E / GeV	$\kappa / \%$	σ_x / mm	σ_z / mm
1.2	1	1.03 ± 0.01	0.10 ± 0.01
1.2	10	1.00 ± 0.01	0.31 ± 0.01
3.2	1	2.80 ± 0.02	0.28 ± 0.01
3.2	10	2.73 ± 0.02	0.84 ± 0.01

Table 4.2: Expected beam size at the M7 beamline source point for varying beam energies E and coupling factors κ . As in Table 4.1, the error marks the deviation for longitudinal source point uncertainty of $\Delta g = \pm 0.05 \text{ m}$.

and $\sigma_v = 0.9$ to 2.1 mm and show a mean value of $\overline{\sigma_h} = (4.8 \pm 0.8) \text{ mm}$ and $\overline{\sigma_v} = (1.5 \pm 0.5) \text{ mm}$, the measurement exceeds the expected values beyond the estimated error. As discussed in Section 3.2.1, the imperfect focusing lens positions are considered to be the main cause for precision-limiting systematic errors. Nevertheless, a 10σ tolerance of the calculated smallest (1.2 GeV at $\kappa = 10\%$) and largest (3.2 GeV at $\kappa = 1\%$) beam sizes gives a proficient estimation of the required object field span G for the visual monitoring of the electron beam at the M7 SR diagnostic beamline, as declared in Section 3.1.2:

$$G = 3.1 \text{ to } 28 \text{ mm} . \quad (3.3 \text{ revisited})$$

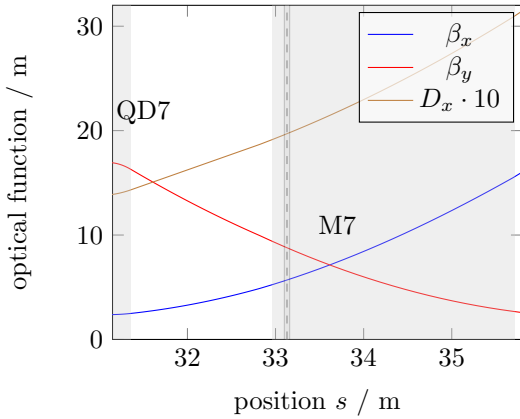


Figure 4.11: Optical functions around the M7 beamline source point (dashed line) with position uncertainty indicated.

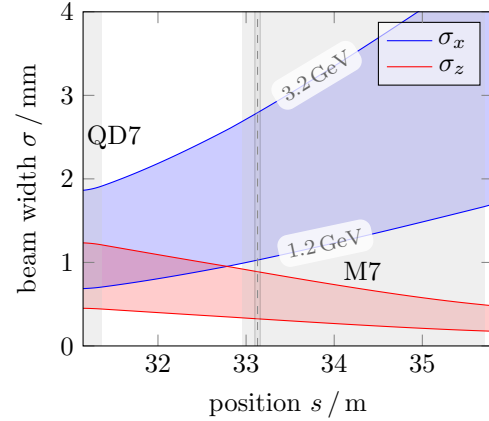


Figure 4.12: Electron beam size at the M7 beamline source point for 1.2 to 3.2 GeV beam energy and emittance coupling $\kappa = 10\%$.

4.4 Filling Pattern

The streak camera allows precise measurements of the storage ring's 548 ns long filling pattern through the analysis of the streak trace's amplitude distribution. Figure 4.13 shows exemplary images of the filling pattern in slow sweep mode. Therein, the vertical sweep window of $1.02 \mu\text{s}$ at 512 pixels provides a resolution of 1.99 ns/pixel , providing a close match to the bucket distance. When the absolute beam current I is known (e.g. by measurement with an integrated current transformer¹²), the bunch current

¹²Bergoz integrated current transformer (ICT) is used in the ELSA storage ring.

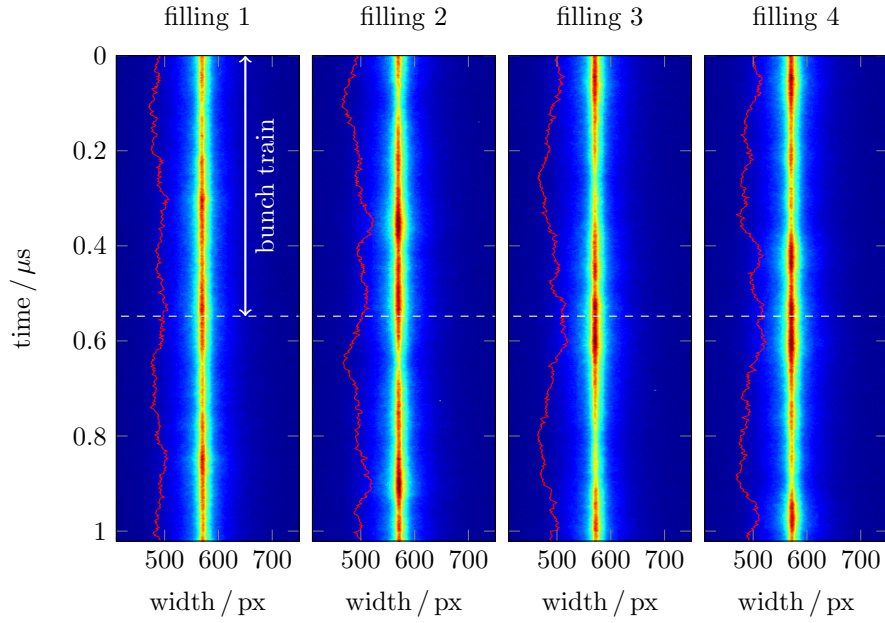


Figure 4.13: Multiple filling patterns of the standard injection scheme observed with the streak camera’s slow sweep unit.

example	mean bunch current $\bar{I}_b / \mu\text{A}$	total current I / mA	deviation
filling 1	53.7 ± 4.9	14.7	9.1 %
filling 2	46.9 ± 6.9	12.9	14.7 %
filling 3	40.1 ± 5.6	11.0	14.0 %
filling 4	49.0 ± 6.4	13.4	13.1 %

Table 4.3: Comparison of homogeneity of the filling patterns shown in Fig. 4.13.

computes to

$$I_b = \frac{A_i I}{\bar{A} h}, \quad (4.43)$$

where A_i is the profile amplitude of bunch i and \bar{A} is the mean amplitude of the bunch train. Table 4.3 compares the filling pattern homogeneity of those measurements shown in Fig. 4.13. In 33 user operation sample fillings, a beam homogeneity deviation of $(13.0 \pm 6.1) \%$ was obtained. This value includes the precision error of the measurement, which can be estimated by comparing the two successively recorded bunch trains in one trace, as exemplarily shown in Fig. 4.14 for *filling 1* of Fig. 4.13. The average precision from all sample measurements is 5.4 %.

The filling pattern monitoring allowed the calibration and verification of functionality of the novel **field programmable gate array (FPGA)** based timing system for the ELSA facility. Therein, the injection scheme was optimized to the verified length of the injected bunch train (compare with Fig. 3.10(b)) in order to maximize the filling pattern’s homogeneity with a deviation of approximately 8 % [Pro18, Section 6.5].

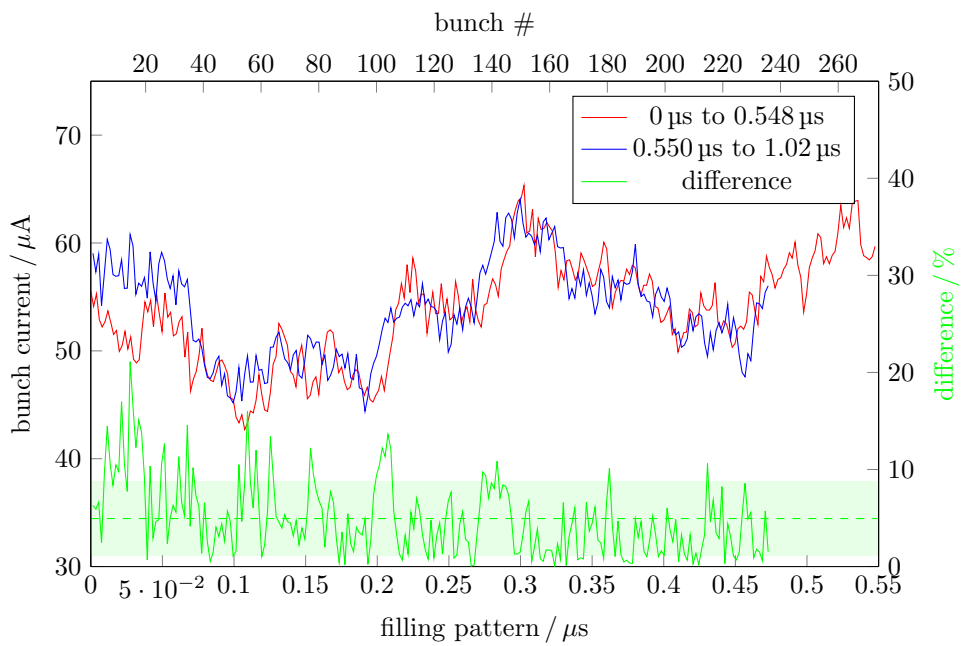


Figure 4.14: Filling pattern of *filling 1* in Fig. 4.13. The intensity measurement of the successively recorded bunch train (red and blue) shows a difference (green), whose mean amounts $(4.9 \pm 3.9)\%$ for the available 236 nodes.

Compton Backscattering and Polarimetry

The principles of the electron polarization measurement through CBS are explicated in this chapter. The properties of the Compton effect, the interaction cross sections of circularly polarized photons scattering off spin-polarized electrons and the technique and fundamentals for detecting the scattering products are described.

5.1 Compton Scattering

The process of X-ray photons scattering off atomic shell electrons was first measured and characterized by Arthur H. Compton in 1922 [Com22]. An incident photon with normalized energy

$$\vec{K}_i = \frac{\hbar c}{m_e c^2} \vec{k}_i \quad (5.1)$$

transfers momentum to a scattering electron and retains

$$K_f \equiv |\vec{K}_f| = \frac{1}{1 - \cos \vartheta + \frac{1}{|\vec{K}_i|}} \quad (5.2)$$

as final photon, where ϑ is the scattering angle. In the following, the vector's absolute value is abbreviated (e.g. $|\vec{K}_f| \rightarrow K_f$). Figure 5.1 visualizes the kinematic parameters: ϑ , the incident angle α and the

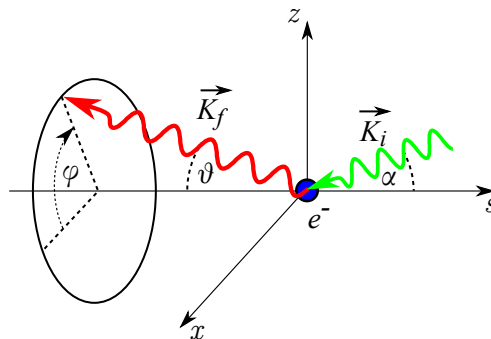


Figure 5.1: Kinematics parameters of Compton scattering with the photon incident angle α and the azimuthal and polar scattering angles φ and ϑ .

azimuthal angle φ . It is later shown that the Compton effect cross section has a maximum for energetic X-ray (keV) photons and is negligible for the much lower energetic VIS (eV). However, if the scattering electron travels at relativistic velocities, the transformed photon energy in the electron's rest frame is increased (boosted) and the Compton effect becomes utilizable for laser polarimetry.

5.1.1 Scattering on Relativistic Electrons

In the rest frame (*) of a relativistic electron, the scattering photon's energy is boosted according to Lorentz's transformation for opposing velocities (see [Appendix C.2](#) for details):

$$K_i^* = \gamma(1 + \beta \cos(\alpha)) K_i \approx 2\gamma K_i, \quad (5.3)$$

where the approximation holds for small incident angles (e.g. $\alpha \approx 3$ mrad). For example, in case of a 2.3 eV photon beam ($\lambda_{\text{ph}} = 532$ nm) and the ELSA electron beam energy ranging from 0.5 to 3.2 GeV, one obtains $K_i^* = 0.009$ to 0.057, which corresponds to photon energies of $E_i^* = 4.6$ to 29.1 keV. The transformed incident angle α^* in the electron's rest frame

$$\alpha^* = \arctan\left(\frac{\sin \alpha}{\gamma(1 + \beta \cos(\alpha))}\right) \approx \alpha/2\gamma \quad (5.4)$$

justifies the assumption of a head-on collision of electrons and photons. According to [Eq. \(5.2\)](#), the angular energy distribution is approximately isotropic due to $|K_i^*| \ll 1$, as shown in [Fig. 5.2](#). The largest momentum transfer to the electron is provoked at $\vartheta^* = 180^\circ$.

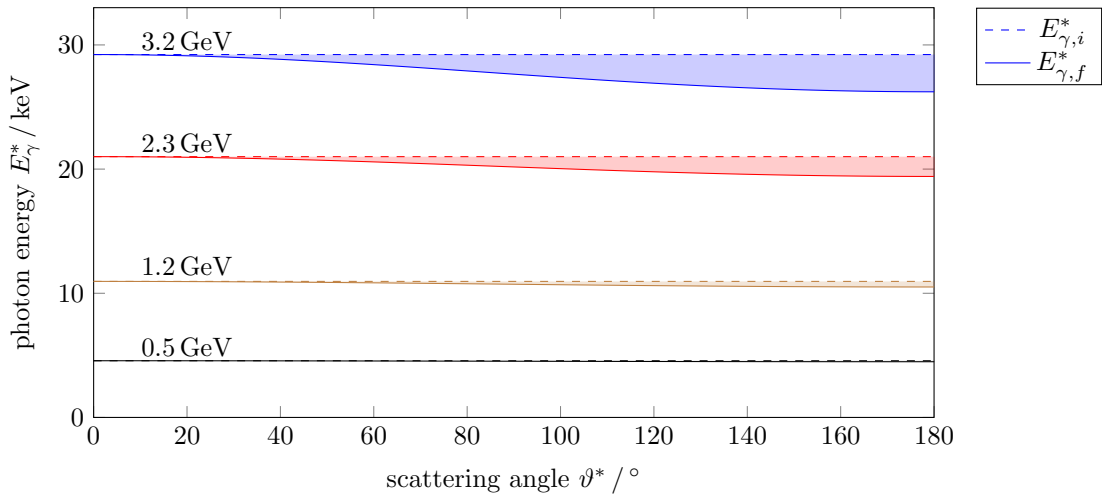


Figure 5.2: Angular distribution of scattered photon energies $E_{\gamma,f}^*(\vartheta)$ for varying electron beam energies. The dotted line marks the initial photon energy $E_{\gamma,i}^*$ in the electron's rest frame.

5.1.2 Backscattered Photons in the Laboratory Frame

In the laboratory frame one observes the scattered photons of Eq. (5.2) once again Lorentz-transformed:

$$K_f = \gamma(1 - \beta \cos \vartheta^*) K_f^*, \quad (5.5)$$

$$\vartheta = \arctan\left(\frac{\sin \vartheta^*}{\gamma(1 - \beta \cos \vartheta^*)}\right), \quad (5.6)$$

where the maximum energy transfer takes place at $\vartheta^* = 180^\circ$, yielding

$$K_{f,\max} = 2\gamma K_f^* \stackrel{\text{Eq. (5.3)}}{\approx} 4\gamma^2 K_i \quad (5.7)$$

for the CBS γ -photons. For example, an $E_i = 2.3$ eV incident photon scattering off a 3.2 GeV electron ($\gamma \approx 6262$) reaches a maximum observable energy of $E_{f,\max} = 328$ MeV. The photon energy in dependence of the observation angle ϑ is shown in Fig. 5.3. The approximately isotropically scattered photons of Eq. (5.2) in the electron's rest frame (compare with Fig. 5.2) are observed as narrow cone of width $\vartheta \approx 1/\gamma$ in the laboratory frame, comparable to the shape of the SR emission cone (see Section 2.2.2 and Eq. (2.27)). The width of the photon profile for an infinitesimal interaction point (IP) in 15 m distance is therefore approximately 2.4 to 15 mm wide for the corresponding storage ring beam energy. Due to the transverse size of the electron and photon beam, the effective backscattering photon profile is of larger size, as later shown in simulations (compare with Section 5.5).

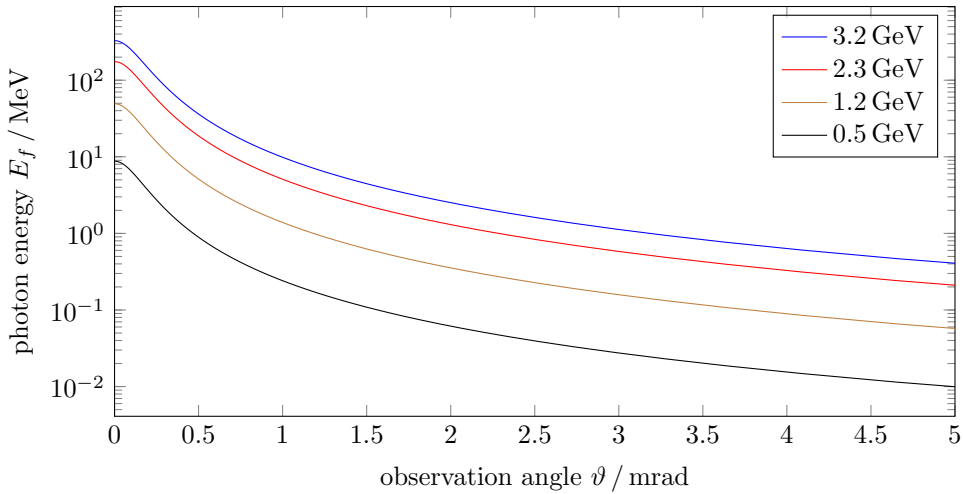


Figure 5.3: Energy dependence on observation angle ϑ in the laboratory frame.

5.1.3 The Compton Cross Section

The Compton scattering cross section was first theoretically obtained by Klein and Nishina in 1929 [KN29]:

$$\frac{d\sigma_c}{d\Omega} = \frac{r_e^2}{2} \frac{1}{[1 + K_i^*(1 - \cos \vartheta^*)]^2} \left(1 + \cos^2 \vartheta^* + \frac{K_i^{*2}(1 - \cos \vartheta^*)^2}{1 + K_i^*(1 - \cos \vartheta^*)} \right), \quad (5.8)$$

where r_e denotes the classical electron radius. Angular integration gives the total Compton cross section [Leo87, sec. 2.7.2]:

$$\sigma_c = 2\pi r_e^2 \left\{ \frac{1 + K_i^*}{(K_i^*)^2} \left[\frac{2(1 + K_i^*)}{1 + 2K_i^*} - \frac{1}{K_i^*} \ln(1 + 2K_i^*) \right] + \frac{1}{2K_i^*} \ln(1 + 2K_i^*) - \frac{1 + 3K_i^*}{(1 + 2K_i^*)^2} \right\}. \quad (5.9)$$

Equations (5.8) and (5.9) are visualized in Figs. 5.4 and 5.5, respectively. For storage ring energies of 0.5 to 3.2 GeV one obtains $\sigma_c \approx 599$ to 651 mb.

However, the above equations do not account for the influence of the electron's and photon's spin. A complete description of the Compton cross section was finally given by Lipps and Tolhoek in 1954 [LT54], following the recent developments of quantum electrodynamics. The Compton cross section in its general form is

$$\frac{d\sigma_c}{d\Omega} = \sum_{j=0}^4 \Phi_j(K_i^*, K_f^*, \vec{S}_i, \vec{S}_f, \vec{P}_i, \vec{P}_f) \propto \left(r_e \frac{K_f^*}{K_i^*} \right)^2, \quad (5.10)$$

including the photon and the electron polarization \vec{S} and \vec{P} in their initial and final states. The index j enumerates the number of dependent polarization variables of the corresponding summand. For example, Φ_0 is independent of \vec{S} and \vec{P} , and $\Phi_1 = \Phi_1(\vec{S}_i) + \Phi_1(\vec{S}_f) + \Phi_1(\vec{P}_i) + \Phi_1(\vec{P}_f)$. The observation of the relevant scattering processes at the ELSA Compton polarimeter is based on the measurement of the initial electron and photon polarization \vec{P}_i and \vec{S}_i . In the following, unindexed vectors will therefore refer to their initial states (e.g. $\vec{S}_i \rightarrow \vec{S}$). The summands of interest in the explicit form of Eq. (5.10) are

$$\frac{d\sigma_c}{d\Omega}(\vec{S}, \vec{P}) = \Phi_0 + \Phi_1(S_1) + \Phi_2(S_3, \vec{P}), \quad (5.11)$$

where S_j refers to the Stokes parameter of the initial photon (compare with Appendix D). For these

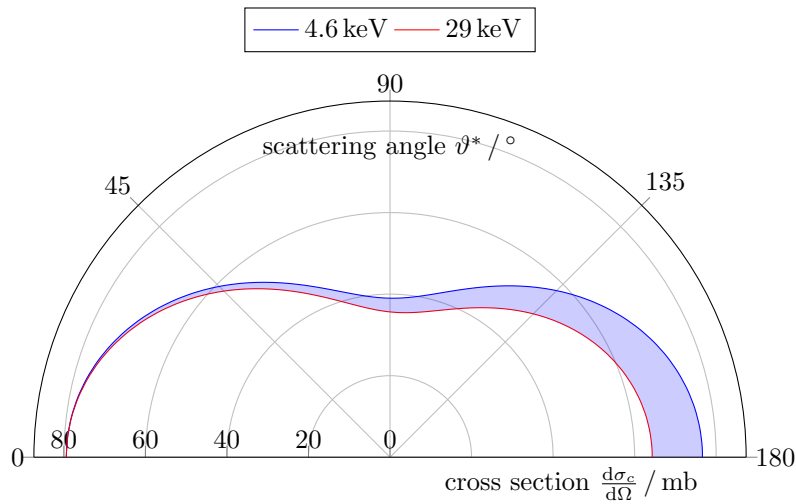


Figure 5.4: Partial Compton cross section for keV photons. The shaded area marks the interaction photon energy obtained at ELSA.

summands Fano [Fan49] was the first to state their explicit relation:

$$\Phi_0 = C \left[(1 + \cos^2 \vartheta^*) + (K_i^* - K_f^*)(1 - \cos \vartheta^*) \right], \quad (5.12)$$

$$\Phi_1(S_1) = CS_1 \sin^2 \vartheta^*, \quad (5.13)$$

$$\Phi_2(S_3, \vec{P}) = -CS_3(1 - \cos \vartheta^*)(\vec{K}_i^* \cos \vartheta^* + \vec{K}_f^*) \cdot \vec{P}, \quad (5.14)$$

$$\text{with } C = \frac{1}{2} \left(r_e \frac{K_f^*}{K_i^*} \right)^2.$$

$\Phi_2(S_3, \vec{P})$ is proportional to electron polarization \vec{P} and circular photon polarization $S_{\text{circ}} = |S_3|$ and thus, constitutes the functionality of the ELSA Compton polarimeter. Equation (5.14) can be rewritten to separate the summands including the factors of vertical and longitudinal electron polarization P_z and P_s [Bar+93]:

$$\Phi_2(S_3, \vec{P}) = S_3 P_z \sin \varphi^* \cdot \Phi_{2,z} + S_3 P_s \cdot \Phi_{2,s}, \quad (5.15)$$

where the factors $\sin \varphi^*$ and P_z comprehend the measurable electron polarization information in the form of a vertical scattering probability modulation. The remaining factors of Eq. (5.15) are

$$\Phi_{2,z} = -C(1 - \cos \vartheta^*)K_f^* \sin \vartheta^*, \quad (5.16)$$

$$\Phi_{2,s} = -C(1 - \cos \vartheta^*)(K_f^* + K_i^*) \cos \vartheta^*. \quad (5.17)$$

The energy spectrum is obtained by integrating Eq. (5.11) over $d\varphi$ and substituting $d\vartheta$ with dE via Eq. (5.2). For $P_s = 0$ (transverse electron polarization), only Φ_0 contributes to the spectrum as $\int_0^{2\pi} \sin \varphi^* = 0$ in Eq. (5.15). The spectrum is shown in Fig. 5.6 for different electron energies.

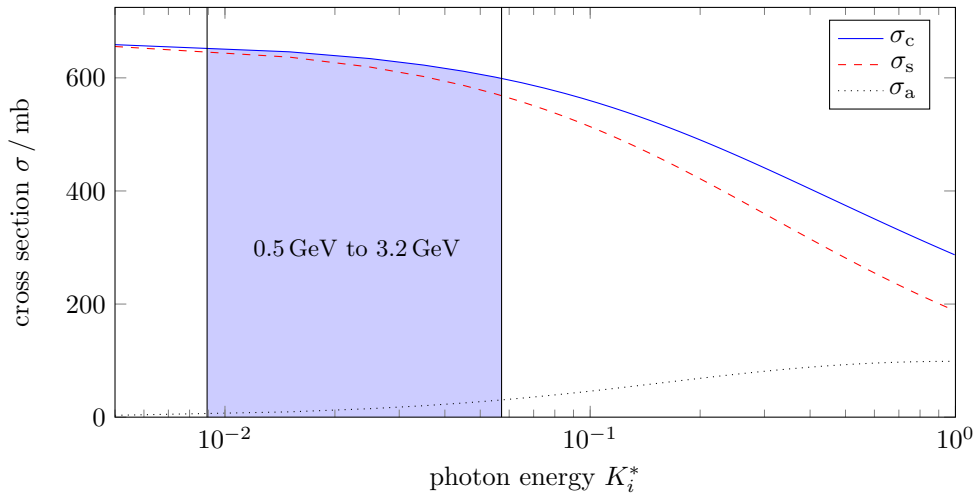


Figure 5.5: Total Compton cross section σ_c in dependence of incident photon energy K_i^* . The Compton scattering and Compton absorption cross sections in $\sigma_c = \sigma_s + \sigma_a$ indicate the average fraction of total energy contained in the final photon or in the scattered electron, respectively [Leo87, Eq. (2.107) and Eq. (2.108)]. The shaded area marks the K_i^* relevant for the ELSA storage ring.

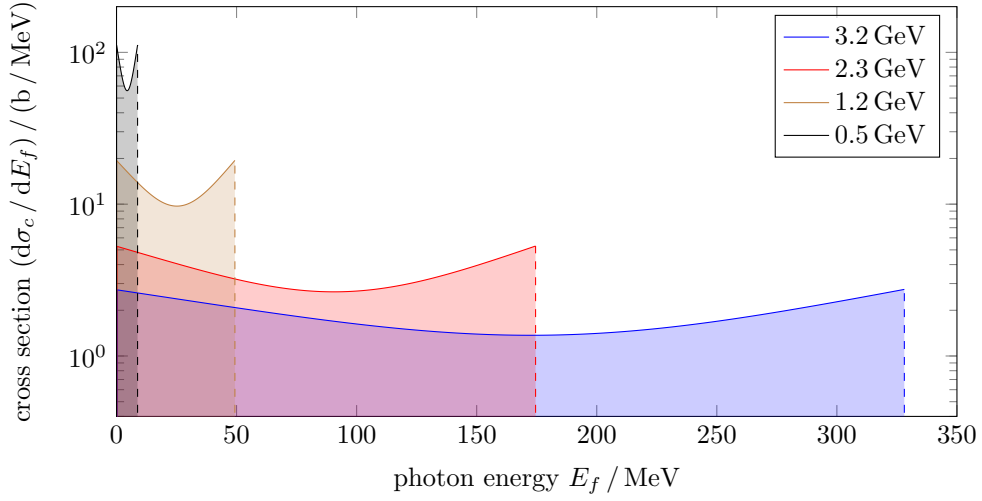


Figure 5.6: Spectrum of backscattered photons for varying storage ring energies for $P_s = 0$ and a laser beam at wavelength $\lambda = 532$ nm.

5.2 Polarization Measurement Technique

The spatial $\sin \varphi^*$ -modulation of the scattering cross section in Eq. (5.15) results in an asymmetry of the scattered photon profile

$$\mathcal{A} = \frac{\Phi_{2,z}}{\Phi_0}. \quad (5.18)$$

The measurement of the transverse electron polarization P_z may occur by observing the corresponding backscattering profile's

- count rate asymmetry, or
- shift in the means asymmetry.

Both methods are described in the following.

5.2.1 Count Rate Asymmetry Method

The cross section asymmetry manifests itself as count rate asymmetry of photons scattered to the upper (+) or lower (-) hemisphere in respect to the accelerator plane:

$$N^+ \propto \int_0^\pi d\varphi \int_0^\pi d\vartheta \left(\sin \vartheta \frac{d\sigma}{d\Omega} \right), \quad (5.19)$$

$$N^- \propto \int_\pi^{2\pi} d\varphi \int_0^\pi d\vartheta \left(\sin \vartheta \frac{d\sigma}{d\Omega} \right). \quad (5.20)$$

The asymmetry \mathcal{A} of Eq. (5.18) is obtained via

$$\mathcal{A} = \frac{N^+ - N^-}{N^+ + N^-}. \quad (5.21)$$

As the center of the hemisphere is difficult to determine in the experiment, the alternation of photon polarization from left- (L : $S_3 = +1$) to right-circular (R : $S_3 = -1$) allows to determine the asymmetry via

$$\mathcal{A} = \frac{(N_R^+ + N_L^-) - (N_R^- + N_L^+)}{(N_R^+ + N_L^-) + (N_R^- + N_L^+)}. \quad (5.22)$$

Since $N_R^+ = N_L^-$ and $N_L^+ = N_R^-$, the asymmetry can also be obtained by observing one of the two hemispheres:

$$\mathcal{A} = \frac{N_L - N_R}{N_L + N_R}. \quad (5.23)$$

The asymmetry error computes for $N_L^+ + N_R^+ = N_L^- + N_R^- = N$ and $\Delta N_L = \Delta N_R = 1/\sqrt{N}$ to

$$\Delta \mathcal{A} = \sqrt{\frac{1}{2N}}. \quad (5.24)$$

The count rate asymmetry method requires a strong stability of the electron beam and is less suited if the γ -photon cone is small compared to the size of the detector. Test trials at [ELSA](#) with lead glass detectors performed by Menze [[Men09](#)] were not able to determine the polarization degree with this method.

5.2.2 Shift in the Means Method

The backscattered photon profile's center of gravity (mean) is obtained by measuring the position dependent count rate $N(x, z)$ in the laboratory frame via

$$\bar{z} = \frac{\int dx \int dz (z \cdot N(x, z))}{\int dx \int dz (N(x, z))}. \quad (5.25)$$

A proportionality of \bar{z} and the desired measurands S_3 and P_z is comprehensible by transforming [Eq. \(5.25\)](#) into a spherical coordinate system (φ, ϑ) :

$$\bar{z} \propto \frac{\int_0^{2\pi} d\varphi^* \int_0^\pi d\vartheta^* \left(\frac{\partial(x,z)}{\partial(\varphi^*, \vartheta^*)} \cdot z(\varphi^*, \vartheta^*) \cdot [\Phi_0(\vartheta^*) + S_3 P_z \sin \varphi^* \Phi_{2,z}(\vartheta^*)] \right)}{\int_0^{2\pi} d\varphi^* \int_0^\pi d\vartheta^* \left(\frac{\partial(x,z)}{\partial(\varphi^*, \vartheta^*)} \cdot [\Phi_0(\vartheta^*) + S_3 P_z \sin \varphi^* \Phi_{2,z}(\vartheta^*)] \right)}. \quad (5.26)$$

With $z(\varphi^*, \vartheta^*) \propto \sin \varphi^*$, which is independent of ϑ^* , and $\frac{\partial(x,z)}{\partial(\varphi^*, \vartheta^*)} = r \sin \vartheta^*$ being independent of φ^* , [Eq. \(5.26\)](#) simplifies to

$$\bar{z} \propto S_3 P_z \cdot \frac{\int_0^{2\pi} d\varphi^* \int_0^\pi d\vartheta^* \left(\frac{\partial(x,z)}{\partial(\varphi^*, \vartheta^*)} \cdot z(\varphi^*, \vartheta^*) \cdot \sin \varphi^* \Phi_{2,z}(\vartheta^*) \right)}{\int_0^{2\pi} d\varphi^* \int_0^\pi d\vartheta^* \left(\frac{\partial(x,z)}{\partial(\varphi^*, \vartheta^*)} \Phi_0(\vartheta^*) \right)}. \quad (5.27)$$

For a microstrip detector with vertical binning z_i , a profile's center of gravity is obtained from

$$\bar{z} = \frac{\sum_{i=1}^N z_i}{N}, \quad \Delta\bar{z} = \frac{\sigma}{\sqrt{N}}, \quad (5.28)$$

where z_i is the position of the i -th counter event, and σ is the standard deviation of the distribution. For a detector with limited vertical resolution due to finite binning z_b and corresponding resolution error Δz_b (compare with microstrip detector, described in Section 5.4.2 and Eq. (5.51)) one obtains for the individual error of the shift in the mean

$$\Delta\bar{z} = \sqrt{\frac{\sigma^2}{N} + \Delta z_b^2 \sum_i \left(\frac{n_i}{N}\right)^2}, \quad (5.29)$$

where n_i is the bin count of the i -th bin.

As the CBS signal originates from the Φ_0 and Φ_2 term in Eq. (5.11), the center of gravity naturally computes to

$$\bar{z} = \frac{\sum_i^{N_0} z_{0,i} + \sum_j^{N_2} z_{2,j}}{N_0 + N_2}. \quad (5.30)$$

However, for opposing left-handed and right-handed laser beam helicities (L/R), the contribution from Φ_0 is identical, while the contribution from Φ_2 generates opposing centers:

$$\bar{z}_L(\Phi_0) = \bar{z}_R(\Phi_0) \quad \text{and} \quad \bar{z}_L(\Phi_2) = -\bar{z}_R(\Phi_2). \quad (5.31)$$

The shift of the means Δz is then obtained through

$$\Delta z = \bar{z}_L - \bar{z}_R = \frac{2 \sum_j^{N_2} z_{2,j}}{N_0 + N_2} = \mathcal{D} \cdot P_z \cdot S_3, \quad (5.32)$$

where \mathcal{D} is the so called analyzing power. As a detector does not distinguish between a contribution from Φ_0 or Φ_2 , Δz is obtained by determining \bar{z}_L and \bar{z}_R and subtracting the two quantities.

5.3 Photon Rates

A detector for CBS photons is situated in an environment, where multiple sources for ionizing radiation occur. Photon radiation background is expected in the form of SR and bremsstrahlung from the collision of stored electrons with residual gas molecules or ions within the vacuum chamber. The CBS photon rate and the influence of background radiation on the polarization measurement is explicated in this section.

5.3.1 Photon Backscattering Rate

The photon backscattering rate results from the product of Compton cross section σ_c (see Eq. (5.9)) and luminosity \mathcal{L} of the electron-photon interaction:

$$\frac{dN}{dt} = \sigma_c \mathcal{L}. \quad (5.33)$$

The luminosity for two Gaussian beams with small vertical crossing angle α amounts [Suz76]

$$\mathcal{L} = \sqrt{\frac{2}{\pi}} \frac{I_e \lambda_\gamma}{e \alpha} \frac{1}{\sqrt{\sigma_{e,x}^2 + \sigma_\gamma^2}}, \quad (5.34)$$

where I_e is the electron current, $\sigma_{e,x}$ and σ_γ are the corresponding horizontal electron and photon beam sizes at the IP, and λ_γ is the photon line density

$$\lambda_\gamma = \frac{P_\gamma \lambda}{2\pi \hbar c^2} \quad (5.35)$$

with laser power P_γ at wavelength λ . For example, one obtains $\lambda_\gamma = 8.9 \times 10^{10}$ photons/m for $P_\gamma = 10$ W at $\lambda = 532$ nm. Therefore, a round 3.2 GeV electron beam of width $\sigma_e = 1$ mm and current $I_e = 1$ mA colliding with a round laser beam of the same size yields a luminosity of $\mathcal{L} \approx 3.1 \times 10^{28} \text{ cm}^{-2}$. In this case, the expected Compton scattering rate is of the order $dN/dt \approx 18.6 \text{ kHz mA}^{-1}$.

For increasing electron energies the scattering rate reduces, as

- σ_c decreases with electron energy E (compare with Fig. 5.5), and
- \mathcal{L} decreases due to growing beam emittance and the subsequent growth of $\sigma_{e,x}$ (compare with Section 4.3), which then deviates from the circularity of the laser beam.

5.3.2 Radiation Background

Synchrotron Radiation

SR photons from the ELSA storage ring reach maximum energies of 100 keV, as shown in Fig. 2.5. Since the detector module of the Compton polarimeter utilizes charges from pair-production, those photons do not contribute to the measurement of the backscattering photon profile. In addition, the SR intensity is significantly reduced by interjacent matter such as the vacuum flange and the lead bulk of the detector's front-end (compare with Sections 5.4.1 and 6.3). However, for the guidance of laser light, optical mirrors should not be irradiated by SR to prevent loss of reflectivity through surface reactions. As energetic SR is emitted at angles < 1 mrad (compare with Fig. 2.6), the VIS laser mirrors are located outside of this perimeter.

Gas Bremsstrahlung

The bremsstrahlung cross section reads [KM59; Ham95]

$$\frac{d\sigma}{dE_\gamma} = \frac{4Z^2 r_0^2}{137} \frac{1}{E_\gamma} \frac{E - E_\gamma}{E_\gamma} \left[\left(\frac{2E^2 + E_\gamma^2 - 2EE_\gamma}{E(E - E_\gamma)} - \frac{2}{3} \right) \cdot 4.67 + 0.11 \right], \quad (5.36)$$

where E_γ is the energy of the scattered photon, E the electron energy and Z the mean atomic number of the residual gas. The integration over a relevant range of E_γ above a threshold value $\epsilon_{\text{th}} = E_\gamma/E$ yields the total cross section for a mean atomic number $\langle Z \rangle = 5$ [PR89]:

$$\sigma(\epsilon_{\text{th}}) = 57.3 \left(6.37(\epsilon_{\text{th}} - \ln \epsilon_{\text{th}}) - 2.34\epsilon_{\text{th}}^2 - 4.03 \right) \quad (5.37)$$

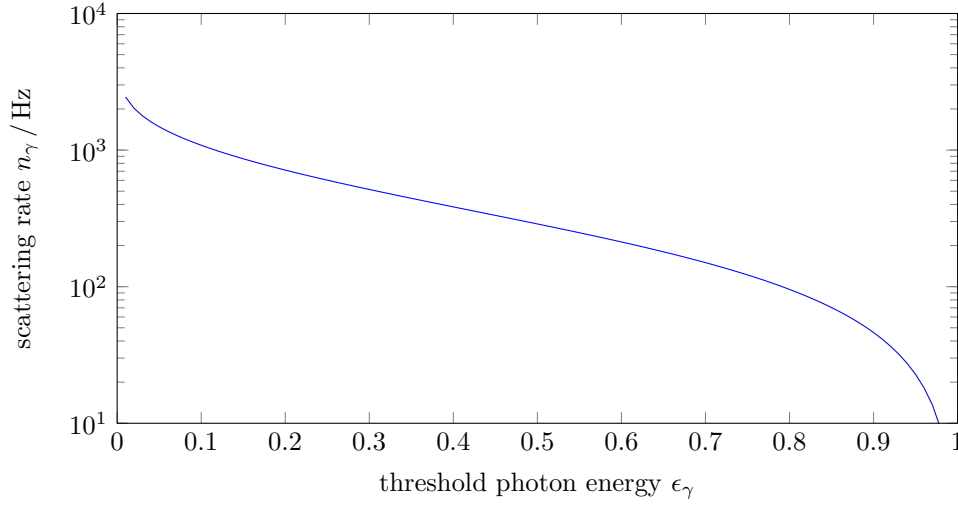


Figure 5.7: Gas bremsstrahlung count rates n_γ as function of cut-off energy ϵ_γ for $I_e = 100$ mA and a vacuum pressure of $p = 1 \times 10^{-8}$ mbar.

and thus a gas bremsstrahlung event rate of

$$n_\gamma = 1.53 \times 10^7 \cdot L \cdot I_e / \text{mA} \cdot p / \text{mbar} \cdot \sigma(\epsilon_{\text{th}}), \quad (5.38)$$

with electron current I_e , pressure p and length of interaction straight L . The expected count rates at the ELSA storage ring are shown in Fig. 5.7.

A FLUKA [Fer+05] based evaluation of gas bremsstrahlung fluence rate Φ in synchrotrons was performed by Ferrari et. al. [FPS93] on the basis of electron collisions with an air-like molecule distribution:

$$\Phi = 1.9 \times 10^{-18} \gamma^2 \frac{L}{d(L+d)} \frac{I_e}{e} \frac{p}{p_0}, \quad (5.39)$$

with the electron's Lorentz factor γ , length L of the straight section, distance to the detector d from the straight section's end, vacuum pressure p and scaling constant $p_0 = 1.33 \times 10^{-9}$ mbar. The molecule and ion composition in the ELSA storage ring deviates from that of air [Sau19, sec. 3.1], but Eq. (5.39) should nevertheless provide an estimation for the order of magnitude of the expected photon fluence. For example, at $d = 14.5$ m distance from an $L = 1.1$ m long straight section, a 3.2 GeV beam ($\gamma = 6262$) of $I_e = 1$ mA at pressure $p = 1 \times 10^{-9}$ mbar produces a fluence rate of $\Phi = 2.1 \times 10^3 \text{ cm}^{-2} \text{ s}^{-1}$. On a $4 \times 4 \text{ cm}^2$ large detector area the expected rate is then approximately 32 kHz, being of comparable magnitude of the expected backscattering photon rate (compare with Section 5.3.1). However, based on the spectra obtained by [FPS93], the number of photons with energies above the pair production limit $E_{\text{ph}} \approx 1$ MeV is only a fraction of approximately a quarter of the above calculated rate.

5.4 Detection of Backscattered Photons

To obtain the electron polarization degree P_z from a shift in the mean Δz measurement (see Section 5.2.2), the high energy photon beam profile is to be electronically processed for analysis. The backscattered MeV photons (compare with Fig. 5.6) have to be converted to charge carriers as they cannot be directly detected. Multiple detection concepts were considered for the setup at ELSA, including lead glass counters, calorimeters with position resolution, silicon counters and CCDs [Ham95]. Most feasibility was expected from a two-step conversion detector, utilizing a lead conversion target for charge carrier generation through pair production and a subsequent silicon microstrip array for digitization of the charge distribution with vertical resolution. The properties of the implemented γ -ray detection scheme and its conversion to processable data is explained in this section.

5.4.1 Photon to Charge Conversion

Photons interact with matter in multiple ways: At low photon energies $E_\gamma \lesssim 1$ MeV **photoelectric absorption** is the dominating effect, where the incident photon is completely absorbed while exciting an atomic shell electron. In addition, **elastic scattering** on shell electrons occurs, where the photon interacts with either bound electrons (Rayleigh scattering) or (quasi-) free electrons (Thomson scattering) such as in plasmas or in metals, where the electrons are considered gas-like. At photon energies around 1 MeV, inelastic **Compton scattering** becomes the dominating effect where the photon transfers energy and momentum to a charged particle, more likely to an electron rather than to a nucleus. For energies greater than 5 MeV $e^+ - e^-$ **pair production** becomes the dominating interaction process. The annihilation of the positron produces two high energy photons which may again cause pair production. This repetitive process may lead to typical electromagnetic *showers* which are commonly exploited for measurements in high energy physics.

Energy Loss in Matter

The mass attenuation coefficient μ describes the photon absorption by propagation through matter after a distance x :

$$I(x) = I_0 e^{-\mu x}, \quad (5.40)$$

where I_0 is the initial intensity. Figure 5.8 shows μ for the above described interactions for varying photon energies E_γ in lead. The mass attenuation coefficient is linked to the total interaction cross section $\sigma = \sum_i \sigma_i$ (σ_i representing the contribution of the above processes) via the material density ρ [The11]:

$$\frac{\mu}{\rho} = \frac{1}{\rho dx} \frac{dN}{N} = \frac{N_A}{M} \sigma, \quad (5.41)$$

where dN/N is the fraction of scattered particles within a penetration depth dx , N_A is Avogadro's constant and M the molar mass.

The Compton scattered photons at ELSA reach energies $\gtrsim 5$ MeV (compare with Fig. 5.6), where pair production dominates and can be utilized for charge carrier generation. The corresponding mass attenuation coefficient μ_p is related to the radiation length X_0 by [Tav10]

$$\mu = \frac{7}{9} 4\alpha r_e^2 (Z + 1) \ln \left(\frac{183}{3\sqrt{Z}} \right) = \frac{7}{9X_0}, \quad (5.42)$$

where α is the fine structure constant and Z the atomic number. Equation (5.42) allows to calculate the

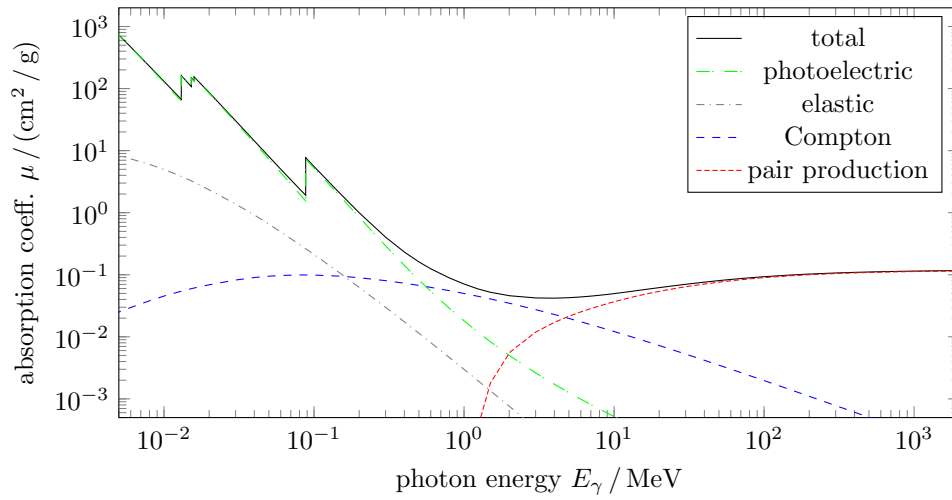


Figure 5.8: Mass attenuation coefficient μ for lead (Pb) as function of photon energy. μ is a measure of the interaction cross section σ via Eq. (5.41). The data is obtained from XCOM (NIST) [Ber+10].

probability P , also called *conversion efficiency*, of a γ -photon to create a positron-electron pair after a penetration depth x [Sob79]:

$$P(E_\gamma, x) = \left(1 - e^{-\mu(E_\gamma) \cdot x}\right) \cdot e^{-a(E_\gamma) \cdot x^2}. \quad (5.43)$$

Therein, $a(E_\gamma) \approx 0.02$ to $0.2 X_0^{-2}$ is an energy-dependent, experimentally determined quantity. The conversion efficiency P is shown in Fig. 5.9 for different converter thicknesses X_0 and photon energies. A lead thickness of $2X_0 = 11.2$ mm compromises a sufficient maximization of P for a charge counting γ -photon detector at the ELSA Compton polarimeter. For photon energies from 44 to 300 MeV the conversion efficiency ranges from approximately 35 to 60 %.

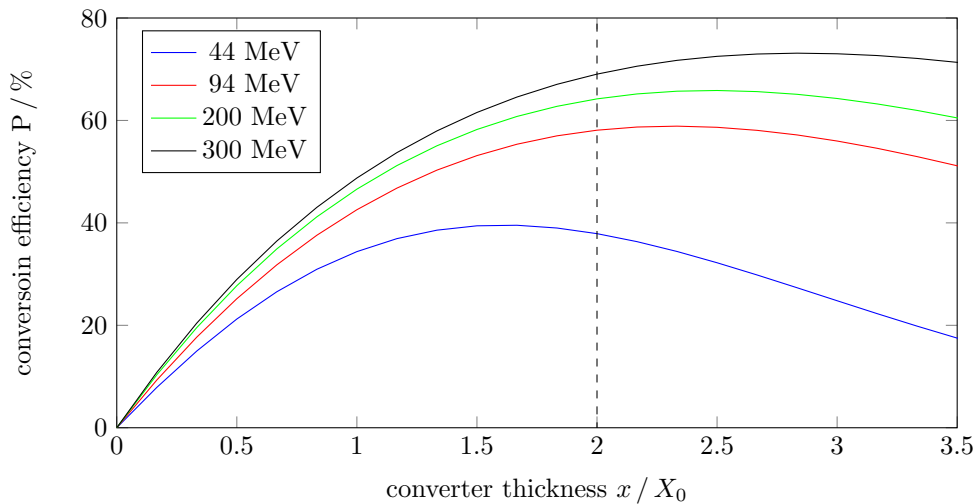


Figure 5.9: Conversion efficiency for different lead converter thicknesses and backscattering photon energies. $X_0 = 2$ compromises for a sufficient maximization of P .

Low energy electrons and positrons deposit their energy through ionization by collision, as described by the Bethe-Bloch equation:

$$-\left(\frac{dE}{dx}\right)_{\text{coll}} = 2\pi N_A r_e^2 m_e c^2 \rho \frac{Z}{A} \frac{1}{\beta^2} \left[\ln \frac{\tau^2(\tau+2)}{2(I/m_e c^2)^2} + F(\tau) - \delta - 2\frac{C}{Z} \right], \quad (5.44)$$

where τ / eV is the particle kinetic energy, I / eV the mean excitation energy, and $F(\tau)$, δ and C are correction terms, which are extensively described in e.g. [Leo87, sec. 2.4.1 and 2.4.2]. In addition, the low mass of electrons and positrons leads to energy loss due to bremsstrahlung radiation:

$$-\left(\frac{dE}{dx}\right)_{\text{rad}} = \rho \frac{N_A}{A} E_0 \Theta_{\text{rad}}(E_0), \quad (5.45)$$

where E_0 is the energy of the incident particle and $\Theta_{\text{rad}}(E_0)$ is a material function describing the amount of atomic shielding¹. The total energy loss then computes to

$$\left(\frac{dE}{dx}\right)_{\text{tot}} = \left(\frac{dE}{dx}\right)_{\text{coll}} + \left(\frac{dE}{dx}\right)_{\text{rad}}. \quad (5.46)$$

The critical energy at which losses due to bremsstrahlung exceed collision losses is $E_c = 9.51 \text{ MeV}$ in lead [Leo87, sec. 2.4.4], hence an overall higher contribution due to bremsstrahlung is expected. The resulting stopping power dE / dx for electrons in lead is shown in Fig. 5.10. The mean energy loss is expressed through the radiation length:

$$\langle E \rangle = E_0 e^{-x/X_0}. \quad (5.47)$$

In the bremsstrahlung dominated energy range the energy deposition of several MeV/mm creates energetic photons which may again cause pair production. This results in a cascading *electron-photon*

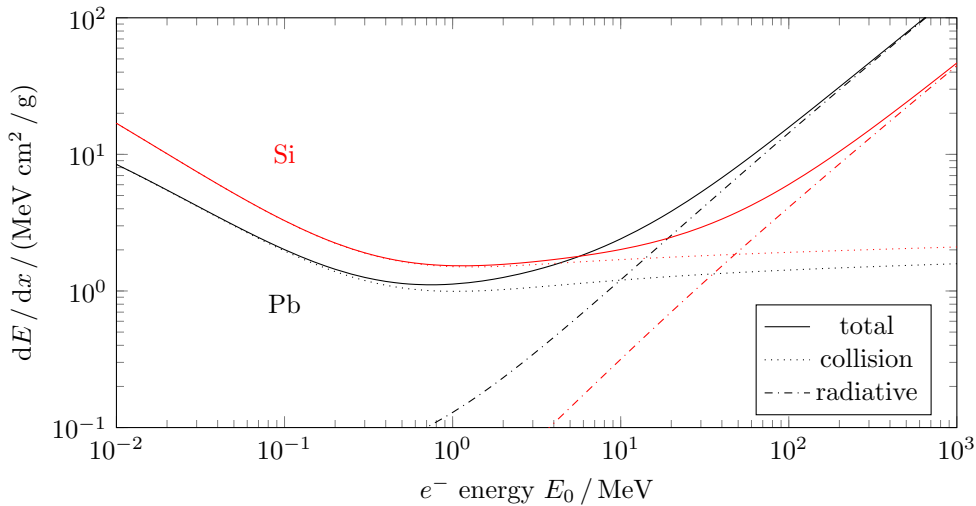


Figure 5.10: Stopping power for electrons in lead ($\rho_{\text{Pb}} = 11.34 \text{ g/cm}^3$) and silicon ($\rho_{\text{Si}} = 2.3 \text{ g/cm}^3$) [Ber+17]. The stopping power is normalized to the density ρ .

¹Reduction of the effective nuclear charge due to the screening of the electric field by shell electrons.

shower process which holds until the critical energy E_c is reached. The penetration depth of such a shower computes to [Leo87, sec. 2.7.4]

$$x_{\max}/X_0 = \frac{\ln \frac{E_0}{E_c}}{\ln 2}. \quad (5.48)$$

For example, 40 MeV incident photons cause a shower of penetration depth $2X_0$ in lead, 100 MeV photons reach $3.4X_0$. The maximum number of particles produced is

$$N_{\max} = \frac{E_0}{E_c}, \quad (5.49)$$

whose transverse distribution is described by the Molière radius

$$R_m = 21 \text{ MeV} \frac{X_0}{E_c}, \quad (5.50)$$

defining a cylinder which contains 90 % ($2R_m(95\%)$) of shower particles. For lead, one obtains $R_m = 12 \text{ mm}$.

Note that the above considerations and relations represent a simplified model with validity for high incident photon energies E_0 . The processes at the ELSA storage ring involve photon energies above and below E_c . To obtain a realistic number of charge carriers emitted from a converter material, EGS4 [NHR85] simulations were carried out by F. Hamburger [Ham95]. Incident photon beams from 20 to 300 MeV were analyzed for charge carrier generation, conversion probability and shower widths for multiple radiation lengths X_0 . The simulation included effects due to bremsstrahlung, positron annihilation, Molière multiple scattering, Møller ($e^- - e^-$) and Bhabha ($e^+ - e^-$) scattering, pair-production, Compton scattering, Rayleigh scattering and photoelectric interaction. As result, an optimum converter thickness of $2X_0$ was obtained, providing a conversion efficiency of $P \approx 75\%$ for 300 MeV photons, and $P \approx 15\%$ for 50 MeV photons. In-between the relation is approximately linear. The simulation results are integrated in the Compton scattering simulation tool COMPTONSIM, which is described in Section 5.5.

5.4.2 Silicon Microstrip Detector

The charged particles leaving the lead converter material penetrate the silicon (Si) microstrip detector, as shown in Fig. 5.11. The silicon bulk has aluminum (Al) strips coated on top of a strongly p -doped layer (p^+). The aluminum strips are separated by an AlO_2 isolation layer with pitch of $50 \mu\text{m}$. The silicon bulk is weakly n -doped (n^-), whereas its bottom layer is strongly n -doped (n^+) and coated with an aluminum surface electrode. The opposing p^+ and n^+ layers may create a depletion zone of up to $500 \mu\text{m}$ thickness, when a bias voltage U_b of some hundred volts is applied.

Charged particles penetrating the depleted zone create electron-hole pairs along their path of flight. As explicated in [KW16], the band gap energy of silicon is 1.1 eV at a temperature of 300 K. However, the creation of electron-hole pairs requires a mean of 3.65 eV, since approximately two thirds of the energy is lost in lattice vibrations. The mean energy loss of a minimum ionizing particle (MIP) amounts $\langle dE / dx \rangle = 117 \text{ keV} / 300 \mu\text{m}$, the most probable value is $84 \text{ keV} / 300 \mu\text{m}$, creating a charge of $32\,000 e^-$ (5 fC) and $23\,000 e^-$ (3.7 fC), respectively. The charge carriers propagate through the material at typically $50 \mu\text{m} / \text{ns}$, making Si-detectors *fast* detectors. The subsequent processing electronics generate a digital count signal when the strip charge exceeds a settable discrimination value.

For the center of gravity \bar{z} measurement of a charge distribution, the position error due to the strip pitch d

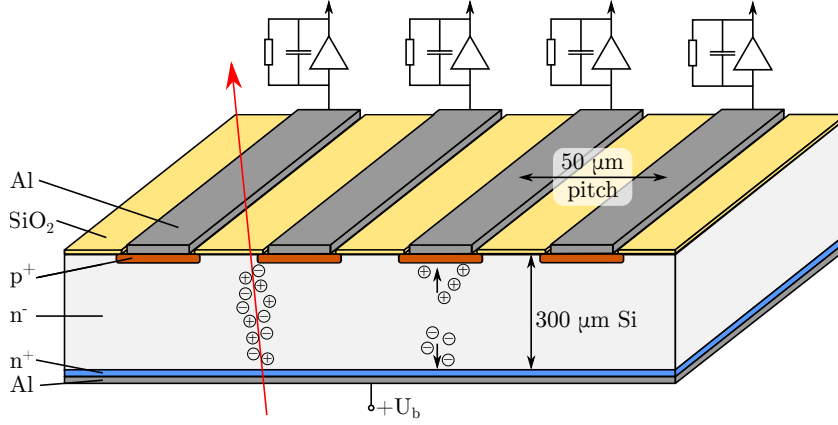


Figure 5.11: Working principle of a microstrip detector. The passage of charged particles through the $\sim 300 \mu\text{m}$ weakly doped depleted zone (n^-) creates electron-hole pairs which propagate towards the corresponding aluminum electrode, when a bias voltage $U_b \approx 1 \text{ kV}$ is applied. The depleted zone is created by strongly doped, opposing n^+ and p^+ layers. The charge reaching the aluminum strips is then amplified and electronically processed.

and hence, finite binning, is [KW16, Eq. 8.75]:

$$\Delta z_b = \left(\frac{1}{d} \int_{-d/2}^{d/2} z^2 dz \right)^{-1/2} = \frac{d}{\sqrt{12}}. \quad (5.51)$$

For a pitch of $d = 50 \mu\text{m}$ one obtains $\Delta z_b = 14 \mu\text{m}$ (compare with Eq. (5.29)).

5.5 Numerical Simulation of Scattering on a Realistic Electron Beam

The scattering rates calculated in Section 5.3 apply for cylindrical electron and photon beams. To investigate realistic scattering rates at a position (a, b) on a detector area with influence of beam divergences and varying beam cross sections around the IP, the simulation program COMPTONSIM [Hil95] has been developed. It calculates the backscattering rate at specific voxels incorporating the spatial density functions of the incident photon and electron beam $\rho_\gamma(x, z, s)$ and $\rho_e(x, z, s)$, respectively. The simulation software performs a five-dimensional numerical integration across the transverse and longitudinal planes x, z, s , including the transverse divergences x' and z' of the electron beam:

$$N(a, b) = \int_{s_0}^{s_1} ds \int_{z_0}^{z_1} dz \int_{x_0}^{x_1} dx \int_{z'_0}^{z'_1} dz' \int_{x'_0}^{x'_1} dx' \left(\frac{d\sigma}{d\Omega}(\varphi, \vartheta) \sin \vartheta \frac{\partial(\varphi, \vartheta)}{\partial(x, z)} \cdot \rho_e(x, x', z, z', s) \cdot \rho_\gamma(x, z, s) \right). \quad (5.52)$$

COMPTONSIM may also include the conversion process of the lead-converter (see Section 5.4.1). An example profile for a 2.4 GeV electron beam is illustrated in Fig. 5.12 for the parameters listed in Table 5.1. The scattering rate difference for circular right ($S_3 = -1$) and circular left ($S_3 = +1$) photon helicity is shown in Fig. 5.13. The electron beam size is calculated from the optical functions at the corresponding IP (see Section 6.2.1) with the beam emittance for the corresponding electron energy (compare with Section 4.3).

The simulation provides key parameters for the design and accuracy of the polarimeter setup. For example, the asymmetry \mathcal{A} and the analyzing power \mathcal{D} for the explicit polarimeter setup (as described

beam	intensity	energy	polarization	size	inclination
e^-	100 mA	2.4 GeV	$P_z = +100\%$	see Fig. 6.9	—
γ	10 W	2.33 eV	$S_3 = +100\%$	$\sigma = 1$ mm	$\alpha = 3$ mrad

Table 5.1: COMPTONSIM parameters for the simulation shown in Fig. 5.12.

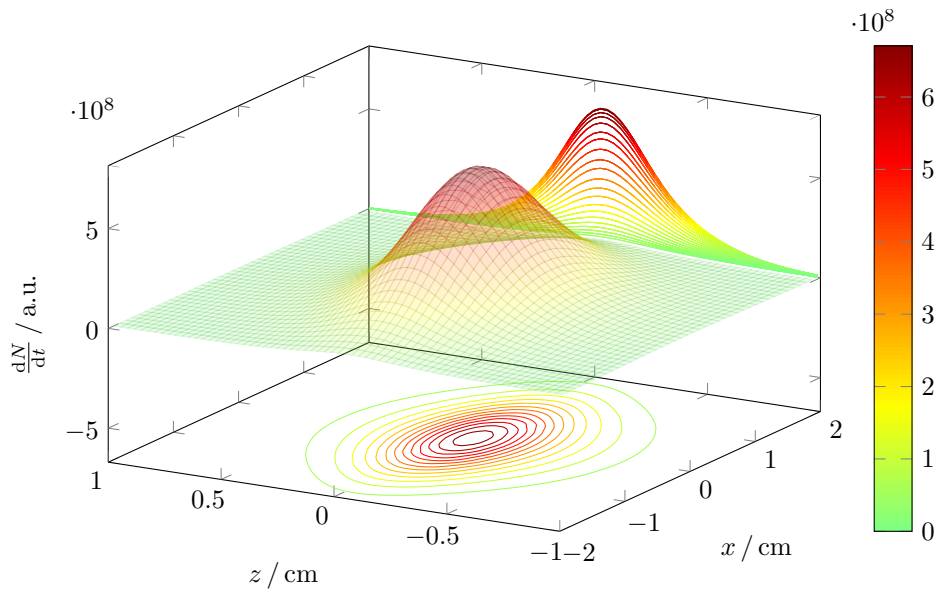


Figure 5.12: Simulated Compton backscattered photon profile from a 2.4 GeV electron beam energy without background radiation.

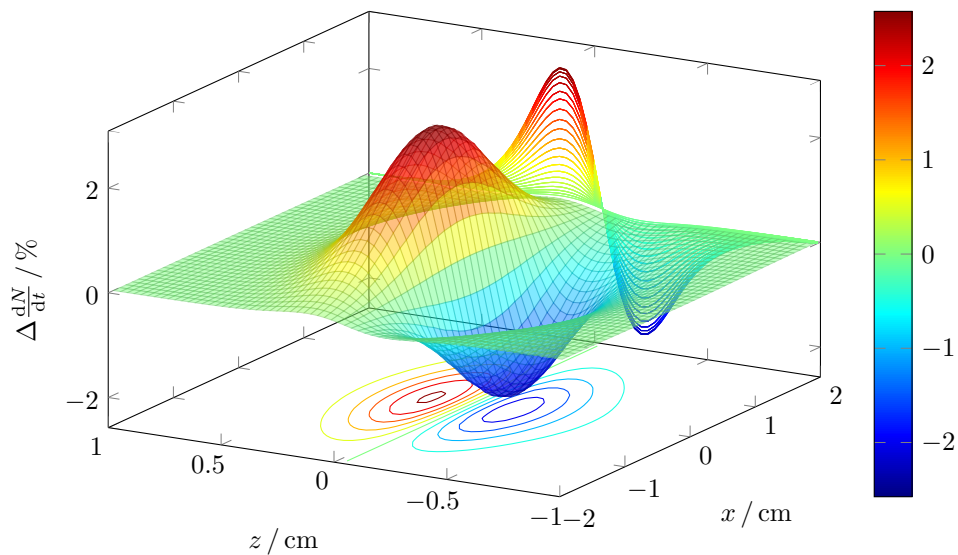
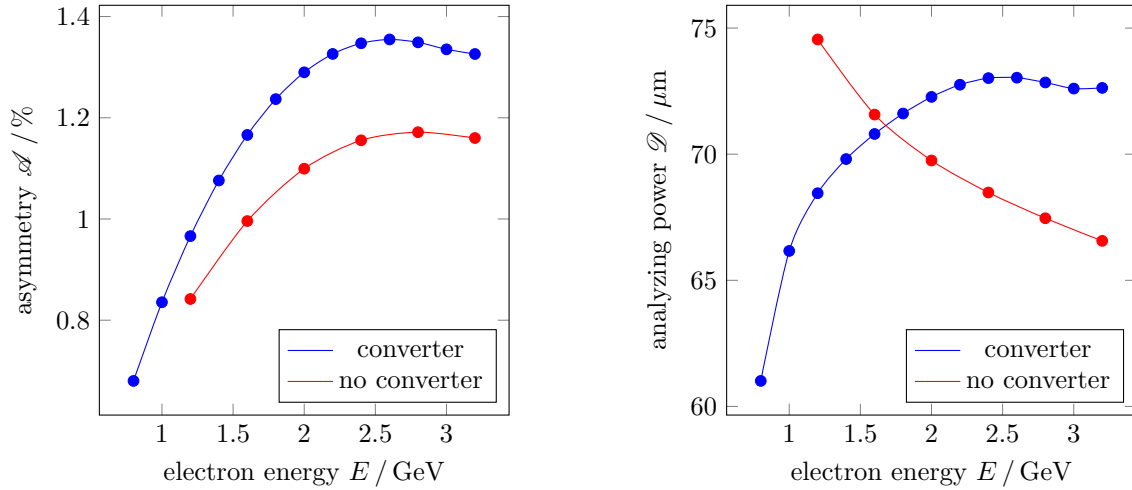


Figure 5.13: Simulated difference of Compton backscattered photon profiles from a 2.4 GeV electron beam with positive and negative photon helicity.

in Chapter 6) are shown in Fig. 5.14 for varying storage ring energies. Therein, the beneficial impact of the lead-converter on asymmetry and analyzing power is visible. Exemplary profiles of background and backscattering signals from $S_3 = \pm 1$ laser radiation for 1.2 GeV and 3.2 GeV electron beams are shown in Fig. 5.15, where the diminutive profile mean shift is emphasized through the magnification windows. The profile's skewness results from the incident angle $\alpha > 0$. The bremsstrahlung background is simulated for a pressure of 2.5×10^{-8} mbar in the vacuum chamber, being a realistic value for the designated IP during electron beam storage.



(a) Asymmetry \mathcal{A} for varying ELSA storage ring energies.

(b) Analyzing power \mathcal{D} for varying ELSA storage ring energies.

Figure 5.14: Key parameters for the ELSA Compton polarimeter obtained from COMPTONSIM.

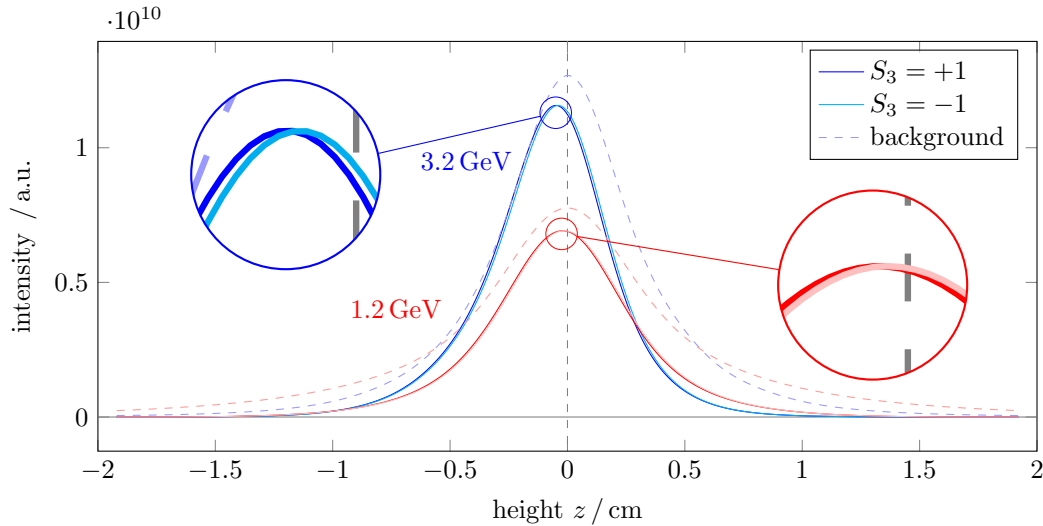


Figure 5.15: Simulation of photon and background profiles at a detector surface in 15 m distance from the IP for 1.2 GeV and 3.2 GeV beam energy and a gas pressure of 2.5×10^{-8} mbar in the vacuum chamber.

The ELSA Compton Polarimeter

The polarization of the stored electron beam is measurable via CBS, as described in the previous chapter. A drawing of the ELSA Compton polarimeter is shown in Fig. 6.1. The polarimeter beamline guides circularly polarized laser photons into the vacuum system of the storage ring where they scatter off the circulating electrons. The beam profile of the backscattered γ -photons holds the electron polarization information and is detected by a lead-conversion silicon microstrip detector. Non-interacting laser photons leave the vacuum system into an optical container where the circular polarization degree is measurable.

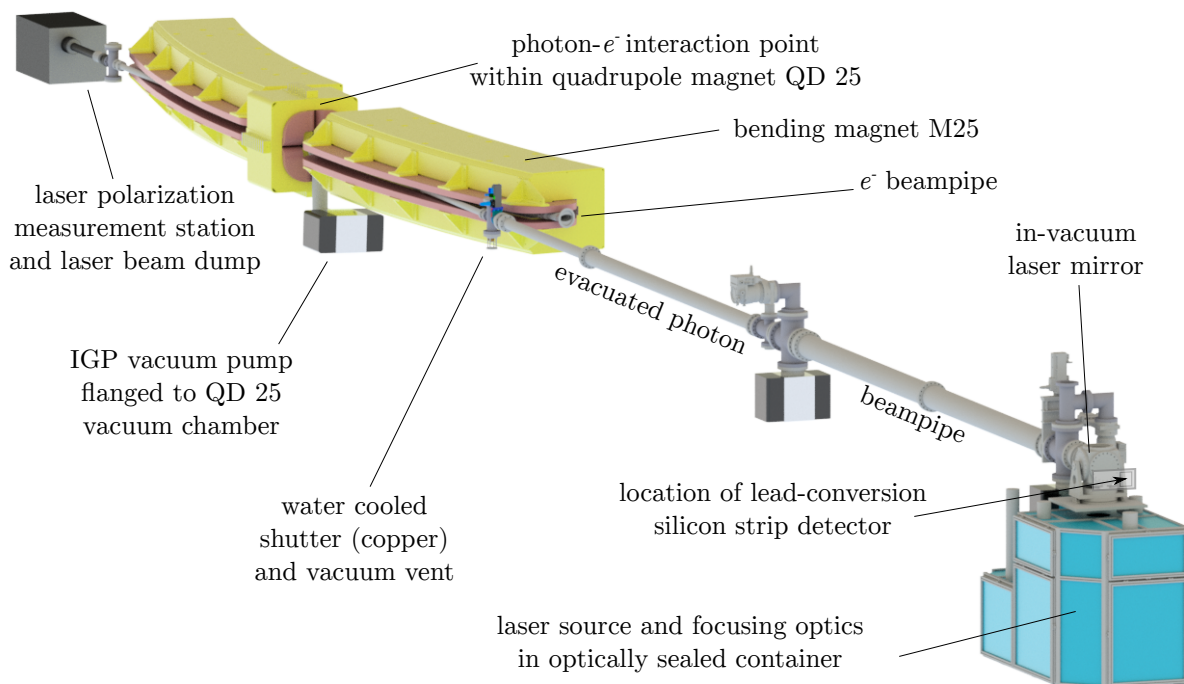


Figure 6.1: Technical drawing of the Compton polarimeter beamline at the ELSA storage ring. The laser beam is guided from an optically sealed container into the storage ring's vacuum system. The laser beam interacts with the electrons within quadrupole magnet QD 25. The profile of the backscattered γ -photons is detected by a silicon microstrip detector which is located above the optical container. Non-interacting photons are coupled out of the vacuum and their circular polarization is measured within a second optical box, in which the laser beam is dumped.

The current laser beamline setup is based on the design of J. Wittschen and B. Aurand [Aur08, ch. 3] (2008), and has been improved with laser beam adjustment capabilities and both, a reliable photon source and silicon microstrip detector. Before the properties of the current setup are discussed in Section 6.2, a historical overview of the laser source development and the past polarimeter commissioning attempts at ELSA is given.

6.1 Historical Overview of Compton Polarimetry at ELSA

The experimental Compton polarimeter setup at ELSA has been majorly dependent on the reliable functionality of a silicon microstrip detector module, and on the size and operational conditions of the utilized laser device. For the latter, space restrictions necessitated either a long laser transfer beamline or a compact optical setup (compare with floor plan in Fig. 1.2). As laser devices have become more compact and less energy consuming over the past decades, the polarimeter setup could be adjusted accordingly. The properties of eligible continuous wave (CW) photon sources with output power above 10 W and the corresponding polarimeter operation experience with those devices at ELSA is discussed in the following sections.

6.1.1 Ar⁺ Laser Polarimeter

The first realization of a Compton polarimeter at ELSA was commissioned by D. Doll and W. Hillert in 1998 [Dol98; Hil00]. The laser source was an Ar⁺-laser¹ with maximum output power of $P_\lambda = 10$ W at $\lambda = 514.5$ nm wavelength. A schematic drawing of an Ar⁺ laser is shown in Fig. 6.2. The remarkable output power and beam quality of this gas laser device was realized through a large argon discharge tube setup, including multiple automated optical elements for the optimization of the beam profile. Disadvantageous was, however, the large size of the laser source, the limited lifetime of the expensive discharge tube, and its electric inefficiency of approximately 1% (compare with e.g. [Coha]). Due to the laser size the laser system was positioned in a laboratory outside the accelerator shielding tunnel and the beam was guided over a 48 m long transfer beamline with seven mirrors onto the laser interaction region (LIR), of which the last mirror was installed within the accelerator's vacuum system, 15 m away from the electron beam (compare with [Dol98, Chapter 5]). Due to the long transfer beamline and several beam deflections, an estimated laser power of $P_\lambda \approx 6.5$ W was available for electron interaction. The

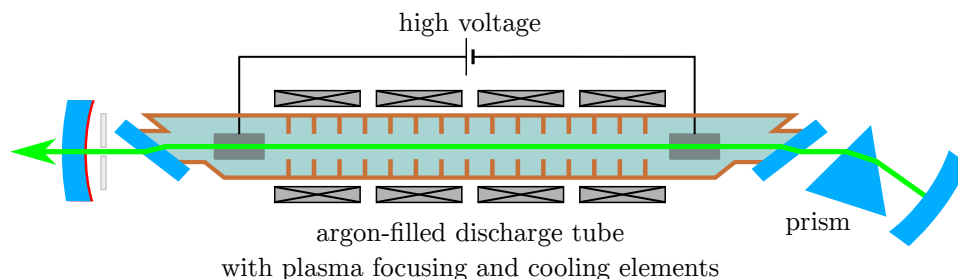


Figure 6.2: Schematic drawing of an Ar⁺ gas laser. The active lasing medium is a plasma, which is created by a current flowing between anode and cathode. The plasma is confined by focusing elements and dissipates several Kilowatts of power, which is removed by a water cooling system. The output wavelength is adjustable.

¹Innova Sabre 25 TSM by Coherent Inc.

alternating circular polarization of the linearly polarized laser beam was achieved by an electro-optical Pockels cell, which was situated in the laser laboratory.

Beamline operation experience showed that building vibrations lead to a laser beam pointing (in)stability of 0.5 mm RMS at the LIR, whose impact on the backscattered beam displacement was estimated to be of unacceptable 30 μm RMS [Hi100, 5.2.4]. Active laser beam positioning with Piezo actuators and position feedback via PSDs at every mirror eventually improved the RMS pointing stability to $< 50 \mu\text{m}$. In test measurements at 2.3 GeV the signal-to-background ratio of the backscattered photons amounted 1/4 [Hi100, 2.5.6]. This rather poor value was caused by an insufficient vacuum pressure (estimated $P_{\text{vac}} \approx 10^{-7}$ mbar) at the LIR and due to the reduced photon beam power through reflectivity losses in the transfer beamline. The analyzing power of the detector system (compare with Eq. (5.32)) was estimated to be $\mathcal{D} = (60 \pm 15) \mu\text{m}$ while simulations yielded $\mathcal{D}_{\text{num}} = 70 \mu\text{m}$ accordingly (compare with Fig. 5.14(b)). The desired polarization measurement error of $\Delta P \approx \pm 3\%$ for a measurement time of $t_{\text{meas}} = 5$ min could not be achieved and the overall performance of the measurement system, including the sophisticated correction systems, revealed operational disadvantages. Despite of comparable Compton polarimeter setups operating at e.g. DESY² [Bar+93], the concept did not provide sufficient data quality for the circumstances at ELSA.

6.1.2 DPSS Laser Polarimeter

The advent of diode pumped solid state (laser)s (DPSSs) significantly improved the laser operation efficiency over gas lasers. The reduced size of the laser system and its electrical efficiency allowed to install the laser closer to the electron interaction region, abrogating the problems with the long transfer beamline of the previous design. In addition, a higher laser output power of $P_{\gamma} \approx 40$ W was available.

A DPSS disk laser³ was purchased and installed in 2008 [Aur08, ch. 4]. A schematic of the DPSS working principle is shown in Fig. 6.3. Therein, a $\lambda = 1030$ nm beam is excited by two diode-pumped

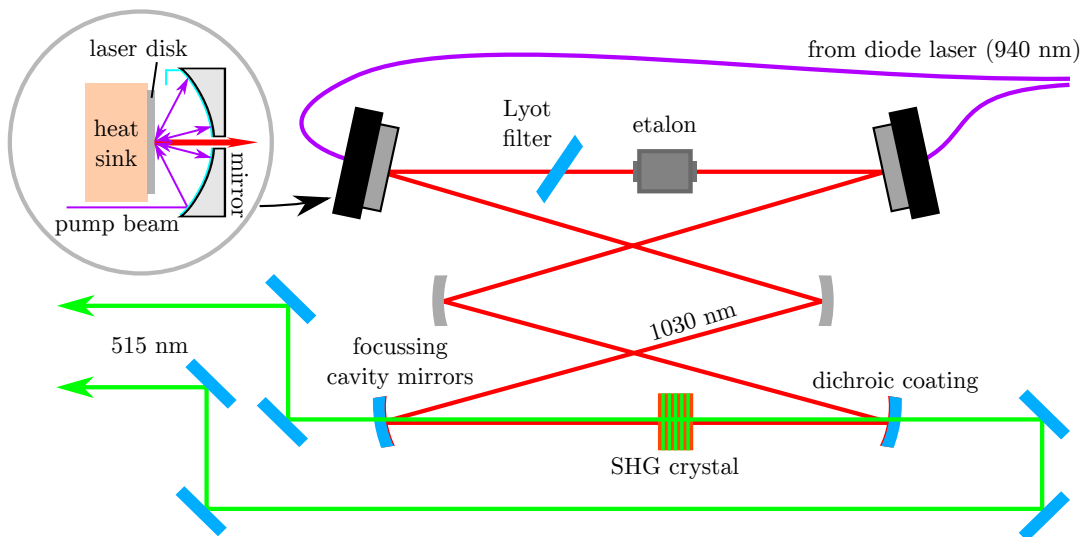


Figure 6.3: Schematic drawing of the ELS Monodisk DPSS laser. The diode laser pumps the Yb:YAG disk material via a multiply reflecting optical configuration. An internal second harmonic generation (SHG) crystal generates the VIS, which is coupled out of the resonator by dichroic mirrors.

²Deutsches Elektronen SYNchrotron facility in Hamburg, Germany

³MonoDisk Gemini 20 by Elektronik Laser System GmbH (ELS)

Yb:YAG disks within a double-folded resonator, in which mode control is realized through a Lyot filter and a Fabry-Pérot etalon. Two 20 W laser beams at $\lambda = 515$ nm are generated by a frequency doubling intra-cavity **SHG** crystal and are coupled out of the resonator through dichroic mirrors.

Initially excellent beam properties and the remarkable output power were decreasing soon after purchase, culminating in complete failure due to corrosion of the disk cooling fingers. Replacement with slightly thicker disks from the only available manufacturer changed the resonator geometry and laser operation became quickly insufficient and unreliable after resonator retuning: The formation of multiple longitudinal modes could not be satisfactorily suppressed, resulting in increasingly chaotic amplitude fluctuations known as *green noise*, where the **SHG** process is disturbed by the competing sum-frequency generation process (compare with e.g. [Cohc]). In addition, the complicated resonator geometry was prone to temperature and mechanical movement, resulting in power drop-offs and transverse beam profile degradation during operation. Resonator re-adjustment could not be performed in the designated operation location and implied tedious service procedures. Furthermore, the fragile **SHG** crystal cracked multiple times and several repairs and improvement attempts did not result in reliable operation. A characterization of the laser device, the photon beamline and initial measurements of the backscattering profile with an improved microstrip detector were conducted by F. Hinterkeuser, R. Koop and the author [Hin15; KHS16]. However, the laser was last used in a test measurement in 2016, before its **SHG** was again damaged. Eventually, the polarimeter could not be operated reliably with this laser source.

6.1.3 OPSL Polarimeter

The design disadvantages of **DPSS** lasers were overcome by **optically pumped semiconductor lasers (OPSLs)** which contain a simplified resonator geometry and use a semiconductor as active medium (see Fig. 6.4). Its upper state lifetime is much shorter than those in **DPSS** lasers, eliminating the *green noise* problem mentioned in the previous section (compare with [Coha; Cohc]). Similar to **DPSS** lasers, a diode array is used to irradiate the solid state active medium, which is contained in a **VCSEL** chip, consisting of multiple layers of near-**IR** absorption and quantum wells (InGaAs layer between GaAs). Its emission frequency can be adjusted by the design of doping and layer thickness. A **distributed Bragg reflector**

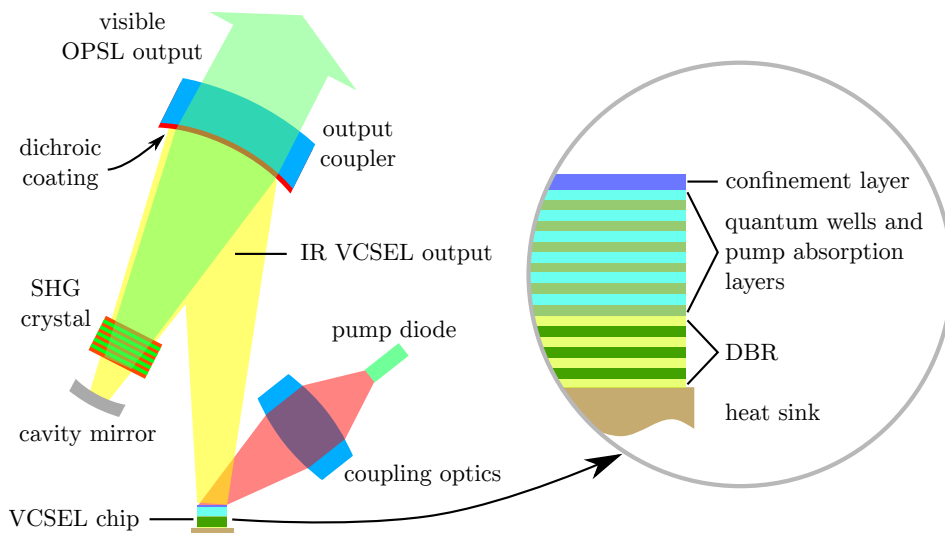


Figure 6.4: Schematic drawing of an **OPSL** resonator geometry, including a **vertical-cavity surface-emitting laser (VCSEL)** chip and **SHG** crystal (compare with e.g. [Cohc]).

(DBR) on top of a heat sink grants high reflectivity for the laser light and suppresses the formation of interfering higher order modes. An intra-cavity SHG crystal converts the IR into visible light. The technology became commercially available in 2009 and initially provided output powers below 10 W. Years later, laser models with output power up to 25 W became available. The ELSA Compton polarimeter was successfully tested with the Verdi G18⁴⁵ [Cohb] OPSL laser, operating with 18.5 W output power at $\lambda = 532$ nm.

6.2 The Compton Polarimeter Beamline

For the electron beam polarization measurement during accelerator operation the photon beamline and γ -detector setup (compare with technical drawing in Fig. 6.1) provides the following functionality: It

1. generates an alternatingly left- and right-handed circular polarized photon beam,
2. steers the high intensity CW laser beam to the LIR with RC micrometer transverse alignment capability and allows adjustments of the focal distance for photon beam size variation at the LIR,
3. provides diagnostic devices for the measurement of laser beam polarization, power, position and size, and
4. measures the vertical distribution of the backscattered γ -beam profile resulting from photon- e^- interaction. It distinguishes between photons resulting from left- and right-handed circular laser interaction as well as from background radiation.

A sketch of the contemporary polarimeter realization is shown in Fig. 6.5. The linearly polarized laser beam penetrates a $\lambda/4$ retarder waveplate, which changes the photon polarization from linear to circular. The retarder plate is mounted on a pneumatically driven mount, which rotates the plate by 90° and returns it to its initial position, allowing a change from left- to right-handed polarization and vice-versa. A concave lens widens the narrow input beam in order to refocus the photon beam by a second convex lens onto the LIR in approximately 15 m distance. Two beamline mirrors can be tilted by RC Piezo actuators for angular and position adjustment of the laser beam at the LIR. A fast shutter rapidly blocks the beam, when the γ -detector performs background measurements during the rotational motion of the pneumatically driven retarder plate. Photographs of the laser box setup and the LIR in the accelerator shielding tunnel are shown in Fig. 6.6, a photograph of the subsequent laser beam diagnostics section behind the LIR is shown in Fig. 6.7. Thereat, the laser beam position, size and intensity is monitored by a CCD camera and multiple four-quadrant PSDs. The devices are located behind consecutive reflecting mirrors, which guide the laser beam through a polarization measurement setup and eventually into copper beam dumps. The laser beam polarization is measured by linearizing the circularly polarized beam through a $\lambda/4$ retarder plate. The polarization degree is obtained by beam intensity measurements through four-quadrant PSDs, which are located at a PBS's reflection and transmission path, respectively. The beam intensity measured by the PSDs can be calibrated by deflecting the beam onto a power meter through a flip mirror. An alternative option to measure the photon beam polarization is by utilizing a rotating linear polarizing filter device, which can be inserted behind the outcoupling window, if the laser shielding is removed.

The properties of the laser beam and details of the individual beam manipulation and diagnostic devices are explicated in the following sections.

⁴by Coherent Inc.

⁵Special thanks to Prof. Dr. Meschede and his research group for providing the laser device for the required test period.

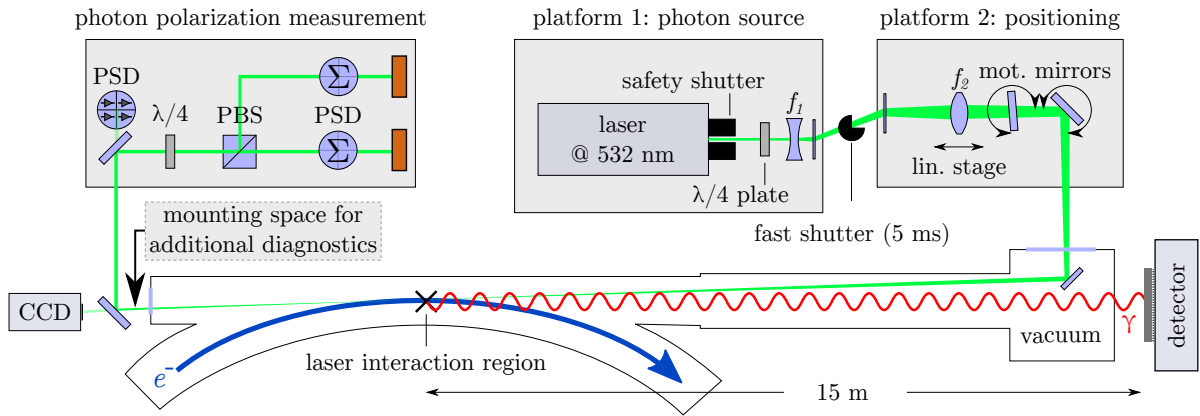


Figure 6.5: Schematic drawing of the ELSA Compton polarimeter photon beamline. The laser beam is circularly polarized and widened in order to be refocused at the downstream LIR. Movable RC optical elements allow adjustment of the laser beam size and position (all mirrors reflect the beam by $\sim 90^\circ$). A CCD camera and a PSD monitor the outcoupled laser beam before its polarization is measured at the back-end: A second $\lambda/4$ retarder plate changes the circular polarization to linear, whose s -component is deflected by a polarizing beam splitter (PBS). The photon polarization degree is then obtained via PSD intensity measurements of the transmitted and deflected beam, before the laser beam is dumped in copper blocks. Additional diagnostics can be temporarily mounted behind the vacuum outcoupling window.

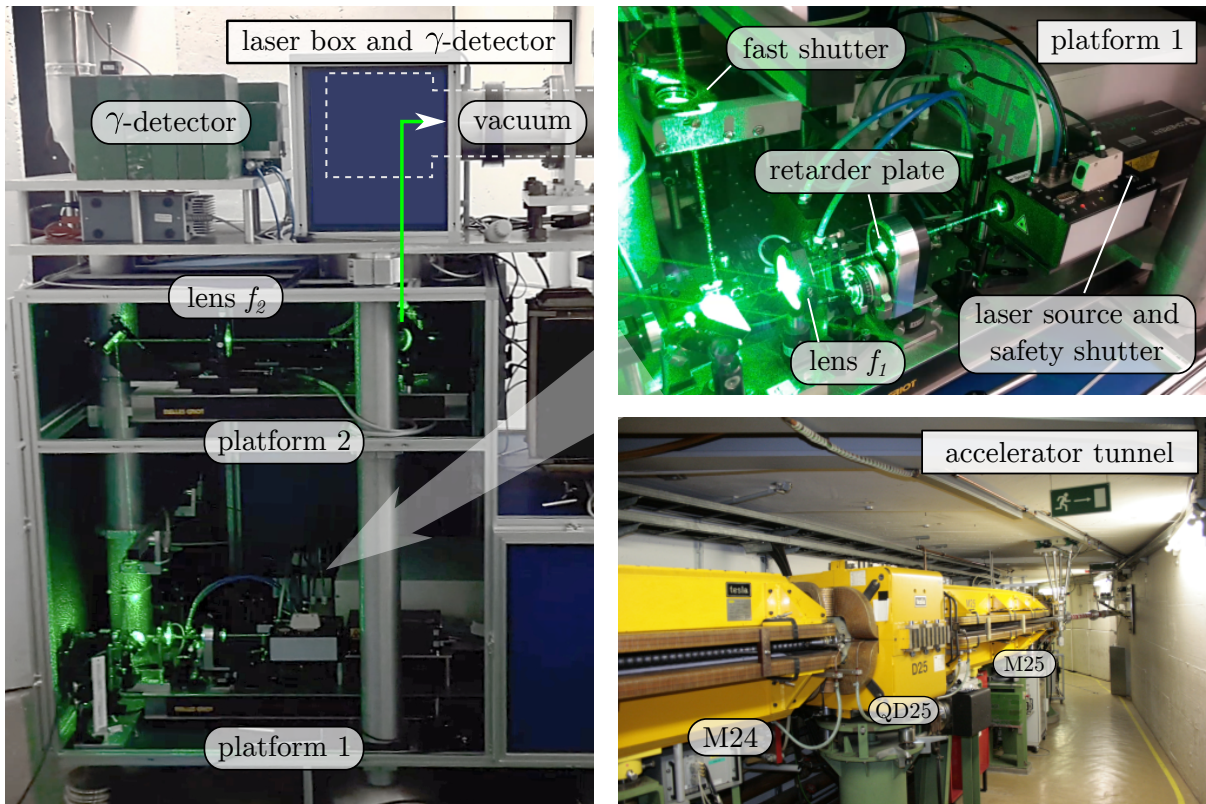


Figure 6.6: Photographs of the ELSA Compton polarimeter laser box and γ -detector stand (behind lead shielding) with partially removed laser shielding, close-up of optics platform 1 and LIR view from within the accelerator shielding tunnel.

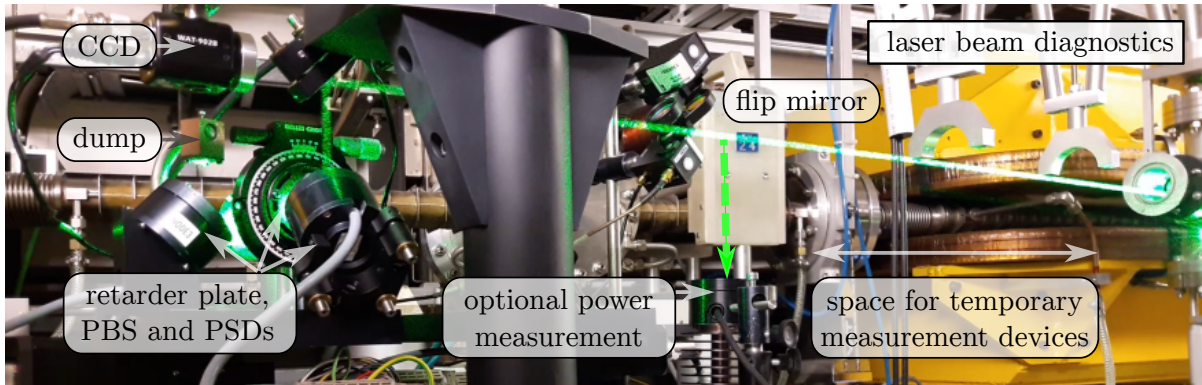


Figure 6.7: Photograph of the Compton polarimeter laser beam analysis section with removed laser shielding. The transverse photon profile is monitored by a CCD camera situated behind a deflecting mirror, which guides the beam to the photon polarization measurement station. An RC flip mirror may deflect the beam onto a calibrated power meter.

6.2.1 Electron Beam Size at the Photon Interaction Point

The laser beam size and position is to be matched to the position and size of the stored electron beam to maximize the photon backscattering rate (see Section 5.3.1). The electron beam size is calculated from the corresponding optical functions shown in Fig. 6.8 (compare with Section 4.3 and Fig. 4.2). The size of the elliptical electron beam around the LIR is shown in Fig. 6.9 for the typical storage ring energy range and under the assumption of 10 % emittance coupling (compare with Section 4.3). The LIR is chosen so that the electron beam cross section is close to circular. At the designated LIR the electron beam size amounts $\sigma_x = 0.71$ to 1.36 mm and $\sigma_z = 0.49$ to 0.60 mm from 1.2 to 3.2 GeV beam energy. The beamline objective is to provide a photon beam cross section with approximately matched values.

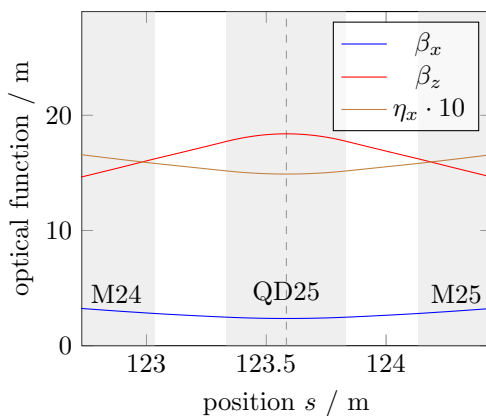


Figure 6.8: Optical functions at the electron-photon LIR within quadrupole magnet QD 25.

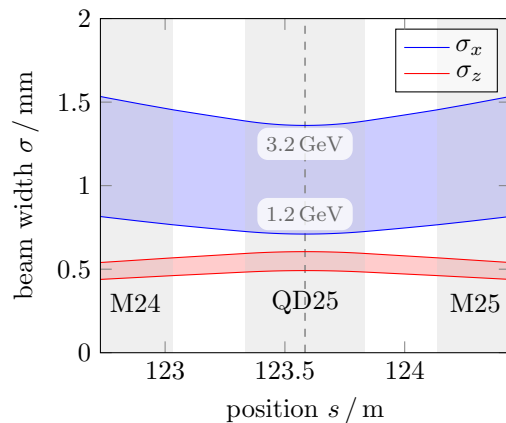


Figure 6.9: Electron beam size at the electron-photon LIR for 1.2 to 3.2 GeV beam energy.

6.2.2 The Photon Beam

Optical Setup

The laser device is situated approximately 17 m away from the designated LIR. With a given beam waist size $2w_0 = (2.25 \pm 0.23)$ mm at the laser output and an estimated $M^2 = 1.05$ (see specifications of the OPSL Verdi G18 laser in Table 6.1), the Rayleigh length⁶ (compare with Appendix E) computes to

$$z_R = \frac{\pi(2w_0)^2}{4\lambda} = 7.47 \text{ m} , \quad (6.1)$$

yielding a laser beam divergence of

$$\Theta = \frac{2w_0}{z_0} = 0.32 \text{ mrad} . \quad (6.2)$$

The unmanipulated beam size at LIR distance would then amount $w_{\text{LIR}} = 2.4$ mm and thus, be too large for a sufficient electron interaction rate (compare with Section 5.3.1 and Fig. 6.9).

Hence, an optical system is required to adjust the laser beam size. At the current polarimeter setup, it consists of a biconcave ($f_1 = -400$ mm) and a biconvex lens ($f_2 = 1300$ mm), and five deflecting laser mirrors which bend the laser beam into the accelerator's vacuum system and onto the LIR. The last mirror is mounted within the vacuum system. The biconvex lens is mounted on a linear stage with 100 mm longitudinal travel range, which allows to move the focal point across the LIR to change the size of its interacting area. Figure 6.10 shows the beam size of the laser beam across the beamline, when the bi-concave lens (f_1) is placed 16.34 m in front of the LIR and the biconvex lens (f_2) 1.02 m behind the first lens. In this case, the divergence at the LIR amounts $\Theta_{\text{LIR}} = 0.56$ mrad, yielding a Rayleigh length of $z_{R,\text{LIR}} = 1.29$ m and a minimum beam waist of $2w_{0,\text{LIR}} = 0.66$ mm.

A technical drawing illustrating realistic sizes of the colliding photon and electron beam within quadrupole magnet QD 25 is shown in Fig. 6.11. An IGP vacuum pump, which is flanged directly to the quadrupole vacuum chamber, provides additional suction capacity to improve the vacuum pressure at the LIR.

property	Verdi G18 specification
wavelength λ	(532 ± 2) nm
output power P	18 W
M^2	< 1.1
beam circularity	1.0 ± 0.1
beam waist diameter $2w_0$	(2.25 ± 0.23) mm (FW, $1/e^2$)
beam divergence Θ	< 0.5 mrad (FW, $1/e^2$)
polarization ratio	linear, $> 100:1$
polarization direction	vertical ($\pm 5^\circ$)
power stability (pk-pk)	$\pm < 1\%$
pointing stability	< 2 $\mu\text{rad}/^\circ\text{C}$

Table 6.1: Verdi G18 laser properties from specification [Cohb] and measurement.

⁶Note that the nomenclature for the coordinate system of the laser beam is chosen in accordance with common optics literature as (x, y, z) , with z being the longitudinal component. In accelerator physics literature, including this work, the nomenclature is often (x, z, s) , where s represents the longitudinal component (compare with Fig. 4.1).

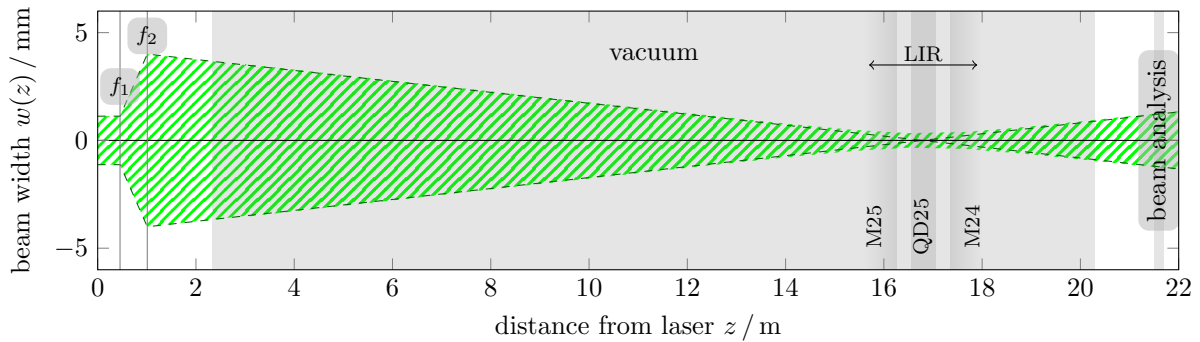


Figure 6.10: Laser beam cross section along the Compton polarimeter photon beamline.

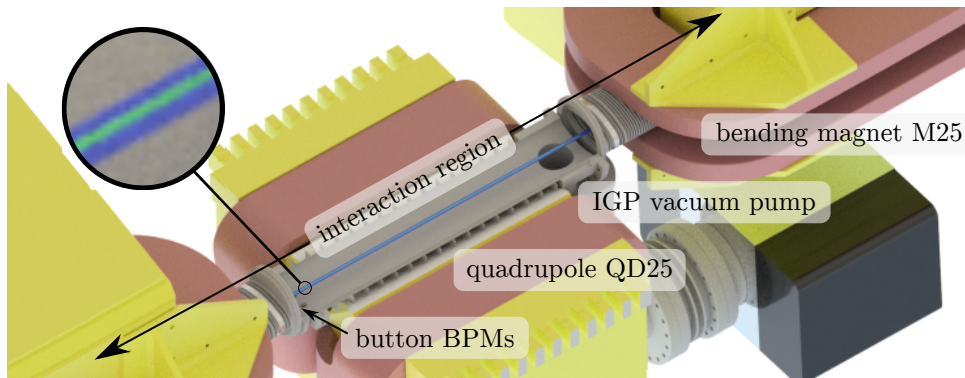


Figure 6.11: Illustration of laser beam (green) crossing the electron beam (blue) within the vacuum chamber of quadrupole QD 25 (section view). The beam sizes are close to scale for a beam energy of 3.2 GeV. An additional IGP vacuum pump reduces the gas pressure within the interaction region. The button BPMs measure the position of the electron beam's centroid.

It significantly reduces the background radiation from collisions between electrons and residual gas molecules compared to the previous polarimeter versions (see Sections 5.3.2 and 6.1.1).

The properties of the laser beam propagating through the optical beamline were selectively measured using the knife-edge method (see e.g. [SSJ91]), which is utilized by the commercially available measurement device ModeMaster PC⁷. This device can be placed behind the vacuum outcoupling window and measures the distance to the beam waist z_0 , the beam size $w(z)$ and the beam divergence Θ at its front bezel, from which the beam parameters at the designated IP (center of quadrupole magnet QD25) are extrapolated according to the Gaussian beam propagation formalism (see Appendix E). The change of the beam properties for different lens f_2 positions on the linear stage are shown in Fig. 6.12.

⁷Product of Coherent, Inc., see [Coh15]

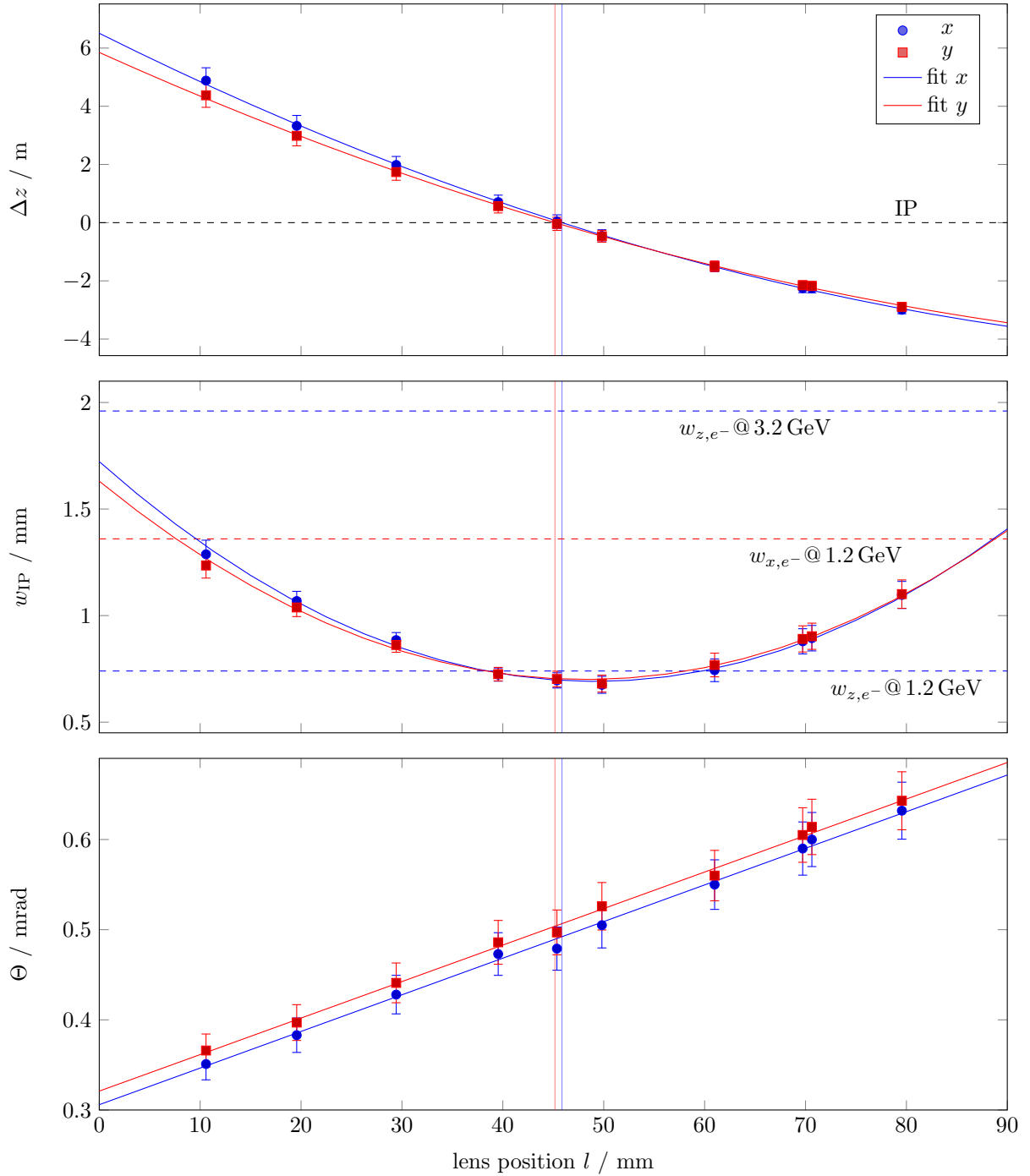


Figure 6.12: The effect of lens f_2 position l on laser beam waist distance Δz from the design IP (top), the waist size w_{IP} at the IP (center) and divergence Θ (bottom) measured with the ModeMaster PC. Negative distances Δz indicate positions towards the source. Hence, the beam waist can be moved up to 6 m behind the IP (for $l = 0$ mm), at which the beam size w_{IP} is largest and sufficiently matches the horizontal electron size w_{x,e^-} @ 3.2 GeV. The vertical markings indicate the lens position at which the waist position coincides with the IP position. Note that the right-handed Cartesian photon frame coordinate system reads (x, y, z) in contrast to the electron frame coordinate system (x, z, s) : y and z each indicate the vertical coordinate, respectively.

Photon Polarization

The circular photon polarization degree \mathcal{P}_γ can be measured by *division of amplitude* after penetrating a $\lambda/4$ retarder waveplate and a PBS, or through a rotating linear polarization filter. The PBS setup is a stationary installation within the photon analyzing box, whereas the rotation device was used for temporary, but more precise measurements.

Photon Polarization Measurement via Polarizing Beam Splitter In the laser beam diagnostics box a second $\lambda/4$ retarder plate linearizes the circular photon polarization. A subsequent PBS transmits the p -polarized and reflects the s -polarized photons. The beam power at each branch is then measured by the sum signal of the corresponding four-quadrant PSD. Due to finite transmission and reflection efficiencies the measured beam power at each branch corresponds to

$$\tilde{P}_p = P_p T_p + P_s T_s \quad (6.3)$$

$$\tilde{P}_s = P_p(1 - T_p) + P_s(1 - T_s), \quad (6.4)$$

where $T_p = 99.5\%$ is the transmission efficiency of s -polarized light and $E = T_p/T_s = 500$ is the extinction ratio of the utilized PBS (compare with [Aur08, Fig. A.2]). The true s - and p -polarized beam power is determined from both branches through Eqs. (6.3) and (6.4), yielding

$$P_p = \left[\tilde{P}_p - \tilde{P}_s \frac{1}{E - T_p} \right] \frac{1}{T_p} \chi \quad (6.5)$$

$$P_s = \left[\tilde{P}_s - \tilde{P}_p \left(\frac{1}{T_p} - 1 \right) \right] \left(\frac{1}{1 - \frac{T_p}{E}} \right) \chi \quad (6.6)$$

with $\chi = \frac{E-1}{E-T_p} \approx 1$. The polarization degree is then obtained by division of amplitude:

$$\mathcal{P}_\gamma = \frac{P_s - P_p}{P_s + P_p}. \quad (6.7)$$

A technical drawing of the setup is shown in Fig. 6.13 and an exemplary measurement is given in Fig. 6.14. The data obtained therein yields circular laser beam polarization degrees of

$$\mathcal{P}_\cup = (90.3 \pm 0.4)\% \quad \text{and} \quad \mathcal{P}_\ominus = (94.6 \pm 0.4)\%, \quad (6.8)$$

resulting in a mean photon polarization degree of

$$\mathcal{P}_\gamma = (93.0 \pm 0.5)\%. \quad (6.9)$$

These results assume a retarder waveplate in optimum position, but on the contrary represent a non-ideal setting which was obtained during beamline commissioning. Experience with this measurement method showed that readjustments and reproducibility of the contemporary PBS setup is insufficient: The measured beam power varies strongly with the transverse beam position or the position of the longitudinal beam waist, since the laser beam size is similar to the size of the device's apertures. During polarimeter operation the laser position is usually adjusted to maximize the backscattering rate. The required repositioning of the optical table is possible through two installed transverse linear stages, but plane-coupling due to imperfect mirror-positions prevented a convenient usage of this method.

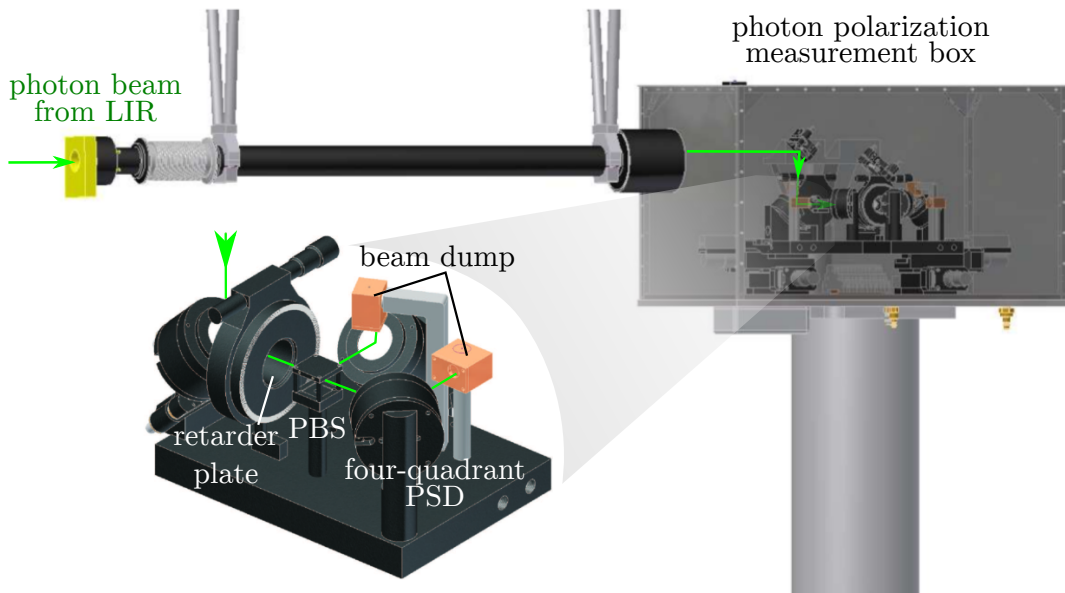


Figure 6.13: Technical drawing of the photon polarization analysis box [Aur08, Fig. 3.4, 3.5], including a CCD camera and three four-quadrant PSDs for position and intensity measurement. The retarder plate and the PBS allow photon polarization measurements via intensity comparison on both back-end PSDs.

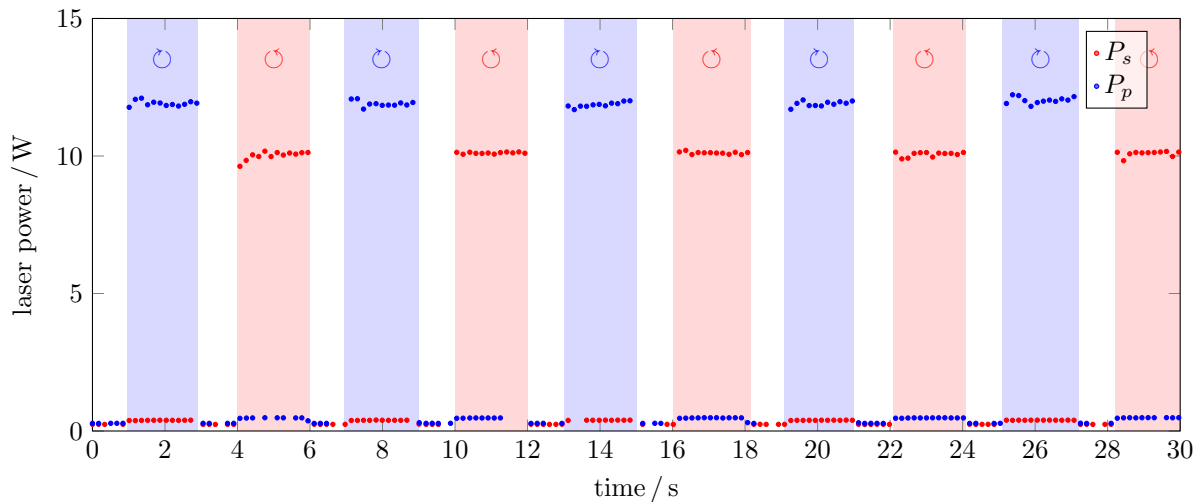


Figure 6.14: Measurement of the circular photon polarization degree by *division of amplitude*. The power of the transmitted p -component P_p and the reflected s -component P_s are measured to obtain the degree of circular left (red background) and circular right (blue background) laser polarization.

Photon Polarization Measurement via Rotating Linear Filter Due to the difficult adjustment procedure of the previous method, determination and optimization of the circular photon polarization was performed using a rotating linear polarization filter⁸ in front of the photon analyzer box (compare with Fig. 6.7). With this method, the attenuated laser beam penetrates the rotating linear polarization filter and the beam power function $P(\theta) = P_0 \cos^2 \theta$ is measured to determine the difference of maximum and minimum beam power $\Delta P = 2P_0 = P_{\max} - P_{\min}$. The total power is given by $P_{\text{tot}} = P_{\max} + P_{\min}$. First, the retarder waveplate in front of the photon source is removed (compare with Fig. 6.5) to obtain the degree of linear (\Downarrow) beam polarization through a sinusoidal function fit, as illustrated in Fig. 6.15. The (linear) beam polarization thus amounts

$$\mathcal{P}_{\Downarrow} = \frac{\Delta P_{\Downarrow}}{P_{\Downarrow,\text{tot}}} = (98.58 \pm 0.03) \% . \quad (6.10)$$

The polarization ratio of the source is specified with $> 100:1$ ($>98\%$, see Table 6.1). Hence, polarization losses due to deflection within the laser beamline seem negligible. A higher amount of polarization may be achieved by placing a PBS in front of the photon source, but the obtained amount is expected to be sufficient for the CBS measurement procedure.

The circular photon polarization is obtained by re-inserting the retarder waveplate and fixing it at the angular position of the pneumatic mount at which the amplitude of $P(\theta)$ is minimal. The degree of circular polarization of a completely polarized beam is obtained through [Gow01, Chapter 4.4.3]

$$\mathcal{P}_{\circlearrowleft} = \frac{2 \sqrt{P_{\circlearrowleft,\max} \cdot P_{\circlearrowleft,\min}}}{P_{\circlearrowleft,\text{tot}}} , \quad (6.11)$$

and in analogy for $\mathcal{P}_{\circlearrowright}$. However, as Eq. (6.11) holds for a completely polarized incident beam, the true degree of circular polarization is estimated by multiplying Eq. (6.11) with Eq. (6.10). The maximum

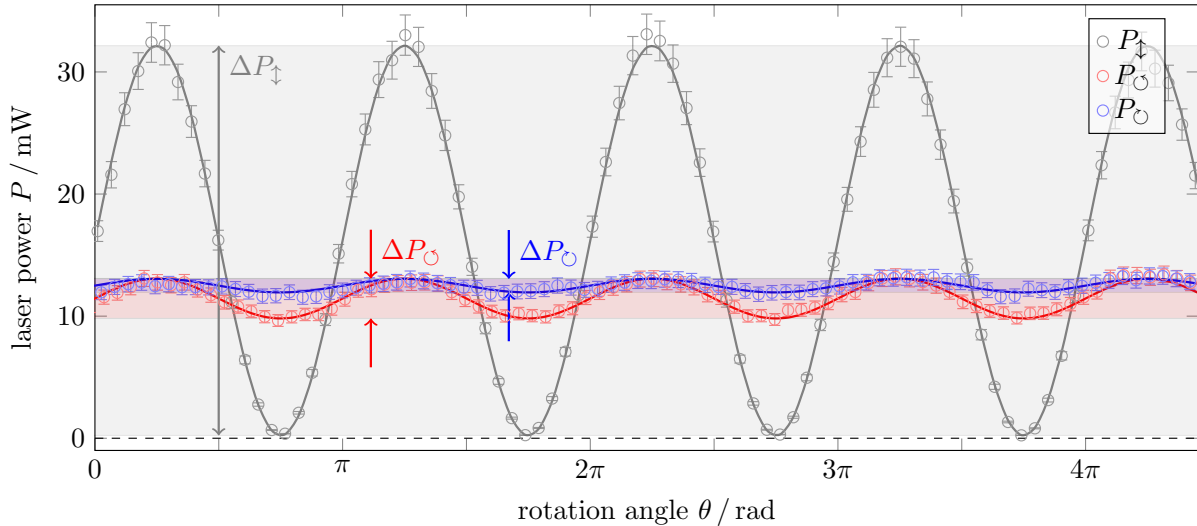


Figure 6.15: Measurement of laser power versus rotation angle of a linear polarization filter to obtain the circular polarization degree. The ΔP_i denote the difference of maximum and minimum intensity measured for the corresponding photon polarization state.

⁸Dichroic film polarizer with extinction ratio $> 5000 : 1$ sandwiched between two glass disks.

degrees of circular polarization obtainable with the contemporary optical setup are thus

$$\mathcal{P}_{\odot} = (97.57 \pm 0.03) \% \quad \text{and} \quad \mathcal{P}_{\ominus} = (98.48 \pm 0.03) \% , \quad (6.12)$$

resulting in a mean circular photon polarization degree of

$$\mathcal{P}_{\gamma} = (98.03 \pm 0.02) \% , \quad (6.13)$$

which is of sufficient magnitude. However, higher degrees of polarization could be achieved by the following actions:

- As mentioned above, the degree of linear polarization can be increased by inserting a **PBS** in front of the laser source.
- The evacuated mirror's coating is optimized for a laser wavelength of 515 nm. The reflectivity difference for *s*- and *p*-polarized light at 532 nm is unknown and could deviate from an optimal value. A replacement of that mirror is likely to improve the polarization degree, but the expected improvement hardly justifies the tedious replacement within vacuum conditions.
- The procedure to find the maximum degree of circular polarization involves the variation of the $\lambda/4$ retarder plate's tilt. The locking mechanism of the mount is, however, only reproducible with a precision of a few degrees. A more accurate mechanical setup may improve the situation, but was not available at the time.

Note that in the measurement shown in Fig. 6.15 the mean values (offset of the sinusoidal function) of P_{\odot} and P_{\ominus} are expected to coincide with that of P_{\downarrow} , but a reduction of available beam intensity inbetween those measurements is responsible for the deviation. As the laser source is very stable, a likely cause is a transverse beam drift in combination with beam loss at an aperture. Such drifts were occasionally observed and were correlated to temperature changes of the optics mounting structure.

Laser Beam Power

The laser beam is guided through multiple optical elements, each with finite reflectivity or transmission, respectively. An evaluation of the transmission efficiency of the polarimeter beamline was estimated by B. Aurand for a 515 nm laser beam [Aur08, Sec. 4.4]. A transmission efficiency of 77 % at the **LIR** and 65 % after the last vacuum coupling-window was estimated. For a 532 nm laser, the beamline transmission is expected to be marginally lower due to the unadapted coating of the evacuated mirror. For an initial beam power $P_0 = 18.5 \text{ W}$ one therefore expects $P_{\text{LIR}} \leq 14.2 \text{ W}$ and $P_{\text{out}} \approx 12 \text{ W}$ after the vacuum window. Beam power measurements were conducted with the laser power measurement device PM150-19C⁹. It is installed within the polarization measurement box and can be used when an **RC** flip mirror is inserted into the beamline (compare with Fig. 6.7). With an initial laser power of $P_{0,\text{meas}} = (19.1 \pm 0.4) \text{ W}$ and an outcoupled intensity of $P_{\text{out,max}} = (13.7 \pm 0.3) \text{ W}$, the measured transfer efficiency is $(71.7 \pm 6.0) \%$. Operation experience has shown, however, that the narrow vacuum chamber opposes an aperture which can easily be hit by the laser beam when its transverse position is adjusted for maximizing the γ -backscattering rate. As mentioned above, also temperature drifts may cause a (slow) transverse laser beam drift. Therefore, in some electron polarization measurements a laser power $< 14 \text{ W}$ was determined at the **LIR**.

⁹Product of Coherent, Inc.

Laser Beam Stability

The transverse laser beam stability (pointing stability) was measured with the CCD camera at the beamline diagnostics back-end (see Fig. 6.7). An exemplary data set of obtained beam centroids \bar{x} and \bar{z} is shown in Fig. 6.16. It yields pointing stabilities of

$$7.9 \mu\text{m} < x_{\text{RMS}} < 18.9 \mu\text{m} \quad \text{and} \quad 7.6 \mu\text{m} < z_{\text{RMS}} < 17.5 \mu\text{m}, \quad (6.14)$$

where the minima and maxima correspond to the values obtained from the four shown measurement intervals. Therein, the individual mean within the corresponding interval was determined, from which the RMS deviation was calculated. The RMS values are of acceptable magnitude and smaller compared to previous Compton polarimeter versions (compare with Section 6.1.1). However, it is noticeable that the horizontal and vertical beam centroids change by up to

$$\Delta\bar{x}_{\text{max}} = 64.7 \mu\text{m} \quad \text{and} \quad \Delta\bar{z}_{\text{max}} = 147 \mu\text{m} \quad (6.15)$$

for different laser beam helicities (those jumps are omitted from the RMS stability measurement of Eq. (6.14)), being in the order of the analyzing power (compare with Fig. 5.14(b)). It is not clear, however, if the major contributor to this difference is a laser beam movement itself, or a defective centroid measurement under non-ideal measurement conditions:

- The CCD image shows an intensity distribution deviating from a Gaussian ellipsoid, including reflection fragments from the narrow beam pipe.
- Diffraction patterns are formed by a few dust particles on optical surfaces (from the accelerator shielding tunnel environment) which distort the profile fit function of the digitized image.
- The beam image is partially saturated and control of the electronic shutter of the CCD camera¹⁰ could not be achieved.

For example, a combination of the above error sources is likely to induce the transient drift responses of the vertical centroid observed in Fig. 6.16 (when the laser shutter is opened) due to intensity adjustments of the CCD camera. However, as the selected measurement intervals for the RMS pointing stability fall into *steady state* shutter conditions of the camera, sufficient measurement accuracy can be expected.

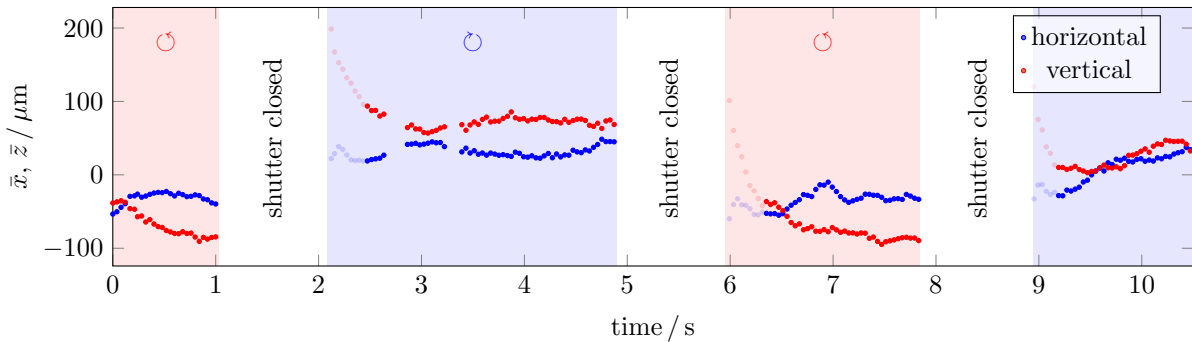


Figure 6.16: Pointing stability of the Verdi G18 laser measured with a CCD camera in 4.5 m distance behind the LIR. The background indicates the sign of the laser beam helicity. The opaque data points are omitted in the stability measurement, as those are correlated to the CCD intensity adjustment in combination with image defects.

¹⁰WAT-902B by Watec Co., Ltd.

6.3 The Silicon Microstrip Detector

The vertical profile of the CBS γ -rays is detected by a lead conversion silicon microstrip detector¹¹. The backscattered photons create charge carriers within the lead through e^+e^- pair production. Those ionizing charge carriers subsequently create electron-hole pairs during the passage through the silicon strips (see Section 5.4.2 for details). The accumulated electron-hole charges are deposited on 768 horizontally orientated, AC-coupled silicon strips with 50 μm pitch. The charge deposits are processed to digital counts by an in-house developed application-specific integrated circuit (ASIC) [Koo19]. The detector module was commissioned by R. Koop and was successfully tested by mid 2016. A photograph of the detector module is shown in Fig. 6.17, a sketch of the signal processing scheme is given in Fig. 6.18.

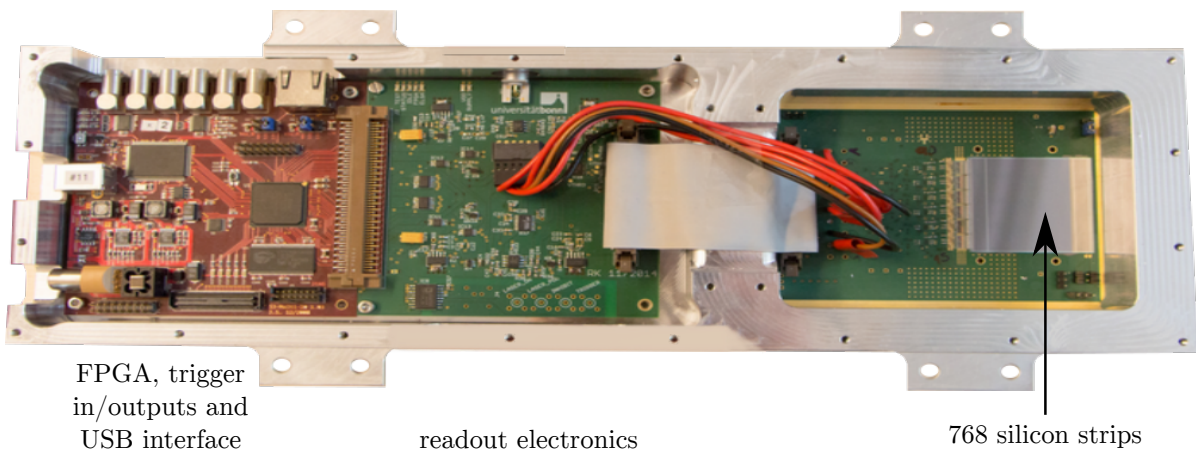


Figure 6.17: Photograph of the Compton polarimeter detector module with removed top cover.

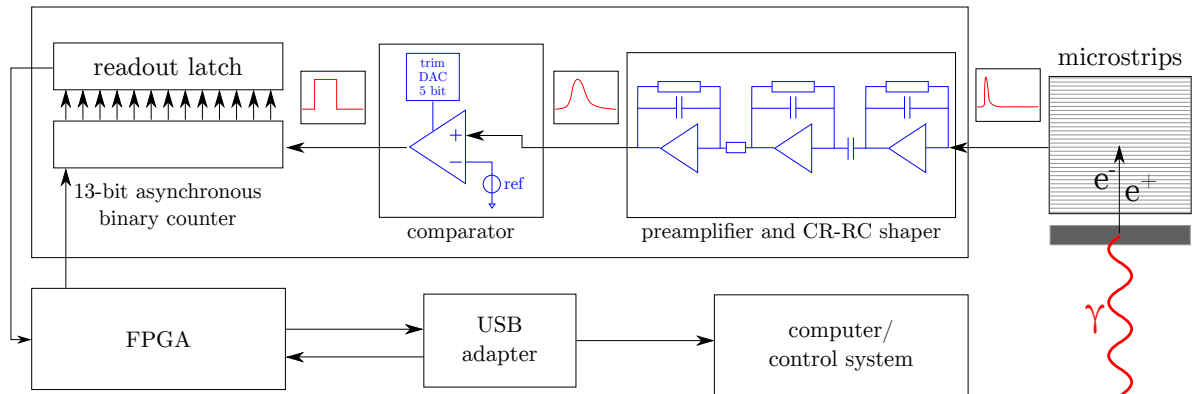


Figure 6.18: Schematic drawing of the signal processing circuitry of the γ -detector. The microstrip charge pulse is reshaped, amplified and digitized by a comparator, whose threshold is settable by a 5-bit trim digital-to-analog converter (DAC). The binary counter module is read out by an FPGA which transfers the obtained data with timestamp and trigger status as data file to a computer.

¹¹Design and manufacturing by SiLab, Physics Institute, Bonn University.

6.3.1 Measurement Procedure

For data taking, the detector module controls the positions of the pneumatically driven retarder waveplate and the fast shutter. In a polarization measurement the γ -beam profiles are recorded for positive and negative laser beam helicities (\odot/\ominus). Inbetween the helicity switching motion, the background profile from gas bremsstrahlung is measured with blocked laser beam. The background can be subtracted from each adjacent laser profile measurement to obtain the unadulterated laser interaction profiles. Hence, a total of six profile measurements contribute to one measurement cycle, as illustrated in Fig. 6.19. If the electron polarization alternates from cycle to cycle in booster mode (compare with Fig. 1.1) – as is the case when the polarizing source is used – the polarization degrees of spin-up and spin-down electrons e_{\uparrow}^- and e_{\downarrow}^- are compared, and one measurement consists of 12 profiles. The detector module itself can be triggered by the ELSA cycle trigger signal, which may initiate the measurement procedure after the storage ring is filled. An e^- -polarity status trigger signal is provided by the ELSA timing system. Under the assumption of a constant electron extraction rate and for stable beam conditions¹², the integrated count rate in a measurement cycle (+/0/ - | - /0/+ \rightarrow +/0/-) is equal for left-handed (+) and right-handed (-) photon helicity measurements.

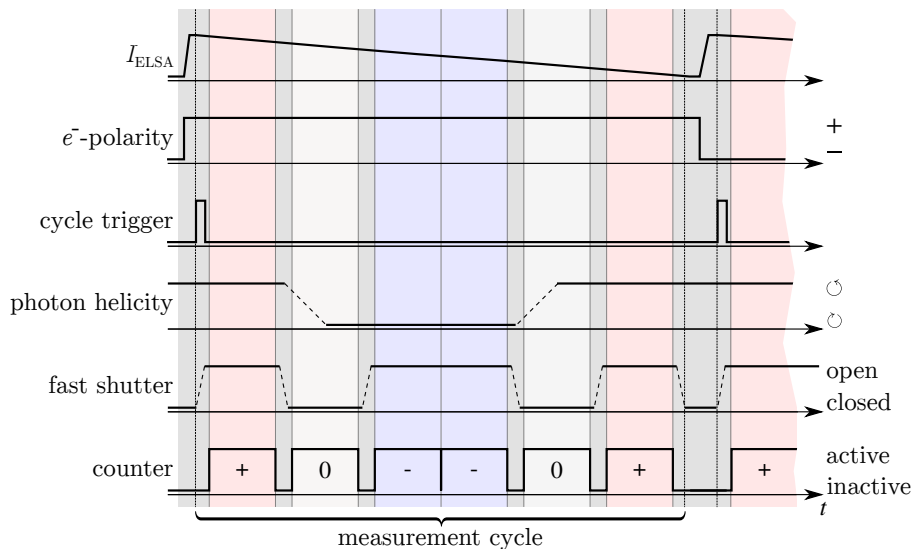


Figure 6.19: Standard detector measurement intervals during an ELSA cycle in *booster* mode. The measurement is started by the cycle trigger signal, which opens the laser shutter. While the laser helicity is changed by pneumatically rotating the waveplate holder, a background measurement is performed with closed fast shutters. The count rates for positive and negative laser signals are equal for a constant decrease of the stored electron current I_{ELSA} .

6.3.2 Beam Profiles

Measured beam profiles of the background radiation from electron scattering on residual gas molecules (compare with Section 5.3.2) and the superimposed laser signal are shown in Fig. 6.20. The measured profiles demonstrate the general quality of the obtained data and show the magnitude of the individual detector channel count deviations and inherent defects, such as statistical noise, trim inaccuracy, and potentially dysfunctional channels.

¹²Stable beam conditions refer to the absence of e^- and laser beam drifts or laser intensity fluctuations.

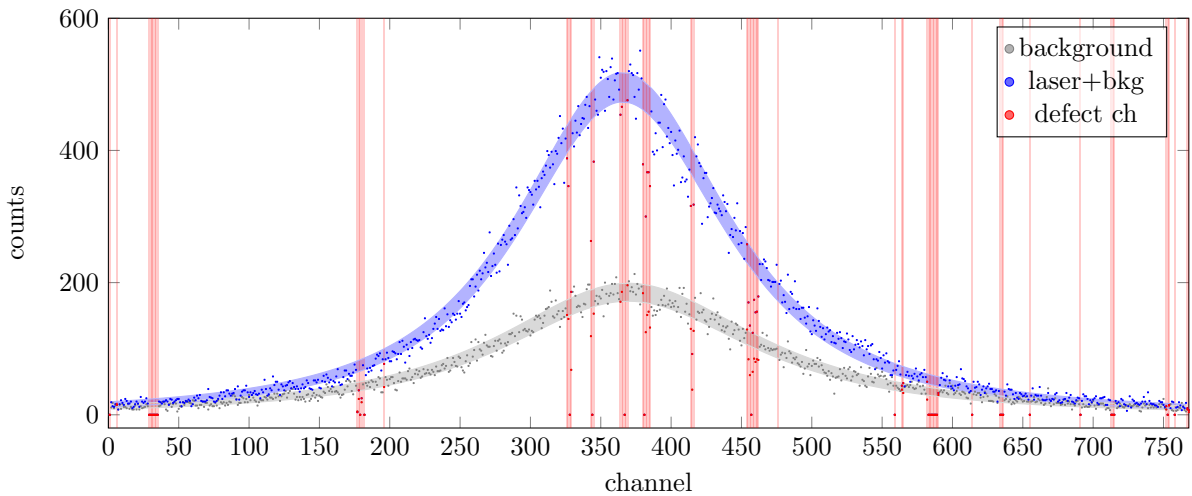


Figure 6.20: Raw profile data of γ -photons from laser-electron interaction (blue) superimposed on background radiation (gray) at $E = 1.32$ GeV, $I_{e^-} = 32$ mA, $P_{\text{las}} = 9$ W during a 955 ms long measurement. The vacuum pressure at the IR amounted 2.6×10^{-8} mbar. The expected statistical error is indicated as background for a *Pearson VII* peak shape function fit. Those channels marked red are either fully dysfunctional or not sufficiently correctable.

Channel Defects

In total, 96 defect channels were identified (12.5%). Despite of a lifetime limitation of individual channels due to radiation damage (compare with [Section 3.3.1](#)), the number of initially dysfunctional channels was found surprisingly large when first operation tests were performed. The defects, such as dysfunction or cross-talking, are assumed to originate from the [ASIC](#) design, manufacturing and bonding process. The erroneous channels include

- 32 fully dysfunctional channels for which the counter values remain zero,
- 32 dysfunctional channels whose counter values deviate significantly from neighboring channels, and
- 32 channels which are precautionarily muted when a scaling correction value was below 0.9 or above 1.1 (see below and [Appendix F](#)).

Operation experience with this detector showed, however, that the amount of defect channels is bearable for adequate electron polarization measurements.

Profile Scaling Correction

To some extent each channel has a marginally individual response to the accumulated charges. To obtain a preferably uniform response, the detector's individual channel responses have to be calibrated. On a hardware level, equal test charges can be injected to each channel, whose discrimination response is scaleable through a corresponding 5 bit trim [DAC](#) (compare with [Fig. 6.18](#)). The contemporary correction settings are visualized in [Fig. F.1](#) in [Appendix F](#). These correction values are loaded upon detector startup. In addition, a software scaling correction factor can be applied to each channel, which is obtained from comparing a data set with a large amount of events to a reasonable smooth function (see [Figs. F.2](#) and [F.3](#) in [Appendix F](#)). The impact of scaling correction by software is visualized in [Fig. 6.21](#) where the profile

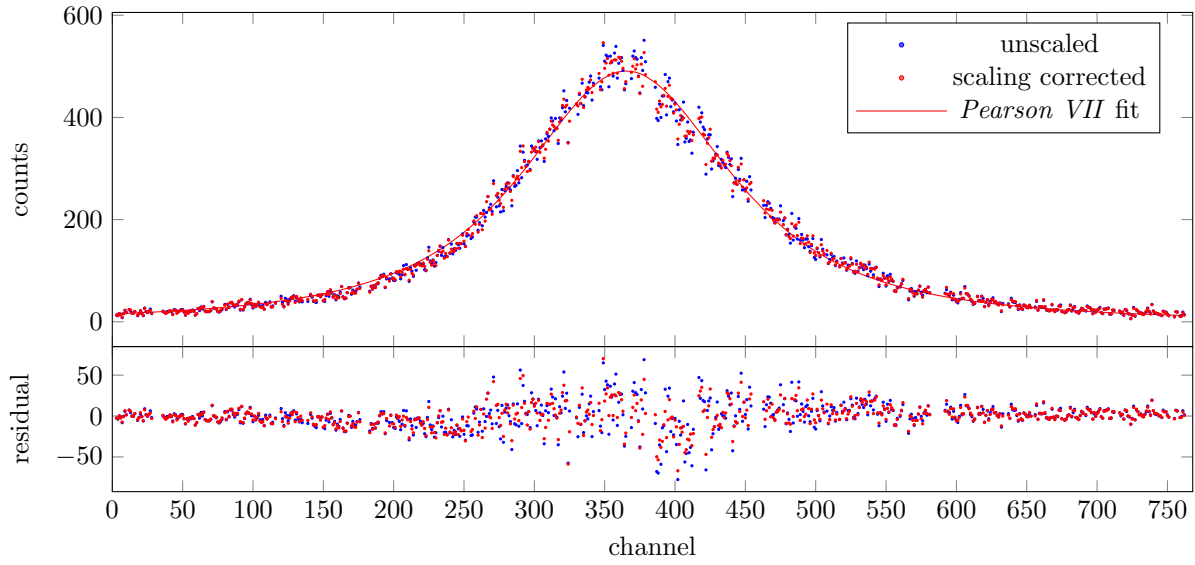


Figure 6.21: Software scaled and unscaled photon profile including residuals to a *Pearson VII* function fit. The scaling correction reduces the standard deviation of the residuals from 23.9 to 18.9 counts, but may introduce artifacts.

of Fig. 6.20 is compared to a scaling corrected profile. The residuals¹³ of the corrected profile show a reduced standard deviation of 18.9 counts in comparison to 23.9 counts of the original profile. The improvement may, however, be insignificant considering that potential artifacts are introduced through the scaling process. Hence, the upcoming beam profile analysis is performed without software scaling correction.

6.4 Shift in the Means Analysis

For electron beam polarization measurements utilizing the *shift in the means* method (see Section 5.2.2) the measurand is the difference of the background-subtracted γ -beam profile's center of gravity

$$\Delta z = \bar{z}_L - \bar{z}_R \quad \text{or} \quad \Delta z = \bar{z}_\cup - \bar{z}_\ominus \quad (5.32 \text{ revisited})$$

for left- and right-handed circular photon helicity. To obtain the above figures the stored detector profile data is processed by a GNU Octave [Eat+17] script algorithm, which was developed by the author and is visualized in Fig. 6.22: The data of laser and background profiles (+/0/-) may be scaling corrected (compare with Section 6.3.2) before the background is subtracted from the adjacent profile measurement (+ \rightarrow \cup and - \rightarrow \cup). Data from the same measurement cycle (compare with Fig. 6.19) is combined and multiple profiles are summed up until a user-defined criterium is fulfilled (e.g. minimum sum of counts or minimum statistical error obtained). During the summation, various accelerator parameters are monitored and data sets are omitted when unstable accelerator conditions are identified (e.g. laser and electron beam stability fluctuations). In addition, identified erroneous profile data (e.g. profile distortion by stray radiation) is omitted. The centers of gravity of the summed profiles (\bar{z}_\cup and \bar{z}_\ominus) are determined for each laser beam helicity through statistical analysis or by utilizing a proper fit function, as discussed below. With a series of Δz measurements, a proper analyzing power \mathcal{D} (polarimeter calibration factor,

¹³count difference to the model function (fit)

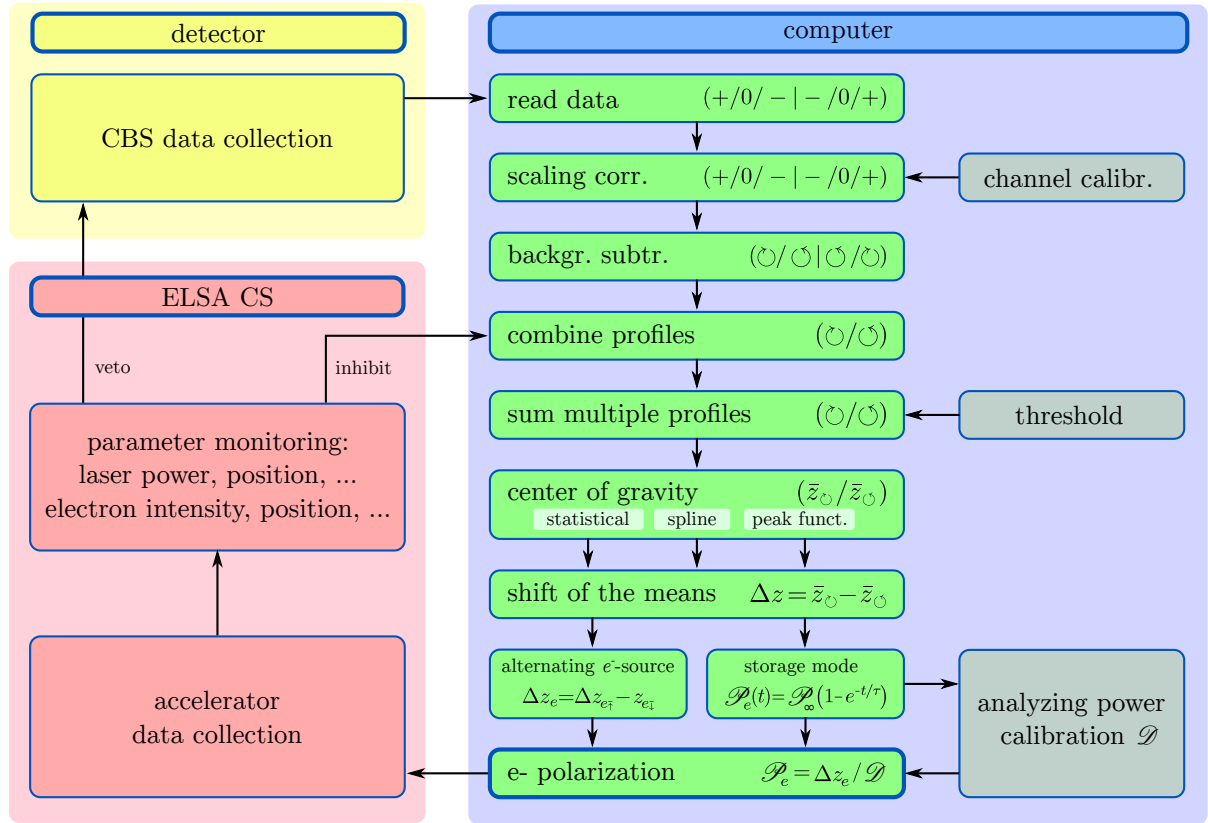


Figure 6.22: Analysis process of the electron polarization measurement data. The raw detector data is transferred to a computer, where it is analyzed in respect to measured electron and photon beam data processed by the ELSA CS. Data sets which indicate poor quality (deviation, fluctuation, etc.) are filtered out and omitted when a set threshold value is exceeded. The polarimetry result is provided to the ELSA CS.

compare with Section 6.4.3) can be determined, or the degree of electron polarization \mathcal{P}_e itself, if \mathcal{D} is known. In the following section attention is drawn to the data quality enhancement by fitting a peak function to the profile data.

6.4.1 Determining the Profile's Center of Gravity

According to the simulation results of Fig. 5.14(b) the maximum expected profile shift (analyzing power) is $\mathcal{D} \approx 73 \mu\text{m}$, affecting 1.9‰ of the $768 \times 50 \mu\text{m} = 38.4 \text{ mm}$ wide active detector area. To increase the robustness of the *shift in the means* measurement by reducing the impact of statistical and systematic channel noise, the measured profile may be fit to a proper and smooth peak function. The simulated CBS profiles in Section 5.5 show that the CBS distribution possesses a moderate skewness from -0.02 to -0.26 (from 1.2 to 3.2 GeV) due to the 3 mrad laser beam incident angle. Hence, the fit function should account for this, especially for profiles from higher beam energies. Candidates are e.g. piecewise polynomials (splines) and the *Pearson type IV* distribution function [Pea01]. The benefits and disadvantages of the methods for determining the center of gravity \bar{z} are discussed in the following paragraphs.

1. Statistical Following Eq. (5.28) for a given distribution of $N = \sum_i^m n_i$ counting events from m bins with individual counter values n_i , one obtains the center of gravity from

$$\bar{z} = \frac{\sum_i^m z_i \cdot n_i}{N}, \quad (6.16)$$

where z_i is the position of bin i . Advantageous of statistical evaluation is that the measurement data is not modified, except for the scaling procedure described in Section 6.3.2 and Appendix F. However, the statistical method is prone to noise and fluctuating peaks resulting from occasional energy deposition from stray radiation.

2. Spline A piecewise polynomial smoothens the obtained profile and suppresses the influence of outliers in the distribution. However, it follows a numerical approach with various setting options for robustness, such as node distance and polynomial order. This method is prone to structural errors such as deviant scaling factors for a group of neighboring channels. A spline¹⁴ is parameterized by

$$\mathcal{S}(x) = \sum_{j=0}^{m-2} \sum_{i=0}^d c_{i,j} (x - \tau_j)_+^i, \quad \text{with} \quad (x)_+^i := \begin{cases} 0 & \text{for } x < 0 \\ x^i & \text{for } x \geq 0 \end{cases}. \quad (6.17)$$

The center of gravity is determined through integration of the parameterized function:

$$\bar{z} = \frac{\int_a^b \mathcal{S}(x) \cdot x \, dx}{\int_a^b \mathcal{S}(x) \, dx}, \quad (6.18)$$

where a and b are the boundaries of the data abscissa. For the contemporary detector profile analysis typically $m = 20$ intervals $[\tau_i, \tau_{i+1}]$ and a maximum order of $d = 3$ are used to meet an adequate robustness and to prevent overfitting non-smooth data intervals. A disadvantage of a spline fit is the arbitrariness of sample point breaks and polynomial coefficients with lack of physical meaning.

3. Pearson type IV/VII The Pearson distribution family subsumes many of commonly used peak functions such as the Lorentz distribution. The non-normalized form of the Pearson type IV distribution is parameterized as

$$\mathcal{P}_{IV}(x) = h \cdot \left[1 + \left(\frac{x - x_0}{s} \right)^2 \right]^{-l} \cdot \exp \left[-\nu \cdot \arctan \left(\frac{x - x_0}{s} \right) \right], \quad (6.19)$$

with profile height h , center position x_0 , scaling parameter s and shape parameters $l > 1/2$ and ν , where ν controls the skewness. For $\nu = 0$ the distribution holds no skewness and it is then called Pearson type VII. The center of gravity is obtained by indefinite integration

$$\bar{z} = \frac{\int_{-\infty}^{\infty} \mathcal{P}(x) \cdot x \, dx}{\int_{-\infty}^{\infty} \mathcal{P}(x) \, dx}, \quad (6.20)$$

where the improper integrals can be calculated numerically by adaptive integration, e.g. through the efficient Gauss-Kronrod algorithm¹⁴ [Sha08].

¹⁴Algorithm implemented in GNU Octave[Eat+17].

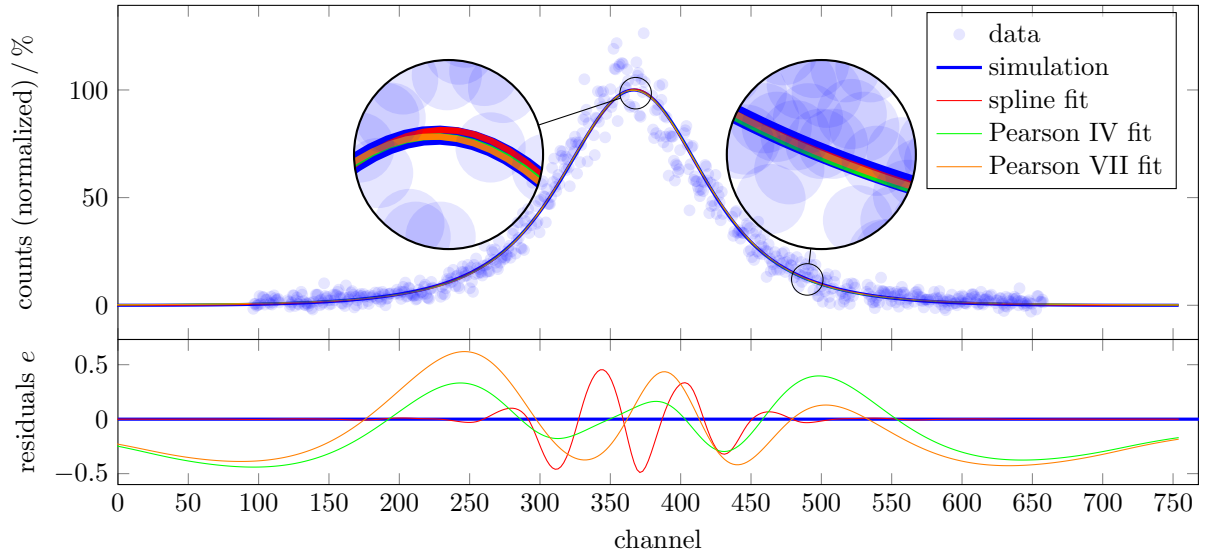


Figure 6.23: Comparison of peak fit functions to a simulated CBS profile with subtracted background at 1.32 GeV and a corresponding normalized measurement data set. The experimental data set is narrowed by a factor 0.74 in order to fit the simulation.

In Fig. 6.23 the above peak functions $y(x) \in \{\mathcal{S}, \mathcal{P}_{IV}, \mathcal{P}_{VII}\}$ are compared to a corresponding COMPTONSIM profile simulation $f(x)$ and to a 1.32 GeV measurement data set, where the peak values of the parameterized functions were normalized to a value of 100%. It is visible in Fig. 6.23 that the corresponding residuals

$$e(x) = y(x) - f(x) \quad (6.21)$$

of the peak model functions \mathcal{P}_{IV} and \mathcal{P}_{VII} are sufficiently small ($\lesssim 0.5\%$) and in the order of the more flexible spline function \mathcal{S} , confirming the appropriate fit quality of the Pearson type functions. Table 6.2 compares the obtained centers of gravity \bar{z} , the goodness-of-fit indicator R^2 [DS81] and the sum of residuals $\sum |e_i|$. It shows that the spline fit performs best on a simulated profile, but experience shows that its quality may decrease drastically if non-smooth experimental data is applied. In that case a more robust fit result is expected from a Pearson type function fit due to the reduced number of deployed variables (degrees of freedom). Following this argument, Pearson type VII contains a less complex parameterization with one less degree of freedom than type IV. It is shown in the following sections that

function	1.2 GeV			3.2 GeV		
	\bar{z}/ch	R^2	$\sum e_i $	\bar{z}/ch	R^2	$\sum e_i $
statistical	365.0	1	0	352.8	1	0
spline	365.0	1.000	18.55	352.8	0.99972	44.9
Pearson type IV	367.1	0.9999	98.7	351.2	0.99982	113.2
Pearson type VII	365.3	0.99988	110.3	357.2	0.99776	358.5

Table 6.2: Quality comparison of different peak function data fits for normalized profile simulations at the lower and upper electron energy range at ELSA, including the resulting center of gravity \bar{z} , goodness of fit R^2 and sum of residuals $\sum |e_i|$. The skewness at higher beam energies shows a significant impact on the residuals from the Pearson type VII fit.

the greater robustness of type VII makes it the primary choice as CBS profile analysis model.

6.4.2 Exemplary Measurements with Source-Polarized Electrons

A *shift in the means* measurement of CBS profiles obtained with 1.32 GeV source-polarized electrons with polarization degree of approximately $\mathcal{P}_e \approx 86\% \times 0.85 = 73\%$ (compare with source polarization [Hei14, Section 1.1] and booster synchrotron polarization transfer efficiency in Section 7.2.1) is given in Fig. 6.24. Therein, the *shift in the means* Δz for the above described profile analysis methods, the center positions \bar{z} of the radiation background and laser CBS profiles (Pearson VII fit), the transverse electron and laser positions and their corresponding intensities are shown. The data is obtained by a continuous summation of profiles from electrons with anti-parallel polarization to the bending field ($\Delta z_{e\downarrow}$) and from those with parallel polarization ($\Delta z_{e\uparrow}$)¹⁵. The absolute mean is then determined by

$$\Delta z_{e\downarrow\uparrow} = \frac{|\Delta z_{e\downarrow}| + |\Delta z_{e\uparrow}|}{2}. \quad (6.22)$$

The numerical results for Δz are summarized in Table 6.3. The performance of the different profile analysis methods is visible in the top axis of Fig. 6.24: For the Pearson type VII profile fit the final value of Δz is obtained within the first minute of measurement time, remaining within the decreasing error interval for the rest of the data accumulation time. Other methods show abrupt changes (e.g. at $t \approx 1$ min) and deviations beyond the corresponding measurement errors. This behavior is commonly observed in the majority of measurements.

The obtained profile centers \bar{z} (Pearson type VII fit) are shown in the second axis for all combinations of electron and photon polarization states, as well as for the radiation background. In this case, the radiation background and photon profile centers are shifted by approximately 400 μm (8 channels). However, no indication was observed that a shift of this magnitude impacts the measurement of Δz .

To ensure qualitative data recording over multiple accelerator cycles at repetitive beam conditions, the transverse electron beam position is monitored through a button BPM mounted close to the IP at quadrupole magnet QD25 (compare with Fig. 6.11). The transverse laser beam position and its intensity for both polarization helicities is monitored through a four quadrant PSD (see Fig. 6.5). If deviations beyond a given threshold occur measurements at specific time intervals are inhibited, which is indicated by gray background markings (including the storage ring injection). For example, a threshold exceedance is visible at $t = 3.5$ min, where data from a failed injection is inhibited. One notices that the vertical laser beam position shows an inherent asymmetry for circular-left and circular-right polarized photons ($\bar{z}_{\cup} - \bar{z}_{\cap} \approx 117 \mu\text{m} \approx 0.05$ a.u.), which is likely to be artificially caused by the position monitor evaluation (compare with Section 6.2.2). This behavior is not observed in the majority of measurements of Δz .

model	$\Delta z_{e\uparrow} / \mu\text{m}$	$\Delta z_{e\downarrow} / \mu\text{m}$	$\Delta z_{e\downarrow\uparrow} / \mu\text{m}$
statistical	57.87 ± 3.18	-39.47 ± 3.18	48.67 ± 2.25
spline	57.71 ± 3.16	-36.84 ± 3.16	47.27 ± 2.23
Pearson IV	67.24 ± 3.14	-41.92 ± 3.14	54.58 ± 2.22
Pearson VII	49.82 ± 3.14	-44.28 ± 3.13	47.05 ± 2.22

Table 6.3: Results for different profile fit models for the shift in the mean Δz measurement in Fig. 6.24 with antiparallel ($e \downarrow$), parallel ($e \uparrow$), and combined ($e \downarrow\uparrow$) electron polarizations.

¹⁵The polarization direction usually alternates for every storage ring filling.

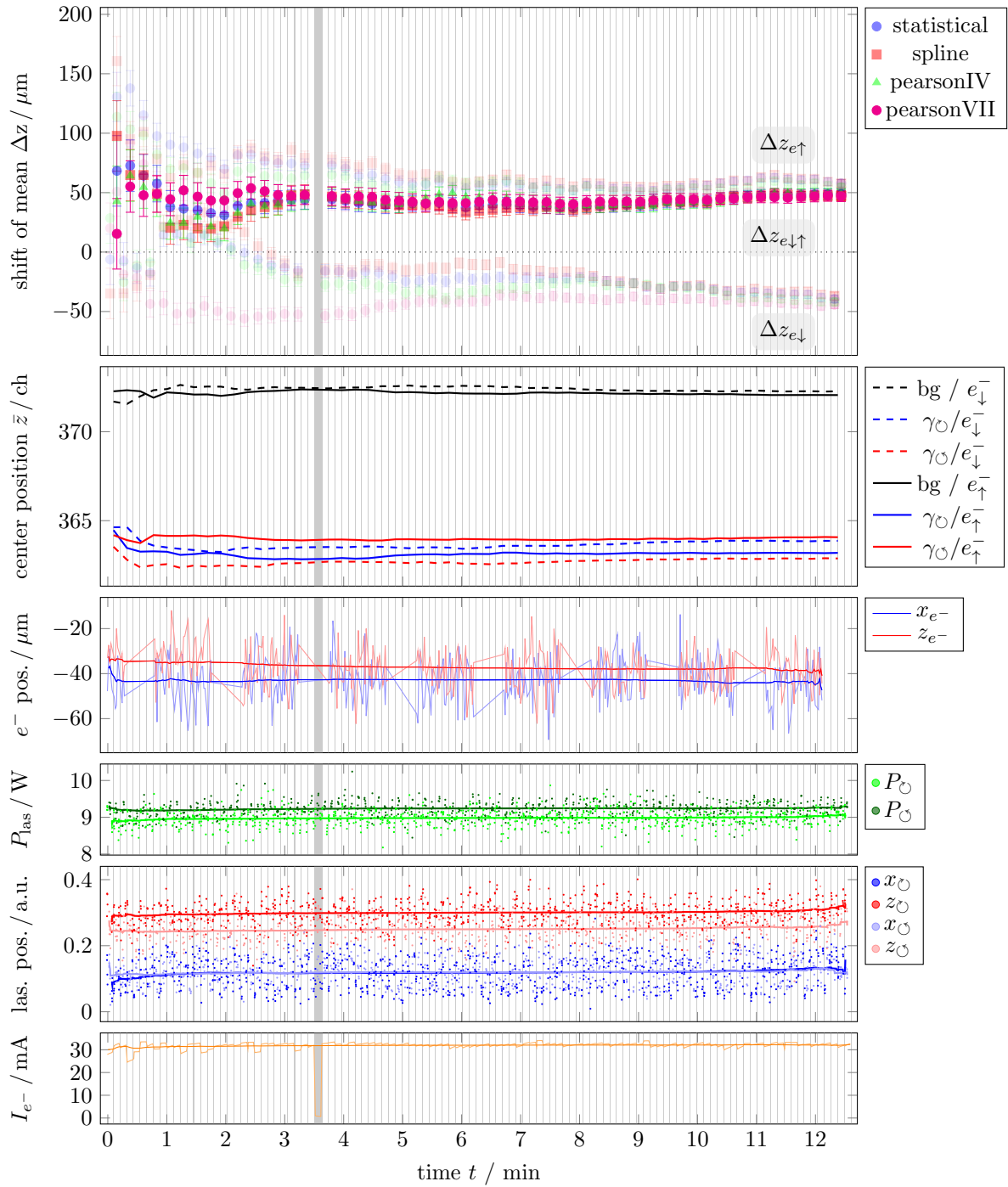


Figure 6.24: Measurement of the *shift in the means* Δz of a polarized 1.32 GeV electron beam in booster mode for different profile analysis methods. The gray background indicates inhibited time intervals, which occur at storage ring injection or when a monitoring value exceeds a given threshold. Monitored are the position of laser and radiation background profiles, as well as the position of the electron and laser beam and their intensities.

6.4.3 Analyzing Power and Detector Calibration Through Self-Polarization

As described in Section 2.3.2 the inequality of SR emission probability occurring from radiation with spin-flip and no spin-flip leads to an exponential build-up of electron beam polarization over time (Sokolov-Ternov effect) according to

$$\mathcal{P}(t) = \mathcal{P}_\infty (1 - e^{-t/\tau}) \quad \equiv \quad \Delta z(t) = \Delta z_\infty (1 - e^{-t/\tau}) , \quad (2.48 \text{ revisited})$$

which is observable through an equivalently increasing $\Delta z(t)$. Therewith, the Compton polarimeter's analyzing power \mathcal{D} (compare with Eq. (5.32)) can be determined in storage mode via

$$\mathcal{D} = \frac{\Delta z_\infty}{\mathcal{P}_\infty \cdot \mathcal{P}_\gamma} , \quad (5.32 \text{ revisited})$$

where the asymptotic electron polarization \mathcal{P}_∞ is obtained from calculation (Eq. (2.47)) or simulation (see Sections 2.3.2 and 7.2.4). The circular photon polarization was determined in Eq. (6.13) and amounts $\mathcal{P}_\gamma = (98.0 \pm 0.1) \%$ for the corresponding measurements. Δz_∞ can be obtained from a fit of Eq. (2.48) to measured *shift in the means* data.

An exemplary measurement of the observed beam polarization build-up of a 2.73 GeV electron beam is shown in Fig. 6.25, where the data analysis functionality was verified by inhibiting the $\lambda/4$ retarder waveplate rotation in order to observe a zeroed response for two specific time intervals (gray background). The obtained parameters for the polarization build-up with time constant $\tau = 33.8$ min are shown in Table 6.4 for the corresponding profile fit models of Section 6.4.1. Therein, the results for two different precision values for the center of gravity uncertainty are compared ($\Delta \bar{z} \leq 1.7 \mu\text{m}$ and $\Delta \bar{z} \leq 4 \mu\text{m}$ according to Eq. (5.29)). The differing precision values compromise single data point precision and the available number of data points for the function fit. The most accurate result is obtained from the Pearson VII fit model, yielding

$$|\Delta z_{\infty, \text{meas}}| = (55.38 \pm 5.67) \mu\text{m} . \quad (6.23)$$

In comparison, the COMPTONSIM simulation results of Fig. 5.14(b) suggest a *shift in the means* of $\Delta z_{\infty, \text{sim}} = 72.9 \mu\text{m}$ for a 2.73 GeV electron beam, assuming an electron and photon polarization of 100 %. For the photon polarization of $\mathcal{P}_\gamma = (98.0 \pm 0.1) \%$ achieved in the experiment and the expected asymptotic electron polarization $\mathcal{P}_\infty = 92.38 \%$ the simulated *shift in the means* computes to

$$\Delta z_{\infty, \text{sim}} = (66.0 \pm 0.1) \mu\text{m} , \quad (6.24)$$

model	$\Delta \bar{z} \leq 4 \mu\text{m}$ precision		$\Delta \bar{z} \leq 1.7 \mu\text{m}$ precision	
	$\Delta z_\infty / \mu\text{m}$	R^2	$\Delta z_\infty / \mu\text{m}$	R^2
statistical	-56.77 ± 6.08	0.67	-56.70 ± 17.49	0.89
spline	-52.56 ± 5.77	0.61	-52.52 ± 16.16	0.90
Pearson IV	-83.64 ± 9.64	0.43	-66.86 ± 20.44	0.92
Pearson VII	-55.38 ± 5.67	0.82	-55.45 ± 16.84	0.96

Table 6.4: Parameters for fitting Eq. (2.48) to the data shown in Fig. 6.25. Increased fit precision is obtained by summing multiple profiles to obtain a larger number of count events N at the expense of the number of data nodes for the exponential fit, resulting in increased fit parameter errors. For lower profile center accuracy the number of data nodes is large, which decreases the uncertainties of the fit parameters.

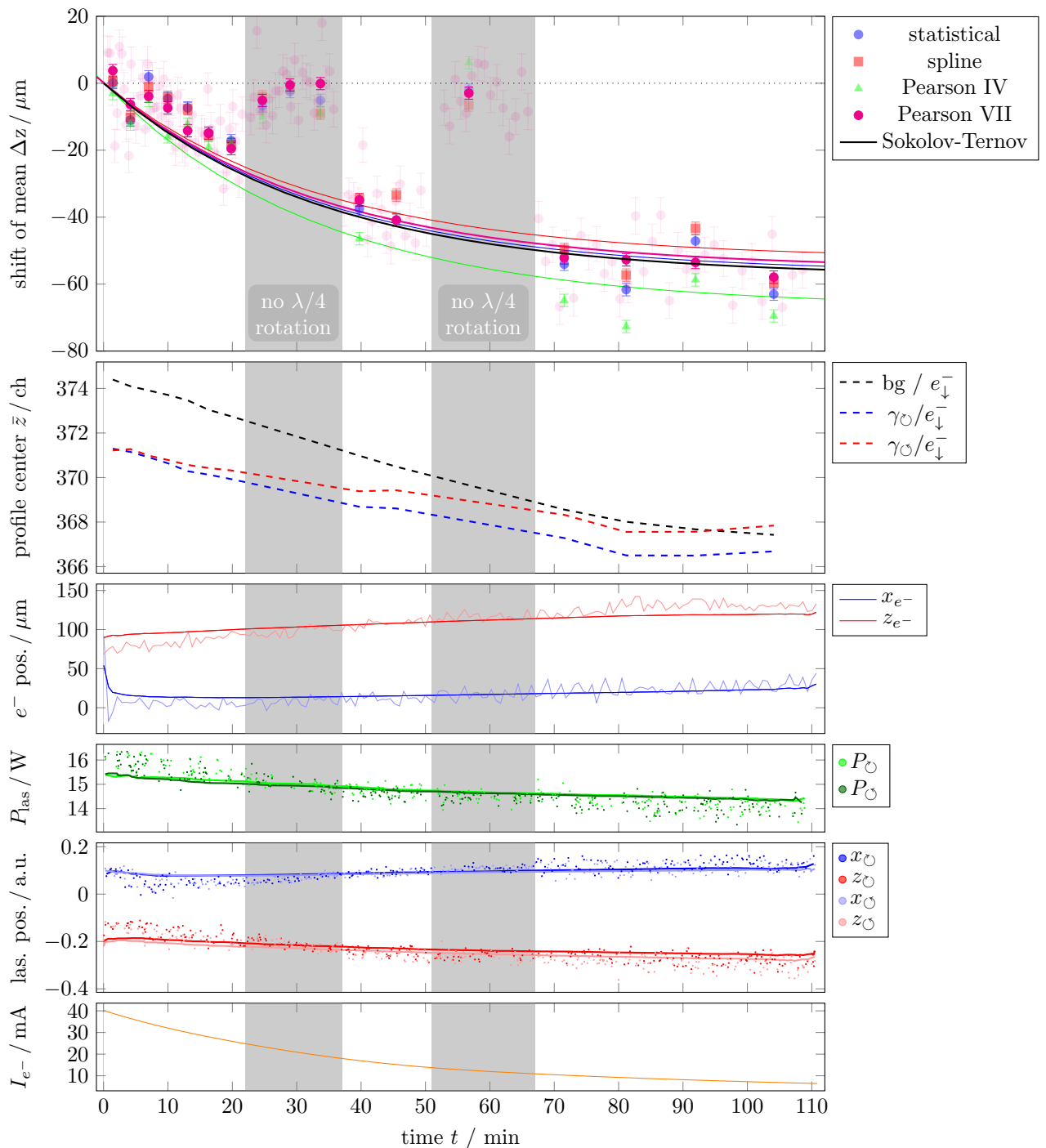


Figure 6.25: Exponential polarization build-up of a stored 2.73 GeV electron beam at ELSA, analyzed with different profile fit models. Measurement profiles were summed until a precision of at least $4\ \mu\text{m}$ (opaque) and $1.7\ \mu\text{m}$ (solid) were obtained. The trigger for the $\lambda/4$ retarder plate rotation was removed twice (gray background) to verify the profile analysis functionality. A drift of background and laser profiles, laser power and electron beam position is observed, which is correlated to a verified temperature change within the shielding tunnel ($\Delta T = 0.5$ to 2°C , depending on the measurement position). The shift of the mean Δz seems unaffected by the temperature drift.

deviating by 19 % from the measurement result and exceeding its error margin. As shown in Table 6.4 the magnitude of the error has a strong dependency on the chosen analysis parameters, such as the profile center precision. However, similar measurements show that the value obtained in Eq. (6.23) has a sufficient representation character. Analysis results in analogy to Table 6.4 including depolarizing effects, which in this case reduce the asymptotic polarization degree to 78.5 % (compare with Sections 2.1.3 and 7.2.4), show a minorly reduced asymptotic *shift in the means* of $(52.4 \pm 5.4) \mu\text{m}$. The simulations of depolarizing effects are, however, complex and hold unknown uncertainties. Therefore, their impact on the determination of Δz_∞ is omitted in the following calculations.

With the above figures the analyzing power of the Compton polarimeter computes to

$$\mathcal{D} = (61.2 \pm 8.9) \mu\text{m}/100 \% , \quad (6.25)$$

showing a deviation of 16 % from the COMPTONSIM simulation results. However, due to the reduced photon polarization $\mathcal{P}_\gamma < 1$ the polarimeter operates with an effective analyzing power of

$$\mathcal{D}_{\text{eff}} = \mathcal{D} \cdot \mathcal{P}_\gamma = (60.0 \pm 8.8) \mu\text{m}/100 \% . \quad (6.26)$$

The effective analyzing power can now be used as polarimeter calibration factor in order to obtain the electron polarization through a measurement of the *shift in the means*:

$$\mathcal{P}_e = \frac{\Delta z}{\mathcal{D}_{\text{eff}}} . \quad (6.27)$$

For example, the measurement with source-polarized electrons shown in Fig. 6.24 has a *shift in the means* of $\Delta z = (47.2 \pm 4.7) \mu\text{m}$, which yields a polarization degree of $\mathcal{P}_e = (78.6 \pm 14.0) \%$ according to Eq. (6.26). The result is in accordance to the expected value which lies in the order of 73 to 86 % (compare with Section 6.4.2), depending on beam polarization loss during the transfer from the electron source to the storage ring.

The obtained value for the analyzing power \mathcal{D} is acceptable, but it is clear that its given measurement uncertainty necessitates a more precise measurand Δz , including the verification over a span of electron beam energies allowing a comparison to Fig. 5.14(b). Improvement can be obtained through the following actions:

- The asymptotic *shift in the means* Δz_∞ is to be measured more repetitively with more accurate exponential polarization build-up data sets (e.g. through better beam drift stabilization) to reduce statistical errors and to identify and quantify systematic errors.
- The expected asymptotic electron polarization degree \mathcal{P}_∞ is to be profoundly determined on the basis of depolarizing effects regarding the specific electron beam energy under consideration of the storage ring's tune (compare with Sections 4.1.2 and 7.2.4). As this measure does not directly improve the analyzing power's accuracy, its precise value may assist in identifying disadvantageous measurement regions (beam energies and tunes) where Δz_∞ changes thoroughly in the respective measurement vicinity.
- The uncertainty of the shift-in-the-means $\Delta(\Delta z)$ is to be minimized by increasing the scattering rate (see Section 5.3.1) through e.g. an increase of laser power in the LIR.

6.4.4 Photon Scattering Rates

As explicated in Section 5.3.1, the γ -photon backscattering rate dN/dt is determined by the Compton scattering cross section σ_b and the luminosity \mathcal{L} :

$$\frac{dN}{dt} = \sigma_c \mathcal{L}, \quad (5.33 \text{ revisited})$$

where \mathcal{L} is directly dependent on the laser power and electron intensity (compare with Eqs. (5.34) and (5.35)). For the measurement in Fig. 6.24 one obtains a scattering rate of (110.8 ± 21.2) Hz/(W mA), normalized to $P_{\text{las}} = 1$ W of laser power and $I_{e^-} = 1$ mA of electron current. Scattering rates for exemplary measurements at varying electron beam energies are shown in Fig. 6.26, where a tendency of increasing rates towards higher electron beam energies is observable. However, the varying magnitudes per energy bin indicate that the scattering rate is significantly depending on the beamline setting. For example, photon or electron beam drifts may reduce the actual or measured scattering rate. The highest measured count rate value is approximately 350 Hz/(W mA), which is below the expected scattering rate of 1.89 kHz/(W mA). In addition, the expected background radiation rate is approximately 8 kHz/mA (compare with Section 5.3.2) and is significantly undermatched by the measured count rate of about 300 Hz/mA at 3.2 GeV. One may conclude that the photon-to-detector count conversion described in Section 5.4 has an efficiency of approximately 10%.

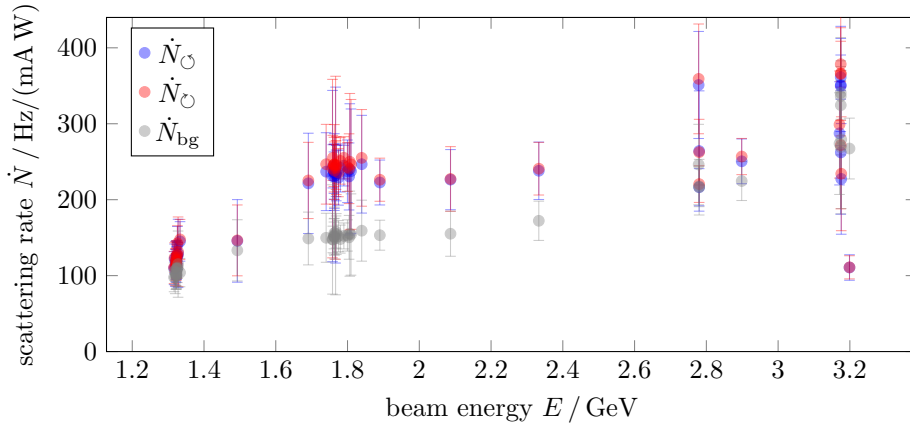


Figure 6.26: Scattering rates $\dot{N}_{\cup, \cup}$ from the background-subtracted laser signals and from the bremsstrahlung background \dot{N}_{bg} for varying electron beam energies normalized to 1 W laser power and 1 mA of stored electron current. The varying magnitudes per energy bin indicate a change of the beamline setting (e.g. photon beam position), which significantly influences the scattering rate.

6.4.5 Polarization Measurement Accuracy

The accuracy of the measured electron polarization degree \mathcal{P}_e (see Eq. (6.27)) is determined by the statistical uncertainty of $\Delta z = \bar{z}_L - \bar{z}_R$ and by systematic errors, which may be included in the uncertainty of the analyzing power \mathcal{D}_{eff} (compare with Section 6.4.3):

$$\Delta \mathcal{P}_e = \sqrt{\underbrace{\left(\frac{1}{\mathcal{D}_{\text{eff}}} \Delta(\Delta z)\right)^2}_{\text{statistical}} + \underbrace{\left(\frac{\Delta z}{\mathcal{D}_{\text{eff}}^2} \Delta \mathcal{D}_{\text{eff}}\right)^2}_{\text{systematic}}}. \quad (6.28)$$

The statistical error decreases for increasing event counts N and is individually determined for every measurement:

$$\Delta\bar{z} = \sqrt{\frac{\sigma^2}{N} + \Delta z_b^2 \sum_i \left(\frac{n_i}{N}\right)^2}. \quad (5.29 \text{ revisited})$$

Figure 6.27 shows the corresponding reduction of $\Delta\mathcal{P}_e$ with time for exemplary data sets at different beam energies (omitting systematic errors). The achieved accuracy was 2 % within 5 minutes of measuring time, and 1.4 % within 15 minutes for a 2.9 GeV electron beam at $I_{e^-} \approx 30$ mA ($\dot{N} \approx 250$ Hz, see Fig. 6.26). A precise quantification of the systematic error necessitates numerous self-polarization data sets, which could not be obtained in the required quality within the available polarimeter testing period. However, the number of evaluable self-polarization measurements and the results of e.g. Table 6.3 ($\Delta_{e,\uparrow} - \Delta_{z_{e,\downarrow}} = 5.54 \mu\text{m}$) suggest that the quantity obtained in Eq. (6.26) represents a sufficient approximation for the expected systematic error:

$$\Delta\mathcal{D}_{\text{eff,sys}} = 8.8 \mu\text{m}/100\% . \quad (6.29)$$

This figure is dependent on the measured polarization degree and may amount up to 14.7 % for a hypothetical value of $\mathcal{P}_e = 100$ %. It is included in all measurements throughout the next chapter.

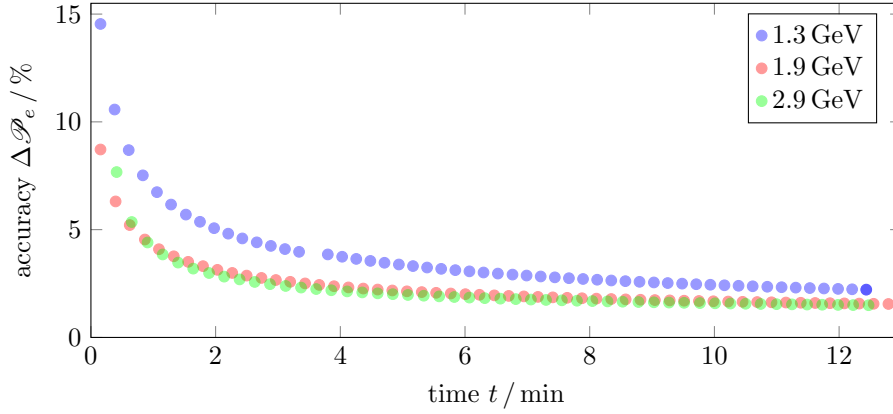


Figure 6.27: Polarization measurement accuracy under regular beam conditions for exemplary measurements at different beam energies, omitting systematic errors.

Observation of Spin Dynamics via Compton Scattering

The Compton polarimeter allows the measurement of spin dynamics occurring in the [ELSA](#) storage ring. [Section 2.1](#) explicates the fundamentals of spin precession in a circular accelerator and illustrates depolarizing effects, which are exemplified in the following chapter by Compton polarimeter measurements.

7.1 Effects due to Larmor Precession

A magnetic field parallel to the particle momentum induces a rotation of the spin axis according to

$$\vec{\Omega}_L = (1 + a)\vec{B}_{\parallel}. \quad (2.13 \text{ revisited})$$

To exploit this effect multiple solenoid magnets are installed in the transfer beamline between polarizing source and [linac](#) (compare with [Fig. 1.2](#)). Those manipulate the direction of the transverse spin axis at booster and storage ring injection, ideally aligning it parallel or antiparallel to the vertical bending fields of the synchrotrons. Total or partial horizontal spin axis alignment will lead to losses in polarization, as explicated in [Section 2.1.3](#). [Figure 7.1](#) shows the polarization measurement in the storage ring at 1.75 GeV as function of the magnetic strength of a solenoid doublet, expressed in spin rotation degrees. Therein, the shift in the means Δz is obtained from a Pearson type VII profile analysis (compare with [Section 6.4.1](#)) and the calibrated polarization degree \mathcal{P}_e includes the Compton polarimeter's analyzing power \mathcal{D} of [Eq. \(6.26\)](#). The fit to a sinus function yields a maximum obtainable electron polarization degree of $\mathcal{P}_{e,\max} = (96.8 \pm 14.2) \%$, where the error is dominated by the estimated systematic error of the analyzing power (compare with [Section 6.4.3](#)). However, this value largely exceeds the maximal value of 86 % [[Hei14](#), Section 1.1], which is expected to further decrease due to depolarizing effects occurring during the energy increase in the synchrotrons.

7.2 Depolarizing Resonances

Depolarizing resonances occur in periodic structure lattices, where horizontal or longitudinal perturbing magnetic fields repetitively affect the tilt of the spin precession vector (compare with [Fig. 2.2](#)). While longitudinal magnetic fields are not eminent in the [ELSA](#) storage ring, horizontal fields play a major

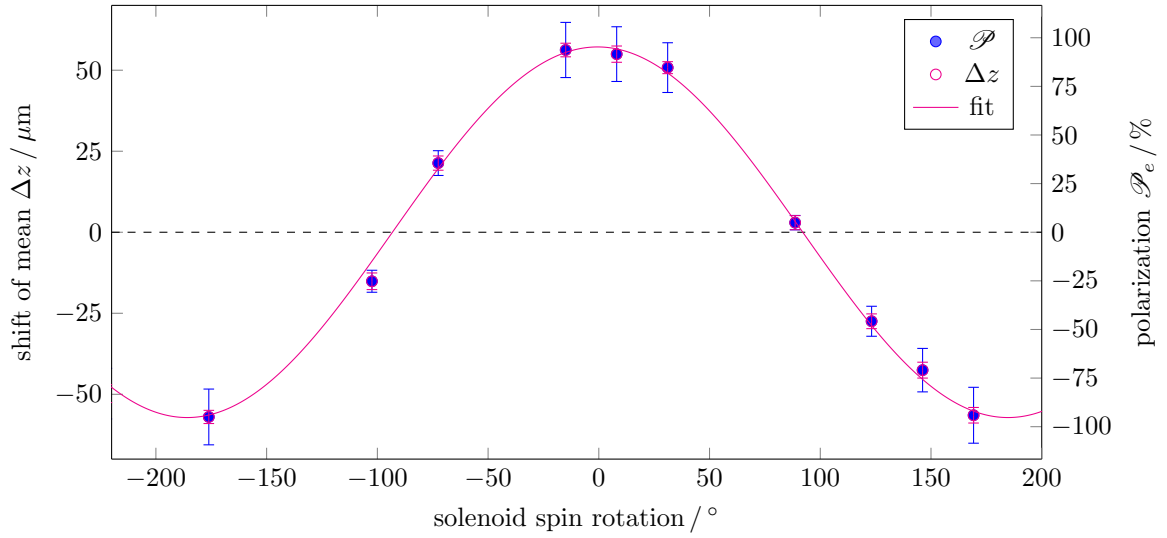


Figure 7.1: Shift in the mean Δz (Pearson type VII) and calibrated beam polarization degree \mathcal{P} for a 1.75 GeV electron beam in dependence of the solenoid spin rotation angle. The solenoid magnet is installed between polarizing source and [linac](#).

role through quadrupole magnets, which act upon particles with vertical displacement – as visualized in [Fig. 7.2](#) – and through inevitable misalignments (tilts) of the bending magnets.

To minimize the magnitude of affecting horizontal fields it is desirable to place the stored beam precisely in the center of each quadrupole magnet. However, to achieve this, additional corrector magnets (dipoles) are installed throughout the lattice, whose horizontal magnetic fields act in turn upon the spin precession angle. In addition, the macroscopic beam is formed by individual particles (compare with [Section 4.1](#)) which propagate always with vertical or angular displacement throughout the lattice. The amplitude of their individual trajectories are determined by the betatron tune (see [Section 4.1.2](#)) of the storage ring's ion optical setting. As each particle may encounter a perturbation on its spin vector rotation, the overall polarization degree will be influenced when the frequency of the perturbing fields match the spin rotation frequency. Overall, two resonance types dominate the spin dynamics at the [ELSA](#) storage ring:

Integer resonances occur when the spin tune Q_{sp} (see [Eq. \(2.16\)](#)) satisfies the condition

$$\gamma a = n, \quad n \in \mathbb{N}. \quad (7.1)$$

The driving force is a periodic horizontal magnetic field distribution which acts upon the particles due to coherent orbit displacements, magnet misalignments and corresponding field errors. Due to the anomalous magnetic dipole moment of the electron a (see [Section 2.1.2](#)) integer resonances occur at every $\Delta E = 440.65$ MeV.

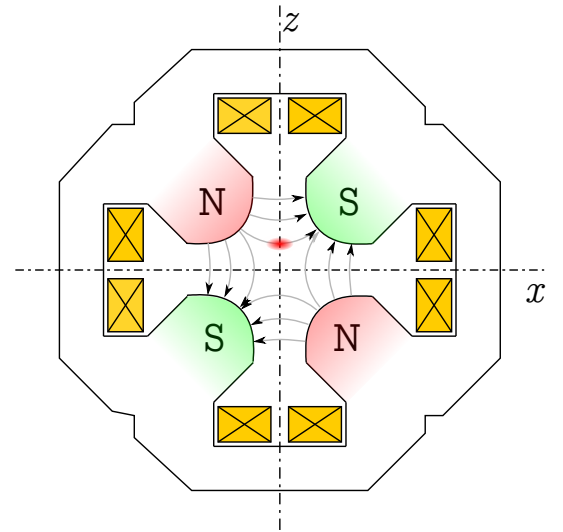


Figure 7.2: A particle beam propagating through a quadrupole magnet with vertical displacement encounters a horizontal magnetic field.

Intrinsic resonances are driven by the betatron oscillation amplitudes of the individual particles. Hence, intrinsic resonances occur even for a perfectly aligned lattice when the following condition is satisfied:

$$\gamma a = m_p P + m_x Q_x + m_z Q_z + m_s Q_s, \quad m_i \in \mathbb{Z}, \quad (7.2)$$

where P is the superperiodicity¹ of the lattice and Q_i are the betatron and synchrotron tunes, respectively. At **ELSA**, the summands of Eq. (7.2) have different magnitudes of impact:

- The **superperiodicity** to first order magnetic fields (compare with Eq. (4.3)) amounts $P = 2$ (see Fig. 4.2). The impact of integer resonances is expected to supersede the impact of superperiodicity.
- **Horizontal** orbit displacements couple into the vertical plane (compare with coupling constant κ in Section 4.3). As the effect is suppressed by $\kappa \lesssim 10\%$, resonances with $m_x \neq 0$ are expected to be of minor significance.
- **Vertical** displacements induce the impact of horizontal quadrupole fields, whose strength increases with distance from the design orbit. Resonances with $m_z \neq 0$ play a major role for depolarizing effects.
- **Synchrotron** oscillations (compare with Section 4.1.4) induce an intrinsic energy deviation of the particle beam. Hence, every resonance (including imperfection resonances) possesses *synchrotron sidebands* ($m_s \neq 0$) at a distance of $\Delta E = \pm 21.6$ MeV for a typical synchrotron tune of $Q = 0.049$, and multiples of it.

The impact of all resonances generally decreases with increasing order

$$\mathcal{O} = |m_x| + |m_z| + |m_s|. \quad (7.3)$$

However, not every low-order resonance is necessarily strong, as shown in the following sections.

7.2.1 Depolarization in the Booster Synchrotron

Figure 7.3 shows the dependence of beam polarization and beam energy at the **ELSA** booster synchrotron, as obtained by Brefeld [Bre+85] at the time when this synchrotron provided the final acceleration stage for nuclear physics experiments. The characteristics regarding beam polarization are expected to be prevailing for its service as booster synchrotron for the **ELSA** storage ring². Significant polarization loss is observed for energies above the imperfection resonance $\gamma a = 3$ (1.32 GeV) while the imperfection resonance at $\gamma a = 2$ (0.88 GeV) has comparably low impact on the overall polarization. For this reason, extraction into the storage ring takes place at 1.2 GeV. The ratio of beam polarization at booster extraction and source polarization is estimated to be approximately 85 %.

7.2.2 Depolarization in the ELSA Storage Ring

Compton polarimeter measurements for different beam energies in the **ELSA** storage ring are shown in Fig. 7.4. As expected, the crossing of multiple depolarizing resonances during the energy increase from 1.2 to 3.2 GeV causes a complete loss of the initial polarization. It is therefore necessary to implement polarization-preserving countermeasures to obtain reasonable polarization degrees at storage ring energies above 1.7 GeV (see e.g. [Ste99; Hof01; Sch17] for details).

¹Number of repetitive identical lattice structures in a storage ring.

²Mainly the **RF** power was reduced by removing one of two accelerating cavities.

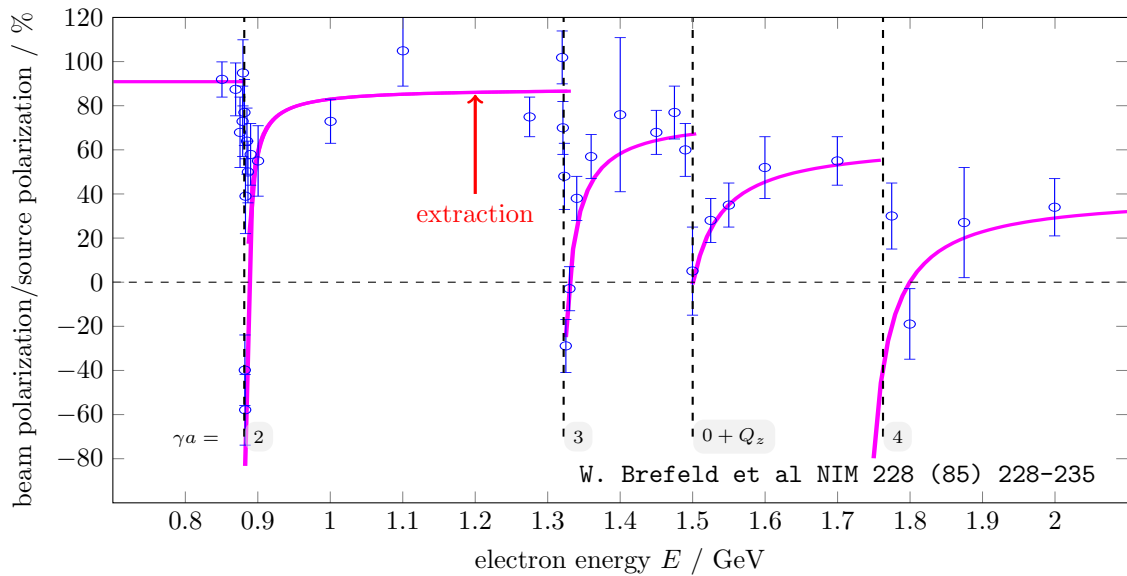


Figure 7.3: Beam polarization of the ELSA booster synchrotron for different electron energies [Bre+85]. Depolarizing imperfection and intrinsic resonances due to the periodic structure of the magnetic lattice cause loss of beam polarization. Extraction from the booster synchrotron takes place before major losses occur.

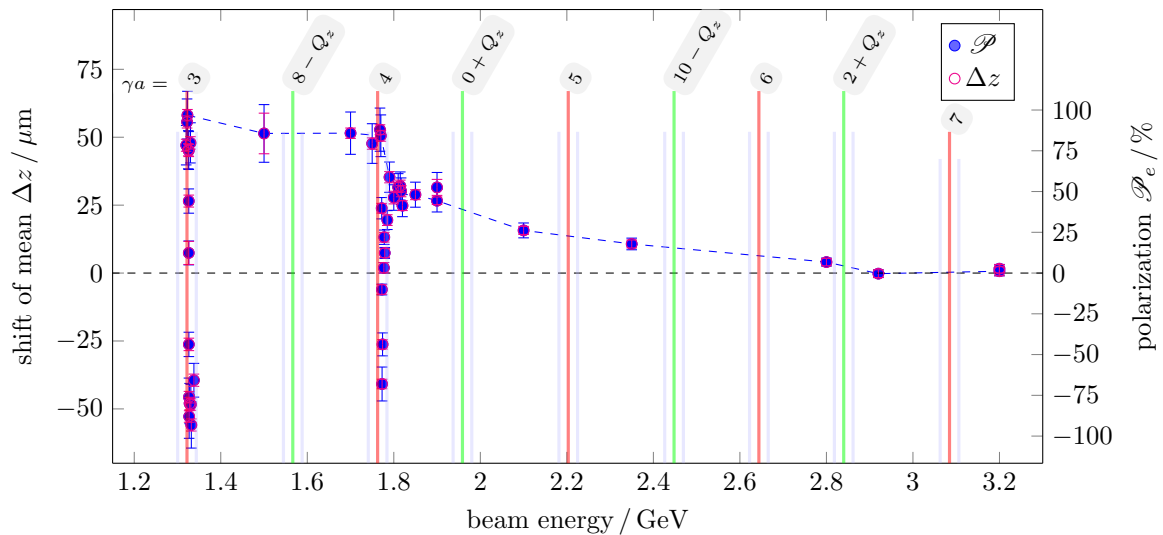


Figure 7.4: Beam polarization at different stored beam energies measured with the ELSA Compton polarimeter. The polarization is completely lost above energies of 2.9 GeV when no countermeasures for polarization preservation are applied. Prominent depolarizing resonances are indicated. A significant reduction of polarization is observed at $\gamma_a = 4$.

7.2.3 Resonance Strength and Spin Flip

The strength of a resonance can be interpreted as the *Fourier* coefficient of a reoccurring field disturbance $Q_r = \gamma a$ matching the movement of the spin rotation precession angle θ [CR80]:

$$\epsilon_r = \frac{1}{2\pi} \oint_0^{2\pi} \frac{\zeta(s)}{R(s)} e^{iQ_r\theta(s)} ds, \quad (7.4)$$

where the complex function $\zeta(s)$ describes the transverse (horizontal) and longitudinal magnetic field disturbances b_{\perp} and b_{\parallel} [Sch17, Sec 3.4.2]:

$$\zeta(s) = R(s) \cdot \left[(1 + \gamma a)b_{\perp}(s) - i(1 + a)b_{\parallel}(s) \right]. \quad (7.5)$$

The resonance strength ϵ_r is obtainable through spin-tracking simulation or by measurement of initial and final electron polarization through the *Froissart-Stora* relation [FS60]:

$$\frac{P_f}{P_i} = 2 \cdot e^{-\frac{\pi|\epsilon_r|^2}{2|\alpha|}} - 1, \quad \text{with} \quad \alpha = \frac{\dot{\gamma}a}{\omega_0}, \quad (7.6)$$

where α represents the resonance crossing velocity and ω_0 is the particle revolution frequency. Equation (7.6) holds for the crossing of single resonances at constant velocity and is suited for the description of imperfection resonances. Figure 7.5 visualizes Eq. (7.6) and explains the spin flip occurrence $P_f/P_i < 0$ in Figs. 7.3 and 7.4 when a resonance is crossed which is either strong (large ϵ_r), or the crossing velocity α is slow, or both.

Experimental verification of Eq. (7.6) regarding the imperfection resonances $\gamma a = 3$ to 5 at ELSA, as well as Eq. (7.6)'s modification for intrinsic resonances and the impact of stochastic energy oscillations due to the emission of SR can be found in [Ste99; Hof01; Sch17].

The resonance strengths ϵ can be determined by fitting Eq. (7.6) to a corresponding data set with varying resonance crossing speed, as exemplarily demonstrated by J. Schmidt [Sch17, Sec. 7.4], where

$$\epsilon_{\gamma a=3} = (5 \pm 3) \times 10^{-5} \quad \text{and} \quad \epsilon_{\gamma a=5} = (1.4 \pm 0.3) \times 10^{-4}$$

were obtained.

A close-up of Fig. 7.4 around the $\gamma a = 3$ imperfection resonance is shown in Fig. 7.6. The measurement was obtained with an energy ramping velocity of $\dot{E} = 6$ GeV/s and an artificially increased resonance strength by forcing the electron orbit off the quadrupole centers so that $\epsilon_r/\sqrt{a} > 1$. One notices that the resonance position ($E_{r,\text{fit}} = 1.3261$ MeV) shows a mismatch between measured and calculated resonance energy ($E_{r,\text{fit}} = 1.3219$ MeV), which is due to a deviating energy calibration of the storage ring (see [Sch17, Chapter 7.1] for details).

Figure 7.7 shows the crossing of the imperfection resonance $\gamma a = 4$ with aligned orbit, where no spin flip occurs and a polarization loss of approximately 50% is observed.

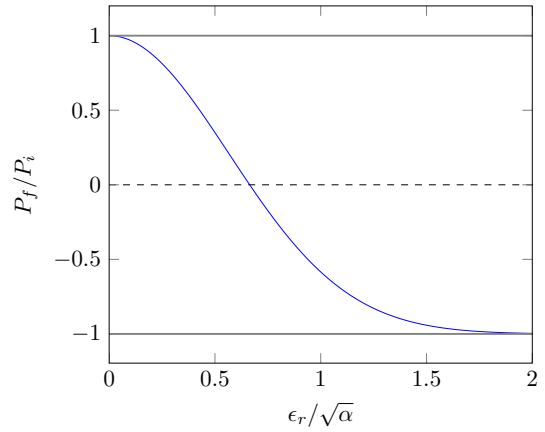


Figure 7.5: Visualization of the *Froissart-Stora* relation (Eq. (7.6)).

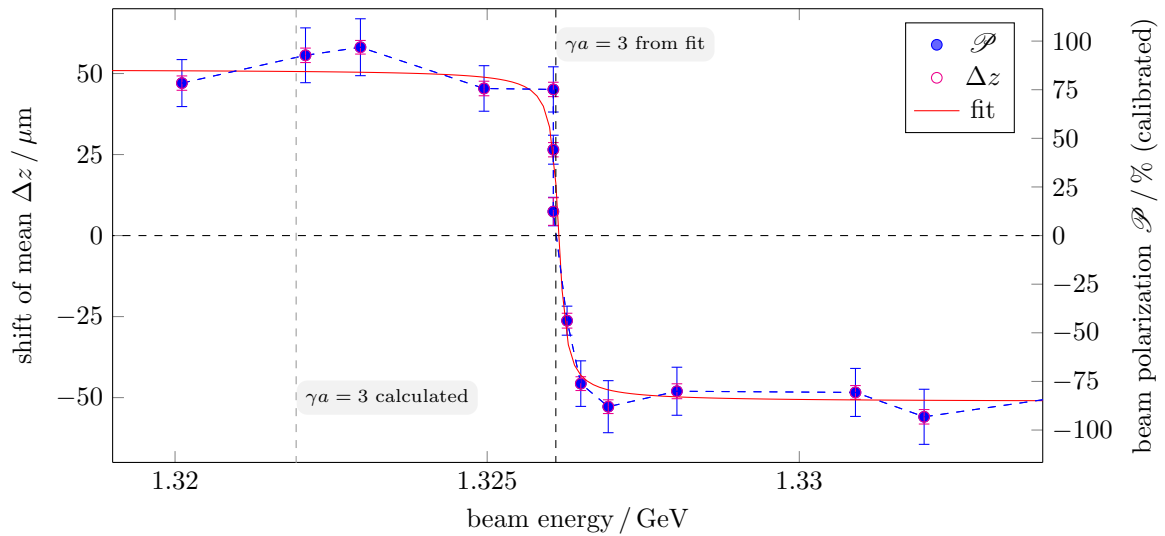


Figure 7.6: Crossing of the $\gamma a = 3$ imperfection resonance with $\dot{E} = 6$ GeV/s crossing speed. The resonance is artificially excited through orbit displacements resulting in a full spin flip $P_f/P_i \approx -1$. The resonance is indicated at the zero-crossing of the fit to an arc tangent function. The mismatch of calculated and obtained resonance energy results from an incorrect storage ring energy calibration.

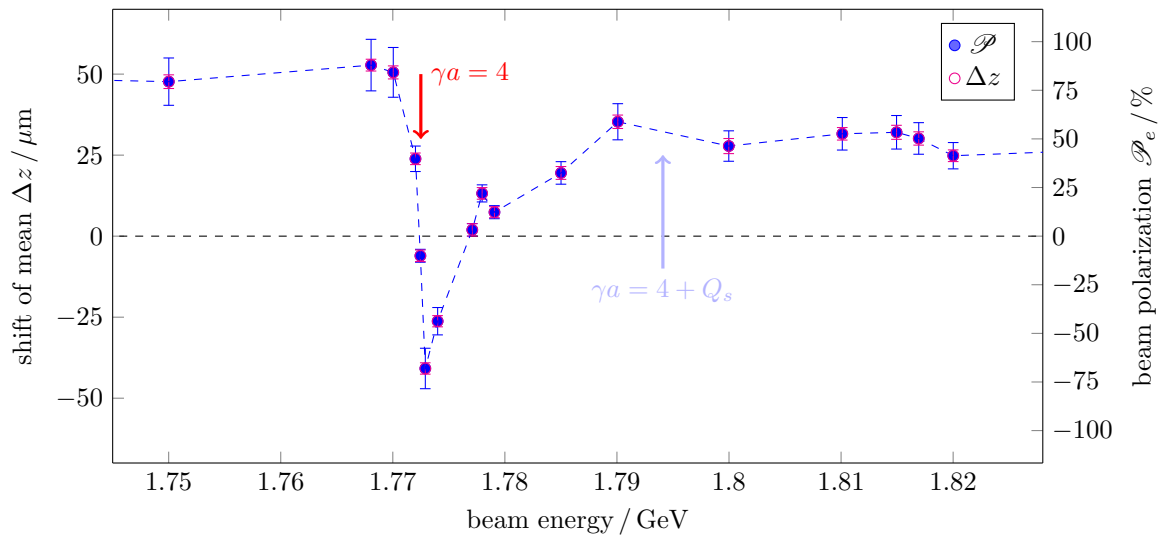


Figure 7.7: Crossing of the $\gamma a = 4$ imperfection resonance with aligned orbit and ramping velocity of $\dot{E} = 6$ GeV/s. A spin flip occurrence is yet observable despite the large ramping velocity due to the finite response of the bending magnet current ramp. After the resonance is crossed a polarization loss of approximately 50% is observable.

7.2.4 Equilibrium of Depolarization and Self-Polarization

As described in the previous section, the depolarizing resonance strengths ϵ_r can be calculated or measured, but they generally vary with the setting of the storage ring. In storage mode, the depolarization effect competes against the Sokolov-Ternov polarization build-up mechanism (compare with Section 2.3.2):

$$\mathcal{P}(t) = \mathcal{P}_\infty (1 - e^{-t/\tau}), \quad (2.48 \text{ revisited})$$

where the time constant $\tau_{\text{ST}}(E)$ (Eq. (2.49)) is reduced by the depolarization time constant $\tau_d(E, Q_x, Q_z)$:

$$\tau = \tau_{\text{ST}} \frac{\tau_d}{\tau_{\text{ST}} + \tau_d}. \quad (2.52 \text{ revisited})$$

The asymptotic polarization degree is reduced accordingly:

$$\mathcal{P}_\infty = \mathcal{P}_{\text{ST}} \frac{\tau_d}{\tau_{\text{ST}} + \tau_d}, \quad (2.53 \text{ revisited})$$

where $\tau_d(E, Q_x, Q_z)$ is energy- and tune dependent. As \mathcal{P}_∞ is determined by τ_d , its knowledge is required for the choice of a storage ring energy where the Compton polarimeter's analyzing power (see Section 6.4.3) can be determined. Corresponding simulations were performed by O. Boldt [Bol14, Sec. 3.5] using the spin tracking and simulation tool SLICKTRACK [BR99] based on a MAD-X³ [FSM02] model of the ELSA storage ring. The tune-dependency of the simulated equilibrium polarization \mathcal{P}_∞ at fixed beam energy is illustrated in Fig. 7.8. Figure 7.9 shows the equilibrium polarization \mathcal{P}_∞ , the Sokolov-Ternov self-polarization constant τ_{ST} and the effective polarization constant τ as function of beam energy E at fixed standard ELSA tunes $Q_{x,z}$. A reasonable measurement of τ is obtainable at those energy intervals where $\tau_{\text{ST}} < 100$ min and where \mathcal{P}_∞ is large. One notices that the asymptotic polarization degree \mathcal{P}_∞ always differs from \mathcal{P}_{ST} . This difference opposes a non-circumventable source of calibration error and must be minimized, which is the case around $E \approx 2.5$ GeV and 2.8 GeV. The

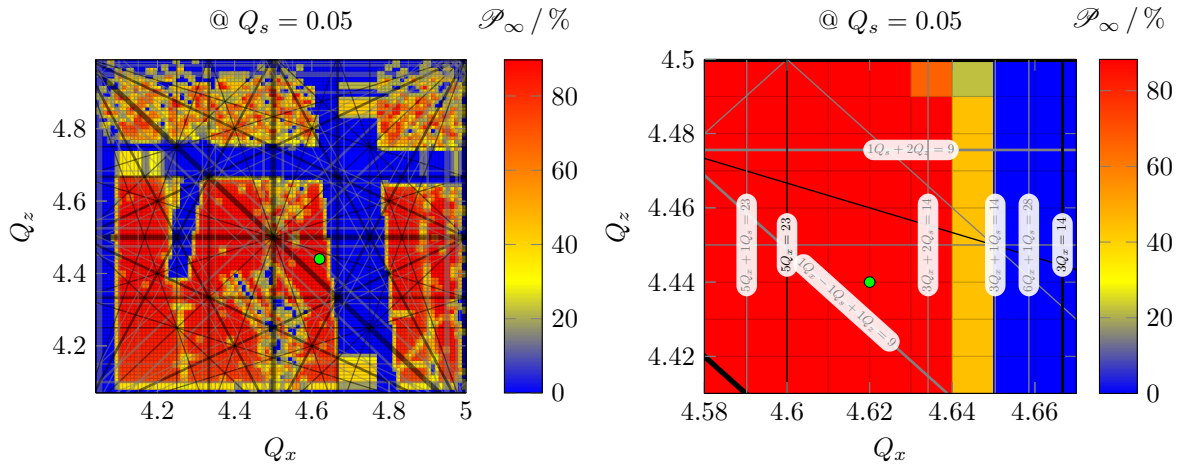


Figure 7.8: SLICKTRACK simulation of equilibrium polarization P_{max} at ELSA at 2.5 GeV beam energy. The tune diagram displays optical resonances up to 4th order at the standard longitudinal tune $Q_s = 0.05$ ($f_s \approx 88$ MHz). A typical ELSA tune of $Q_x = 4.62$ and $Q_z = 4.44$ is indicated by the green dot. Blue areas indicate a tracking simulation failure (e.g. due to particle loss). Data obtained from [Bol14].

³MAD-X is a general-purpose tool for charged-particle design and studies.

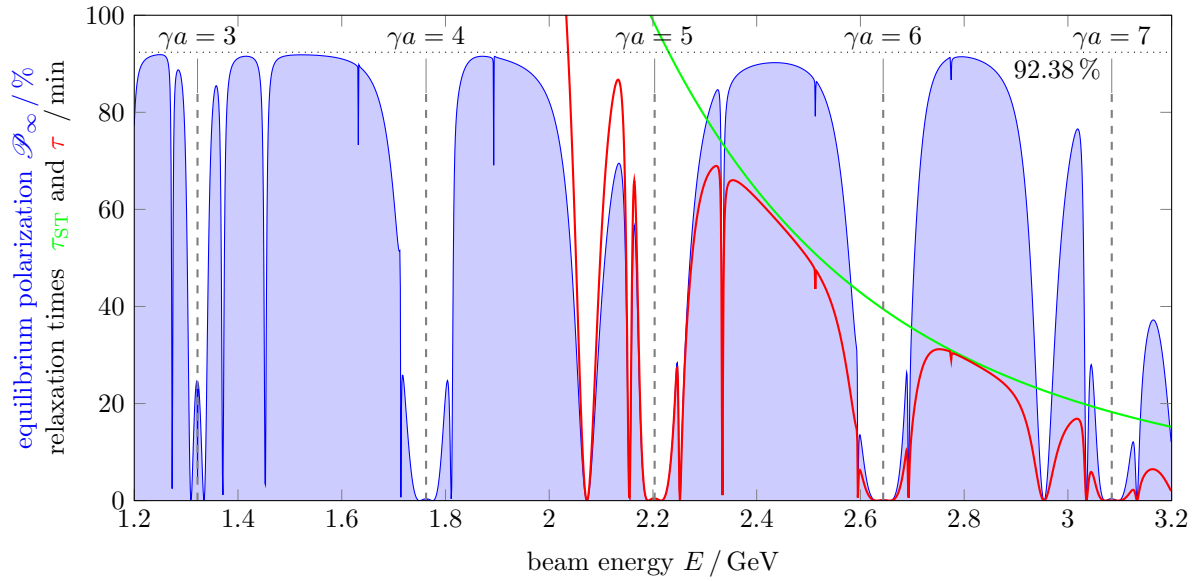


Figure 7.9: Simulated equilibrium polarisation at ELSA with tunes $Q_x = 4.62$ and $Q_z = 4.46$. Based on resonance impact, the ideal polarization time constant τ_{ST} is compared to measurable time constant τ . Resonance data obtained from [Bol14].

calibration example of Section 6.4.3 was conducted at 2.73 GeV, where the expected polarization time constant is $\tau_{\text{ST}} \approx 33.8$ min. According to Fig. 7.9 one obtains $\tau = 28.7$ min, resulting in $\tau_d = 190.2$ min and a corresponding $\mathcal{P}_\infty = 78.5\%$. The simulation shows that the impact of depolarizing resonances may significantly influence the value obtained for the analyzing power \mathcal{D} . However, the numerical results obtained from the simulation require verification, as the simulation parameters may not necessarily represent the settings of the contemporary lattice. A measurement of $\tau(E)$ in a distinctive energy interval around the vicinity of a resonance could verify the validity of the spin tracking model. As those measurements are time-consuming, they could not be conducted within the available polarimeter testing period.

Conclusion and Outlook

Within the scope of this work the beam diagnostic capabilities of the [ELSA](#) storage ring have been extended by a [SR](#) beamline with fast optical recorder for three-dimensional photometry of the electron beam and by a laser [CBS](#) polarimeter for monitoring the polarization degree of the stored electrons. At both beamlines the hardware performance allows extensive analysis procedures and parameter monitoring for the improvement of the accelerator's operation.

8.1 Synchrotron Radiation Diagnostic Beamline

The M7 photon beamline enables a temporal monitoring and analysis method of the electron beam with single bunch resolution. [Chapter 3](#) summarizes the optical properties and functioning principles of the beamline and demonstrates the versatile fields of application of the contemporary setup, such as simultaneous monitoring of the horizontal, vertical and longitudinal beam profile on various observation field spans from 3.1 to 28 mm and time ranges from 74 ps to 100 ms. For the monitoring of single bunches (resolution < 1 ps) it is shown that the dispersive photon signal dilatation due to the usage of broadband [VIS](#) has negligible effect for the bunch length measurements obtained at the [ELSA](#) storage ring. Therefore, more intensity is available in comparison to the usage of monochrome [VIS](#). The visualization and measurement quality of important accelerator parameters – such as beam size, tune, damping times, bunch length and filling pattern – is demonstrated in [Chapter 4](#). It is observed that the numerical analysis shows limits of validity in some cases, such as the inconsistent measurement results of the transverse beam size and bunch length (up to 10.3 % discrepancy). The beamline magnification seems too inaccurate to precisely measure the transverse beam profile of the electron beam and hence, obtained parameters such as the beam emittance and emittance coupling remain inaccurate. The bunch length measurement precision seems limited due to the streak camera deflection units' imperfect calibration. Dynamic beam behavior is, however, well observable and quantifiable. Transverse and longitudinal beam oscillation images are numerically analyzed and properties such as the storage ring tune, as well as the filling pattern are accurately determined.

For further improvement of the beamline performance, the following enhancements are suggested:

- More precision for bunch length measurements can be obtained by re-calibrating the sweeping units of the streak camera. This requires, for example, an attenuated, short-pulsed (picoseconds) gauge laser operating in the [VIS](#) spectrum.
- Improved adjustment of the optical magnification elements in order to precisely measure the transverse beam profile including the capability to change the optical magnification settings

without the need of the photon beam position.

- Simplification of the optics control through the [ELSA CS](#) and implementation of pre-set measurement routines for bunch length or filling pattern measurements. As this requires comprehensive failure-mode analysis in order to protect the fragile optical recorder, this automation was not performed within the scope of this work.

8.2 Compton Polarimeter

A polarimeter based on [CBS](#) was successfully tested at the [ELSA](#) storage ring. Its fundamental relations of operation and corresponding simulations are explicated in [Chapter 5](#). [Chapter 6](#) describes the laser beamline which has been adjusted from previous designs to operate with an [OPSL](#) source at 532 nm wavelength. The optical setup allows for user manipulation of the laser beam cross section and position at the [IP](#) in order to optimize the photon-electron-interaction rate for different electron beam energies. In addition, it offers diverse laser beam diagnostics for photon beam polarization and power verification. The measurement routine includes the alternation of the circular photon polarization in combination with fast shutters for background subtraction and enables the measurement of qualitative γ -photon profiles through a silicon microstrip detector. Measurements of shift in the means of γ -profiles could be obtained with Pearson type VII peak function fits, which have shown to provide the most robust and accurate measurement result. An absolute value of the beam polarization was obtained by determining the polarimeter's analyzing power $\mathcal{D} = (61.2 \pm 8.9) \mu\text{m}/100\%$ (at 2.73 GeV beam energy) through observation of the self-polarization build-up (Sokolov-Ternov effect). However, the magnitude of the determined systematic error and the mismatch of the obtained electron polarization degree of $(96.8 \pm 14.2) \%$ for a data set at 1.75 GeV beam energy (compared to an expected source polarization of maximum 86 %), suggest that the analyzing power has to be determined with more precision. On the other hand, a statistical measurement accuracy of 2 % within 5 minutes of measurement time could be achieved (1.4 % within 15 minutes). Further measurements in [Chapter 7](#) verify the functionality of the Compton polarimeter, being able to resolve known spin dynamical effects occurring in the [ELSA](#) storage ring such as spin flips at integer resonance crossings and spin rotation through the application of solenoid magnetic fields.

Compared to polarimetry through Møller scattering, the Compton polarimeter allows the measurement of beam polarization within a comparably short processing time, which makes it suitable for the effective implementation of polarization preserving countermeasures such as *tune jumps* and *harmonic corrections*. The hardware allowing the application of those mechanisms is implemented in the [ELSA](#) storage ring and was successfully tested during brief Compton polarimeter test runs. To additionally obtain a more precise absolute polarization degree, the polarimeter beamline performance may be improved by:

- Increasing the polarimeter accuracy by reducing the systematic error of the analyzing power \mathcal{D} by obtaining multiple qualitative measurements of the self-polarization effect at different electron beam energies.
- Increasing the statistical measurement accuracy by increasing the scattering rate, e.g. by installing a stronger laser source to obtain 1 % accuracy within 5 minutes. The beamline and vacuum system have originally been developed to guide two parallel laser beams onto the interaction point. Hence, laser power could be increased by installing an additional laser source.
- Improving the profile analysis quality by installing a silicon microstrip detector with 100 % channel functionality.

- Improving the optical design of the photon beam analyzer box to avoid beam loss at apertures in order to ensure a consistent measurement of the laser beam position, intensity and hence, photon polarization.
- Increasing the circular photon polarization by improving the angular fixation mechanism of the pneumatic quarter waveplate mount, by exchanging the in-vacuum deflection mirror to ensure a suitable reflectivity for the utilized laser beam wavelength and by placing a [PBS](#) in front of the laser source.
- Reducing the polarimeter measurement setup time through the implementation of automated laser beam adjustment routines.

Quantum Mechanical Description of Synchrotron Radiation

A.1 Total Emission Power

Spin-light contribution due to quantum-mechanical effects (see [Section 2.3](#)) to the emission power of SR (compare with [Eq. \(2.35\)](#) [BT08]):

$$P_{\text{SR}}^{\text{tot}} = P_{\text{SR}} (f_e + f_r + f_{e\mu} + f_{\mu}^{\text{L}} + f_{\mu}^{\text{L-Th}} + f_{\mu}^{\text{Th}} + f_{\mu}^{\text{a}}) \quad \text{with} \quad (\text{A.1})$$

$$P_{\text{SR}} = \frac{2}{3} \frac{e^2 c}{4\pi\epsilon_0 \beta^4} \frac{\gamma^4}{R^2}, \quad (\text{A.2})$$

$$f_e = 1, \quad (\text{A.3})$$

$$f_r = \frac{55\sqrt{3}}{24} \xi + \frac{175}{9} \xi^2, \quad (\text{A.4})$$

$$f_{e\mu} = \frac{1 + \zeta\zeta'}{2} \left[-\zeta \left(\xi - \frac{245\sqrt{3}}{48} \xi^2 \right) \right], \quad (\text{A.5})$$

$$f_{\mu}^{\text{L}} = \left[\frac{1 + \zeta\zeta'}{2} \frac{1}{9} + \frac{1 - \zeta\zeta'}{2} \left(\frac{14}{9} + \frac{385\sqrt{3}}{432} \zeta \right) \right] \xi^2, \quad (\text{A.6})$$

$$f_{\mu}^{\text{Th}} = \left(\frac{1 + \zeta\zeta'}{2} \frac{7}{9} + \frac{1 - \zeta\zeta'}{2} \frac{1}{9} \right) \xi^2, \quad (\text{A.7})$$

$$f_{\mu}^{\text{L-Th}} = \left[\frac{1 + \zeta\zeta'}{2} \frac{1}{3} + \frac{1 - \zeta\zeta'}{2} \left(-\frac{1}{3} - \frac{35\sqrt{3}}{216} \zeta \right) \right] \xi^2, \quad \text{and} \quad (\text{A.8})$$

$$f_{\mu}^{\text{a}} = \frac{1 + \zeta\zeta'}{2} \left[\zeta \frac{a}{3} \left(\xi - \frac{245\sqrt{3}}{72} \xi^2 \right) - \frac{a}{9} \xi^2 \right] + \frac{1 - \zeta\zeta'}{2} \left(49 + \frac{175\sqrt{3}}{6} \zeta \right) \frac{a}{9} \xi^2. \quad (\text{A.9})$$

A.2 Photon Polarization

Radiation power of polarized SR photons with spin projection angles ν (polar) and λ (azimuthal) [BTB95]:

$$\begin{aligned}
 P_{\text{SR}}^{\sigma} = P_{\text{SR}} & \left\{ \frac{1 + \zeta\zeta'}{2} \left\langle \frac{7}{8} - \frac{25\sqrt{3}}{12}\xi + \frac{325}{18}\xi^2 \right. \right. \\
 & - \xi \cos \nu \left[\xi - \frac{245\sqrt{3}}{48}\xi^2 - \frac{1}{6}a \left(\xi - \frac{245\sqrt{3}}{72}\xi^2 \right) \right] \\
 & + \cos^2 \nu \frac{5-a}{9}\xi^2 - \sin^2 \nu \cos^2 \lambda \frac{1+2a}{18}\xi^2 \left. \right\rangle \\
 & + \frac{1 - \zeta\zeta'}{2} \left\langle \frac{5-a}{9} \sin^2 \nu + (\cos^2 \nu + \sin^2 \nu \sin^2 \lambda) \frac{1+2a}{18} \right. \\
 & \left. + \zeta \cos \nu \frac{35\sqrt{3}}{216}a \right\rangle \xi^2 \left. \right\}
 \end{aligned}$$

$$\begin{aligned}
 P_{\text{SR}}^{\pi} = P_{\text{SR}} & \left\{ \frac{1 + \zeta\zeta'}{2} \left\langle \frac{1}{8} - \frac{5\sqrt{3}}{24}\xi + \frac{25}{18}\xi^2 \right. \right. \\
 & - a\zeta \cos \nu \left(\frac{1}{6}\xi - \frac{245\sqrt{3}}{432}\xi^2 \right) \\
 & + \left[\frac{5+22a}{9} \sin^2 \lambda + \frac{13}{18}(1+4a) \cos^2 \lambda \right] \sin^2 \nu \xi^2 \left. \right\rangle \\
 & + \frac{1 - \zeta\zeta'}{2} \left\langle \frac{5+22a}{9} (\cos^2 \nu + \sin^2 \nu \cos^2 \lambda) \right. \\
 & + \frac{13}{18} (1+4a) (\cos^2 \nu + \sin^2 \nu \cos^2 \lambda) \\
 & \left. + \zeta \cos \nu \frac{35\sqrt{3}}{48} \left(1 + \frac{38}{9}a \right) \right\rangle \xi^2 \left. \right\}
 \end{aligned}$$

$$\begin{aligned}
 P_{\text{SR}}^{\text{tot}} = & \left\{ \frac{1 + \zeta\zeta'}{2} \left\langle 1 - \frac{55\sqrt{3}}{24}\xi + \frac{175}{9}\xi^2 \right. \right. \\
 & - \zeta \cos \nu \left(\xi - \frac{245\sqrt{3}}{48}\xi^2 \right) + \cos^2 \nu \frac{5-a}{9}\xi^2 \\
 & + \sin^2 \nu \left(\frac{5+22a}{9} \sin^2 \nu + \frac{7+27a}{9} \cos^2 \lambda \right) \xi^2 \left. \right\rangle \\
 & + \frac{1 - \zeta\zeta'}{2} \left\langle \frac{5-a}{9} \sin^2 \nu + \frac{5+22a}{9} (\cos^2 \nu + \sin^2 \nu \cos^2 \lambda) \right. \\
 & + \frac{7+27a}{9} (\cos^2 \nu + \sin^2 \nu \cos^2 \lambda) \\
 & \left. + \zeta \cos \nu \frac{35\sqrt{3}}{48} \left(1 + \frac{40}{9}a \right) \right\rangle \xi^2 \left. \right\}
 \end{aligned}$$

Exemplary Analysis of Streak Camera Photon Profiles

The bunch length measurements in Figs. 4.9(a) and 4.10 (Section 4.2) show deviations of up to approximately 10 % for comparable accelerator settings. For the bunch length profile analysis method described in Section 3.2.3, systematic errors are introduced through the variation of sweep velocities, profile position, intensity, and granularity. Exemplary measurements of comparable accelerator conditions at different streak camera settings are shown in Figs. B.1 to B.3. A comparison of the analysis results is given in Table B.1. Therein, the coefficient of determination R^2 (see e.g. [DS81]) and the reduced χ^2_ν (see e.g. [Pre+92]) indicate a robust fit to the Gaussian profile in each case. For demonstration, the first profile of each column and corresponding fit function are shown in Fig. B.4. The granularity of Fig. B.3 results from the intensity amplification through the streak tube MCP (compare with Fig. 3.7).

The influence of the span of the intensity profile's fit interval is shown in Fig. B.5. Therein, the obtained fit result of the profile width $\sigma_{s,\tau}$ is compared for a varying AOI width around the center. The precision is based on the result of the maximum available profile span and is in all cases $< 1\%$ above 3.5σ (one-sided), and $< 5\%$ above 2.3σ . As for most measurements the AOI width is approximately $> 3.5\sigma$, the contribution of this effect is considered to be $< 1\%$.

Example	$\overline{\sigma_{s,\tau}}$	$\overline{R^2}$	$\overline{\chi^2_\nu}$
Fig. B.1	(59.6 ± 0.7) ps	0.998	18.2
Fig. B.2	(57.5 ± 0.8) ps	0.997	14.9
Fig. B.3	(53.7 ± 1.3) ps	0.990	48.9

Table B.1: Comparison of mean bunch length $\overline{\sigma_{s,\tau}}$, mean coefficient of determination $\overline{R^2}$ and reduced $\overline{\chi^2_\nu}$ for the 2×512 measured profiles in each of the measurements at equal accelerator conditions.

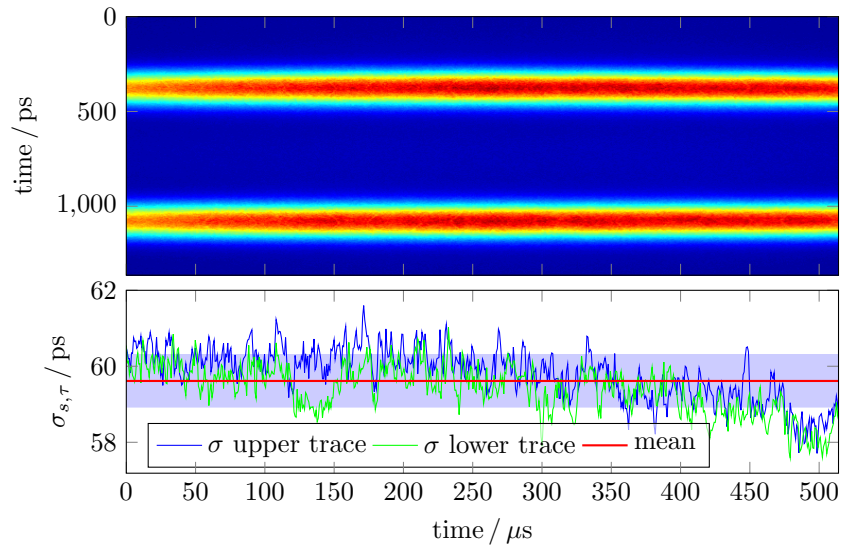


Figure B.1: Bunch length measurement in dual base synchroscan mode with broadband VIS at a vertical time span of 1 363.7 ps. The result for each individual profile is shown on the bottom.

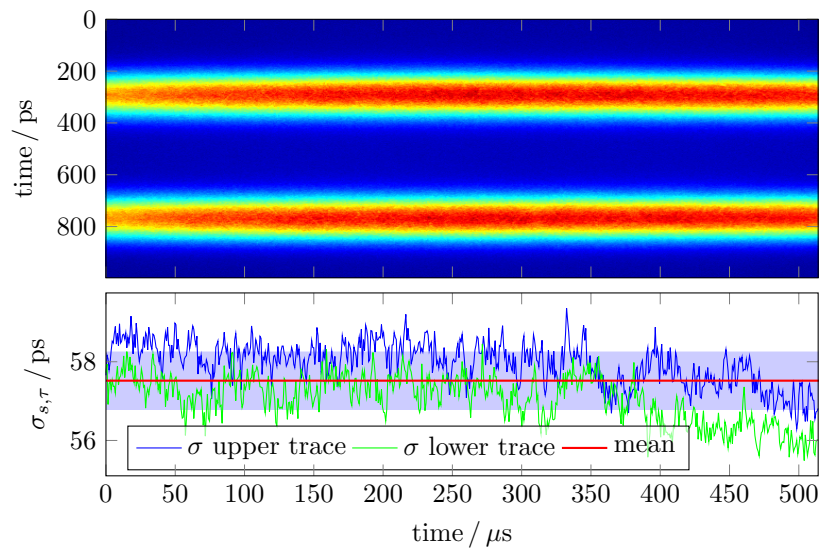


Figure B.2: Bunch length measurement in dual base synchroscan mode with broadband VIS at a vertical time span of 997.9 ps. The result for each individual profile is shown on the bottom.

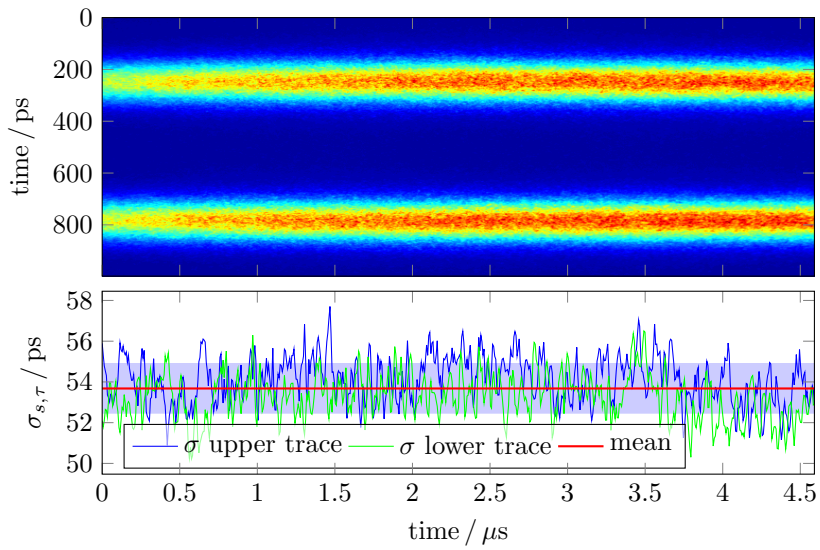


Figure B.3: Bunch length measurement in dual base synchroscan mode with monochromatic VIS at a vertical time span of 997.9 ps. The result for each individual profile is shown on the bottom.

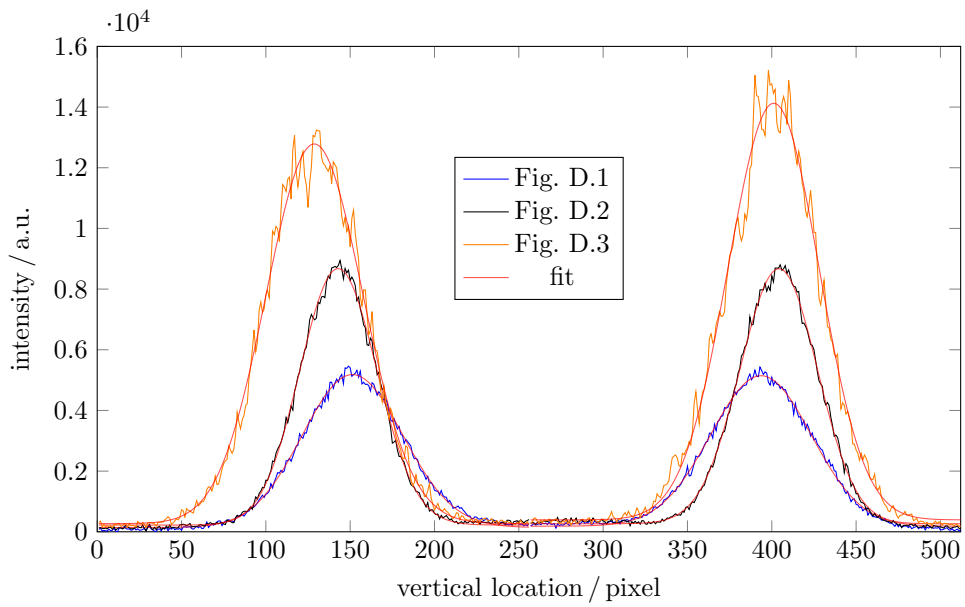


Figure B.4: Signal profiles and corresponding fits of the first column in Figs. B.1 to B.3, respectively.

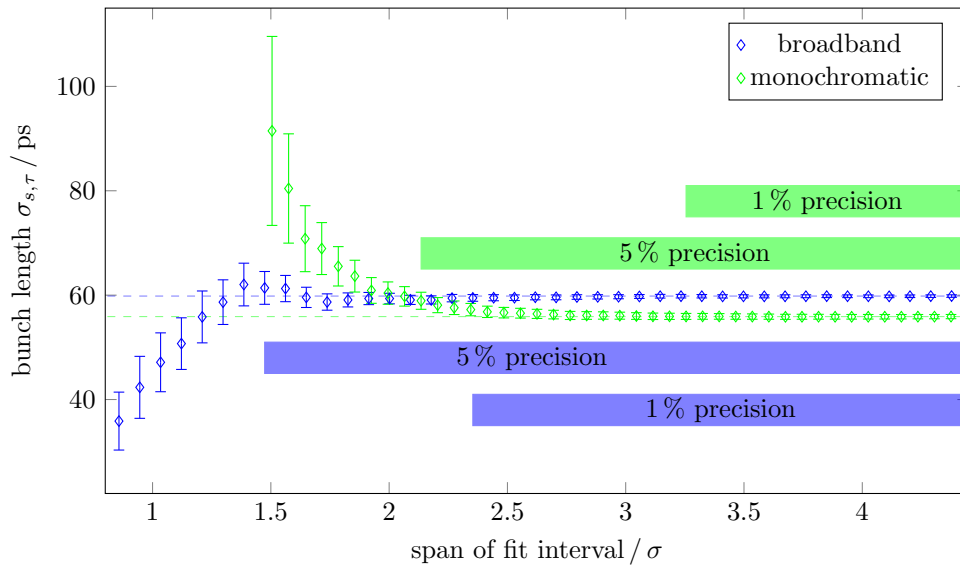


Figure B.5: Comparison of measurement precision for varying width of AOI based on the result at maximum available span of fit interval for the two bunch length measurements shown in Figs. B.2 and B.3.

Relativistic Kinematics

C.1 Kinematic Parameters

A particle's total energy E is related to its kinetic energy T , the particle mass $E_0 = m_0c^2$ and momentum p by

$$E = T + E_0 = \sqrt{(pc)^2 + (m_0c^2)^2}. \quad (\text{C.1})$$

The relativistic γ corresponds to the particle's velocity \vec{v} via

$$\gamma = \frac{1}{\sqrt{1 - \beta^2}} \quad \text{with} \quad \vec{\beta} = \vec{v}/c. \quad (\text{C.2})$$

The parameters of [Eq. \(C.2\)](#) are related to particle energy E , momentum p and mass E_0 via

$$\gamma = \frac{E}{E_0}, \quad \beta = \frac{pc}{E}. \quad (\text{C.3})$$

C.2 Lorentz Transformation and Compton Scattering

For an incident photon with energy $E_i = |\vec{p}_i|c$ and anti-parallel inclination angle α towards the s -axis of a Cartesian coordinate system (x, z, s) , the four-vector reads

$$P_i = \begin{pmatrix} E_i/c \\ 0 \\ -p_i \sin \alpha \\ -p_i \cos \alpha \end{pmatrix}. \quad (\text{C.4})$$

The Lorentz transformation into the rest frame of a relativistic scattering electron

$$P_i^* = \begin{pmatrix} \gamma & 0 & 0 & -\gamma\beta \\ 0 & 1 & 0 & 0 \\ 0 & 0 & 1 & 0 \\ -\gamma\beta & 0 & 0 & \gamma \end{pmatrix} \cdot P_i = \begin{pmatrix} \gamma E_i/c + \gamma\beta p_i \cos \alpha \\ 0 \\ -p_i \sin \alpha \\ -\gamma\beta E_i/c - \gamma p_i \cos \alpha \end{pmatrix} \quad (\text{C.5})$$

yields for the obtained photon energy in the electron's rest frame

$$E_i^* = \gamma E_i (1 + \beta \cos \alpha) \stackrel{\alpha \ll 1}{\approx} 2\gamma E_i. \quad (\text{C.6})$$

For a Compton scattered photon (compare with [Section 5.1](#)) the retained energy E_f^* in the electron's rest frame reads in four-vector notation

$$P_f^* = \begin{pmatrix} E_f^*/c \\ -p_f^* \sin \vartheta^* \sin \varphi^* \\ -p_f^* \sin \vartheta^* \cos \varphi^* \\ -p_f^* \cos \vartheta^* \end{pmatrix}. \quad (\text{C.7})$$

The Lorentz transformation into the laboratory frame

$$P_f = \begin{pmatrix} \gamma & 0 & 0 & \gamma\beta \\ 0 & 1 & 0 & 0 \\ 0 & 0 & 1 & 0 \\ \gamma\beta & 0 & 0 & \gamma \end{pmatrix} \cdot P_f^* = \begin{pmatrix} \gamma E_f^*/c - \gamma\beta p_f^* \cos \vartheta^* \\ -p_f^* \sin \vartheta^* \sin \varphi^* \\ -p_f^* \sin \vartheta^* \cos \varphi^* \\ \gamma\beta E_f^*/c - \gamma p_f^* \cos \vartheta^* \end{pmatrix} \quad (\text{C.8})$$

yields the obtained photon energy observable in the laboratory

$$E_f = \gamma E_f^* (1 - \cos \vartheta^*), \quad (\text{C.9})$$

where the scattering angle is transformed to

$$\tan \vartheta = \frac{\sin \vartheta^*}{\gamma(1 - \cos \vartheta^*)}. \quad (\text{C.10})$$

Stokes Parameters and Photon Polarization

The Stokes vector $\vec{S} = (S_0, S_1, S_2, S_3)$ [BW70, sec. 1.4] describes the photon polarization of a plane monochromatic wave

$$S_0 = E_1^2 + E_2^2, \quad (\text{D.1})$$

$$S_1 = E_1^2 - E_2^2, \quad (\text{D.2})$$

$$S_2 = 2E_1E_2 \cos \delta, \quad (\text{D.3})$$

$$S_3 = 2E_1E_2 \sin \delta, \quad (\text{D.4})$$

through the absolute value of the transverse and perpendicular electric field vectors E_1 and E_2 with phase difference δ . The identity

$$S_0^2 = S_1^2 + S_2^2 + S_3^2 \quad (\text{D.5})$$

holds and allows a normalization of the stokes vector: $S_0 = 1$. Linear and circular polarized light are described through [Bar+93, sec. 2.1]

$$S_{\text{lin}} = \sqrt{S_1^2 + S_2^2}, \quad (\text{D.6})$$

$$S_{\text{circ}} = |S_3| = \sqrt{1 - S_{\text{lin}}^2}. \quad (\text{D.7})$$

The sign of S_3 denotes the polarization helicity with convention

$$S_3 < 0 : \textit{right-handed} \text{ helicity, and} \quad (\text{D.8})$$

$$S_3 > 0 : \textit{left-handed} \text{ helicity.} \quad (\text{D.9})$$

Gaussian Beam Propagation Theory

The waist form of a photon beam is sufficiently described by Gaussian beam optics. An exemplary beam waist is visualized in Fig. E.1. In Gaussian beam propagation theory the beam is characterized by the Rayleigh length z_R , wavefront radius R , beam width $w(z)$, divergence (Θ) [Mes04], and for realistic beams by the *beam propagation factor* M^2 [Sie98]. The latter characterizes the deviation of realistic beams from the ideal TEM₀₀ mode, which generally results in a broadened beam waist. The above figures are briefly described below.

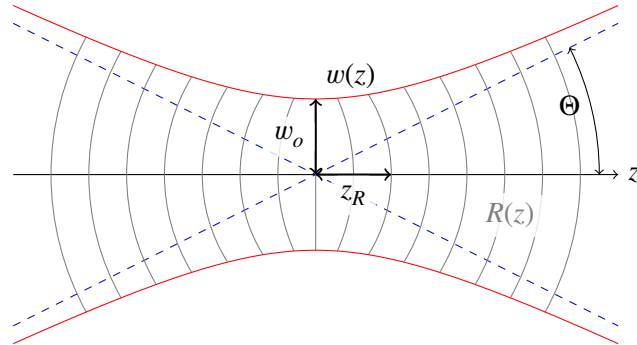


Figure E.1: Exemplary beam waist of a propagating Gaussian beam with $w_0 = 1$ and $z_R = 1$, illustrating the beam width (red), wavefront radius (gray) and the beam width in geometric optics (blue).

Rayleigh length z_R and wavefront radius $R(z)$: The Rayleigh length marks the *near field* or *depth of focus* within $-z_R \leq z_0 \leq z_R$ and determines the wavefront radius

$$R(z) = z \left(1 + \left(\frac{z_R}{z} \right)^2 \right). \quad (\text{E.1})$$

Within the Rayleigh length the wavefront forms *approximately* a plane wave, whereas in the *far field* ($z \gg z_R$) the wave propagation follows the properties of a spherical wave: $R(z) \approx z$.

Beam width $W(z)$ and divergence Θ : The width of a photon beam's intensity distribution $I(x, y)$ is well described through its variance, exemplarily in the horizontal case:

$$\sigma_x^2 = \frac{\int (x - x_0)^2 I(x, y) dx dy}{\int I(x, y) dx dy}, \quad (\text{E.2})$$

where x_0 is the center of gravity. The full beam width is commonly described through $W = 2\sigma$. The narrowest beam width at a focal point is $2W_0$, which is determined by wavelength λ and Rayleigh length z_R :

$$W_0 = \sqrt{\frac{\lambda z_R}{\pi n}}, \quad (\text{E.3})$$

where n is the refractive index of the medium. The beam width $W(z)$ propagates according to

$$W^2(z) = W_0^2 + \Theta^2 (z - z_0)^2, \quad (\text{E.4})$$

where the divergence Θ is given by

$$\Theta = \frac{W_0}{z_R} = \sqrt{\frac{\lambda}{\pi z_R n}}. \quad (\text{E.5})$$

Thus, the beam width propagation takes the form

$$W(z) = W_0 \sqrt{1 + \left(\frac{z}{z_R}\right)^2}. \quad (\text{E.6})$$

The change in width is particularly small within the Rayleigh length z_R .

Realistic beams and beam propagation factor M : As realistic beams usually deviate from the ideal TEM_{00} mode, the beam waist at identical divergences is larger:

$$\omega(z) = W(z) \cdot M, \quad (\text{E.7})$$

where the beam propagation factor $M^2 \geq 1$ describes the *quality* of the real beam in respect to the TEM_{00} mode. One generally obtains

$$w_0 \Theta = \frac{\lambda}{n\pi} M^2. \quad (\text{E.8})$$

Silicon Microstrip Detector Channel Correction

The 768 silicon microstrip channels are individually correctable. On the **hardware** level, the shaped electronic channel pulse is processed by a comparator, whose threshold is adjustable by a 5 bit trim DAC (compare with Fig. 6.18). The correctional values are determined by injection of calibrated charge amounts into each channel's processing electronics. The trim values of the contemporary detector setup¹ are shown in Fig. F.1. Except for clustered and saturated channels (erroneous channels are marked red, compare with Section 6.3.2), no abnormalities of the remaining correctional values are observed. However, the trim DAC corrected profile may still hold irregularities whose origins are hardware-based.

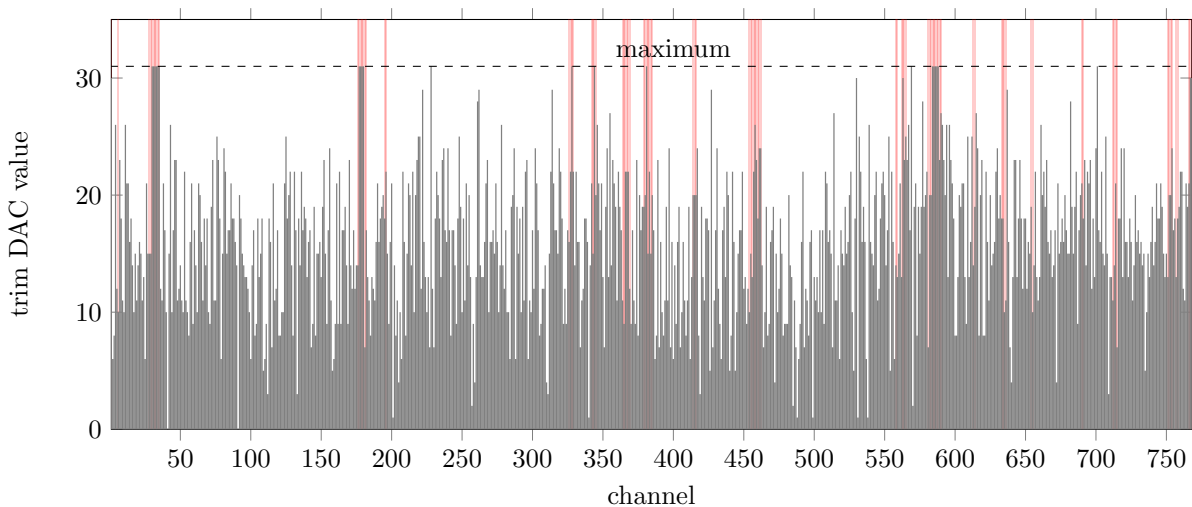


Figure F.1: 32-bit trim DAC channel correction. Erroneous and deviating channels are marked red.

An example beam profile with set trim DACs is shown in Fig. F.2. The deviations therein may be corrected with a scaling factor which is applied to each channel at the **software** processing level. The scaling may be generated from a fit of any reasonable smooth function to the data. Figure F.3 shows scaling correction values obtained from electron radiation at the tagger magnet¹ (compare with Fig. 1.4), and from a spline fit to a summed profile with a large amount of events. For the latter, the relative statistical error of the peak value in Fig. F.2 is $< 0.3\%$. The scaling result from electron irradiation and the spline fit shows no distinctive differences.

¹ Data of the continuous horizontal electron distribution acquired by R. Koop.

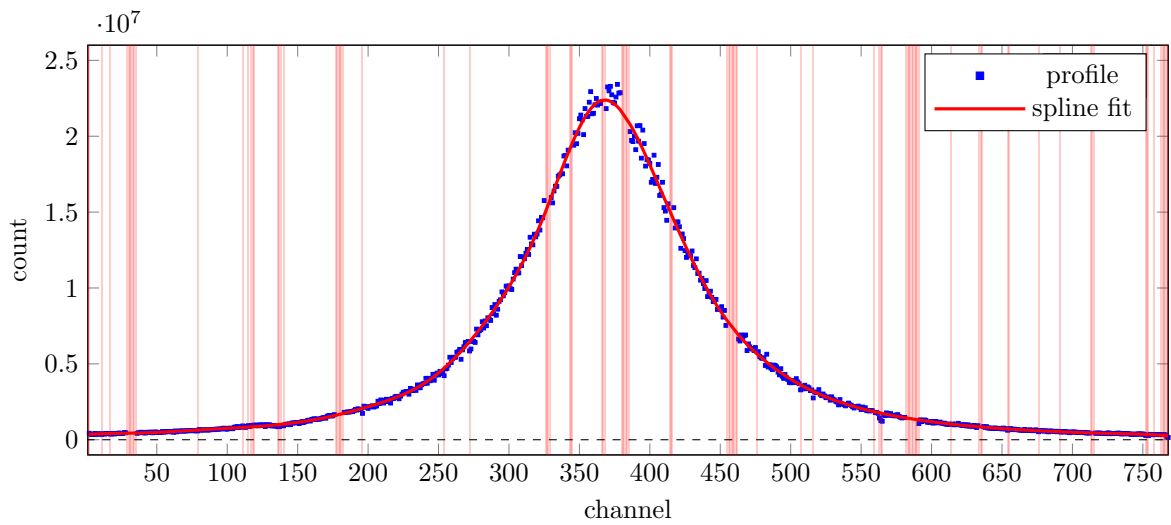


Figure F.2: Sum of 43806 profiles from four different measurement sets, including data from laser profiles of both circular polarization states and background measurements. The fraction of channel count (blue) and spline fit value (red) determines the correctional scaling value for each channel. Erroneous and deviating channels are marked red.

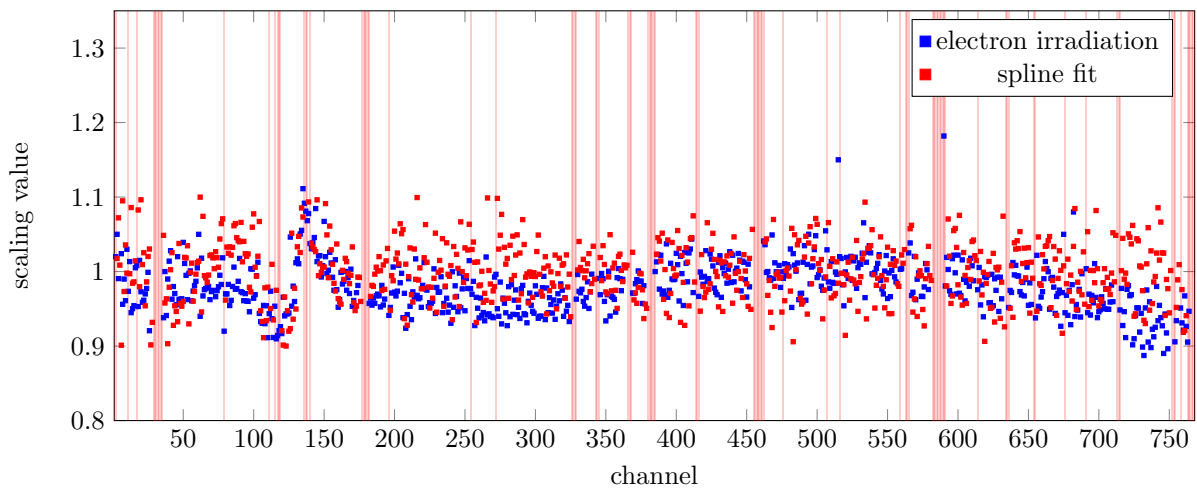


Figure F.3: Software scaling correction values determined by electron irradiation (red) and by fitting the spline obtained from Fig. F.2 (blue). Both correction methods show similar results, indicating a minor structural deviation between channels 100 to 175.

References

- [Abe+01] K. Abe et al., *Particle Physics Experiments at JLC*, ACFA Linear Collider Working Group Report, 2001, URL: <http://arxiv.org/pdf/hep-ph/0109166.pdf> (cit. on p. 44).
- [AC90] G. R. Aiello and F. Cavazzoni, *The Beam Profile Monitors for Elettra*, European Particle Accelerator Conference (1990) 747, URL: <http://cds.cern.ch/record/963887> (cit. on p. 29).
- [Alt+68] K. Althoff et al., *The 2.5 GeV Electron Synchrotron of the University of Bonn*, *Nuclear Instruments and Methods* **61** (1968) 1, ISSN: 0029-554X, URL: <http://www.sciencedirect.com/science/article/pii/0029554X68904436> (cit. on p. 1).
- [Aur08] B. Aurand, *Die Laserstrahlführung des neuen Compton-Polarimeters an ELSA*, MA thesis: Rheinische Friedrich-Wilhelms-Universität Bonn, 2008, URL: https://www-elsa.physik.uni-bonn.de/Publikationen/texte/aurand_diplom.pdf (cit. on pp. 86, 87, 95, 96, 98).
- [Bar+93] D. Barber et al., *The HERA Polarimeter and the First Observation of Electron Spin Polarization at HERA*, *Nuclear Instruments and Methods in Physics Research Section A: Accelerators, Spectrometers, Detectors and Associated Equipment* **329** (1993) 79, ISSN: 0168-9002, URL: <http://www.sciencedirect.com/science/article/pii/0168900293909247> (cit. on pp. 20, 21, 71, 87, 135).
- [Bas02] N. Bassler, *Radiation Damage In Scientific Charge-Coupled Devices*, MA thesis: Institute of Physics and Astronomy, University of Aarhus, DK, 2002, URL: <https://neptun.phys.au.dk/~bassler/THESIS/thesis.pdf> (cit. on p. 44).
- [BDS75] I. S. Barker, A. Donnachie, and J. K. Storrow, *Complete Experiments in Pseudoscalar Photoproduction*, *Nuclear Physics B* **95** (1975) 347, ISSN: 0550-3213, URL: <http://www.sciencedirect.com/science/article/pii/0550321375900498> (cit. on p. 6).
- [Bel+84] S. A. Belomesthnykh et al., *An Observation of the Spin Dependence of Synchrotron Radiation Intensity*, *Nuclear Instruments and Methods in Physics Research Section A: Accelerators, Spectrometers, Detectors and Associated Equipment* **227** (1984) 173, ISSN: 0168-9002, URL: <http://www.sciencedirect.com/science/article/pii/0168900284901190> (cit. on p. 19).
- [Ber+10] M. J. Berger et al., *XCOM: Photon Cross Sections Database*, (2010), URL: <https://www.nist.gov/pml/xcom-photon-cross-sections-database> (cit. on p. 78).
- [Ber+17] M. J. Berger et al., *ESTAR: Stopping Power and Range Tables*, (2017), URL: <https://www.nist.gov/pml/stopping-power-range-tables-electrons-protons-and-helium-ions> (cit. on p. 79).

-
- [BMT59] V. Bargmann, L. Michel, and V. L. Telegdi, *Precession of the Polarization of Particles Moving in a Homogeneous Electromagnetic Field*, *Phys. Rev. Lett.* **2** (10 1959) 435, URL: <https://link.aps.org/doi/10.1103/PhysRevLett.2.435> (cit. on p. 11).
- [Bol14] O. Boldt, *Spindynamik von Elektronenstrahlen in Kreisbeschleunigern*, PhD thesis: Rheinische Friedrich-Wilhelms-Universität Bonn, 2014, URL: <http://nbn-resolving.de/urn:nbn:de:hbz:5n-36455> (cit. on pp. 11, 12, 121, 122).
- [Bor01] M. Borland, *Simple Method for Particle Tracking with Coherent Synchrotron Radiation*, *Phys. Rev. ST Accel. Beams* **4** (7 2001) 070701, URL: <https://link.aps.org/doi/10.1103/PhysRevSTAB.4.070701> (cit. on pp. 51, 58).
- [BR99] D. Barber and G. Ripken, *Radiative Polarization, Computer Algorithms and Spin Matching in Electron Storage Rings*, tech. rep. DESY 99-095, 1999, URL: <https://arxiv.org/pdf/physics/9907034.pdf> (cit. on p. 121).
- [Bre+85] W. Brefeld et al., *Measurement of the Polarization Degree of Accelerated Polarized Electrons at the 2.5-GeV Synchrotron in Bonn for Energies Between 0.85-GeV and 2-GeV*, *Nucl. Instrum. Meth.* **A228** (1985) 228 (cit. on pp. 117, 118).
- [BS82] A. E. Bondar and E. L. Saldin, *On the Possibility of Using Synchrotron Radiation for Measuring the Electron Beam Polarization in a Storage Ring*, *Nuclear Instruments and Methods in Physics Research* **195** (1982) 577, ISSN: 0167-5087, URL: <http://www.sciencedirect.com/science/article/pii/0029554X82900210> (cit. on pp. 16, 19).
- [BT08] V. A. Bordovitsyn and V. V. Telushkin, *Spin Light Identification in the Presence of Power Synchrotron Radiation*, *Nuclear Instruments and Methods in Physics Research Section B: Beam Interactions with Materials and Atoms* **266** (2008) 3708, Radiation from Relativistic Electrons in Periodic Structures, ISSN: 0168-583X, URL: <http://www.sciencedirect.com/science/article/pii/S0168583X08005466> (cit. on pp. 18, 127).
- [BTB95] V. A. Bordovitsyn, I. M. Ternov, and V. G. Bagrov, *Spin Light*, *Physics-Uspekhi* **38** (1995) 1037, URL: <http://stacks.iop.org/1063-7869/38/i=9/a=A05> (cit. on p. 128).
- [BV06] J. C. Bergstrom and J. M. Vogt, *The Optical Diagnostic Beamline at the Canadian Light Source*, *Nuclear Instruments and Methods in Physics Research Section A: Accelerators, Spectrometers, Detectors and Associated Equipment* **562** (2006) 495, ISSN: 0168-9002, URL: <http://www.sciencedirect.com/science/article/pii/S0168900206004761> (cit. on p. 29).
- [BW70] M. Born and E. Wolf, *Principles of Optics*, 4th ed., Pergamon Press, Ltd., Oxford, 1970 (cit. on p. 135).

- [Coha] Coherent, Inc., *Advances in Laser Diode and OPSL Technologies Render Ion and Metal Vapor Lasers Obsolete*, White paper, URL: <https://cohrcdn.azureedge.net/assets/pdf/Advances-in-Laser-Diode-and-OPSL-Technologies.pdf> (cit. on pp. 86, 88).
- [Cohb] Coherent, Inc., *Coherent Verdi G-18 specifications*, URL: https://cohrcdn.azureedge.net/assets/pdf/COHR_Verdi_G-SeriesFamily_DS_0917_4.pdf (cit. on pp. 89, 92).
- [Cohc] Coherent, Inc., *Sapphire Advantage: Low-Noise*, White paper, URL: <https://edge.coherent.com/assets/pdf/Sapphire-Advantage-Low-Noise.pdf> (cit. on p. 88).
- [Coh15] Coherent, Inc., *ModeMaster PC User Manual*, Coherent Inc., 2015, URL: <https://www.coherent.com/measurement-control/measurement/laser-beam-diagnostics/modemaster-pc-m-squared-m2-beam-propagation-analyzer> (cit. on p. 93).
- [Com+17] N. Compton et al., *Measurement of the Differential and Total Cross Sections of the $\gamma d \rightarrow K^0 \Lambda(p)$ Reaction within the Resonance Region*, *Phys. Rev. C* **96** (6 2017) 065201, URL: <https://link.aps.org/doi/10.1103/PhysRevC.96.065201> (cit. on p. 8).
- [Com22] A. Compton, *Secondary Radiations Produced by X-Rays and Some of Their Applications to Physical Problems*, *Bulletin of the National Research Council* **4** (1922) (cit. on p. 67).
- [CR80] E. Courant and R. Ruth, *The Acceleration of Polarized Protons in Circular Accelerators*, 1980, URL: https://inis.iaea.org/collection/NCLCollectionStore/_Public/12/592/12592357.pdf (cit. on p. 119).
- [CS58] E. D. Courant and H. S. Snyder, *Theory of the Alternating-Gradient Synchrotron*, *Annals of Physics* **3** (1958) 1, ISSN: 0003-4916, URL: <http://www.sciencedirect.com/science/article/pii/0003491658900125> (cit. on p. 51).
- [Der06] L. Derr, *Photography for Students of Physics and Chemistry*, Macmillan & Co., Ltd., London, 1906 79 (cit. on p. 29).
- [Dol98] D. Doll, *Das Compton-Polarimeter an ELSA*, PhD thesis: Rheinische Friedrich-Wilhelms-Universität Bonn, 1998, URL: https://www-elsa.physik.uni-bonn.de/Publikationen/texte/dis_bonn-ir-98-08_dietmar_doll.pdf (cit. on p. 86).
- [DS81] N. R. Draper and H. Smith, *Applied Regression Analysis*, 3rd ed., John Wiley & Sons, Inc., Hoboken, 1981, ISBN: 978-3-642-00828-3 (cit. on pp. 42, 106, 129).
- [Eat+17] J. W. Eaton et al., *GNU Octave Version 4.2.1 Manual: A High-Level Interactive Language for Numerical Computations*, 2017, URL: <https://www.gnu.org/software/octave/doc/v4.2.1/> (cit. on pp. 42, 103, 105).
- [Ebe10] M. Eberhardt, *Messung und Korrektur der Arbeitpunkte während der Energierampe am Stretcherring von ELSA*, PhD thesis: Rheinische Friedrich-Wilhelms-Universität Bonn, 2010, URL: <http://nbn-resolving.de/urn:nbn:de:hbz:5N-23789> (cit. on p. 52).

-
- [Fan49] U. Fano,
Remarks on the Classical and Quantum-Mechanical Treatment of Partial Polarization,
J. Opt. Soc. Am. **39** (1949) 859,
URL: <http://www.osapublishing.org/abstract.cfm?URI=josa-39-10-859>
(cit. on p. 71).
- [Fer+05] A. Ferrari et al., *FLUKA: A Multi-Particle Transport Code (Program Version 2005)*, (2005),
URL: <http://cds.cern.ch/record/898301/files/CERN-2005-010.pdf>
(cit. on pp. 46, 76).
- [FPS93] A. Ferrari, M. Pelliccioni, and P. R. Sala, *Estimation of Fluence Rate and Absorbed Dose Rate due to Gas Bremsstrahlung from Electron Storage Rings*,
Nuclear Instruments and Methods in Physics Research Section B: Beam Interactions with Materials and Atoms **83** (1993) 518, ISSN: 0168-583X, URL:
<http://www.sciencedirect.com/science/article/pii/0168583X93958815>
(cit. on p. 76).
- [Fre17] O. Freyermuth, *Studies of ω Photoproduction off Proton at the BGO-OD Experiment*,
PhD thesis: Rheinische Friedrich-Wilhelms-Universität Bonn, 2017,
URL: <http://nbn-resolving.de/urn:nbn:de:hbz:5n-48397> (cit. on p. 7).
- [FS60] M. Froissart and R. Stora,
Depolarisation d'un Faisceau de Protons Polarises Dans un Synchrotron,
Nuclear Instruments and Methods **7** (1960) 297, ISSN: 0029-554X,
URL: <http://www.sciencedirect.com/science/article/pii/0029554X60900331>
(cit. on p. 119).
- [FSM02] E. Forest, F. Schmidt, and E. McIntosh, *Introduction to the Polymorphic Tracking Code*,
European Organization for Nuclear Research (2002),
URL: <http://mad.web.cern.ch/mad/> (cit. on p. 121).
- [Gow01] M. Gowin, *Optimierung der laserinduzierten Photoemission zur Erzeugung polarisierter Elektronenstrahlen an der 50 keV-Quelle der Bonner Beschleunigeranlage ELSA*,
PhD thesis: Rheinische Friedrich-Wilhelms-Universität Bonn, 2001, URL:
https://www-elsa.physik.uni-bonn.de/Publikationen/texte/gowin_dr.pdf
(cit. on p. 97).
- [GS22] W. Gerlach and O. Stern,
Der experimentelle Nachweis der Richtungsquantelung im Magnetfeld,
Zeitschrift für Physik **9** (1922) 349, ISSN: 0044-3328,
URL: <https://doi.org/10.1007/BF01326983> (cit. on p. 9).
- [Haf81] H. Haferkorn, *Optik: Physikalisch-technische Grundlagen und Anwendungen*,
Harri Deutsch, Thun, Frankfurt/M., 1981, ISBN: 978-3-87-144570-5 (cit. on p. 29).
- [Ham13] Hamamatsu Photonics K. K., “Universal Streak Camera C10910 Test Report,” 2013
(cit. on p. 60).
- [Ham16] Hamamatsu Photonics Deutschland GmbH,
Hamamatsu Streak Camera C10910 Data Sheet, 2016, URL:
http://www.hamamatsu.com/resources/pdf/sys/SHSS0016E07_C10910s.pdf
(cit. on pp. 25, 31, 32, 42).
- [Ham95] F. Hamburger, *Detektorkonzept für das Laserpolarimeter an ELSA*,
MA thesis: Rheinische Friedrich-Wilhelms-Universität Bonn, 1995 (cit. on pp. 75, 77, 80).

- [Har17] J. Hartmann, *Measurement of Double Polarization Observables in the Reactions $\gamma p \rightarrow p\pi^0$ and $\gamma p \rightarrow p\eta$ with the Crystal Barrel/TAPS Experiment at ELSA*, PhD thesis: Rheinische Friedrich-Wilhelms-Universität Bonn, 2017, URL: <http://nbn-resolving.de/urn:nbn:de:hbz:5n-48336> (cit. on p. 5).
- [Hei14] D. Heiliger, *Erzeugung intensiver Spinpolarisierter Elektronenstrahlen an der Beschleunigeranlage ELSA*, PhD thesis: Rheinische Friedrich-Wilhelms-Universität Bonn, 2014, URL: <http://nbn-resolving.de/urn:nbn:de:hbz:5n-37259> (cit. on pp. 2, 107, 115).
- [Heu17] N. Heurich, *Die externe Strahlführung für Detektortests X3ED an der Elektronen-Stretcher-Anlage ELSA*, PhD thesis: Rheinische Friedrich-Wilhelms-Universität Bonn, 2017, URL: <http://nbn-resolving.de/urn:nbn:de:hbz:5n-49191> (cit. on pp. 7, 46).
- [Hil00] W. Hillert, *Erzeugung eines Nutzstrahls spinpolarisierter Elektronen an der Beschleunigeranlage ELSA*, habilitation: Rheinische Friedrich-Wilhelms-Universität Bonn, 2000, URL: https://www-elsa.physik.uni-bonn.de/Publikationen/texte/hillert_habil.pdf (cit. on pp. 2, 86, 87).
- [Hil95] W. Hillert, *Comptonsim: Ein Programm zur Integration des Wirkungsquerschnitts der Compton-Streuung*, ELSA internal report, 1995 (cit. on p. 81).
- [Hin15] F. Hinterkeuser, *Setup and Studies of the Laser Beamline at the Compton Polarimeter at ELSA*, MA thesis: Rheinische Friedrich-Wilhelms-Universität Bonn, 2015, URL: https://www-elsa.physik.uni-bonn.de/Publikationen/texte/hinterkeuser_master.pdf (cit. on p. 88).
- [Hof01] M. Hoffmann, *Beschleunigung polarisierter Elektronen in der Bonner Elektronen-Beschleunigeranlage ELSA*, PhD thesis: Rheinische Friedrich-Wilhelms-Universität Bonn, 2001, URL: <http://nbn-resolving.de/urn:nbn:de:hbz:5n-00512> (cit. on pp. 117, 119).
- [Hof98] A. H. Hofmann, "Diagnostics with Synchrotron Radiation," *Proc. of CERN Accelerator School (CAS'96): Synchrotron Radiation and Free Electron Lasers* (Grenoble, France), CERN Accelerator School CERN-98-04, 1998, URL: <http://cdsweb.cern.ch/record/362891/files/CERN-98-04.pdf> (cit. on p. 16).
- [Jac67] J. Jackson, *Classical Electrodynamics*, John Wiley & Sons, Inc., New York, 1967 (cit. on pp. 10, 13, 14).
- [Jac76] J. D. Jackson, *On Understanding Spin-Flip Synchrotron Radiation and the Transverse Polarization of Electrons in Storage Rings*, *Rev. Mod. Phys.* **48** (3 1976) 417, URL: <https://link.aps.org/doi/10.1103/RevModPhys.48.417> (cit. on p. 20).
- [Kam10] S. Kammer, *Strahlpolarimetrie am CBELSA/TAPS Experiment*, PhD thesis: Rheinische Friedrich-Wilhelms-Universität Bonn, 2010, URL: <http://nbn-resolving.de/urn:nbn:de:hbz:5N-20564> (cit. on p. 4).

-
- [KHS16] R. Koop, W. Hillert, and M. T. Switka, “Compton Polarimetry at ELSA - Beamline and Detector Optimization,” *Proc. of International Particle Accelerator Conference (IPAC’16)* (Busan, Korea), International Particle Accelerator Conference 7, JACoW, 2016 95, ISBN: 978-3-95450-147-2, URL: <http://jacow.org/ipac2016/papers/mopmb010.pdf> (cit. on p. 88).
- [KM59] H. W. Koch and J. W. Motz, *Bremsstrahlung Cross-Section Formulas and Related Data*, *Rev. Mod. Phys.* **31** (4 1959) 920, URL: <https://link.aps.org/doi/10.1103/RevModPhys.31.920> (cit. on p. 75).
- [KN29] O. Klein and Y. Nishina, *Über die Streuung von Strahlung durch freie Elektronen nach der neuen relativistischen Quantendynamik von Dirac*, *Zeitschrift für Physik* **52** (1929) 853, ISSN: 0044-3328, URL: <http://dx.doi.org/10.1007/BF01366453> (cit. on p. 69).
- [Koo19] R. Koop, *About the Silicon Microstrip Detector of the ELSA Compton Polarimeter*, PhD thesis in preparation: Rheinische Friedrich-Wilhelms-Universität Bonn, 2019 (cit. on p. 100).
- [Kri07] H. Krieger, *Grundlagen der Strahlungsphysik und des Strahlenschutzes*, 2nd ed., Vieweg+Teubner Verlag, Wiesbaden, 2007, ISBN: 978-3-8351-0199-9 (cit. on p. 45).
- [KW16] H. Kolanoski and N. Wermes, *Teilchendetektoren*, 1st ed., Springer, Heidelberg-New York, 2016 (cit. on pp. 80, 81).
- [Lar97] J. Larmor, *LXIII. On the Theory of the Magnetic Influence on Spectra; and on the Radiation from Moving Ions*, *The London, Edinburgh, and Dublin Philosophical Magazine and Journal of Science* **44** (1897) 503, URL: <https://doi.org/10.1080/14786449708621095> (cit. on p. 13).
- [Lee04] S. Lee, *Accelerator Physics*, 2nd ed., World Scientific Publishing, New Jersey, 2004, ISBN: 978-981-256-200-5 (cit. on pp. 15, 16, 21, 58, 61).
- [Leo87] W. R. Leo, *Techniques for Nuclear and Particle Physics Experiments*, 1st ed., Springer-Verlag Berlin, 1987, ISBN: 3-540-17386-2 (cit. on pp. 70, 71, 79, 80).
- [LT54] F. W. Lipps and H. A. Tolhoek, *Polarization Phenomena of Electrons and Photons. II: Results for Compton Scattering*, *Physica* **20** (1954) 385, ISSN: 0031-8914, URL: <http://www.sciencedirect.com/science/article/pii/S0031891454800541> (cit. on p. 70).
- [MB06] A. Marbs and F. Boochs, *Investigating the Influence of Ionizing Radiation on Standard CCD Cameras and a Possible Impact on Photogrammetric Measurements*, ISPRS Commission V Symposium: Image Engineering and Vision Metrology (2006) 184, URL: https://www.isprs.org/proceedings/XXXVI/part5/paper/MARB_645.pdf (cit. on p. 44).
- [Men09] D. Menze, *Konzeption eines Bleiglasdetektors zum Nachweis von Compton-Photonen*, ELSA internal report, Physics Institute of Bonn University, 2009 (cit. on p. 73).
- [Mes04] D. Meschede, *Optics, Light and Lasers: The Practical Approach to Modern Aspects of Photonics and Laser Physics*, Wiley-VCH Verlag GmbH & Co. KGaA, Weinheim, 2004 (cit. on p. 137).

- [MNT14] P. Mohr, D. Newell, and B. Taylor, *The 2014 CODATA Recommended Values of the Fundamental Physical Constants*, National Institute of Standards and Technology, 2014, URL: https://physics.nist.gov/cgi-bin/cuu/Value?gammae%7Csearch_for=all! (cit. on p. 10).
- [MSY05] S. R. Mane, Y. M. Shatunov, and K. Yokoya, *Siberian Snakes in High-Energy Accelerators*, *Journal of Physics G: Nuclear and Particle Physics* **31** (2005) R151, URL: <http://stacks.iop.org/0954-3899/31/i=9/a=R01> (cit. on p. 18).
- [NHR85] W. R. Nelson, H. Hirayama, and D. W. Rogers, *The EGS4 Code System*, tech. rep., 1985, URL: <http://www.slac.stanford.edu/cgi-wrap/getdoc/slac-r-265.pdf> (cit. on p. 80).
- [Pea01] K. Pearson, *XI. Mathematical Contributions to the Theory of Evolution.—X. Supplement to a Memoir on Skew Variation*, *Philosophical Transactions of the Royal Society of London. Series A, Containing Papers of a Mathematical or Physical Character* **197** (1901) 443, eprint: <https://royalsocietypublishing.org/doi/pdf/10.1098/rsta.1901.0023>, URL: <https://royalsocietypublishing.org/doi/abs/10.1098/rsta.1901.0023> (cit. on p. 104).
- [Pol] M. N. Polyanskiy, *Refractive Index Database*, URL: <https://refractiveindex.info> (visited on 01/02/2018) (cit. on p. 31).
- [PR89] M. Placidi and R. Rossmanith, $e^+ - e^-$ Polarimetry at LEP, *Nuclear Instruments and Methods in Physics Research Section A: Accelerators, Spectrometers, Detectors and Associated Equipment* **274** (1989) 79, ISSN: 0168-9002, URL: <http://www.sciencedirect.com/science/article/pii/0168900289903677> (cit. on p. 75).
- [Pre+92] W. H. Press et al., *Numerical Recipes in C – The Art of Scientific Computing*, 2nd ed., Cambridge University Press, Cambridge, 1992, ISBN: 0-521-43108-5 (cit. on p. 129).
- [Pro18] D. Proft, *Das Neue Timing-System an ELSA*, PhD thesis: Rheinische Friedrich-Wilhelms-Universität Bonn, 2018 (cit. on pp. 56, 64).
- [Rau99] R. Rausch, “Electronic Components and Systems and their Radiation Qualification for Use in the LHC Machine,” *Proc. of 5th Convergence on Electronics for LHC Experiments* (Snowmass, CO, USA), CERN-SL-99-004-CO, 1999 7, URL: <https://cds.cern.ch/record/406280> (cit. on p. 46).
- [RD04] M. S. del Rio and R. J. Dejus, *Status of XOP: an X-ray Optics Software Toolkit*, *Proc. SPIE* **5536** (2004) 171, URL: <https://doi.org/10.1117/12.560903> (cit. on pp. 15, 17).
- [Rot12] A. Roth, *Breitbandige Feedback-Systeme zur Dämpfung kohärenter Strahlinstabilitäten am Stretcherring ELSA*, PhD thesis: Rheinische Friedrich-Wilhelms-Universität Bonn, 2012, URL: <http://nbn-resolving.de/urn:nbn:de:hbz:5n-30908> (cit. on pp. 2, 52).
- [Sab73] A. P. Sabersky, *The Geometry And Optics Of Synchrotron Radiation*, Part. Accel. **5** (1973), URL: <http://cds.cern.ch/record/1107936> (cit. on p. 28).

-
- [Sau19] D. Sauerland, *About Ion Studies at ELSA*, PhD thesis in preparation: Rheinische Friedrich-Wilhelms-Universität Bonn, 2019 (cit. on p. 76).
- [Sch15] M. Schedler, *Intensitäts- und Energieerhöhung an ELSA*, PhD thesis: Rheinische Friedrich-Wilhelms-Universität Bonn, 2015, URL: <http://nbn-resolving.de/urn:nbn:de:hbz:5n-42070> (cit. on pp. 2, 52, 55, 57).
- [Sch17] J. Schmidt, *Spindynamik in Elektronensynchrotronen*, PhD thesis: Rheinische Friedrich-Wilhelms-Universität Bonn, 2017, URL: <http://nbn-resolving.de/urn:nbn:de:hbz:5n-48314> (cit. on pp. 12, 117, 119).
- [Sch95] F. Schwabl, *Quantum Mechanics*, 2nd ed., Springer-Verlag Berlin Heidelberg, 1995, ISBN: 3-540-56812-3 (cit. on p. 10).
- [Sha08] L. Shampine, *Vectorized Adaptive Quadrature in MATLAB*, *Journal of Computational and Applied Mathematics* **211** (2008) 131, ISSN: 0377-0427, URL: <http://www.sciencedirect.com/science/article/pii/S037704270600700X> (cit. on p. 105).
- [Sie98] A. E. Siegman, *How to (Maybe) Measure Laser Beam Quality*, *DPSS (Diode Pumped Solid State) Lasers: Applications and Issues* (1998), URL: <http://www.osapublishing.org/abstract.cfm?URI=DLAI-1998-MQ1> (cit. on p. 137).
- [Sob79] D. Sober, *A Semi-Empirical Formula for Single-Converter Photon Detection Efficiency Below 500 MeV*, *Nuclear Instruments and Methods* **166** (1979) 555, URL: <https://www.sciencedirect.com/journal/nuclear-instruments-and-methods/vol/166/issue/3> (cit. on p. 78).
- [SSJ91] A. E. Siegman, M. W. Sasnett, and T. F. Johnston, *Choice of Clip Levels for Beam Width Measurements using Knife-Edge Techniques*, *IEEE Journal of Quantum Electronics* **27** (1991) 1098, ISSN: 0018-9197, URL: <https://ieeexplore.ieee.org/document/83346> (cit. on p. 93).
- [ST86] A. Sokolov and I. Ternov, *Radiation from Relativistic Electrons*, ed. by C. Kilmister, trans. from the Russian by S. Chomet, American Institute of Physics, Maryland, 1986, ISBN: 0-88318-507-5 (cit. on pp. 18, 20, 21).
- [Ste99] C. Steier, *Polarisierte Elektronen in der Elektronen-Stretcher-Anlage ELSA*, PhD thesis: Rheinische Friedrich-Wilhelms-Universität Bonn, 1999, URL: https://www-elsa.physik.uni-bonn.de/Publikationen/texte/steier_dr.pdf (cit. on pp. 50, 117, 119).
- [Suz76] T. Suzuki, *Luminosity for Electron-Proton Collision in TRISTAN (Coasting Proton Beam)*, (1976), URL: www.iaea.org/inis/collection/NCLCollectionStore/_Public/08/340/8340872.pdf (cit. on p. 75).
- [Tav10] S. Tavernier, *Experimental Techniques in Nuclear and Particle Physics*, Springer-Verlag Berlin Heidelberg, 2010, ISBN: 978-3-642-00828-3 (cit. on p. 77).

- [The11] The International Commission on Radiation Units and Measurements, *Report 85: Fundamental Quantities and Units for Ionizing Radiation (Revised)*, *Journal of the ICRU* **11** (2011), ed. by S. M. Seltzer, URL: <https://academic.oup.com/jicru/article-pdf/11/1/NP/2440176/ndr012.pdf> (cit. on p. 77).
- [Tho] U. Thoma, *Collaborative Research Centre 16: Subnuclear Structure of Matter*, URL: <http://sfb-tr16.physik.uni-bonn.de/vfs/en/homepage/> (cit. on p. 1).
- [Tho27] L. H. Thomas, I. *The Kinematics of an Electron With an Axis*, *The London, Edinburgh, and Dublin Philosophical Magazine and Journal of Science* **3** (1927) 1, URL: <http://dx.doi.org/10.1080/14786440108564170> (cit. on p. 11).
- [UG25] G. E. Uhlenbeck and S. Goudsmit, *Ersetzung der Hypothese vom unmechanischen Zwang durch eine Forderung bezüglich des inneren Verhaltens jedes einzelnen Elektrons*, *Die Naturwissenschaften* **13** (1925) 953, ISSN: 1432-1904, URL: <https://doi.org/10.1007/BF01558878> (cit. on p. 9).
- [Wen94] J. Wenzel, *Entwicklung und Test eines Simulators der Teilchenbewegung in der Bonner 3.5 GeV-Elektronen-Stretcher-Anlage ELSA*, PhD thesis: Rheinische Friedrich-Wilhelms-Universität Bonn, 1994, URL: https://www-elsa.physik.uni-bonn.de/Publikationen/texte/wenzel_dr.pdf (cit. on p. 62).
- [Wie93] H. Wiedemann, *Particle Accelerator Physics - Basic Principles and Linear Beam Dynamics*, Springer-Verlag Berlin Heidelberg, 1993 (cit. on pp. 56, 58).
- [Wil00] K. Wille, *The physics of Particle Accelerators: An Introduction*, ed. by J. McFall, Oxford university press, 2000, ISBN: 0-19-850550-7 (cit. on pp. 15, 50, 52, 54, 55, 57, 62).
- [Wun97] R. Wunstorf, *Radiation Hardness of Silicon Detectors: Current Status*, *IEEE Transactions on Nuclear Science* **44** (1997) 806, ISSN: 0018-9499 (cit. on p. 44).
- [Zan+12] S. Zander et al., “A New Diagnostic Beamline at ELSA,” *Proc. 3rd International Particle Accelerator Conference (IPAC’12)* (New Orleans, USA), International Particle Accelerator Conference 6, JACoW, 2012 795, ISBN: 978-3-95450-115-1, URL: <http://accelconf.web.cern.ch/Accelconf/IPAC2012/papers/moppr011.pdf> (cit. on p. 24).
- [Zan13] S. Zander, *Optische Strahldiagnose an der Elektronen-Stretcher-Anlage ELSA*, PhD thesis: Rheinische Friedrich-Wilhelms-Universität Bonn, 2013, URL: <http://nbn-resolving.de/urn:nbn:de:hbz:5n-33659> (cit. on pp. 23, 24, 27, 50).

List of Figures

1.1	ELSA storage ring cycle.	2
1.2	ELSA facility drawing.	3
1.3	Total photoabsorption cross section of $\vec{\gamma}\vec{p} \rightarrow X$ reactions [Har17].	5
1.4	Setup of the crystal-barrel experiment at ELSA [Har17].	5
1.5	Setup of the BGO-OD experiment at ELSA.	7
2.1	Electron spin vector \vec{S} rotating in the magnetic field [Bol14] of a circular accelerator.	11
2.2	The particle spin vector \vec{S} precessing around the vertical spin axis.	12
2.3	Power loss due to the emission of synchrotron radiation at ELSA for several stored beam currents.	14
2.4	Synchrotron radiation cone sweeping across an observation point.	15
2.5	Calculated frequency spectrum of bending magnet radiation.	16
2.6	Flux dependence on vertical emission angle of SR as function of photon energy E_γ	17
2.7	Angular flux distribution for σ - and π -polarized VIS SR.	17
3.1	Technical drawing of the M7 SR diagnostic beamline.	24
3.2	Layout of the M7 diagnostic beamline optics.	26
3.3	Photograph of the M7 diagnostic beamline's back-end.	28
3.4	Refractive index of NBK-7 glass.	31
3.5	The streak camera's photocathode sensitivity.	31
3.6	Signal elongation due to dispersive light propagation in NBK-7 glass.	31
3.7	Working principle of a streak camera.	32
3.8	Streak camera operating in focus mode.	34
3.9	Streak camera apertures.	35
3.10	Streak camera slow sweep operation.	35
3.11	Injected bunch train image with intensity fluctuation artifacts and spectral analysis.	36
3.12	Slow sweep image with dual time base extension.	37
3.13	Schematic drawing of the synchroscan measurement principle with dual time base extension.	38
3.14	Bunch length measurements in one transverse dimension.	39
3.15	Streak camera image of longitudinal beam oscillations.	40
3.16	Dual time base synchroscan bunch length measurement.	40
3.17	Bunch length measurements in two transverse dimensions.	41
3.18	Flow diagram of the streak camera's subsystems.	43
3.19	Wiring at the patch panel for the streak camera's trigger distribution.	43
3.20	Experimental area $E3$ with electron and photon beamline.	44
3.21	Equivalent dose of photons and neutrons measured at the streak camera.	45
3.22	Simulated radiation dose in the $E3$ area.	47
4.1	Orientation of the moving, curvilinear coordinate system for electrons at ELSA.	49

4.2	Optical functions $\beta_x(s)$, $\beta_z(s)$ and $D_x(s)$ of the ELSA storage ring.	51
4.3	Determining the horizontal betatron tune Q_x through a streak image.	53
4.4	Longitudinal phase focusing of relativistic particles.	54
4.5	Streak camera image of longitudinal beam oscillations.	55
4.6	Tune diagram with resonance stop bands and typical ELSA working point.	56
4.7	Synchroscan measurement of an excited and damped longitudinal oscillation.	57
4.8	Streak camera measurements of longitudinal damping times.	58
4.9	Bunch length measurements with varying beam energy and synchrotron frequency.	59
4.10	Bunch length in dependence of normalized beam energy \mathcal{E}	60
4.11	Optical functions around the M7 beamline source point.	63
4.12	Electron beam size at the M7 beamline source point.	63
4.13	Streak camera filling pattern images of the standard injection scheme.	64
4.14	Analysis of filling pattern deviation in a single streak image.	65
5.1	Kinematics parameters of Compton scattering.	67
5.2	Angular distribution and energy of Compton scattered photons.	68
5.3	Energy dependence on observation angle ϑ in the laboratory frame.	69
5.4	Partial Compton cross section for keV photons.	70
5.5	Total Compton cross section in dependence of incident photon energy.	71
5.6	Spectrum of backscattered photons for varying storage ring energies.	72
5.7	Gas bremsstrahlung count rates.	76
5.8	Photon mass attenuation coefficient for lead.	78
5.9	Conversion efficiency for different lead converter thicknesses.	78
5.10	Stopping power for electrons in lead.	79
5.11	Working principle of a microstrip detector.	81
5.12	Compton backscattered profile at 2.4 GeV beam energy.	82
5.13	Difference of Compton backscattered profiles at 2.4 GeV.	82
5.14	Key parameters for the ELSA Compton polarimeter obtained from COMPTONSIM.	83
5.15	Simulation of Compton photon and background profiles.	83
6.1	Technical drawing of the Compton polarimeter beamline.	85
6.2	Schematic drawing of an Ar ⁺ gas laser.	86
6.3	Schematic drawing of the ELS Monodisk Gemini DPSS laser.	87
6.4	Schematic drawing of an OPSL.	88
6.5	Schematic drawing of the Compton polarimeter photon beamline.	90
6.6	Photographs of the Compton polarimeter photon beamline.	90
6.7	Photograph of the Compton polarimeter laser beam analysis section.	91
6.8	Optical functions around the Compton polarimeter interaction point.	91
6.9	Electron beam size at the Compton polarimeter interaction point.	91
6.10	Laser beam cross section along the Compton polarimeter photon beamline.	93
6.11	Illustration of the electron-photon interaction point.	93
6.12	The effect of lens position on beam waist position, width and beam divergence.	94
6.13	Technical drawing of the laser polarization analysis box.	96
6.14	Measurement of the circular photon polarization degree by <i>division of amplitude</i>	96
6.15	Measurement of circular photon polarization.	97
6.16	Pointing stability measured with a CCD camera.	99
6.17	Photograph of the Compton polarimeter detector module.	100

6.18	Schematic drawing of the signal processing circuitry of the γ -detector.	100
6.19	Compton detector and subcomponent status in ELSA booster mode.	101
6.20	Raw profile data of γ -photons from laser-electron interaction and background radiation.	102
6.21	Scaled and unscaled photon profile.	103
6.22	Flowchart for electron polarization analysis process.	104
6.23	Comparison of fit functions to a simulated CBS profile.	106
6.24	Measurement of a polarized 1.32 GeV electron beam in booster mode.	108
6.25	Exponential polarization build-up of a stored 2.73 GeV electron beam.	110
6.26	Scattering rate from the background-subtracted laser signals and from the bremsstrahlung background.	112
6.27	Polarization measurement accuracy under regular beam conditions.	113
7.1	Beam polarization and solenoid spin rotation angle.	116
7.2	Sketch of a quadrupole magnet with vertically displaced beam.	116
7.3	Beam polarization of the ELSA booster synchrotron for different electron energies.	118
7.4	Beam polarization at different stored beam energies measured with the ELSA Compton polarimeter.	118
7.5	Visualization of the <i>Froissart-Stora</i> relation.	119
7.6	Polarization measurements around the $\gamma a = 3$ imperfection resonance.	120
7.7	Polarization measurements around the $\gamma a = 4$ imperfection resonance.	120
7.8	SLICKTRACK simulation of equilibrium polarization at ELSA.	121
7.9	Simulated equilibrium polarisation at ELSA, with ideal and measurable relaxation times.	122
B.1	Bunch length measurement in dual base synchroscan mode with broadband VIS at a vertical time span of 1 363.7 ps.	130
B.2	Bunch length measurement in dual base synchroscan mode with broadband VIS at a vertical time span of 997.9 ps.	130
B.3	Bunch length measurement in dual base synchroscan mode with monochromatic VIS at a vertical time span of 997.9 ps.	131
B.4	Signal profiles and corresponding fits of bunch length measurements.	131
B.5	Comparison of measurement precision for varying width of AOI.	132
E.1	Exemplary beam waist of a propagating Gaussian beam with $w_0 = 1$ and $z_R = 1$	137
F.1	5 bit trim DAC channel correction.	139
F.2	Sum of 43806 profiles for scaling factor correction.	140
F.3	Software scaling correction values for the Compton microstrip detector.	140

List of Tables

1.1	Comparison of mid-energy accelerator facilities.	8
3.1	Magnification factors for streak camera operation.	27
3.2	Available streak camera deflection units and corresponding time ranges.	32
3.3	Beamline magnification settings.	33
3.4	Exemplary horizontal and vertical images and corresponding measured sizes.	33
3.5	Comparison of bunch length measurements with <i>top-</i> and <i>side view</i>	42
3.6	Neutron equivalent dose measurements at the streak camera with and without water barrier.	47
4.1	Optical functions at the M7 beamline source point.	62
4.2	Expected beam size at the M7 beamline source point for varying beam energies E and coupling factors κ	63
4.3	Comparison of homogeneity of filling patterns.	64
5.1	COMPTONSIM simulation parameters.	82
6.1	Verdi G18 laser properties from specification and measurement.	92
6.2	Quality comparison of different peak function data fits.	106
6.3	Results of a shift in the mean Δz measurement.	107
6.4	Fit parameters of an exemplary self-polarization measurement.	109
B.1	Comparison of mean bunch length, mean coefficient of determination $\overline{R^2}$ and reduced $\overline{\chi^2}$	129

Acronyms

AOI area of interest. [33–35](#), [41](#), [61](#), [129](#), [132](#), [153](#)

ASIC application-specific integrated circuit. [100](#), [102](#)

BBB bunch-by-bunch feedback system. [2](#), [39](#), [57](#)

betatron oscillation transverse particle oscillation around the orbit. [51](#), [52](#), [61](#), [157](#)

betatron tune number of [betatron oscillations](#) per revolution. [50](#), [52](#), [53](#), [55](#)

BGO bismuth germanate ($\text{Bi}_4\text{Ge}_3\text{O}_{12}$) crystal. [4](#), [6](#), [7](#), [157](#)

BGO-OD [BGO](#) crystal calorimeter and open dipole spectrometer experiment. [4](#), [6](#), [7](#)

BPM beam position monitor. [2](#), [93](#), [107](#)

bucket [RF](#) phase boundaries for stable acceleration. It determines the number of bunches in a circular accelerator (see [harmonic number](#)). [53](#)

CBELSA/TAPS crystal barrel experiment at [ELSA](#) with TAPS photon spectrometer. [4–7](#)

CBS Compton backward scattering. [4](#), [8](#), [19](#), [67](#), [69](#), [74](#), [85](#), [97](#), [100](#), [104](#), [106](#), [107](#), [123](#), [124](#), [153](#)

CCD charge-coupled device. [23](#), [26](#), [31–33](#), [43](#), [44](#), [46](#), [60](#), [77](#), [89–91](#), [96](#), [99](#)

circle of confusion spot from point source when image does not come into perfect focus. [28](#), [29](#)

circumference voltage energy added through the accelerating cavities per revolution to compensate [SR](#) emission power losses. [13](#)

coherent oscillating particles have the same frequency and phase, in contrast to [incoherent](#) oscillations. [52](#), [56](#), [158](#)

CRC collaborative research center. [1](#)

CW continuous wave. [86](#), [89](#)

DAC digital-to-analog converter. [100](#), [102](#), [139](#), [153](#)

DBR distributed Bragg reflector. [88](#)

DOF depth of field. [28](#), [29](#)

Dove prism the glass prism rotates the input beam by twice its transverse orientation. Hence, if orientated by 45° , it rotates an image transversely by 90° . [26](#), [27](#), [30](#)

DPSS diode pumped solid state (laser). 87, 88, 152

duty cycle fraction of duration of beam delivery to the experimental site and total cycle time. 1

ELSA Elektronen Stretcher Anlage. 1–4, 7, 8, 14–21, 23, 29, 31, 35, 38, 42, 43, 49–53, 56–59, 62–64, 70, 71, 73, 75–78, 80, 83, 85–87, 89, 90, 101, 106, 110, 115–119, 121, 123, 124, 151–153, 157, 158

ELSA CS ELSA control system. 42, 59, 104, 124

FFT fast Fourier transform. 36

FPGA field programmable gate array. 64, 100

hard X-ray X-ray photons with energies from approx. 5 to 200 keV. 19

harmonic number number of buckets circulating in a storage ring, given by RF wavelength and lattice circumference. 53, 157

HEP high energy particle physics. 4, 7

HOM higher order mode. 57

HPD-TA Hamamatsu streak camera control software and temporal analyzer. 42

hyperfocal distance minimum distance of an object to an optical device, at which objects at infinity are still resolvable. 29

IGP ion getter pump. 23, 92

incoherent oscillating particles have different frequencies and phases, in contrast to **coherent** oscillations. 12, 57, 61, 157

IP interaction point. 69, 75, 81, 83, 93, 94, 107, 124

IR infrared. 2, 88, 89, 102

lattice magnetic structure of an accelerator. 1, 8, 11–13, 49, 50, 52, 53, 57, 58, 62, 158

LHC large hadron collider, located in Geneva. 7

linac linear accelerator. 1, 2, 4, 8, 13, 115, 116

LIR laser interaction region. 86, 87, 89–92, 98, 99, 111

LOI line of interest. 33, 34

MCP micro-channel plate. 32, 33, 129

MIP minimum ionizing particle. 80

momentum compaction factor momentum compaction describes the additional path length in a circular **lattice** in dependence on particle momentum. 53

-
- Mott scattering** inelastic scattering of spin-polarized electrons off the Coulomb field of heavy atoms. [2](#)
- Møller scattering** inelastic scattering of spin-polarized electrons off spin-polarized shell electrons. [4](#), [6](#)
- OPSL** optically pumped semiconductor laser. [88](#), [89](#), [92](#), [124](#), [152](#)
- PBS** polarizing beam splitter. [89](#), [90](#), [95–98](#), [125](#)
- PSD** position sensitive detector. [23](#), [87](#), [89](#), [90](#), [95](#), [96](#), [107](#)
- PWA** partial wave analysis. [6](#), [8](#)
- RC** remote control. [25](#), [33–35](#), [41](#), [89–91](#), [98](#)
- RF** radio frequency. [1](#), [2](#), [19](#), [36](#), [38](#), [42](#), [53](#), [55](#), [59](#), [117](#), [157](#), [158](#)
- RMS** root mean square. [14](#), [16](#), [58](#), [87](#), [99](#)
- SHG** second harmonic generation. [87–89](#)
- SNR** signal-to-noise ratio. [37](#), [39](#)
- spline** piecewise polynomial. [104](#), [105](#)
- SR** synchrotron radiation. [1](#), [2](#), [7](#), [9](#), [13–19](#), [21](#), [23–26](#), [28](#), [44](#), [46](#), [49](#), [53](#), [54](#), [58](#), [60](#), [62](#), [63](#), [69](#), [74](#), [75](#), [109](#), [119](#), [123](#), [127](#), [128](#), [151](#), [157](#)
- synchronous phase** phase of acceleration. Particles oscillate longitudinally around it. [53–55](#), [159](#)
- synchrotron oscillation** longitudinal particle oscillation around the [synchronous phase](#). [54–57](#), [159](#)
- synchrotron tune** number of [synchrotron oscillations](#) per revolution. [55](#), [56](#)
- TCP** transmission control protocol. [42](#)
- TOF** time of flight. [7](#), [41](#)
- TTL** transistor-transistor logic. [38](#), [42](#)
- UHV** ultra high vacuum. [2](#)
- UV** ultraviolet radiation. [8](#), [24](#), [26](#), [27](#)
- VCSEL** vertical-cavity surface-emitting laser. [88](#)
- VIS** visible photon radiation. [2](#), [16](#), [17](#), [23–26](#), [29](#), [30](#), [59](#), [68](#), [75](#), [87](#), [123](#), [130](#), [131](#), [151](#), [153](#)
- X-ray** high energetic electromagnetic radiation with energy from approx. 0.2 to 200 keV. [19](#), [23](#), [24](#), [158](#)
- Yb:YAG** ytterbium (Yb) doped yttrium aluminum garnet (YAG: $Y_3Al_5O_{12}$) crystal. [87](#), [88](#)

Acknowledgements

I would like to express my sincere gratitude to all who have provided good advice for the success and final outcome of the research projects reported in this dissertation.

I owe my profound gratitude to my supervisor Prof. Dr. Wolfgang Hillert for providing the aforementioned research projects, and for useful discussions and comments during his time as group leader.

Furthermore, I would like to thank Prof. Dr. Klaus Desch for the support as co-examiner and his patience as group leader of the ELSA accelerator facility during the development process of this dissertation.

For preparatory work of the hardware installations, I would like to express my gratitude to Dr. Sven Zander for the realization of the synchrotron radiation beamline in 2013, and to Jürgen Wittschen and Dr. Bastian Aurand for their engagement in the realization of the ELSA Compton polarimeter version of 2008, as *picking up the pieces* greatly accelerated the hardware development for the contemporary polarimeter version.

Special thanks go to Rebecca Koop for her commitment to the realization of the silicon microstrip detector, whose functionality was crucial for the testing of the polarimeter.

Many thanks go to Prof. Dr. Dieter Meschede and his research group, who provided the laser source for the three month long testing period.

Special thanks are given to Dr. Frank Frommberger for his scientific advice, many insightful discussions and great support in machine control and software questions.

I am also grateful to Dipl.-Ing. Philipp Hänisch, Jörg Schelske and Michael Brock, who have supplied me with valuable technical and mechanical support.

I would like to thank Dr. Andreas Dieckmann, Dipl.-Ing. Franz-Gerhard Engelmann and Dipl.-Ing. Michael Humpert for providing support in electrical and facility specific matters.

Also, I thank all my academic colleagues, who have willingly shared their precious time during the process of discussion of hardware performance, results, data analysis and programming techniques, proofreading and finalizing this thesis. I want to acknowledge Dr. Dennis Proft, Dennis Sauerland, Jens-Peter Thiry, Dr. Jan Schmidt, Dr. Nicolas Heurich, Rebecca Koop, Florian Hinterkeuser, Tobias Schiffer and Dr. Sven Zander. The group has been a source of friendship as well as good advice and collaboration.

I appreciate the support of all ELSA technical staff members for advice, service and installations, namely Thomas Becker, Klaus-Peter Fassbender, Martin Holzhäuser, Peter Mahlberg, Wolfgang Merfert, Andreas Merzbach, Rolf Müller, Andreas Offermanns, Norbert Rick and Aytakin Yildiz.

I owe my profound gratitude to the developers of free scientific software such as GNU Octave, whose functionality provided the core analysis frame for the data analyzed during the course of this dissertation. For the elegance of appearance and design of this document I like to thank the developers of LaTeX and PGF plots.

My profound gratitude goes to the DFG which has majorly funded these research projects.

Last but not least I would like to thank my loved ones, who have supported me throughout the entire process, both by keeping me harmonious and helping me putting pieces together. Sonja, you gave me your unconditional support through all this long process. Thank you for all your love and attention.